

Sandro A.P. Haddad
Wouter A. Serdijn

ACSP
Analog Circuits And Signal Processing

Ultra Low-Power Biomedical Signal Processing

An Analog Wavelet Filter Approach
for Pacemakers

 Springer

Ultra Low-Power Biomedical Signal Processing

Analog Circuits and Signal Processing

For other titles published in this series, go to
www.springer.com/series/7381

Sandro A.P. Haddad • Wouter A. Serdijn

Ultra Low-Power Biomedical Signal Processing

An Analog Wavelet Filter Approach
for Pacemakers



Springer

Sandro A.P. Haddad
Freescale Semiconductor
Rua James Clerk Maxwell, 400
Condominio Techno Park
13069-380 Campinas-SP
Brazil
sandro.haddad@freescale.com

Wouter A. Serdijn
Delft University of Technology
Electronics Research Lab.
Mekelweg 4
2628 CD Delft
The Netherlands
w.a.serdijn@tudelft.nl

ISBN 978-1-4020-9072-1
DOI 10.1007/978-1-4020-9073-8
Library of Congress Control Number: 2008944291

e-ISBN 978-1-4020-9073-8

© Springer Science + Business Media B.V. 2009

No part of this work may be reproduced, stored in a retrieval system, or transmitted in any form or by any means, electronic, mechanical, photocopying, microfilming, recording or otherwise, without written permission from the Publisher, with the exception of any material supplied specifically for the purpose of being entered and executed on a computer system, for exclusive use by the purchaser of the work.

Cover design: WMXDesign GmbH

Printed on acid-free paper

9 8 7 6 5 4 3 2 1

springer.com

Foreword

As microelectronics has matured in human controlled tools like computers, another era of ubiquitous microelectronics is well underway. Compact, robust and dedicated microelectronic systems are combined with actuators and sensors in an increasing number of life-critical controls. Familiar questions from computer like: “Are you sure you want to do this? (Press OK to proceed)”, are not possible in these self-contained, autonomous control systems. These embedded control systems must make immediate decisions based on whatever information is available from the provided sensors.

The most challenging of these embedded control system are the devices implanted in humans. Not only do they control life-critical functions, but they have to do so under severe power and size constraints. In addition, the sensed signals are often noisy and weak, demanding complicated and computationally intensive signal processing. In spite of these challenges, cardiac pacemakers are implanted in hundreds of thousand humans every year. Some reports indicate battery lives exceeding twenty years of operation.

The implantable pacemaker was first introduced in the late 1950s and has been refined and improved in a number of ways since then. This new book “Ultra Low-Power Biomedical Signal Processing – An Analog Wavelet Filter Approach for Pacemakers” by SANDRO A. P. HADDAD and WOUTER A. SERDIJN is addressing the core problems of efficient linear and nonlinear, signal processing in biomedical devices in general, with special emphasis on pacemaker electronics. The proposed analog wavelet filter approach is demonstrated to be a power efficient and flexible method for integrated pacemaker electronics.

This book should be appreciated by anybody in need of power-efficient, linear and non-linear signal processing suitable for microelectronics. A balanced and understandable discussion of trade-offs towards the more traditional Fourier analysis exposes the benefits of wavelet filters. For pacemakers typical time-domain information like the QRS complex of the ECG signal is sought. Another important insight is how to use the log-domain (dynamic translinear) circuit technique for power efficient electronics. Convincing results are provided.

Although the primary device addressed in this book is the implantable pacemaker, the authors indicate the general properties and usefulness of

wavelet filters in general, not only for biomedical applications. The completeness of wavelet filter theory combined with the transition to practical circuits make this book mandatory for everybody aiming at power efficient embedded control systems.

Oslo, November 2008

Tor Sverre Lande
Nanoelectronics Group
Department of Informatics
University of Oslo
Norway

Contents

| | | |
|----------|--|-----------|
| 1 | Introduction | 1 |
| 1.1 | Biomedical signal processing | 1 |
| 1.2 | Biomedical applications of the wavelet transform | 2 |
| 1.3 | Analog versus digital circuitry – a power consumption challenge for biomedical front-ends | 4 |
| 1.3.1 | Power consumption in analog sense amplifiers | 5 |
| 1.3.2 | Power consumption in digital sense amplifiers | 6 |
| 1.4 | Objective and scope of this book | 9 |
| 1.5 | Outline | 10 |
| 2 | The Evolution of Pacemakers: An Electronics Perspective | 13 |
| 2.1 | The heart | 14 |
| 2.2 | Cardiac signals | 16 |
| 2.2.1 | Surface electrocardiogram | 16 |
| 2.2.2 | Intracardiac electrogram (IECG) | 17 |
| 2.2.3 | Cardiac diseases – arrhythmias | 17 |
| 2.3 | The history and development of cardiac pacing | 18 |
| 2.3.1 | What is an artificial pacemaker? | 18 |
| 2.3.2 | Hyman’s pacemaker | 19 |
| 2.3.3 | Dawn of a modern era – implantable pacemakers | 19 |
| 2.4 | New features in modern pacemakers | 26 |
| 2.5 | Summary and conclusions | 29 |
| 3 | Wavelet versus Fourier Analysis | 33 |
| 3.1 | Introduction | 33 |
| 3.2 | Fourier transform | 33 |
| 3.3 | Windowing function | 34 |
| 3.4 | Wavelet transform | 35 |
| 3.4.1 | Continuous-time wavelet bases | 39 |
| 3.4.2 | Complex continuous-time wavelet bases | 41 |
| 3.5 | Signal processing with the wavelet transform | 42 |
| 3.5.1 | Singularity detection – wavelet zoom | 42 |
| 3.5.2 | Denoising | 47 |
| 3.5.3 | Compression | 47 |

| | | |
|----------|--|-----------|
| 3.6 | Low-power analog wavelet filter design | 48 |
| 3.7 | Conclusions | 49 |
| 4 | Analog Wavelet Filters: The Need for Approximation | 51 |
| 4.1 | Introduction | 51 |
| 4.2 | Complex first-order filters | 51 |
| 4.3 | Padé approximation in the Laplace domain | 56 |
| 4.4 | L_2 approximation | 63 |
| 4.5 | Other approaches to wavelet base approximation | 66 |
| 4.5.1 | Bessel–Thomson filters – a quasi-Gaussian impulse response | 66 |
| 4.5.2 | Filanovsky’s filter approach [15] | 67 |
| 4.5.3 | Fourier-series method | 68 |
| 4.6 | Discussion | 71 |
| 4.7 | Conclusions | 73 |
| 5 | Optimal State Space Descriptions | 75 |
| 5.1 | State space description | 75 |
| 5.2 | Dynamic range | 77 |
| 5.2.1 | Dynamic range optimization | 78 |
| 5.3 | Sparsity | 80 |
| 5.3.1 | Orthogonal transformations | 80 |
| 5.3.2 | Canonical form representations | 82 |
| 5.3.3 | Biquad structure | 84 |
| 5.3.4 | Diagonal controllability Gramian – an orthonormal ladder structure | 85 |
| 5.3.5 | Sparsity versus dynamic range comparison | 88 |
| 5.3.6 | New Sparsity Figure-of-Merit (SFOM) | 89 |
| 5.4 | Sensitivity | 90 |
| 5.4.1 | New Dynamic Range–Sparsity–Sensitivity (DRSS) figure-of-merit | 93 |
| 5.5 | Conclusion | 94 |
| 6 | Ultra Low-Power Integrator Designs | 95 |
| 6.1 | G_m –C filters | 95 |
| 6.1.1 | nA/V CMOS triode transconductor | 96 |
| 6.1.2 | A pA/V Delta– G_m (Δ – G_m) transconductor | 99 |
| 6.2 | Translinear (log-domain) filters | 101 |
| 6.2.1 | Static and dynamic translinear principle | 101 |
| 6.2.2 | Log-domain integrator | 103 |
| 6.3 | Class-A log-domain filter design examples | 105 |
| 6.3.1 | Bipolar multiple-input log-domain integrator | 105 |
| 6.3.2 | CMOS multiple-input log-domain integrator | 106 |

| | | |
|----------|--|------------|
| 6.3.3 | High-frequency log-domain integrator in CMOS technology | 107 |
| 6.4 | Low-power class-AB <i>sinh</i> integrators | 111 |
| 6.4.1 | A state-space formulation for class-AB log-domain integrators | 111 |
| 6.4.2 | Class-AB <i>sinh</i> integrator based on state-space formula- tion using single transistors | 113 |
| 6.4.3 | Companding <i>sinh</i> integrator | 115 |
| 6.4.4 | Ultra low-power class-AB <i>sinh</i> integrator | 118 |
| 6.5 | Discussion | 127 |
| 6.6 | Conclusions | 128 |
| 7 | Ultra Low-Power Biomedical System Designs | 131 |
| 7.1 | Dynamic translinear cardiac sense amplifier for pacemakers . . | 132 |
| 7.1.1 | Differential voltage to single-ended current converter . . | 133 |
| 7.1.2 | Bandpass filter | 134 |
| 7.1.3 | Absolute value and RMS–DC converter circuits | 136 |
| 7.1.4 | Detection (Sign function) circuit | 137 |
| 7.2 | QRS-complex wavelet detection using CFOS | 140 |
| 7.2.1 | Filtering stage – CFOS wavelet filter | 141 |
| 7.2.2 | Decision stage – absolute value and peak detector circuits | 143 |
| 7.2.3 | Measurement results | 144 |
| 7.3 | Wavelet filter designs | 149 |
| 7.3.1 | Gaussian filters | 149 |
| 7.3.2 | Complex wavelet filter implementation | 156 |
| 7.4 | Morlet wavelet filter | 160 |
| 7.4.1 | Circuit design | 163 |
| 7.4.2 | Measurement results of the Morlet wavelet filter | 166 |
| 7.5 | Conclusions | 169 |
| 8 | Conclusions and Future Research | 173 |
| 8.1 | Future research | 175 |
| A | High-Performance Analog Delays | 179 |
| A.1 | Bessel–Thomson approximation | 179 |
| A.2 | Padé approximation | 180 |
| A.3 | Comparison of Bessel–Thomson and Padé approximation delay filters | 183 |
| A.4 | Gaussian time-domain impulse-response method | 183 |
| B | Model Reduction – The Balanced Truncation Method | 189 |
| C | Switched-Capacitor Wavelet Filters | 193 |

| | |
|--|------------|
| D Ultra-Wideband Circuit Designs | 199 |
| D.1 Impulse generator for pulse position modulation | 199 |
| D.2 A delay filter for an UWB front-end | 201 |
| D.3 A FCC compliant pulse generator for UWB communications . . | 203 |
| Summary | 205 |
| Acknowledgements | 209 |
| About the Authors | 211 |
| Index | 213 |

Chapter 1

Introduction

Around 40% of all human deaths are attributed to cardiovascular diseases. A practical way to decrease the overall cardiac mortality and morbidity is to supply patients at risk with an implantable device, known as artificial pacemaker, that is designed to monitor the cardiac status and to regulate the beating of the heart. Cardiac pacing has become a therapeutic tool used worldwide with over 250,000 pacemaker implants every year.

Cardiac pacemakers include real-time sensing capacities reflecting the state of the heart. Current pacemaker detection circuitry can be interpreted as a cardiac electrical signal compression algorithm squeezing the time signal information into a single event representing the cardiac activity. Future cardiac pacing algorithms, however, are believed to take advantage of the morphological aspects of the sensed cardiac signal, improving the analysis and the recording of relevant cardiac activity data via implantable sensors. This will provide, for instance, a new opportunity for monitoring and managing infarct-threatened patients and post-infarction patients outside the hospital.

In implantable medical devices, such as pacemakers, power consumption is critical, due to the limited power density and the longevity of currently available portable batteries. This implies that the design of such devices has to be optimized for very low power dissipation.

The purpose of this book is to detail the significant advances in cardiac pacing systems and to develop novel signal processing methodologies and analog integrated circuit techniques for low-power biomedical systems.

1.1 Biomedical signal processing

Biomedical signal processing centers on the acquisition of vital signals extracted from biologic and physiologic systems. These signals permit us to obtain information about the state of living systems, and therefore, their monitoring and interpretation have significant diagnostic value for clinicians and researchers to obtain information related to human health and diseases.

The processing of biomedical signals strongly depends on the knowledge about the origin and the nature of the signal and poses many special properties, which usually presents some unique problems. The reason for this is mainly due to the complexity of the underlying biologic structures and their signals, and the need to perform indirect, non-invasive measurements. In addition, the detected signals are commonly corrupted with noise, and thus, the relevant information is not “visible” and cannot be readily extracted from the raw signal. For such reasons, advanced signal processing is usually required.

Another important aspect of biomedical signals is that the information of interest is often a combination of features that are well localized temporally (e.g., spikes) and others that are more diffuse (e.g., small oscillations) [1]. This requires the use of analysis methods sufficiently versatile to handle events that can be at opposite extremes in terms of their time–frequency localization. In this book, we will investigate the ability of the wavelet analysis to extract information from a biomedical signal.

1.2 Biomedical applications of the wavelet transform

Physiological signals are mostly non-stationary, such as the electrocardiogram (ECG), the electroencephalogram (EEG) and the electromyogram (EMG). Those signals represent the electrical activity of the heart, the brain and the muscles, respectively. The main difficulty in dealing with biomedical signal processing is the extreme variability of the signals and the necessity to operate on a case by case basis [1]. The Wavelet transform (WT) has been extensively used in biomedical signal processing, mainly due to the versatility of the wavelet tools. It has been shown to be a very efficient tool for local analysis of non-stationary and fast transient signals due to its good estimation of time and frequency (scale) localizations [2], [3]. The wavelet transform is a linear operation that decomposes a signal into components that appear at different scales (or resolutions). The transform is based on the convolution of the signal with a dilated filter, thereby mapping the signal onto a two-dimensional function of time and frequency.

The uses of the WT in biomedical applications are extremely diverse. Signal analysis methods derived from wavelet analysis [2] carry large potential to support a wide range of biomedical signal processing applications including noise reduction [4], feature recognition [1] and signal compression [5]. The discussion here shall deal with wavelet techniques for cardiac signals analysis. It is, however, believed that these techniques can also successfully contribute to the analysis of other types of non-stationary signals, like those present in electroencephalograms (EEGs), i.e., electrical potentials associated with the brain; electrocorticograms (ECoGs), i.e., electrical potentials associated with the cerebral cortex; electromyograms (EMGs), i.e., electrical potentials asso-

ciated with muscles and electroretinograms (ERGs), i.e., electrical potentials associated with retinas.

Cardiac signal analysis

In the past few years, many new approaches to cardiac signal analysis have been proposed [6], e.g., algorithms based on filter banks [5], artificial neural networks [8], non-linear transformations [9] and the wavelet transform [10]. In Fig. 1.1, one can compare the numbers of publications in the IEEE online database related to electrocardiogram (ECG) signal detection for three different types of algorithms, being filter-based, wavelet transform and neural networks. Besides the fact that wavelet analysis is still relatively new, the wavelet-based signal processing methods have been evolving very rapidly and the rate of publication keeps increasing steadily.

There are several reasons for the growing number of algorithms using wavelets. Since usually cardiac signal and noise components share the same spectral bands, the scope of linear signal processing methods (linear filtering) is rather limited. Therefore, signal analysis methods improving discrimination of signals from noise and interference are of great importance. Several approaches [6] have demonstrated the potential of wavelet-based feature extraction for discriminating between normal and abnormal cardiac patterns.

Being a multiscale analysis technique, wavelets allow analysis of the electrogram focusing on the signal at various levels of detail, in analogy with

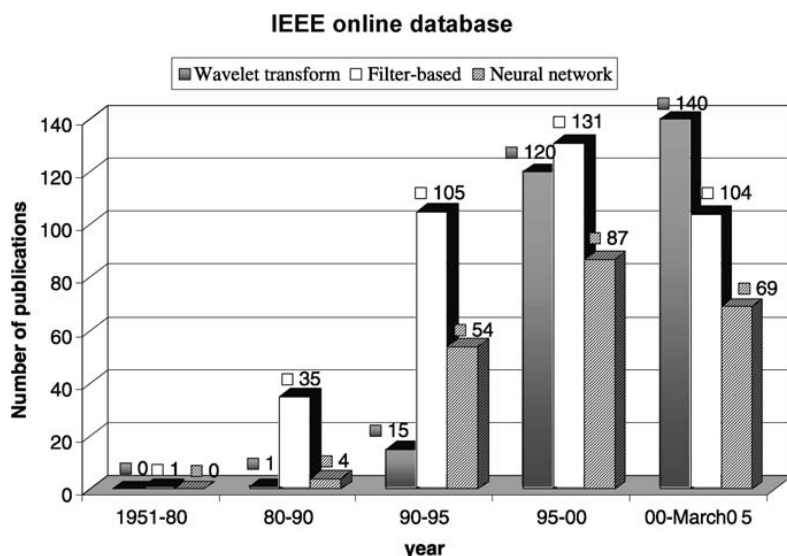


Fig. 1.1. IEEE online database publications of cardiac signal detection for different types of algorithms

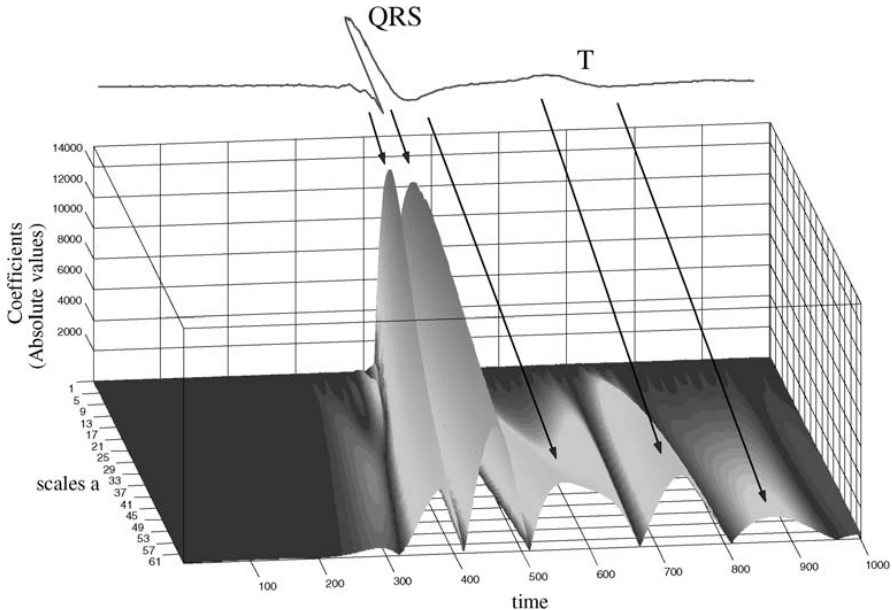


Fig. 1.2. Wavelet analysis of an intra-cardiac signal (IECG). For small values of scale a , the QRS-complex information is dominant, whereas for large values of a both QRS and T waves are well localized

inspection of a sample with a microscope at various levels of magnification. As one can see in Fig. 1.2, at very fine scales (smaller values of scale a), details of the electrogram, e.g., the QRS-complex (most striking waveform within the ECG), are revealed while unimpaired by the overall structure of the signal. At coarse scale (larger values of the scale factor a), the overall structure of the electrogram can be studied while overlooking the details. Note that by this global view, both the QRS-complex and the T-wave can be detected.

1.3 Analog versus digital circuitry – a power consumption challenge for biomedical front-ends

A modern pacemaker consists of a telemetry system to receive and transmit data, a sense amplifier (analog or digital) consisting of passive/active filters, an amplifier and a comparator, analog output circuitry (also known as pulse generator) which stimulates the heart, and a microprocessor acting as a controller for all the settings of the pacemaker system. Moreover, an algorithm in the microprocessor determines whether pacing is needed or not. Nevertheless, the longevity of a pacemaker must not be shortened by new improved features,

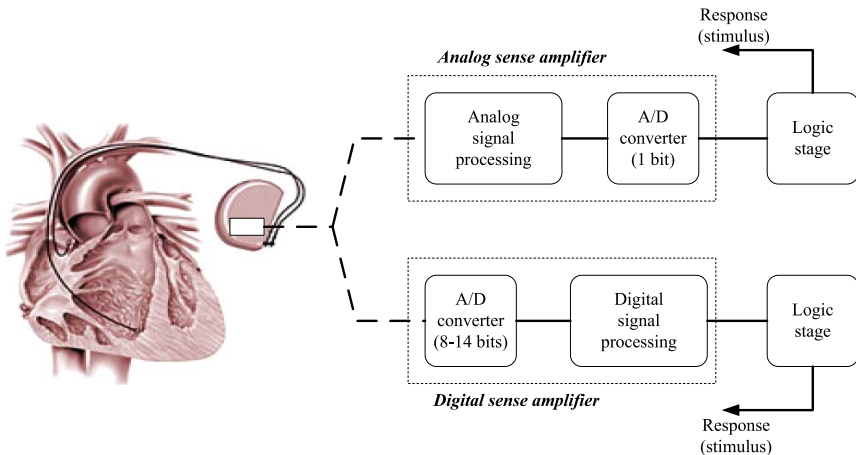


Fig. 1.3. Analog and digital sense amplifiers for pacemakers

so, reliable detection performance as well low power consumption is one of the most challenging design constraints.

The sense amplifier plays a fundamental role in providing information about the current state of the heart. State of the art implantable pulse generators or cardiac pacemakers include real-time sensing capabilities that are designed to detect and monitor intra-cardiac signal events (e.g., R-waves in the ventricle). A sense amplifier and its subsequent detection circuitry, together called the front-end, are shown in the block diagram in Fig. 1.3. As one can see in Fig. 1.3, the signal processing block of the front-end can be implemented with analog or digital circuitry and in the subsections that follow we will compare the minimum power required for both analog and digital implementations.

1.3.1 Power consumption in analog sense amplifiers

Generally, the detection of the electrical activity of the heart requires filtering, where there is a discrimination between cardiac signals and noise based on differences in energy spectra, and comparison to determine if a heart beat has occurred. Therefore, an analog sense amplifier derives only a single event (characterized by a binary pulse from the 1-bit A/D converter) and feeds this to a micro-controller (logic stage) that decides upon the appropriate pacing therapy to be delivered by the stimulator. The system consists of an analog signal processing unit, usually a bandpass filter, and a 1-bit comparator circuit. The bandpass filter is used to specifically select intra-cardiac signals and to minimize the effect of the noise and interference. Normally, an integrated continuous-time filter is realized as a network of integrators and this integration is exclusively performed by capacitive elements. The power per

pole figure of merit [11] gives an indication of the power dissipation associated with the elementary signal processing operation of integration (filtering).

Power per pole for analog filters

From this figure of merit, the minimum power dissipation (P_{an}) of an integrator, connected as a first-order low-pass filter and driven by a sinusoidal input signal, can be expressed in terms of the dynamic range (DR)

$$P_{an} = 8fkT\xi \text{DR} \quad (1.1)$$

where f is the cut-off frequency, kT is the thermal energy and ξ is the excess noise factor of the (trans)conductance element [12]. ξ is fundamentally greater equal than $\frac{1}{2}$. Thus, a large value for the noise factor translates directly to a proportionate disadvantage in terms of power dissipation. For a linearized transconductor, as found, e.g., in a G_m -C structure, the excess noise factor can be significantly larger, with common values of $\xi_{lin} \approx 3\text{--}8$ [13]. Whereas, for log-domain integrators, the noise factor can be approximated as $\xi_{log} \approx \frac{3}{2}$ [13]. This means that log-domain filter allows a substantial power saving compared to more traditional continuous-time filters. This can be partially explained by the fact that log-domain filters do not require any local linearization as traditional filters do [12].

1.3.2 Power consumption in digital sense amplifiers

Digital information is different from its continuous counterpart in two important respects: it is sampled, and it is quantized. In order to interface digital circuitry with the physical world, analog-to-digital converters (ADCs) are required, which convert the continuous-time signals to discrete-time, binary-coded form.

Power consumption in A/D converters

The resolution of the converter indicates the number of discrete values it can produce. The signal-to-noise ratio (SNR) of an ideal ADC is given by

$$\text{SNR}_{\text{dB}} = 6.02N - 1.25 + 10 \cdot \log \frac{f_s}{f_{sig}} \quad (1.2)$$

where N is the stated number of bits, f_s is the sampling frequency and f_{sig} is the highest frequency of the input signal. It can be noticed that for a Nyquist converter, where sampling frequency is defined as $f_s = 2f_{sig}$, the SNR_{dB} is now given by

$$\text{SNR}_{\text{dB}} = 6.02N + 1.76 \quad (1.3)$$

In [14], a figure of merit (F) has been defined that emphasizes efficiency with respect to power dissipation and signal-to-noise-and-distortion ratio SNDR

$$F = \frac{2^N f_s}{P} \quad (1.4)$$

where P is the power dissipation. Here we will consider an optimistic case where SNDR is equal to the Dynamic Range (DR). By this, one can quantify the ADC power consumption performance (P_{ADC}), which can be related to the correspondent DR by

$$P_{\text{ADC}} = \frac{2^{\text{ENOB}} f_s}{F} = \frac{2^{\frac{\text{DR}_{\text{dB}} - 1.76}{6.02}} f_s}{F} \quad (1.5)$$

ENOB being the “effective number of bits” of the ADC.

In this analysis, we will consider F equal to $1.2 \cdot 10^{12}$, which represents the present-day state-of-the-art A/D according to Walden in [14]. Another figure of merit known as the quantization energy (E_Q) per conversion step [15], is based on the effective resolution bandwidth (F_{BW}) instead of the sampling rate. This is defined as

$$E_Q = \frac{P_{\text{ADC}}}{2^N 2 F_{\text{BW}}} \quad (1.6)$$

where for a Nyquist ADC, F_{BW} is equal to f_s . As one can see, this quantity is nearly the inverse of the figure of merit suggested by Walden. Again, the analysis for minimal power consumption will be based on recently published papers, where the lowest reported number for E_Q is 2.8 pJ [16].

Finally, the fundamental limit for the quantization energy can be calculated based on the minimum thermal noise per pole (single capacitor) and the quantization noise [17]. This absolute lower bound on the quantization energy E_Q for an ADC of a given resolution N at any speed is given by [17]

$$E_{Q\min} > 48kT2^N \quad (1.7)$$

Thus, the absolute minimum power per cycle for an analog-to-digital converter can be defined from Eq. 1.6 and Eq. 1.7, resulting in

$$P_{\min,\text{ADC}} > 48kT2^{2N} \quad (1.8)$$

The following analysis relates consumed power to the function of the number of bits (N) representing the filtered information inside the digital filter. In the case of pacemakers, for instance, proper cardiac signal characterization would require at least 8–12 bits A/D conversion, at a sample rate of 1 kHz [18].

Power consumption in digital filters

To have a fair comparison of the minimal power needed in analog and digital filters, we will assume that the only noise source presented in the circuit is the thermal noise integrated on the capacitor, which presents a Gaussian distribution. Note that in a digital filter, the signal is represented by a sequence of bits, rather than a voltage or current. Hence, for digital signals, we can consider the associated noise in terms of probability that a bit-error will occur.

The bit-error function $P_{bit,error}$ is defined by the probability of having an instantaneous noise amplitude exceeding a certain threshold, so that a wrong decision about the logic level will be made. It is known that the power consumed by a digital filter and its corresponding dynamic range depend on the probability of the error we can allow in the logic gates [19], [20]. Hence, the function $P_{bit,error}$ can be defined as [19]

$$P_{bit,error} = \frac{1}{4} \left(\frac{1}{DR} - \frac{1}{2^{2N-1}} \right) = \frac{1}{2} \operatorname{Erfc} \left(\frac{1}{2} \sqrt{\frac{P_{dig}}{fkTN}} \right) \quad (1.9)$$

where Erfc represents the error function given by $\operatorname{Erfc}(x) = 1 - \frac{2}{\sqrt{\pi}} \int_0^x e^{-t^2} dt$. Note that from Eq. 1.9, we can relate the dynamic range (DR) with the corresponding power dissipation (P_{dig}) in a digital filter.

Figure 1.4 shows minimal power consumption per cycle, $(\frac{P_{an}}{f})$, $(\frac{P_{ADC}}{f})$, $(\frac{P_{dig}}{f})$, for the analog (analog filter) and digital (digital filter plus A/D converter) sense amplifiers, respectively, as a function of the DR achieved in the system. One can see that a digital filter presents lower power consumption than the equivalent analog filter. Nevertheless, due to the huge amount of power required for the analog-to-digital conversion, application of a fully digital signal processing in implantable devices like pacemakers is not feasible yet.

As a prediction of the power consumption related to A/D converters over the years, we can use the E_Q figure of merit described before. Figure 1.4 also shows how much the lowest reported quantization energy, and the corresponding $\frac{P_{ADC}}{f}$, decrease yearly [17]. One can see that E_Q decays almost linearly, from 29.3 pJ in 1995 [17] to 2.8 pJ in 2004 [16], with only a factor of ten improvement over nine years.

Thus, we can conclude that the power efficiency of A/D converters needs to improve considerably in order to have the power dissipation of the digital sense amplifier comparable to the analog signal processing and, due to its power constraints, implantable devices will still be implemented using analog signal processing for many years to come.

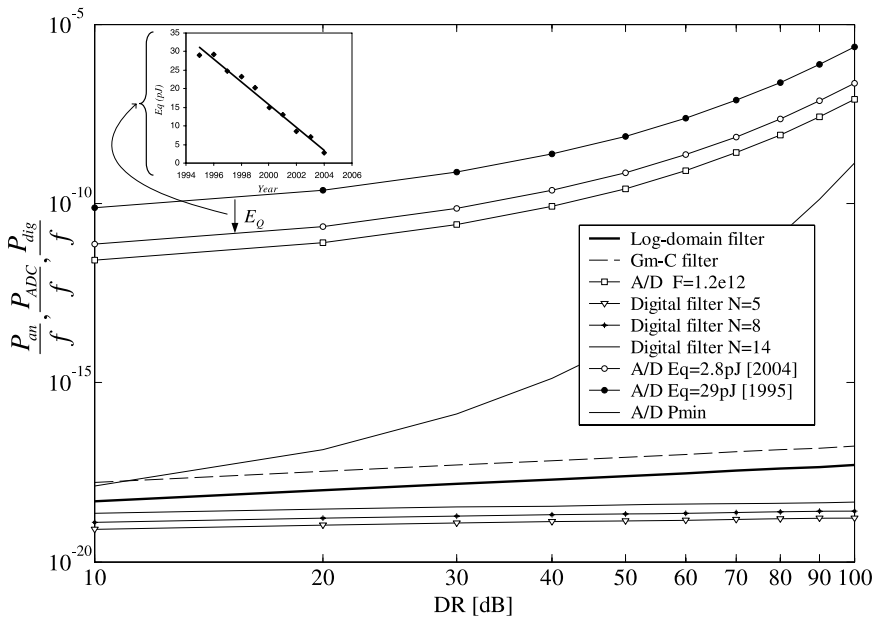


Fig. 1.4. Comparison of the analog and digital sense amplifiers' power consumption

1.4 Objective and scope of this book

The main objective of this book is the design of a novel signal processing system for ultra low-power real-time sensing of cardiac signals in pacemakers. Given the advantages in previous sections, the system will be based on wavelet transform using continuous-time analog circuitry.

The Wavelet Transform (WT) has been shown to be a very efficient tool for analysis of non-stationary signals, like cardiac signals. Being a multiscale analysis technique, it offers the possibility of selective noise filtering and reliable parameter estimation.

Low-power analog realization of the wavelet transform enables its application *in vivo*, e.g., pacemakers. In this application, the wavelet transform provides a means to extremely reliable cardiac signal detection. A promising technique for the design of ultra low-power analog integrated circuits is by means of Dynamic Translinear (DTL) circuits. The DTL principle can be applied to the implementation of functions described by linear and non-linear polynomial differential equations. Another suitable technique for low-power filters design is based on CMOS triode nA/V transconductors for linear G_m -C filters.

In this book, we propose a method for implementing the novel signal processing based on WT in an analog way. The methodology will focus then on

the development of ultra low-power analog integrated circuits that implement the required signal processing, taking into account the limitations imposed by an implantable device.

1.5 Outline

A brief overview of the history and development of circuit designs applied in pacemakers is presented in Chapter 2. The advances in integrated circuit designs have resulted in increasingly sophisticated pacing circuitry, providing, for instance, diagnostic analysis, adaptive rate response and programmability. Also, based on future trends for pacemakers, some features and improvements for modern cardiac sensing systems are described.

Chapter 3 deals with the properties of the WT as well as the definition of some wavelet bases. In addition, an example is given to illustrate the advantages and limitations of the frequency (Fourier transform), time (windowing function) and time-frequency (wavelet transform) representations.

From the wavelet definition, we can state that implementation of the WT is based on a bandpass filter design which presents an impulse response equal to a wavelet base. In order to obtain a suitable transfer function of such a “wavelet filter”, mathematical approximation techniques are required. Some of these approximation methods, i.e., Complex first-order system (CFOS), Padé and least mean square (L_2) approximations, will be presented in Chapter 4.

In Chapter 5, we will see that there are many possible state space descriptions, and, of course, different filter topologies that implement a particular transfer function. By choosing an appropriate state-space description and thus corresponding wavelet filter topology, we are able to achieve the required low power consumption, dynamic range, insensitivity to component variations and sparsity.

The trend towards lower power consumption, lower supply voltage and higher frequency operation has increased interest in new design techniques for analog integrated filters. The class of translinear (TL) filters, also known as log-domain filters, has emerged in recent years as a promising approach to face these challenges and will be presented in Chapter 6. In addition, new class-A log-domain and class-AB *sinh* integrator designs will be presented. In the field of medical electronics, active filters with large time constants are often required to design low cutoff-frequency filters (in the Hz and sub-Hz range), necessitating the use of large capacitors or very low transconductances. To limit capacitors to practical values, a transconductor with an extremely small transconductance G_m (typically a few nA/V) is needed. Ultra low-power CMOS triode nano-A/V and pico-A/V transconductors for low-frequency G_m -C filters are also introduced in this chapter.

In Chapter 7, the methodology presented in the previous chapter will be employed in the design of several ultra low-power biomedical systems. First, a benchmark cardiac sense amplifier, i.e., a standard pacemaker front-end,

based on the Dynamic Translinear (DTL) circuit technique is presented. Then, an analog QRS complex detection circuit, based on the Wavelet Transform (WT) is described. The system uses an CFOS structure to approximate the Gaussian wavelet base and the decision stage detects the wavelet modulus maxima of the QRS complex. Two convenient methods to provide the transfer function of the wavelet filter are given by the Padé and L_2 approximations and, thus, some designs based on these approaches, for Gaussian and Morlet wavelet bases, will also be presented. In addition, a complex wavelet filter design, based on the combination of the real and the imaginary state-space descriptions is described. To fulfill the low-power requirement, the filter's state space description will be optimized. Simulations and measurement results of the various systems are also presented in this chapter.

Finally, Chapter 8 presents the conclusions and suggestions for further research in this area.

References

- [1] M. Unser and A. Aldroubi, *A review of wavelets in biomedical applications*, Proceedings of the IEEE, vol. 84, no. 4, pp. 626-638, April 1996.
- [2] I. Daubechies, *Ten Lectures on Wavelets*, Society for Industrial and Applied Mathematics, Philadelphia, PA, 1992.
- [3] S. Mallat, *A Wavelet Tour of Signal Processing*, Academic Press, San Diego, CA, 2001.
- [4] M. Jansen, *Noise Reduction by Wavelet Thresholding*, Springer-Verlag, Berlin, 2001.
- [5] S. Mallat and W. L. Hwang, *Singularity detection and processing with wavelets*, IEEE Transactions on Information Theory, vol. 38, no. 2, pp. 617-643, March 1992.
- [6] B. U. Kohler, C. Hennig, and R. Orglmeister, *The principles of software QRS detection*, IEEE Engineering in Medicine and Biology, vol. 21, pp. 42-57, February 2002.
- [7] V. X. Afonso, W. J. Tompkins, T. Q. Nguyen, and S. Luo, *ECG beat detection using filter banks*, IEEE Trans. Biomed. Eng., vol. 46, pp. 192-202, 1999.
- [8] Y. H. Hu, W. J. Tompkins, J. L. Urrusti, and V. X. Afonso, *Applications of artificial neural networks for ECG signal detection and classification*, J. Electrocardiology, vol. 26, pp. 66-73, 1993.

- [9] S. Suppappola and Y. Sun, *Nonlinear transforms of ECG signals for digital QRS detection: A quantitative analysis*, IEEE Trans. Biomed. Eng., vol. 41, pp. 397-400, 1994.
- [10] J. S. Sahambi, S. N. Tandon, and R. K. P. Bhatt, *Using wavelet transform for ECG characterization*, IEEE Engineering in Medicine and Biology, vol. 16, pp. 77-83, February 1997.
- [11] E. A. Vittoz, *Future of analog in the VLSI environment*, in: Proc. IEEE Int. Symp. on Circuits and Systems, vol. 2, pp. 1372-1375, 1990
- [12] C. Enz, M. Punzenberger, and D. Python, *Low-voltage log-domain signal processing in CMOS and BiCMOS*, IEEE Transactions of Circuits and Systems – II, vol. 46, no. 3, pp. 279-289, March 1999.
- [13] Y. Tsividis, *Externally linear, time-invariant systems and their applications to compounding signal processors*, IEEE Transactions of Circuits and Systems – II, vol. 44, no. 2, pp. 65-85, February 1997.
- [14] R. H. Walden, *Analog-to-digital converter survey and analysis*, IEEE Journal on Selected Areas in Communication, vol. 17, no. 4, pp. 539-550, April 1999.
- [15] G. Geelen, *A 6b 1.1GSample/s CMOS A/D converter*, IEEE International Solid-State Circuits Conference, Digest of Technical Papers, vol. XLIV, pp. 128-129, February 2001.
- [16] G. Geelen and E. Paulus, *An 8b 600MS/s 200 mV CMOS folding A/D converter using an amplifier preset technique*, IEEE International Solid-State Circuits Conference, Digest of Technical Papers, vol. XLIV, pp. 254-255, February 2004.
- [17] K. H. Lundberg, *High-Speed Analog-to-Digital Converter Survey*, Lecture Notes found at <http://web.mit.edu/klund/www/papers/>
- [18] L. S. Y. Wong, S. Hossain, A. Ta, J. Edvinsson, D. H. Rivas, and H. Naas, *A very low-power CMOS mixed-signal IC for implantable pacemaker applications*, IEEE Journal of Solid-State Circuits, vol. 39, no. 12, pp. 2446-2456, December 2004.
- [19] D. P. W. M. Rocha, *Optimal design of analogue low-power systems, A strongly directional hearing-aid adapter*, PhD thesis, Delft University of Technology, April 2003.
- [20] M. Djurica, *Design of low power analog to digital converter*, PhD thesis, Delft University of Technology, April 2001.

Chapter 2

The Evolution of Pacemakers: An Electronics Perspective

Since the first artificial pacemaker was introduced in 1932, much has changed and will continue to change in the future [1], [2], [3]. The complexity and reliability in modern pacemakers has increased significantly, mainly due to developments in integrated circuit design. Early pacemakers merely paced the ventricles asynchronously, not having the capability of electrogram sensing. Later devices, called demand mode pacemakers, included a sense amplifier measuring cardiac activity, thereby avoiding competition between paced and intrinsic rhythms. By the introduction of demand pacemakers, also the longevity increased since pacing stimuli were only delivered when needed. In 1963, pacemakers were introduced having the capability to synchronize ventricular stimuli to atrial activation. Since that time, clinical, surgical and technological developments have proceeded at a remarkable pace providing the highly reliable, extensive therapeutic and diagnostic devices that we know today.

Modern pacemaker topologies are extremely sophisticated and include an analog part (comprising the sense amplifier and a pacing output stage) as well as a digital part (consisting of a micro controller, and some memory), implementing diagnostic analysis of sensed electrograms, adaptive rate response and device programmability. Pacemakers have become smaller and lighter over the years. Early devices weighed more than 180 g, whereas today devices are available weighting no more than 25 g [4]. This weight reduction has occurred partly due to the development of high energy-density batteries. Finally, there have been remarkable advances in cardiac lead technology. Novel electrode tip materials and configurations have provided extremely low stimulation thresholds and low polarization properties [5]. In this chapter, we will concentrate on the evolution of analog circuit designs applied in cardiac pacemakers.

2.1 The heart

In order to better understand why some patients require pacemakers and how these devices work, it is worth briefly discussing how the heart and its electrical system work. In a global view one can think of the heart as a pumping station which pumps the blood through the body. In order to do so, the heart is divided into four chambers: two atria and two ventricles, as shown in Fig. 2.1. The two atria act as collecting reservoirs (primer pump) for blood returning to the heart while the two ventricles act as pumps to eject the blood to the body. Deoxygenated blood returning from the body via the superior and inferior vena cava, enters the right atrium and passes through the tricuspid valve to the right ventricle, which expels it through the pulmonary artery to the lungs. Oxygenated blood returning from the lungs enters the left atrium via the pulmonary veins, passes via the mitral valve to the left ventricle and is pumped out through the aorta back to the body. The tricuspid and the mitral valves are important to prevent the back flow of blood from the respective ventricle to the atrium [6].

The pumping action starts with the simultaneous contraction of the two atria, called “diastole”. This contraction serves to give an added push to get the blood into the ventricles. Shortly after that, the ventricles contract virtually in unison, making the beginning of “systole”. Therefore, from electrical point of view the heart can, in most instances, be treated as just two chambers.

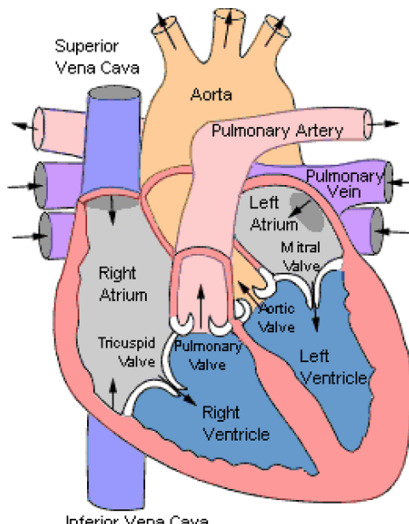


Fig. 2.1. The heart [6]

Excitation and conduction system

The heart is composed basically by three types of cardiac muscle: the atrial muscle, the ventricle muscle and the specialized fibers (which can be further subdivided into excitation and conduction fibers). Both the atrial and the ventricle muscles, which make up the myocardium, each have a similar form of contraction to other muscles of the body, but with a larger period of contraction time. On the other hand, the excitation and conduction fibers have very weak contractions, but do have rhythmicity and variable conduction speed. Once an electrical activation has occurred, contraction of the muscle follows. An orderly sequence of activation of the cardiac muscle in a regularly timed manner is critical for the normal functioning of the heart.

The excitation and conduction system of the heart, responsible for the control of the regular pumping of the heart, is presented in Fig. 2.2. It consists of the sinoatrial node (SA node), internodal tracks and Bachmann's bundle, the atrioventricular node (A-V node), the bundle of His, bundle branches and Purkinje fibers. A heart pacemaker is a device that exhibits automaticity, i.e., generates electrical impulses (known as action potentials) via automatic self-activation, and delivers them to the muscles of the heart in such a way that these muscles contract and the heart beats. Several cells in the heart are able to generate inherent impulses (inherent rate of the A-V node is about 50 beats per minute and of the Purkinje fibers about 40 beats per minute), but at a lower rate than the SA node (which produces about 60–80 beats per minute). The normal rhythm of the heart, between 60 and 100 beats per minute, is controlled by the discharges from the SA node, unless the SA node is non-functional. The Internodal tracks and Bachmann's bundle transmit this excitation throughout the atria and initiate a coordinated contraction of the atrial walls. Meanwhile, the impulse reaches the A-V node, which is the only electrical connection

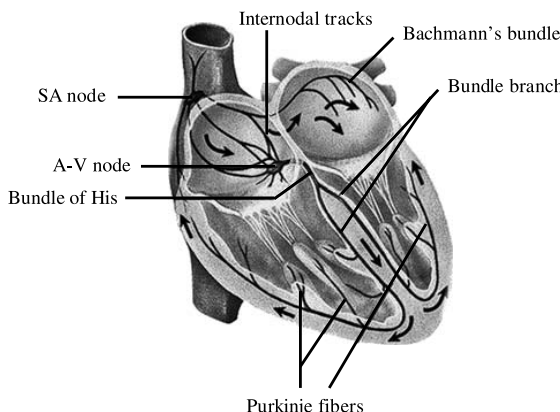


Fig. 2.2. The cardiac conduction system [8]

between atria and ventricles. The A-V node introduces an effective delay, allowing the contraction of the atria to finish before ventricular contraction begins. By this delay, an optimal ventricular filling is achieved. Subsequently, the electrical impulses are conducted very rapidly through the His-Purkinje system (comprising the bundle of His, bundle branches and Purkinje fibers). Once the bundle of His activates, its signal splits into the right bundle branch, which goes to the right ventricle, and the left bundle branch which leads to the left ventricle. Both bundle branches terminate in Purkinje fibers. The Purkinje fibers are responsible for spreading the excitation throughout the two ventricles and causing a coordinated ventricular contraction [6].

2.2 Cardiac signals

2.2.1 Surface electrocardiogram

The electrocardiogram (ECG) is the recording on the body surface of the electrical activity generated by heart. It was originally observed by Waller in 1899 [7]. In 1903, Einthoven introduced some concepts still in use today, including the labelling of the various waves. He chose the letters from P to U to label the waves and to avoid conflict with other physiologic waves being studied at that time [7]. Figure 2.3 depicts a typical ECG signal.

ECG signals are typically in the range of 2 mV peak-to-peak and occupy a bandwidth of 0.05–150 Hz. The character of the body surface waves depends on the amount of tissue activating at one time and the relative speed, direction of the activation waveform (action potentials) and the position of the electrodes. Therefore, the pacemaker potentials, i.e. the SA node potentials, that are generated by a small tissue mass are not seen on the ECG. The first ECG wave of the cardiac cycle is the P wave, and it represents the

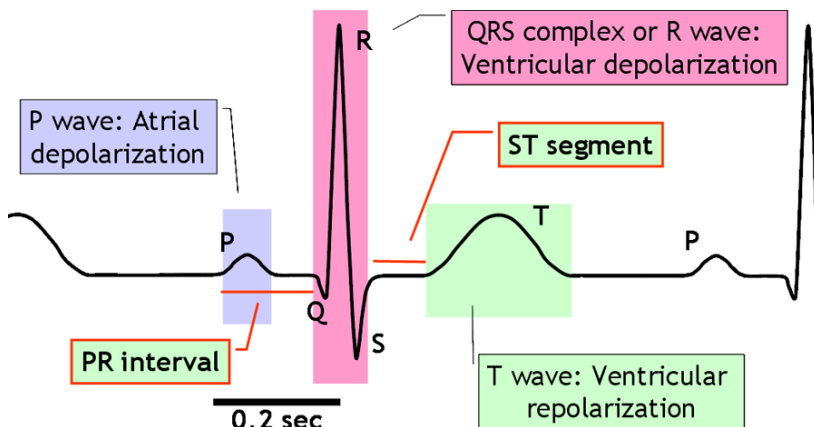


Fig. 2.3. Typical electrocardiogram

depolarization of the atria. Conduction of the cardiac impulse proceeds from the atria through a series of specialized cardiac cells (the A-V node and the His-Purkinje system) as explained in the previous section. Again the total mass is too small to generate a signal large enough to be seen on the ECG. There is a short relatively isoelectric segment following the P wave. This is the P-Q interval which is defined by the propagation delay time of the specialized cells and, usually, is 0.2 s. Once the large muscle mass of the ventricles is excited, a rapid and large deflection is seen on the body surface. This ventricles' depolarization waveform is generically called the QRS complex. Following the QRS complex is another isoelectric segment, the S-T interval. The S-T interval represents the duration of the action potential, normally about 0.25 s to 0.35 s. After this short segment, the ventricles return to their electrical resting state, and a wave of repolarization is seen as a low-frequency signal known as the T wave. In some individuals, a small peak occurs at the end or after the T wave and is called the U wave. Its origin has never been fully established, but it is believed to be a repolarization potential [8].

2.2.2 Intracardiac electrogram (IECG)

An intracardiac electrogram (IECG) is a recording of changes in electric potentials of specific cardiac locations measured by electrodes placed within or onto the heart by using cardiac catheters. The IECG can be recorded between one electrode and an indifferent electrode, usually more than 10 cm apart (unipolar electrogram) or between two more proximate electrodes (<15 mm) in contact with the heart (bipolar electrogram). Sensing the intrinsic activity of the heart depends on many factors related to the cardiac source and the electrode-tissue interface where complex electrochemical reactions take place. In most situations, it is desirable that the IECG does not contain signals from other more distant cardiac chambers. Bipolar lead systems are much less sensitive to far-field potentials and electromagnetic inference (EMI) sources obscuring the cardiac signal.

2.2.3 Cardiac diseases – arrhythmias

Arrhythmias (or dysrhythmias) are due to cardiac problems producing abnormal heart rhythms. In general arrhythmias reduce hemodynamic performance, including situations where the heart's natural pacemaker develops an abnormal rate or rhythm or when normal conduction pathways are interrupted and a different part of the heart takes over control of the rhythm. An arrhythmia can involve an abnormal rhythm increase (tachycardia; >100 bpm) or decrease (bradycardia; <60 bpm), or may be characterized by an irregular cardiac rhythm, e.g. due to asynchrony of the cardiac chambers. An “artificial pacemaker” can restore synchrony between the atria and ventricles.

2.3 The history and development of cardiac pacing

2.3.1 What is an artificial pacemaker?

An artificial pacemaker is a device that delivers a controlled, rhythmic electric stimulus to the heart muscle in order to maintain an effective heartbeat for long periods of time and thereby ensures the pumping capacity of the heart. Indication for permanent pacemaker implantation and the selection of the appropriate pacemaker mode are based mainly on the cardiac diseases such as failure of impulse formation (sick sinus syndrome) and/or conduction (A-V block). Functionally, a pacemaker comprises at least three parts: a electrical pulse generator, a power source (battery) and an electrode (lead) system, as we can see in Fig. 2.4 [9].

Different types of output pulses (monophasic, biphasic, etc.) can be used to stimulate the heart. The output stimulus provided by the pulse generator is the amount of electrical charge transferred during the stimulus (current). For effective pacing, the output pulse should have an appropriate width and sufficient energy to depolarize the myocardial cells close to the electrode. Generally, a pacemaker can provide a stimulus in both chambers of the heart. During A-V block, ventricular pacing is required because the seat of disease is in the A-V node or His-Purkinje system. However, in case of a sick sinus syndrome, the choice of pacemaker will be one that will stimulate the right atrium. A pacemaker utilizes the energy stored in batteries to stimulate the heart. Pacing is the most significant drain on the pulse generator power source. The battery capacity is commonly measured in units of charge (ampere-hours). Many factors will affect the longevity of the battery, including primary device settings like pulse amplitude and duration and pacing rate. An ideal pulse generator battery should have a high energy density, low self-discharge rate and sufficient energy reserve between early signs of depletion and full depletion to allow for safe replacement of the device. The electrical connection between the heart and the implanted pulse generator is provided by an implantable electrode catheter called ‘lead’. In an implantable pulse generator system, commonly two types of lead systems are used. A unipolar lead system has a single isolated conductor with an electrode located at the tip. A bipolar

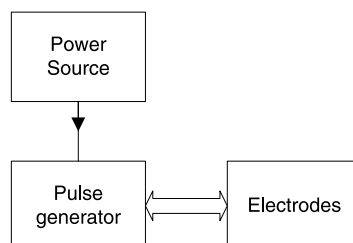


Fig. 2.4. Basic pacemaker functional block diagram

lead has two separate and isolated conductors connecting the two electrodes, i.e. the anode and cathode, usually not more than 15 mm apart. The cathode refers to the electrode serving as the negative pole for delivering the stimulation pulse and the anode to the positive pole. For unipolar pacing-sensing systems, the distance between anode and cathode easily exceeds 10 cm. Its cathode is typically located at the lead tip whereas the pulse generator housing, usually located in the pectoral region, is used as anode. Several types of bipolar leads exist, including the coaxial lead allowing a diameter in the range of 4–5 F (french = 0.33 mm), which is comparable to state-of-the-art unipolar leads. The sensing behavior of bipolar lead systems outperform their unipolar counterparts by providing a better signal to interference ratio. Especially for sensing atrial activation, bipolar electrodes are less sensitive to far-field potentials generated by the ventricles. Moreover, bipolar leads are less sensitive to electromagnetic interference (EMI) sources and skeletal muscle potentials. However, owing to their construction, bipolar leads are stiffer and more complex from a mechanical construction point of view.

2.3.2 Hyman's pacemaker

In the early nineteenth century, many experiments such as drug therapy and electrical cardiac pacing had been conducted for stimulating the heart in cardiac arrest. Previous methods employed in electrically stimulating the heart were performed by applying the same current that would cause contraction of the muscle tissue of the heart. Later, Albert S. Hyman stated that “the introduced electric impulse serves no other purpose than to provide a controllable irritable point from which a wave of excitation may arise normally and sweep over the heart along its accustomed pathways.” Hyman designed the first experimental heart pacemaker in 1932 [10], shown in Fig. 2.5.

Hyman's pacemaker was powered by a hand-wound, spring-driven generator that provided 6 minutes of pacemaking without rewinding. Its operation is as follows: The hand crank (F) winds the spring motor (D) which drives the magneto-generator (A) at a controlled speed (E and H) and causes the interrupter disc (not shown) to rotate. The magneto-generator supplies current to a surface contact on the interrupter disc. The companion magnet pieces (B' and B'') provides the magnetic flux necessary to generate current in the magneto-generator. Subsequently, the interrupter disc produces a pulsed current at 30, 60 or 120 beats per minute, regulated by the impulse controller (G), which represents the periodic pacing waveform delivered to the electrode needle (L). The neon lamp (C) is illuminated when a stimulus is interrupted. In Fig. 2.6 a suitable block diagram of the Hyman's pacemaker is given [11].

2.3.3 Dawn of a modern era – implantable pacemakers

The origin of modern cardiac pacing is defined as the time when the first pacemaker was implanted without the need for opening the chest. The first

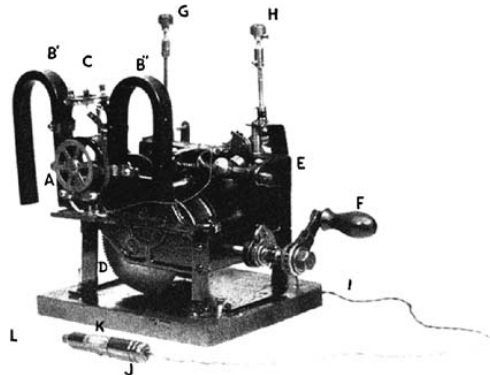


Fig. 2.5. The first artificial pacemaker [10]. A, magneto-generator; B' and B'', companion magnet pieces; C, neon lamps; D, spring motor; E, ballistic governor; F, handle; G, impulse control; H, speed control; I, flexible electric cord; J, insulated handle; K, handle switch, and L, electrode needle

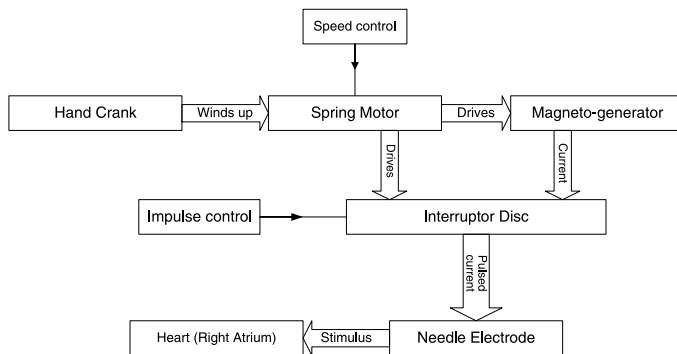


Fig. 2.6. Block diagram of Hyman's pacemaker [11]

pacemaker, developed by Dr. Rune Elmquist, was used in a patient in 1958 by Dr. Ake Senning [12]. In 1959 the engineer Wilson Greatbatch and the cardiologist W. M. Chardack developed the first fully implantable pacemaker [13]. This device was essentially used to treat patients with complete A-V block caused by Stokes–Adams diseases and delivered single-chamber ventricular pacing. It measured 6 cm in diameter by 1.5 cm thick and the total weight of the pacemaker was approximately 180 g. The pacemaker circuit delivered to the electrode pulses 1ms wide, a pulse amplitude of 10 mA and a repetition rate of 60 beats per minute. The average current drain of the circuit under these conditions was about 12 μ A, which, energized by 10 mercury–zinc cells, gave a continuous operation life estimated at 5 years. The schematic of the

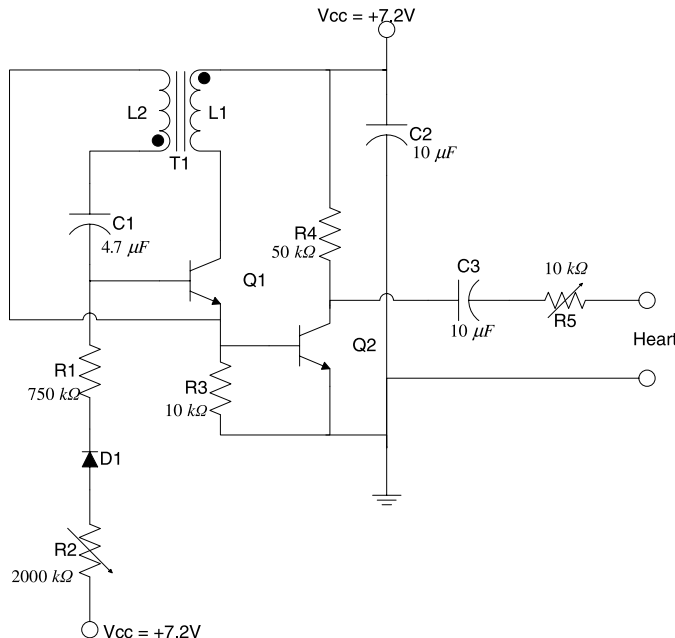


Fig. 2.7. Schematic of the first implanted pacemaker [13]

implanted pacemaker is shown in Fig. 2.7 and consists of a (square) pulse forming oscillator and an amplifier.

Basically, the cardiac pacemaker includes a blocking oscillator [14], which is a special type of wave generator used to produce a narrow pulse. The blocking oscillator is closely related to the two-transistor astable circuit, except that it uses only one amplifying device. The other is replaced by a pulse transformer, which provides inductive regenerative positive feedback. The transistor of the blocking oscillator is normally cut off between pulses and conducting during the time that a pulse is being generated. The operation of a blocking oscillator during a single cycle may be divided into three parts: the turn-on period, the pulse period and the time interval between adjacent pulses (relaxation period).

The turn-on period (t_0) occurs when V_{cc} is applied to the circuit, R_1 and R_2 provide forward bias and transistor Q_1 conducts. Current flow through Q_1 and the primary (L_1) of T_1 induces a current through the secondary (L_2), increasing the voltage across C_1 and thus across the base-emitter junction of Q_1 . The positive voltage of L_2 is coupled to the base of the transistor through C_1 . This provides more collector current and consequently more current through L_1 . Very rapidly, sufficient voltage is applied to saturate the base of Q_1 . Once Q_1 becomes saturated, the circuit can be defined as a series RL (resistance-inductance) circuit and the current increase in L_1 is determined by the time constant of L_1 and the total series resistance. From t_0 to t_1 (pulse

period) the voltage across L1 will be approximately constant as long as the current increase through L1 is linear. The pulse width depends mainly on the time constant $\tau_C = L1/R3$. At time t_1 , L1 saturates. At this time, C1, which has charged during the pulse period, will now discharge through R1 and cut off Q1. This causes its collector current to stop, and, as a consequence, the voltage across L1 returns to 0. The length of the time between t_1 and t_2 is the relaxation period.

Demand pacemaker

As was shown in the previous section, the early pacing devices simply delivered a fixe-rate pulse to the ventricle at a preset frequency, regardless of any spontaneous activity of the heart. These pacemakers, called asynchronous or fixed rate, compete with the natural heart activity and can sometimes induce arrhythmias or ventricular fibrillation. By adding a sensing amplifier to the asynchronous pacemaker in order to detect intrinsic heart activity and thus avoid this competition, one obtains a demand pacemaker, which provides electrical heart-stimulating impulses only in the absence of natural heartbeat. The other advantage of the demand pacemaker compared to the fixed rate system is that now the battery life of the system is prolonged because it is only activated when pacing stimuli are needed.

Berkovits introduced the demand concept in June 1964, which is the basis of all modern pacemakers. In Fig. 2.8 a suitable block diagram of a demand pacemaker is given. Intracardiac electrodes of conventional demand pacemakers serve two major functions, namely pacing and sensing. Pacing is achieved by the delivery of a short, intense electrical pulse to the myocardial wall where the distal end of the electrode is attached, similarly as in the early pacing devices. However the same electrode is used to detect the intrinsic activity of the heart (e.g., R-waves in the ventricle). The electrical pulse generator consists of the following components: a sense amplifier circuit, a timing control circuit and an output driver circuit (electrical impulse former).

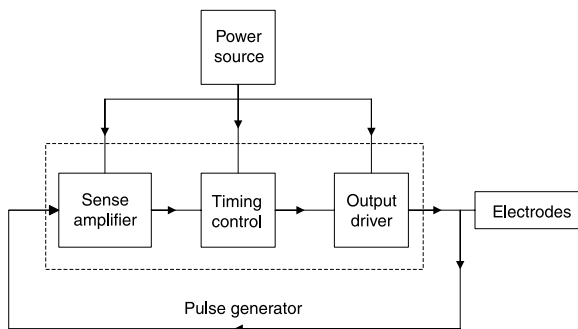


Fig. 2.8. Basic demand pacemaker functional block diagram

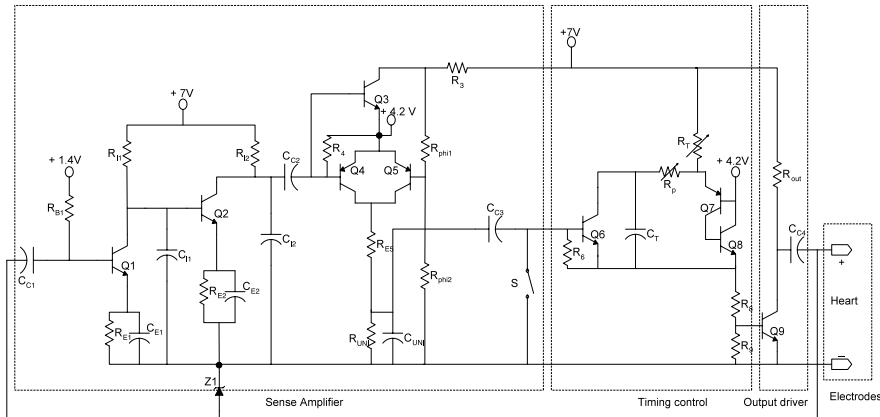


Fig. 2.9. Schematic of the pulse generator of the first demand pacemaker [15]

The schematic of the pulse generator designed by Berkovits is given in Fig. 2.9 [15]. The general function of this circuit was to make the timing circuit responsive to cardiac activity. This allowed inhibition of the pacing pulse from the pulse generator whenever the heart beats on its own. To achieve such function the sense amplifier played a fundamental role. It was designed to amplify and normalize the cardiac signal. Also, the sense amplifier was configured to filter out the undesired signals such as P and T wave and 60 Hz stray signals. The electrical signals picked up by the electrodes are coupled by capacitor C_{C1} into the input of the sense amplifier. The first two transistors, Q_1 and Q_2 , are class A amplifiers. The maximum gain of this amplifier stage is above 50. AC signals at the collector of Q_2 are coupled through capacitor C_{C2} to the bases of both transistors Q_3 and Q_4 . The circuit is symmetrically responsive to negative or positive inputs, since signals of positive polarity turn on Q_3 and signals of negative polarity turn on Q_4 . Either transistor momentarily turns on Q_6 which is the timing capacitor (C_T) discharge switch.

A bandpass filter with a bandwidth of 20–30 Hz was incorporated in the sense amplifier. Three differentiators (R_{B1} and C_{C1} , R_{E1} and C_{E1} , and R_{E2} and C_{E2}) limited the low frequency response of the detecting circuit to discriminate against the P and T waves and any other frequencies well below 20 Hz. Two integrators (R_{I1} and C_{I1} , and R_{I2} and C_{I2}) were designed to reduce high frequency noise components well above 30 Hz. However, these filters were not totally effective in preventing the triggering of Q_6 by 60 Hz signals. For this reason, a rate discrimination stage (comprising transistors Q_3 , Q_4 and Q_5 , resistors R_{E5} and R_{UNI} , and capacitors C_{UNI} and C_{C3}) was provided.

The rate discrimination stage had two functions. First, to provide unipolar current pulses (and thus act as a rectifier) of constant magnitude independent of the amplitude of the input signals above a threshold value (1 V at the

bases of Q3 and Q4). A phase inverter circuit (Q5, $R_{\text{phi}1}$ and $R_{\text{phi}2}$) was provided to invert the polarity signal from transistor Q3. Second, to provide rate discrimination, which avoided triggering of Q6 by signals occurring at a rate greater than a minimum value. The 60 Hz signals have a rate of 120 pulses per second which is much greater than 72 pulses per minute. Each pulse fully charged C_{UNI} and the next pulse was delivered before the capacitor had an opportunity to discharge to any meaningful extent and the increase in the capacitor voltage was negligible. Consequently, steps of negligible magnitude were transmitted through capacitor C_{C3} to the base of transistor Q6.

Switch S was used only to define the operation mode of the system, free-running mode (switch closed) or demand mode (switch opened). In free-running mode, the switch was closed and, therefore, transistor Q6 remained in cut-off condition. When the switch was opened, i.e., in the case of the pacemaker required to operate in demand mode, each pulse transmitted through capacitor C_{C3} to the base of transistor Q6 caused the transistor to conduct. Capacitor C_T discharged through the collector-emitter circuit of the transistor. In this case, the timing cycle was interrupted and the junction of capacitor C_T and resistor R_p did not increase in potential to the point where transistors Q7 and Q8 were triggered to conduction. After capacitor C_T had discharged through transistor Q6, the transistor turned off. The capacitor then started charging once again and the new cycle began immediately after the occurrence of the last heartbeat. The free-running operation would take place were there no input to the base of transistor Q6. Transistor Q6 would remain non-conducting and would not affect the charging of capacitor C_T . The capacitor C_T would trigger, and discharge through transistors Q7 and Q8 to control the generation of a pulse. The timing control circuit which determines the pulse duration (1 ms) and the repetition rate (72 pulses per minute) of the pulse generator, is made up of transistors Q7 and Q8, capacitor C_T and the resistances R_p , R_T , R_8 and R_9 . The pulse duration is determined by the time constant $\tau_p = C_T \cdot R_p$ and the rate mainly by $\tau_T = C_T \cdot R_T$. The capacitor charge current flows through the resistances. During the charging period both transistors are off. As C_T charges, the emitter voltage of Q7 rises and eventually exceeds the 4.2 V reference sufficiently to forward bias the transistor causing collector current to flow. This turns on Q8, raising its emitter voltage, which in turn raises the potential on the lower plate of the capacitor. This creates a regenerative turn on of both Q7 and Q8 which is sustained as long as C_T can supply current, a time determined primarily by resistor R_p . During this discharge time, the output transistor Q9 is turned on, causing current to flow in the electrode circuit. The output driver comprises transistor Q9, resistor R_{out} and capacitor C_{C4} . After 1 ms C_T is discharged, transistors Q7, Q8 and Q9 turn off and the pulse is terminated.

Finally, to avoid damage to the circuit due to high voltage signals from the electrodes, a zener diode (Z1) was placed between the terminals of the electrode.

A variation of this concept is the demand-triggered pacemaker, which stimulates every time it senses intrinsic heart activity, i.e., the stimulus falls directly on the natural QRS.

Dual-chamber pacemaker

A dual-chamber pacemaker typically requires two pacing leads: one placed in the right atrium, and the other placed in the right ventricle. A dual-chamber pacemaker monitors (senses) electrical activity in the atrium and/or the ventricle to see if pacing is needed. When pacing is needed, the pacing pulses of the atrium and/or ventricle are timed so that they mimic the heart's natural way of pumping. Dual-chamber pacemakers were introduced in the 1970s. One of the first description of a dual-chamber pacemaker was given by Berkovits in 1971. Berkovits announced a "bifocal" (AV sequential) pacemaker that sensed only in the ventricle but paced both chambers. In the presence of atrial standstill or a sinus node syndrome plus A-V block, the bifocal pacemaker could deliver a stimulus to the atrium and then, after an appropriate interval, to the ventricle. Berkovits improved on his original design given in Fig. 2.9 with a dual-chamber demand pacemaker. An schematic of this design is given in Fig. 2.10 [16]. In accordance with the principles of the demand pacemaker de-

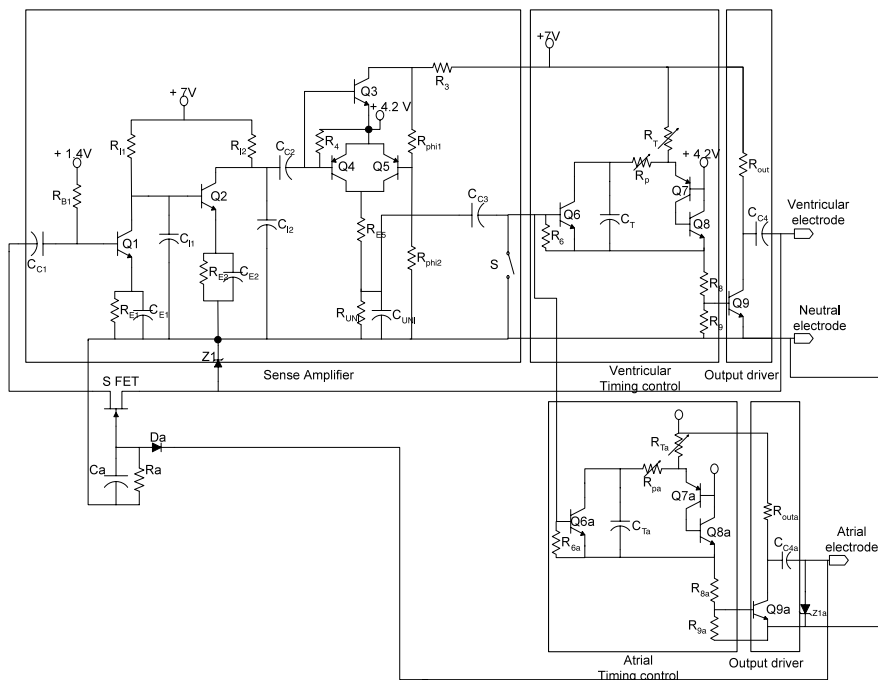


Fig. 2.10. Schematic of the dual-chamber demand pacemaker [16]

sign, a sense amplifier was provided to detect intrinsic ventricular activity. The timing control circuits determined both atrial and ventricular timeout stimulating period. However, the atrial-stimulating impulse was generated first, and, after a predetermined time interval (200 ms), the ventricular-stimulating impulse was generated. Three electrodes were provided, a neutral electrode, an electrode for atrial stimulation and an electrode for ventricular pacing and sensing. The FET switch (S FET) was inserted in the feedback path of the ventricular electrode in order to avoid erroneous detection because of the atrial contraction. The FET switch was normally conducting. The negative pulse generated at the atrial electrode was transmitted through the diode D_a , charging the capacitor C_a and turning off the switch. When the atrial-stimulating terminated, C_a discharged through resistor R_a and turned on the switch again. In this manner, the sense amplifier was disabled during each atrial stimulation and for a short interval thereafter.

More sophisticated dual-chamber pacemakers that sensed intrinsic activity and paced in both chambers were developed, with their first use in late 1977.

Rate-responsive pacemaker

The latest innovations include the development of “rate-responsive” pacemakers in the early eighties, which could regulate their pacing rate based upon the output of a sensor system incorporated in the pacemaker and/or lead. The sensor system consists of a device to measure some relevant parameter from the body (body motion, respiration rate, pH, blood pressure and so forth) and an algorithm in the pacemaker, which is able to adjust the pacemaker response in accordance with the measured quantity. Modern rate-responsive (also called frequency-response) pacemakers are capable of adapting to a wide range of sensor information relating to the physiological needs and/or the physical activity of the patient.

A block diagram of a rate-responsive pacemaker is given in Fig. 2.11. The system is based on a pacemaker having a demand pulse generator, which, in addition, is sensitive to the measured quantity. Many rate-responsive pacemakers currently implanted are used to alter the ventricular response in single-chamber ventricular systems. However, rate-responsive pacing can also be done with a dual-chamber pacing system.

2.4 New features in modern pacemakers

A modern pacemaker consists of a telemetry system, an analog sense amplifier, analog output circuitry, and a microprocessor acting as a controller, as one can see in Fig. 2.12 [4].

Nevertheless, the sense amplifier keeps on playing a fundamental role in providing information about the current state of the heart. State of the art implantable pulse generators or cardiac pacemakers include real-time sensing

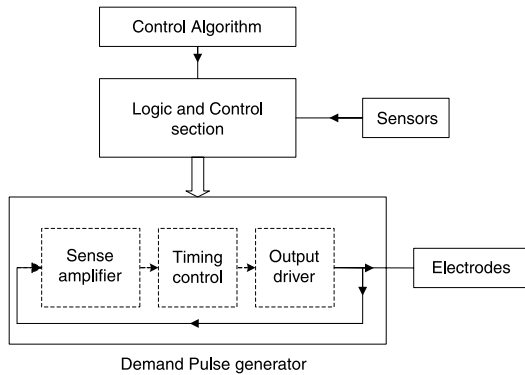


Fig. 2.11. Block diagram of a rate-responsive pacemaker

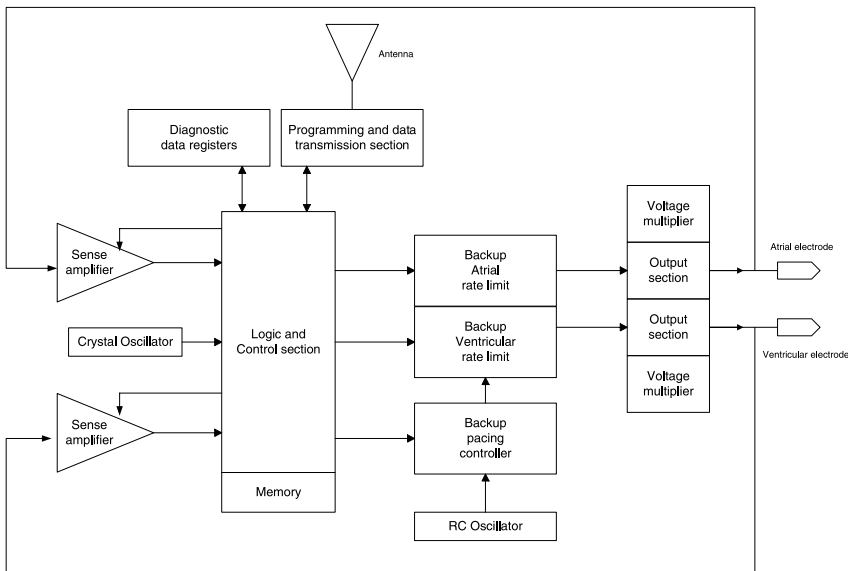


Fig. 2.12. Block diagram of a typical modern pulse generator [4]

capabilities that are designed to detect and monitor intracardiac signal events (e.g. R-waves in the ventricle). A sense amplifier and its subsequent detection circuitry, together called the front-end, derive only a single event (characterized by a binary pulse) and feed this to a micro-controller that decides upon the appropriate pacing therapy to be delivered by the stimulator. Over the years, huge effort is put into the improvement of sense amplifier and detection circuitry. The dynamic range of the atrial and ventricular electrograms sensed by an endocardial lead typically lies between 0.5–7 mV and 3–20 mV respectively. Slew-rates of the signals range between 0.1 and 4 V/s. For the

QRS complex, the spectral power concentrates in the band from 10 to 30 Hz. The T wave is a slower signal component with a reduced amount of power in a band not exceeding 10 Hz. Amplification of intrinsic cardiac signals requires circuitry that is robust against artifacts generated from non-cardiac electromagnetic sources located outside or inside the patient. Introduction of electronic article surveillance systems (EAS) has raised concerns with regard to the possible interaction between emitting field sources and the sense amplifiers of implantable medical devices like pacemakers [17], implantable cardioverter defibrillators and insertable loop recorders [18]. Other sources of electromagnetic inference (EMI) include cellular phones, airport metal detector gates, high voltage power lines [19], electro-cautery devices and MRI equipment [20]. Especially the more sensitive atrial-sensing channel of a brady-arrhythmia device is more prone to detection of EMI. Any type of EMI having sufficient amplitude could cause the pacemaker to react in a clinically undesirable way either inhibiting or triggering stimuli. Fortunately, noise reversion algorithms and circuits mostly provide reliable discrimination between EMI and intrinsic cardiac activity.

Morphological analysis

In pacemakers, one of the challenges is the reduction of unnecessary therapies delivered to the patient's heart when the heart rate dynamics becomes comparable to that of lethal tachyarrhythmias like ventricular tachycardia (VT) or ventricular fibrillation (VF). This situation includes supraventricular tachycardia (SVT) that may occur as a result of atrial fibrillation. As heart rate does not discriminate between lethal tachyarrhythmias like VT/VF and SVT or atrial tachyarrhythmias, the morphology of the QRS complex, or more specifically, the R-wave morphology can be used for a more accurate discrimination between SVT and VT.

In addition, to ensure efficient use of the memory available in an implantable device, the incidence of false positives, erroneously triggering automatic storage, should be minimized. For insertable loop recorders (ILRs), promoting factors include the low amplitude electrogram signal as a result of the limited vector available for pseudo ECG measurement and the presence of muscle EMG and mechanical disturbance of the electrode tissue interface. Therefore, signal analysis methods improving discrimination of signals from noise are of great importance.

Since the information retrieved by the above front-end circuit is reduced to a single event, morphological attributes of the electrogram are completely suppressed. Recent research and clinical studies report details on how morphological aspects of the electrogram relate to various pathological states of the heart and on how the wavelet transform can contribute efficiently to analysis.

Analyzing the structure of the electrogram over multiple scales allows discrimination of electrogram features pertaining over all scales from those only

seen at fine or coarse scales. Based on such observations, the presence or absence of electrogram features related to proximal or distal electrophysiological phenomena can be discriminated. The wavelet transform, being a multiscale analysis technique, offers the possibility of selective noise filtering and reliable parameter estimation. An algorithm based on wavelet analysis that compares morphologies of baseline and tachycardia electrograms based on differences between corresponding coefficients of their wavelet transforms has been found highly sensitive for VT detection [21]. Whereas smoothing attenuates spectral components in the stop band of the linear filter used, wavelet denoising attempts to remove noise and retain whatever signal is present in the electrogram.

Off-line ECG analysis, like Holter analysis, employs the discrete wavelet transform, implemented in the digital domain using multi-rate filter banks [22]. In these applications, the wavelet transform provides a means to reliably detect QRS-complexes. However, in patient worn external applications (e.g. intelligent Holter devices), it is not favourable to implement the WT by means of digital signal processing due to the high power consumption associated with A to D conversion and computation.

2.5 Summary and conclusions

A brief overview of the history and development of circuit designs applied in pacemakers has been presented. The advances in integrated circuit designs have resulted in increasingly sophisticated pacing circuitry, providing, for instance, diagnostic analysis, adaptive rate response and programmability. Also, based on future trends for pacemakers, some features and improvements for modern cardiac sensing systems have been described.

In the next chapters we will investigate a fully integrated implementation of the analog WT circuit to be used in pacemakers. But, before that, the advantages of the wavelet over the Fourier analysis will be the subject of the following chapter.

References

- [1] D. J. Woollons, *To beat or not to beat: the history and development of heart pacemakers*, Engineering Sci. Education J., vol. 4, pp. 259-268, 1995.
- [2] L. A. Geddes, *Historical highlights in cardiac pacing*, IEEE Engineering in Medicine and Biology, vol. 9, pp. 12-18, 1990.
- [3] W. Greatbatch and C. F Holmes, *History of implantable devices*, IEEE Engineering in Medicine and Biology, vol. 10, pp. 38-49, 1991.

- [4] R. S. Sanders and M. T. Lee, *Implantable pacemakers*, Proceedings of the IEEE, vol. 84, no. 3, pp. 480-486, 1996.
- [5] H. G. Mond, *Recent advantages in pacemaker lead technology*, Cardiac Electrophysiology Rev., vol. 3, pp. 5-9, 1999.
- [6] A. C. Guyton and J. E. Hall, *Textbook of Medical Physiology*, 9th edn, W. B. Saunders, Toronto, January 1996.
- [7] J. D. Bronzino, *The Biomedical Engineering Handbook*, 2nd edn, vol. 1, CRC Press and IEEE Press, Boca Raton, FL, 2000.
- [8] R. Sutton and I. Bourgeois, *The Foundations of Cardiac Pacing. Part I*, Futura Publishing Company, Mount Kisco, NY, 1991.
- [9] M. Schaldach and S. Furman, *Advances in Pacemaker Technology*, Springer-Verlag, Berlin, 1975.
- [10] A. A. Hyman, *Resuscitation of the stopped heart by intracardial therapy*, Arch. Intern. Med., vol. 50, pp. 283-305, 1932.
- [11] www.ep-history.org.
- [12] R. Elmquist and A. Senning, *An Implantable Pacemaker for the Heart*, Tliffe, London, pp. 253-254, 1959.
- [13] W. Greatbatch, *Medical cardiac pacemaker*, US Patent 3,057,356, October 1962.
- [14] www.tpub.com.
- [15] B. V. Berkovits, *Demand pacer*, US Patent 3,528,428, September 1970.
- [16] B. V. Berkovits, *Atrial and ventricular demand pacer*, US Patent 3,595,242, July 1971.
- [17] J. W. Harthorne, *Pacemakers and store security devices*, Cardiol. Rev., vol. 9, no. 1, pp. 10-17, 2001.
- [18] C. C. de Cock, H. J. Spruijt, L. M. van Campen, W. A. Plu, and C. A. Visser, *Electromagnetic interference of an implantable loop recorder by commonly encountered electronic devices*, Pacing Clin. Electrophysiol., vol. 23, no. 10, pp. 1516-1518, 2000.
- [19] T. W. Dawson, K. Caputa, M. A. Stuchly, and R. Kavet, *Pacemaker interference by 60-Hz contact currents*, IEEE Trans. Biomed. Eng., vol. 49, no. 8, pp. 878-886, 2002.

- [20] G. Lauck, A. von Smekal, S. Wolke, K. C. Seelos, W. Jung, M. Manz, and B. Luderitz, *Effects of nuclear magnetic resonance imaging on cardiac pacemakers*, Pacing Clin. Electrophysiol., vol. 18, no. 8, pp. 1549-1555, 1995.
- [21] C. D. Swerdlow, M. L. Brown, K. Lurie, J. Zhang, N. M. Wood, H. W. Olson, and J. M. Gillberg, *Discrimination of ventricular tachycardia from supraventricular tachycardia by a downloaded wavelet-transform morphology algorithm: a paradigm for development of implantable cardioverter defibrillator detection algorithms*, Pacing Clin. Electrophysiol., vol. 13, no. 5, pp. 432-441, 2002.
- [22] G. Strang and T. Nguyen, *Wavelets and Filter Banks*, Wellesley-Cambridge Press, Wellesley, MA, 1996.

Chapter 3

Wavelet versus Fourier Analysis

3.1 Introduction

The Fourier transform, named after Jean Baptiste Joseph Fourier, is an integral transform that re-expresses a function in terms of sinusoidal basis functions, i.e. as a sum, possibly infinite, of sines and cosines functions multiplied by some amplitude coefficients. The Fourier transform can thus be defined as frequency–amplitude decomposition [1].

The big disadvantage of a Fourier expansion however is that it has only frequency resolution and no time resolution. This means that, although we might be able to determine all the frequencies present in a signal, we do not know when they are present. To overcome this problem, in the past decades, several solutions have been developed, which are able to represent a signal in the time and frequency domain at the same time. The wavelet transform or wavelet analysis is probably the most recent solution to overcome the shortcomings of the Fourier transform. The idea behind these time–frequency joint representations is to decompose the signal of interest into several parts and then analyze the parts separately. It will be clear from the next sections that analyzing a signal in this way will give more information about the ‘when’ and ‘where’ of different frequency components. In addition, one will see that in contrast to the Fourier filters, a wavelet filter is not exclusively defined by its frequency behavior and one of the most important design aspect for an wavelet filter is its impulse response definition in the time domain.

3.2 Fourier transform

The behavior of a linear, continuous-time, time-invariant system (LTI) with input signal $x(t)$ and output signal $y(t)$ is described by the convolution inte-

gral [5]

$$y(t) = \int_{-\infty}^{\infty} x(\tau)h(t - \tau)d\tau \quad (3.1)$$

where $h(t)$ is the response of the system to a unit impulse input. Since complex sinusoidal waves $e^{j\omega t}$ are eigenvectors of linear time-invariant operators (eigenvectors of convolution operators), the Fourier transform is widely used in LTI signal processing [2]. Another way to think of Fourier analysis is as a mathematical technique for transforming the signal from time-based to frequency-based. This is due to the fact that the Fourier transform of $f(t) = e^{j\omega_0 t}$ is a Dirac function $\hat{f}(\omega) = 2\pi\delta(\omega - \omega_0)$.

The Fourier coefficients are obtained by correlating the input signal $f(t)$ with a sinusoidal wave $e^{j\omega t}$, given by the equation

$$\hat{f}(\omega) = \int_{-\infty}^{\infty} f(t)e^{-j\omega t}dt \quad (3.2)$$

The Fourier integral described in Eq. 3.2 measures the amplitude spectrum of $f(t)$ at frequency ω . Note that the Fourier basis functions are represented by periodic infinite duration functions (sinusoidal waves), giving information only in frequency domain. Hence, when the signals are periodic and sufficiently regular, the Fourier coefficients converge quickly. For non-periodic signals, the Fourier integral gives a continuous spectrum. Hence, the Fourier transform is not satisfactory for analyzing signals whose spectra vary with time. In Fig. 3.1, one can see the Fourier Transform of a non-stationary signal. From the Fourier analysis, the signals' frequency content is easily detected. However the time information, i.e., when the change of the momentary frequency component took place, is lost, as can be seen from the inverse Fourier Transform.

To characterize the time information of $f(t)$ (i.e., the discontinuity) it is necessary to decompose it over waveforms that are also well localized in time.

3.3 Windowing function

To characterize the time information of $f(t)$ (i.e., discontinuities) it is necessary to decompose it over waveforms that are well localized in time. For instance, one can apply a rectangular (so-called Haar-basis) window function [1], which is well localized in time, to “zoom-in” on the singularity of the signal in the time domain. However, its Fourier transform is defined over the entire frequency axis (i.e., it has a poor resolution in frequency domain). As an example, we apply two signals with different frequency components, as depicted in Fig. 3.2a and Fig. 3.2b, respectively. The smaller the window we choose, the better we can locate sudden changes, such as peaks or discontinuities, but the “blinder” we become to the lower frequency components of both signals. The truncated analyzed signal and its Fourier transform are plotted respectively in Fig. 3.2c and Fig. 3.2d. It can be easily seen that the singularity of the signal is now better localized in time, but it is not well represented in frequency by its

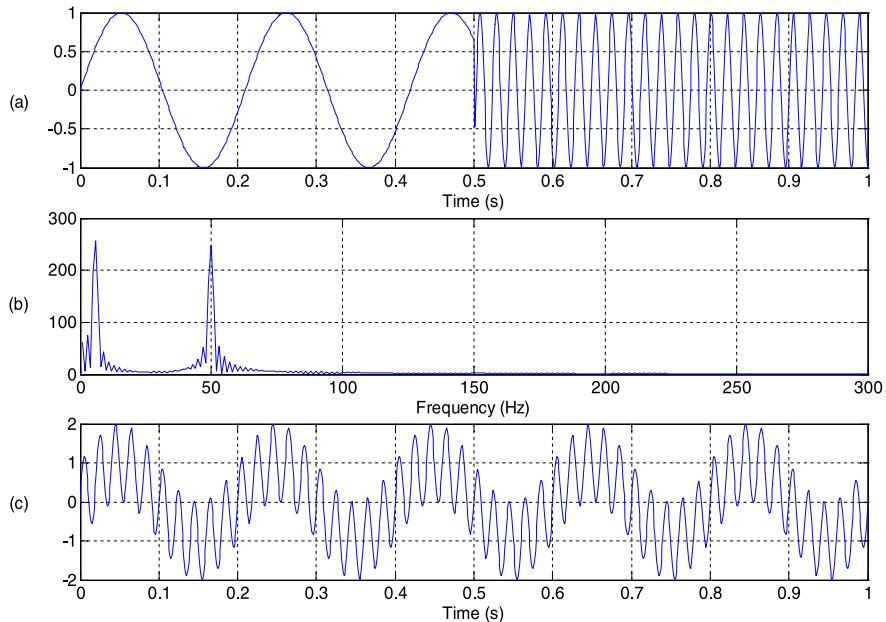


Fig. 3.1. **a** Input signal with two frequency components with different instant in time. **b** Fourier Transform. **c** Inverse Fourier Transform

Fourier transform. Note that we also cannot discriminate both input signals from their frequency components anymore.

3.4 Wavelet transform

The Fourier basis provides a very efficient representation of functions that exhibit long-term oscillatory behavior whereas the Haar basis best represents functions that consist of sharp peaks and discontinuities. Unfortunately, these two representations are orthogonal to each other, meaning that it is not easy to extract frequency information from the time representation and vice versa. To overcome these limitations, we must decompose signals over basis functions that are well concentrated in time and frequency. The Wavelet Transform (WT) is well suitable for local time–frequency decomposition. As an example we can apply the WT to the signal in Fig. 3.1a. The left side of the Fig. 3.3 shows the wavelet mapping of the input signal in the time domain (using a varying scaling parameter a), and their Fourier spectra are plotted on the right. Note that, depending on the value of a , one can zoom in on the singularity or obtain a global view to preserve the frequency information. This is the zooming ability of wavelets that will be explained below.

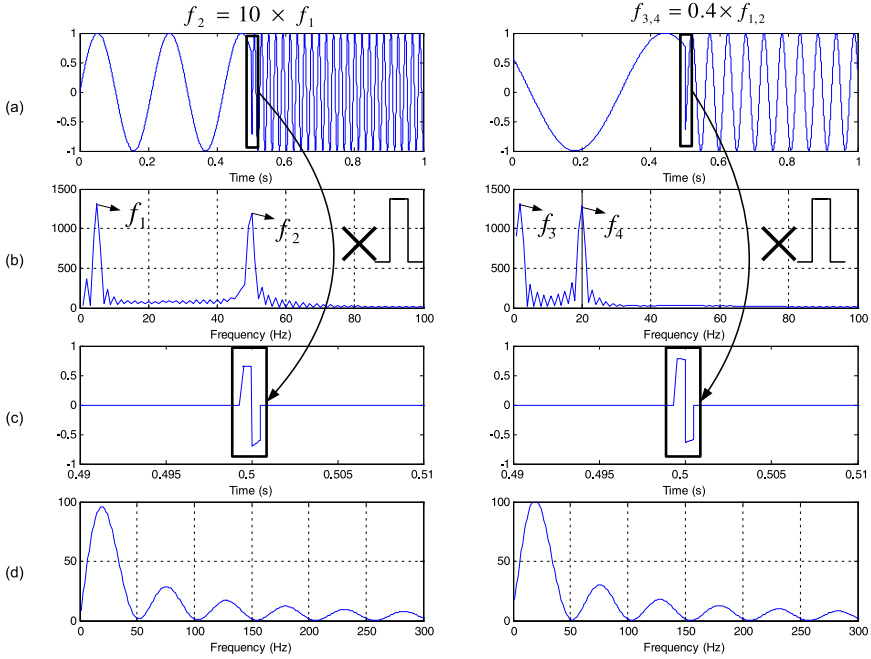


Fig. 3.2. **a** Input signals with two frequency components with different instant in time ($f_1 = 5$ Hz, $f_2 = 50$ Hz, $f_3 = 2$ Hz and $f_4 = 20$ Hz). **b** Fourier Transform. **c** Truncated signals in time domain. **d** Fourier transform of the truncated signals

For signal processing, the Wavelet Transform (WT) has been shown to be a very promising mathematical tool [4], [3], [2], particularly for local analysis of non-stationary and fast transient signals, due to its good estimation of time and frequency localizations. Figure 3.4 shows an example of the WT analysis of an intra-cardiac signal (IECG). In Fig. 3.4a, the WT is applied for QRS-complex detection using a typical IECG signal. As one can see, the maximum values of the WT correspond to the QRS-complex, and thus, the time position of the QRS-complex can be easily identified at several scales, i.e., a varying from 2 to 32. Another important advantage of the WT compared to the Fourier analysis is given by Fig. 3.4b, where a white Gaussian noise is added to an IECG. By definition, white Gaussian noise covers the whole frequency spectrum, so its frequency spectrum overlaps with the cardiac signal. Therefore, the in-band noise cannot be removed by applying a Fourier analysis. In addition, due to the large amplitude of the noise, one cannot discriminate the desired signal from the noise in time-domain (amplitude threshold). Nevertheless, for certain scale values, the WT can distinguish cardiac signal points from noise and the maxima of the QRS-complex can still

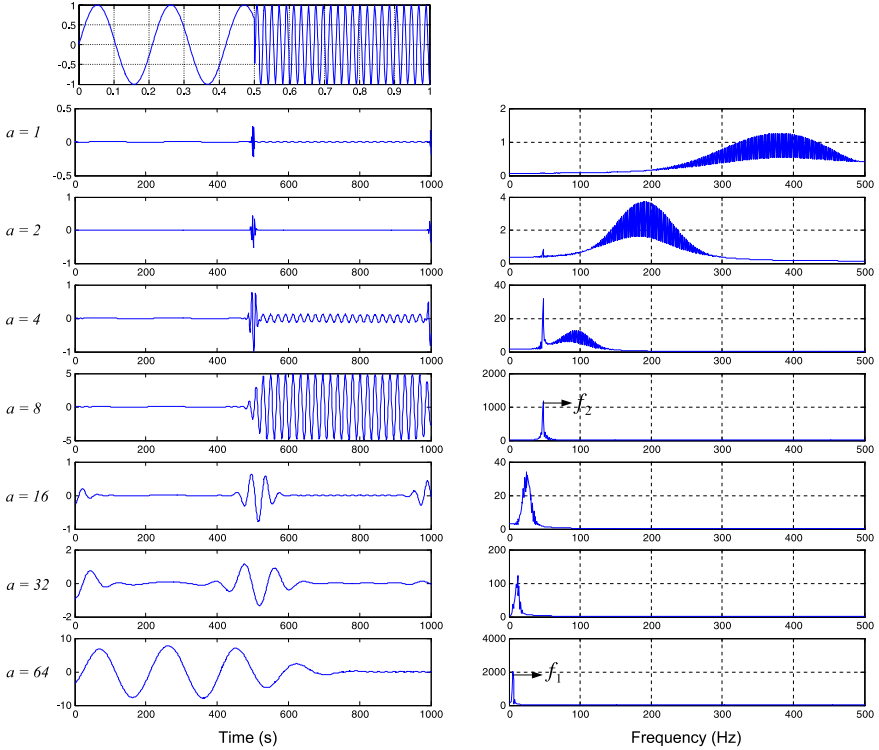


Fig. 3.3. Morlet wavelet transform with 7 scales of the signal in Fig. 3.1a. Time-response is shown in the left side and the corresponding frequency-response is given in the right side

be identified for a equals 8, 16 and 32, as seen from the wavelet analysis in Fig. 3.4b. This denoising characteristic of the WT is based on correlation as will be explained later on.

Wavelet literally means small wave. Wavelet analysis is performed using a prototype function called the wavelet base, which decomposes a signal into components appearing at different scales (or resolutions). Since the Wavelet Transform is a linear operation that decomposes a signal into components that appear at different scales (or resolutions) [2], the WT is a so-called constant-Q analysis (bandpass filters with constant relative bandwidth). The wavelet transform of a function $f(t)$ at scale a and position τ is given by

$$W_f(\tau, a) = \frac{1}{\sqrt{a}} \int_{-\infty}^{\infty} f(t)\psi^*\left(\frac{t - \tau}{a}\right)dt \quad (3.3)$$

where $\psi(t)$ is the wavelet base (or mother wavelet) and $*$ denotes the complex conjugate. The factor $1/\sqrt{a}$ is used for energy normalization. Hence, the WT is based on the convolution of the signal with a dilated impulse response of a

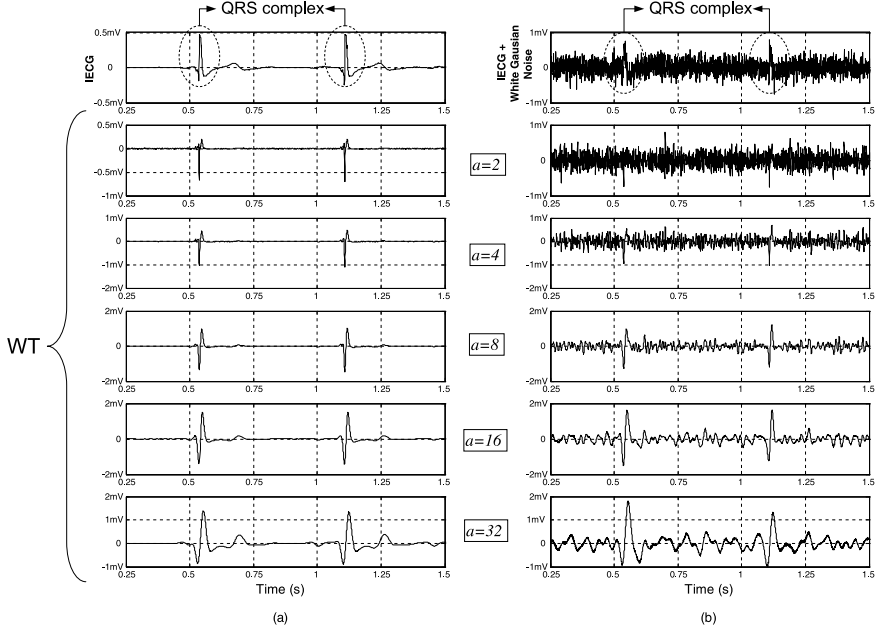


Fig. 3.4. Wavelet analysis of an Intra-cardiac signal. **a** Typical IECG. **b** IECG with additive white Gaussian noise

filter (defined by $\psi(t)$), mapping the signal onto a two-dimensional function of time and frequency. The main idea of the WT is to look at a signal at various windows and analyze it with various resolutions. It provides an alternative to the classical Short-Time Fourier Transform (STFT) or Gabor Transform [4]. In contrast to the STFT, which uses a single analysis window, the WT uses short windows (small a) at high frequencies and long windows (large a) at low frequencies. The time–frequency plane of a WT is shown in Fig. 3.5a. As one can see, the time–frequency (or time-scale) representation has an intrinsic limitation: the product of the resolution in time and frequency is limited by the uncertainty principle (Heisenberg inequality) [1], [4],

$$\Delta t \Delta \omega > \frac{1}{2} \quad (3.4)$$

with

$$\Delta t = \sqrt{\frac{\int t^2 |\psi(t)|^2 dt}{\int |\psi(t)|^2 dt}} \quad (3.5)$$

$$\Delta \omega = \sqrt{\frac{\int \omega^2 |\Psi(\omega)|^2 d\omega}{\int |\Psi(\omega)|^2 d\omega}} \quad (3.6)$$

where $\Psi(\omega)$ is the Fourier transform of the wavelet base $\psi(t)$ and Δt and $\Delta \omega$ are the time and frequency resolution, respectively. Note that the denomi-

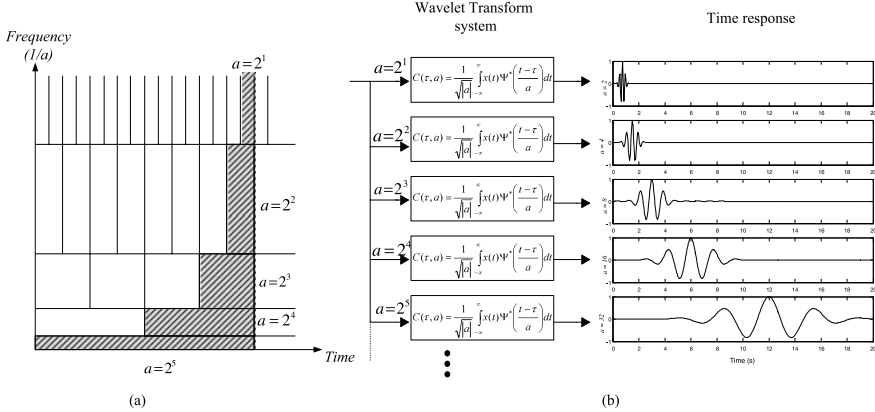


Fig. 3.5. Wavelet transform system: **a** Time–frequency plane; **b** Morlet WT system with multiple scales

nators of Eq. 3.5 and Eq. 3.6 represent the energy of the function related to Parseval’s theorem. The uncertainty principle states that one can only trade time resolution for frequency resolution and vice versa. This means that the resolution in time and frequency cannot be arbitrarily small, because their product is lower bounded.

3.4.1 Continuous-time wavelet bases

The wavelet analysis is thus performed using a prototype function called the wavelet base, $\psi(t)$ ($\psi(t) \in L^2$, i.e., finite energy functions). The main characteristic of the wavelet base is given by

$$\int_{-\infty}^{\infty} \psi(t) dt = 0 \quad (3.7)$$

This means that the wavelet base is oscillatory and has zero mean value. Also, this function needs to satisfy the admissibility condition so that the original signal can be reconstructed by the inverse Wavelet Transform

$$\int_{-\infty}^{\infty} \frac{|\Psi(\omega)|^2}{|\omega|} d\omega = C_\Psi < \infty \quad (3.8)$$

The admissible condition implies that the Fourier transform of the wavelet must have a zero component at zero frequency. Hence, the wavelet transforms are inherently band-pass filters in the Fourier domain, defined as Wavelet Filters (WF). Any function that has finite energy is square integrable and satisfies the wavelet admissibility condition can be a wavelet [3].

There are several types of well-defined wavelet bases, and, depending on the application (and the properties of the wavelet function), one may be preferred

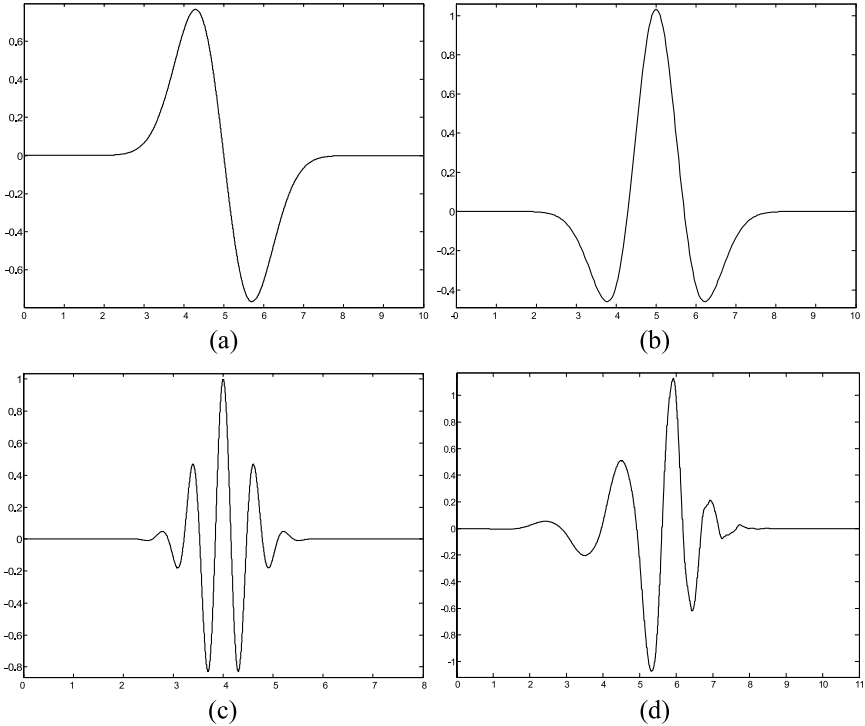


Fig. 3.6. Wavelet bases: **a** First derivative of Gaussian (gaus1); **b** Second derivative of Gaussian (gaus2); **c** Morlet and **d** Daubechies (db6)

over others. Three different types of wavelet bases will be presented here, being Gaussian wavelets (derivatives of a Gaussian function), Morlet and Daubechies Wavelets (dbN). A number of other wavelet bases can be found in [3], [2].

Gaussian wavelets (Gauss) are symmetric with infinite support. The Gaussian wavelet family is defined from the derivatives of the Gaussian function [2] and is given by

$$\psi_n(t) = C_n \cdot \frac{d^n}{dt^n} (e^{-t^2}) \quad (3.9)$$

where n denotes the order, $\frac{d}{dt}$ is the symbolic derivative and C is a normalizing constant, which depends on n . Gaussian functions are often used as mother wavelets since they provide the best resolution in time and in frequency (minimum time-frequency product, $\Delta t \Delta \omega$). The gaus1 and gaus2 (also known as Mexican hat) are depicted in Fig. 3.6a and Fig. 3.6b, respectively.

The Morlet wavelet base is obtained from a Gaussian envelope multiplied by a cosine function [2], and described by

$$\psi(t) = \cos(5\sqrt{2}(t - \tau)) e^{-(t-\tau)^2} \quad (3.10)$$

The Morlet wavelet, shown in Fig. 3.6c, can be defined as the original wavelet, where J. Morlet (a French geophysical engineer), in 1984, came up with, as an alternative to the short-time Fourier transform, windowing a cosine wave using a smooth window (Gaussian window), which is well localized in the time–frequency domain.

A family of orthogonal wavelets was first constructed by Ingrid Daubechies in 1992 [3]. Daubechies wavelets are orthogonal functions with compact support of $2N - 1$ and N vanishing moments, where N is the order of the wavelet. The orthogonality of the Daubechies wavelets has a very important mathematical and engineering consequence: any continuous function may be uniquely projected onto the wavelet basis functions and expressed as a linear combination of the basis functions. Daubechies wavelets are non-symmetric and have no explicit expression except for $N = 1$, which is the Haar wavelet (the Haar wavelet is the simplest orthogonal function). One example of this wavelet family, db6, is depicted in Figure 3.6d.

Furthermore, in order to avoid redundancy, one can sample the scale parameter along the dyadic sequence $(2^j)_{j \in \mathbb{Z}}$, i.e., $a = 2^j$ [2]. Figure 3.5b shows a wavelet system with multiple scales in parallel that can be used to compute the WT in real time. As an example, a Morlet WT system has been represented.

3.4.2 Complex continuous-time wavelet bases

Complex wavelets provide more detail information in transient signal detection than real-valued wavelets. Often the wavelet transform of a real signal by means of a complex wavelet is plotted in modulus–phase form, rather than using the real and imaginary representation. In the complex wavelet transform analysis, the modulus maxima and the phase crossings point out the locations of sharp signal transitions. Nevertheless, the phase information reveals isolated singularities in a signal more accurately than does the modulus [8]. Also, using the phase information, different kinds of transition points of the analyzed signal, i.e. local maxima and inflection points, can be distinguished. For instance, using the first complex Gaussian wavelet (*cga1*), the $-\pi$ to $+\pi$ phase crossings point define the inflection points, whereas $\pm\pi$ to 0 is associated with the local maxima points (peaks), as one can see in Fig. 3.7.

One example of a complex wavelet function is the Gabor wavelet. The Gabor wavelet is obtained from a complex Gaussian function (complex exponential windowed by a Gaussian function) as basic functions [2], described by

$$\psi(t) = C \cdot e^{-j\omega t} e^{-t^2} = C \cos(\omega t) e^{-t^2} - jC \sin(\omega t) e^{-t^2} \quad (3.11)$$

where $e^{-j\omega t} e^{-t^2}$ is the complex Gaussian function and C is a normalizing constant. From the Gabor wavelet one can derive some complex wavelet families, e.g. the complex Gaussian and the complex Morlet.

The modulus, the real and imaginary parts and the phase of the complex Gabor wavelet for $\omega = 2$ are given in Fig. 3.8.

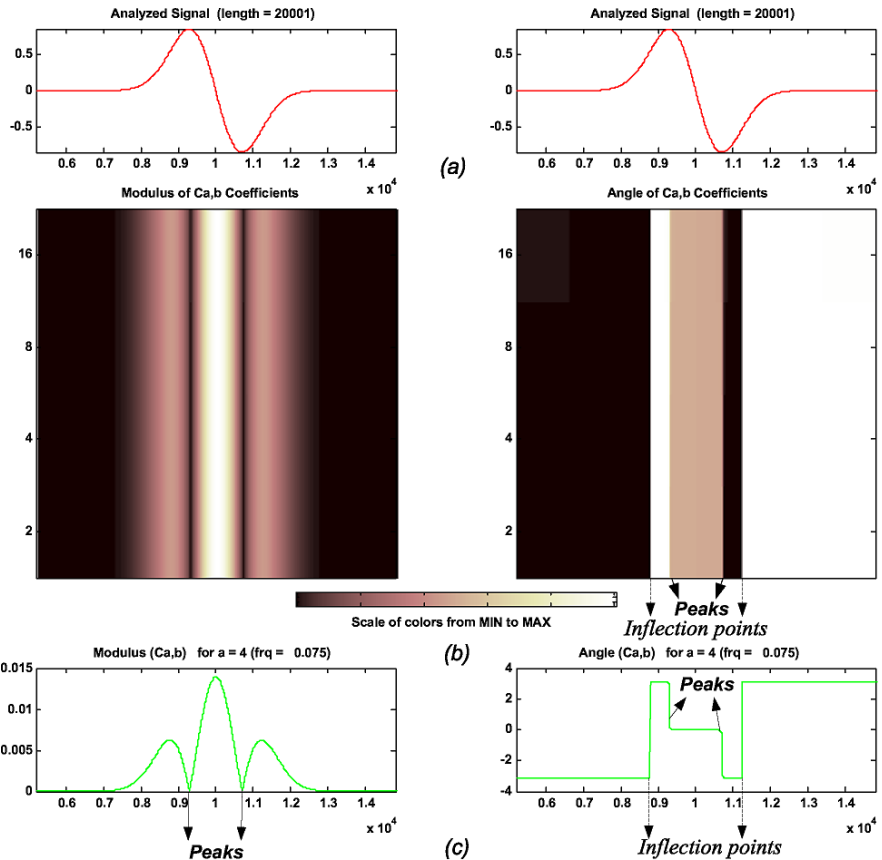


Fig. 3.7. Complex wavelet transform using cgau1. **a** Input signal. **b** Wavelet transform coefficients with four dyadic ($a = 2^i$) scales. **c** One coefficient line ($a = 4$)

3.5 Signal processing with the wavelet transform

Over the last decade, wavelets have had a growing impact on signal processing theory. Wavelets are useful tools for signal processing applications such as singularity detection, denoising and data compression [8]–[17].

3.5.1 Singularity detection – wavelet zoom

Singularities (sharp signal transitions) and irregular structures often carry essential information in a signal. Singularities and edges are detected by following the wavelet transform local maxima at fine scales.

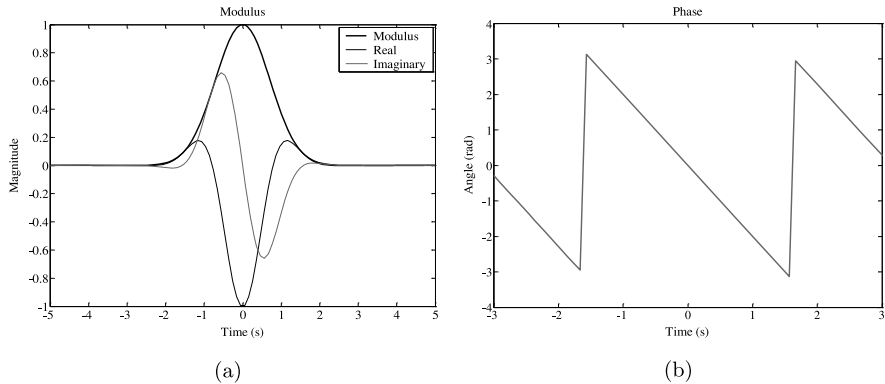


Fig. 3.8. Complex Gabor Wavelet. **a** Modulus. **b** Phase

Modulus maxima

We use the term modulus maxima to describe any point (t_0, a_0) such that $|W_f(t, a)|$ is locally maximum at $t = t_0$. This implies that

$$\frac{\partial W_f(t_0, a_0)}{\partial t} = 0 \quad (3.12)$$

t and a represent the time and scale parameters of the WT, respectively. A definition of a *modulus maximum* of the wavelet transform is given as follows [2]:

“Any point (t_0, a_0) such that $|W_f(t, a_0)| < |W_f(t_0, a_0)|$ when t belongs to either a right or a left neighborhood of t_0 , and $|W_f(t, a_0)| \leq |W_f(t_0, a_0)|$ when t belongs to the other side of the neighborhood of t_0 .”

This local maximum should be a strict local maximum in either the right or the left neighborhood of t_0 , to avoid having any local maxima when $|W_f(t, a_0)|$ is constant. We call a “maxima line” any connected curve $a(t)$ in the scale-space plane (t, a) along which all points are modulus maxima.

The singularities of a non-stationary signal are detected by finding the abscissa where the wavelet modulus maxima converge at fine scales. However, in signal processing, fractal dimensions (e.g., in the form of a Lipschitz component) are increasingly important, especially in the context of singularity processing. Signal characterizations, classifications, and recognition can benefit from information provided by the Lipschitz exponent.

Lipschitz exponent – regularity

To characterize singular structures, it is necessary to precisely quantify the local regularity of a signal $f(t)$. Lipschitz (also known as Holder) exponents provide uniform regularity measurements over time intervals, but also at any point ν . If $f(t)$ has a singularity at ν , which means that it is not differentiable

at ν , then the Lipschitz exponent at ν characterizes this singular behavior. The wavelet theory proves that these Lipschitz exponents can be computed from the evolution across scales of the wavelet transform modulus maxima.

A function f is uniformly Lipschitz α over $[a, b]$ if for all $\nu \in [a, b]$

$$e_\nu(t) = |f(t) - p_\nu(t)| \leq K|t - \nu|^\alpha \quad (3.13)$$

where $p_\nu(t)$ is the Taylor polynomial, $e_\nu(t)$ is the approximation error and K is a positive constant, which is independent of ν . Suppose f is “ m ” times differentiable, the Taylor polynomial is given by

$$p_\nu(t) = \sum_{k=0}^{m-1} \frac{f^{(k)}(\nu)}{k!} (t - \nu)^k \quad (3.14)$$

This means that the m th order differentiability of $f(t)$ in the neighborhood of ν yields an upper bound on the error $e_\nu(t)$ when t tends to ν . The Lipschitz regularity refines this upper bound with non-integer exponents.

As an example, consider a signal

$$f(t) = 1 - |1 - t|^\alpha \quad (3.15)$$

shown in Fig. 3.9. In the intervals, $0 \leq t < 1$ and $1 < t \leq 2$, the signal is regular with Lipschitz exponent α . However the regularity ends at $t = 1$, hence $f(1)$ is singular with the following behavior: on the left side the singular point has a Lipschitz α (increasing from the left to the right) while on the right

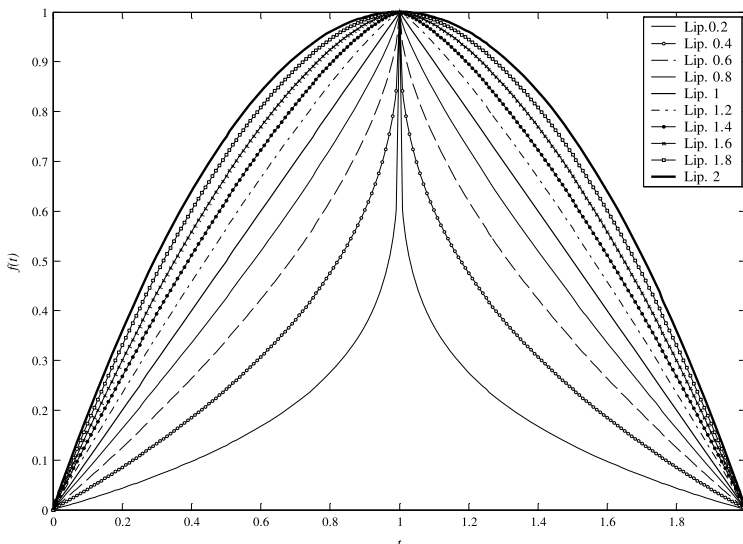


Fig. 3.9. Lipschitz exponent from 0.2 to 2 for $f(t) = 1 - |1 - t|^\alpha$

side it has a Lipschitz α (decaying from the left to the right). The exponent is also called singularity strength.

It is important to observe that knowing the singularity behavior at $f(1)$ is sufficient to describe $f(t)$. Hence, singularities (i.e., α of both sides and their corresponding increasing/decaying trends) contain signal information compactly.

The Fourier transform is a powerful tool for measuring the minimum global regularity of functions. However, it is not possible to analyze the regularity of f at a particular point ν from the decay of $|F(\omega)|$ at high frequencies. In contrast, since wavelets are well localized in time, the wavelet transform gives Lipschitz regularity over intervals and at points.

Wavelet vanishing moments

To measure the local regularity of a signal, it is not important to use a wavelet with narrow frequency support, but vanishing moments are crucial. The vanishing moment can be defined by

$$\int_{-\infty}^{+\infty} t^k \psi(t) dt = 0 \quad (3.16)$$

for $0 \leq k < n$. If the wavelet has n vanishing moments, then the WT can be interpreted as a multiscale differential operator of order n .

Applying the WT to a signal defined by $f(t) = p_\nu(t) + e_\nu(t)$, we obtain

$$Wf(t) = Wp_\nu(t) + We_\nu(t) = We_\nu(t) \quad (3.17)$$

This result shows that a wavelet estimates the exponent α by ignoring the polynomial p_ν (a phenomenon known as polynomial suppression). For this purpose, to calculate the Lipschitz α from a signal, one has to use a wavelet base that presents $n > \alpha$ vanishing moments. For instance, the first derivative of a Gaussian presents one vanishing moment, where the modulus maxima are used to locate discontinuities – a function with $\alpha = 0$ is bounded but discontinuous at ν – and points where the function is not differentiable ($\alpha < 1$). For the second derivative of a Gaussian, the modulus maxima correspond to high curvatures.

Regularity measurements with wavelets

The decay of the modulus maxima amplitude of the WT across scales is related to the Lipschitz regularity (uniform and pointwise) of the signal. Measuring this asymptotic decay is equivalent to zooming into signal structures with a scale that goes to zero.

The decay of $|Wf(t, a)|$ in the neighborhood of ν is controlled by the decay of the modulus maxima included in the *cone of influence* $|t - \nu| \leq Ca$. f is

uniformly Lipschitz α in the neighborhood of ν if and only if there exists $A > 0$ such that each modulus maximum in the cone satisfies

$$|Wf(t, a)| \leq Aa^{\alpha+\frac{1}{2}} \quad (3.18)$$

which is equivalent to

$$\log_2(|Wf(t, a)|) \leq \log_2(A) + \left(\alpha + \frac{1}{2}\right) \log_2(a) \quad (3.19)$$

Equation 3.18 shows that $|Wf(t, a)|$ decays like $a^{\alpha+\frac{1}{2}}$ over intervals where f is uniformly Lipschitz α . Mallat and Hwang [7] have proven that the local maxima of the wavelet transform modulus provide enough information for analyzing such singularities and proved that modulus maxima detect all singularities. The Lipschitz regularity at ν is thus the maximum slope of $\log_2(|Wf(t, a)|)$ as a function of $\log_2(a)$ along the maxima lines converging to ν . Figure 3.10 shows an example of Lipschitz exponent extraction by means of the wavelet modulus maxima across scales. The applied wavelet base is the first derivative of a Gaussian and the input signal has two singular structures, $\alpha = 2$ and $\alpha = 0.5$. Note that for the case of $\alpha = 2$, the Lipschitz exponent is larger than

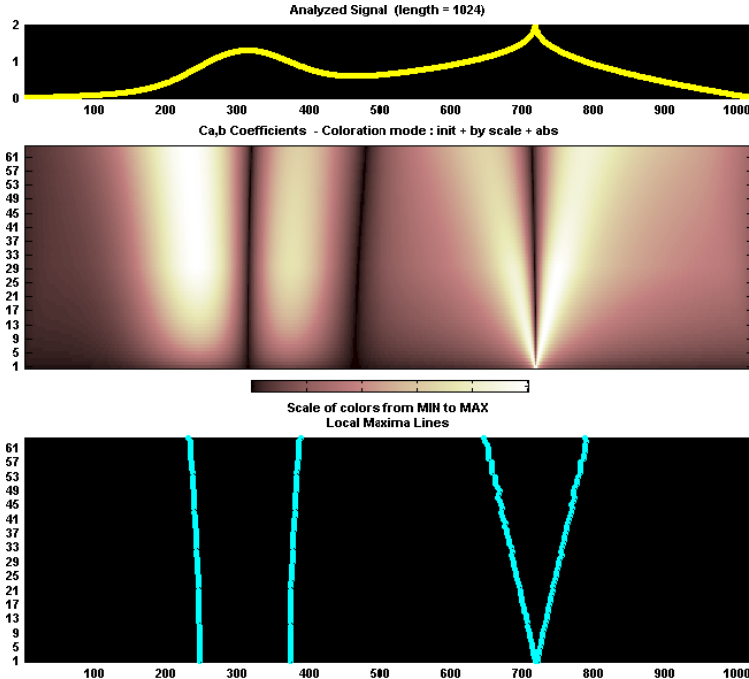


Fig. 3.10. Extraction of the Lipschitz exponent of 0.5 by means of the modulus maxima line using a gaus1 wavelet base

the vanishing moment of the wavelet and the modulus maxima can detect the position of the inflection points, but cannot characterize the singularity type. On the other hand, for $\alpha = 0.5$, the modulus maxima point exactly the position ν and characterize the shape of the singularity by $\log_2(|Wf(t, a)|) = 0.5$.

3.5.2 Denoising

Detection and classification of signals in the presence of noise and interference is a critical issue in many areas of signal and image processing and analysis. The wavelet transform has been generally applied to signal denoising due to its ability to detect transient features in signals. In essence, the WT performs a correlation analysis, so that we can expect its output to be maximum when the input signal most resembles the analysis template $\psi(t)$, and much smaller coefficients when there is mostly noise. This principle is the basis for the matched filter, which is the optimum detector of a deterministic signal in the presence of additive white Gaussian noise. However, the advantage of the WT compared with matched filter is that WT use several scales, and thus, decomposes the signal into several resolutions. Denoising techniques are based on the idea that the amplitude (correlation factor) rather than the location of the spectrum of the signal is different from the noise.

The denoising can be done by simply thresholding the WT coefficients based on the so-called wavelet shrinkage (nonlinear hard or soft thresholding) technique. By selecting an appropriate threshold and applying the inverse wavelet transformation (WT^{-1}), an asymptotically optimal denoising performance can be achieved.

3.5.3 Compression

Wavelet compression is a form of data compression well suited for image compression (sometimes also video compression and audio compression). Compression is possible because most real-world data are very statistically redundant and, by this, the information can be encoded (or transformed) using much less data bits than a one-by-one linear representation would use. Compression is usually achieved by setting small wavelet coefficients to zero, and thus leaving only important components from the original function. A certain loss of quality is accepted (lossy compression). Using a wavelet transform, the wavelet compression methods are better at representing transients, such as percussion sounds in audio, or high-frequency components in two-dimensional images, for example an image of stars on a night sky. This means that the transient elements of a data signal can be represented by a smaller amount of information than would be the case if some other transform, such as the more widespread discrete cosine transform, had been used.

3.6 Low-power analog wavelet filter design

By definition, an electrical or electronic filter is a system that can be used to modify, reshape, or manipulate the frequency spectrum of an electrical signal according to some prescribed requirements [5]. One can represent the filter by an operator L , resulting in

$$L[f(t)] = h(t) \otimes f(t) = \frac{1}{2\pi} \int_{-\infty}^{\infty} \hat{f}(\omega) \hat{h}(\omega) e^{j\omega t} d\omega \quad (3.20)$$

where \otimes denotes convolution.

Thus, operator L amplifies or attenuates the frequency components of f by $\hat{h}(\omega)$. Some well-known types of electrical filters can be found in literature where the corresponding frequency property (L) is completely defined, e.g., Butterworth, Chebyshev and Elliptic filters. Those filters can be classified as Fourier filters. However, a wavelet filter is not exclusively defined by its frequency behavior; another main design aspect for a wavelet filter is its impulse response definition. In contrast to Fourier filters, in a wavelet filter, the signal is decomposed into waves of finite length. For this reason, wavelets allow different parts of the signal frequency spectrum to be filtered individually, whereas Fourier filtering affects all data points in the same manner.

Basically, the design of a low-power analog wavelet filter can be summarized by the steps shown in the block diagram of Fig. 3.11, which will be investigated in the next chapters.

The starting point of an analog filter design trajectory is the definition of the respective transfer function (or, equivalently, a differential equation).

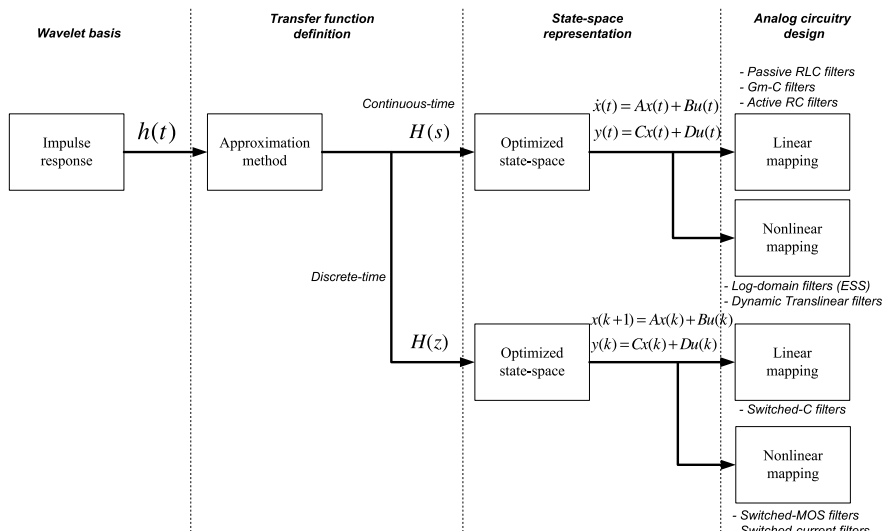


Fig. 3.11. Block diagram of an analog filter design trajectory

However, a linear differential equation having a predefined desired impulse response does not always exist. Hence, one is obliged to use a suitable approximation method, the topic of Chapter 4. There are several mathematical techniques that are frequently used to achieve the best approximation possible. Nonetheless, one of the most important aspects of analog filter synthesis is that the approximating function must lead to a physically realizable network which is dynamically stable.

Next, as there are many possible state-space descriptions and thus filter topologies that implement a particular transfer function, the designer has to find one that fits his specific requirements. For low-power low-voltage applications, we optimize the state-space description of the filter for dynamic range, sensitivity and sparsity requirements (Chapter 5). We will focus on a synthesis technique that is exclusively based on integrators. Note that two general types of analog filters can be identified, namely, continuous-time and discrete-time filters. To implement a discrete-time filter, one must obtain an transfer function in the z-domain whereas a continuous-time filter is described mathematically by a rational function in the Laplace domain.

The last step will be the integrator design, which will be the main building block of the wavelet filter (Chapter 6). For continuous-time filters, there are basically two possible integrator implementations, based on either linear or nonlinear (e.g., log-domain) mapping. One important design aspect of the integrator that will be considered here is its ability to handle a large dynamic range in a low-voltage environment. Moreover, since in conventional ultra low-power designs resistors would become too large for on-chip integration, their superfluity, if possible, would be a very important advantage.

3.7 Conclusions

In this chapter, a comparison between frequency analysis, by means of the Fourier transform, and time-frequency representation, by means of the wavelet transform, was presented. From a non-stationary example signal, the good time and frequency characteristics extraction of the wavelet was pointed out. In addition, the properties of wavelet base functions and WT signal processing applications were described.

In the next chapter, we will describe a methodology to obtain an approximated transfer function that preserves the impulse response of desired ideal wavelet filter, yet is synthesizable and of acceptable order.

References

- [1] A. D. Poularikas (ed.), *The Transforms and Applications Handbook*, 2nd edn, CRC Press, Boca Raton, FL, 2000.

- [2] S. Mallat, *A Wavelet Tour of Signal Processing*, Academic Press, San Diego, CA, 2001.
- [3] I. Daubechies, *Ten Lectures on Wavelets*, Society for Industrial and Applied Mathematics, Philadelphia, PA, 1992.
- [4] O. Rioul and M. Vetterli, *Wavelets and signal processing*, IEEE Signal Processing Magazine, vol. 8, no. 4, pp. 14–38, October 1991.
- [5] W. K. Chen (ed.), *The Circuits and Filters Handbook*, CRC and IEEE Press, Boca Raton, FL, 1995.
- [6] M. Unser and A. Aldroubi, *A review of wavelets in biomedical applications*, Proceedings of the IEEE, vol. 84, no. 4, pp. 626–638, 1996.
- [7] S. Mallat and W. L. Hwang, *Singularity detection and processing with wavelets*, IEEE Transactions on Information Theory, vol. 38, no. 2, pp. 617–643, March. 1992.
- [8] A. Aldroubi and M. Unser, *Wavelets in Medicine and Biology*, CRC Press, Boca Raton, FL, 1996.
- [9] C. K. Chui, *Wavelets: A Mathematical Tool for Signal Analysis*, SIAM, Philadelphia, PA, 1997.
- [10] E. Hernandez and G. L. Weiss, *A First Course on Wavelets*, CRC Press, Boca Raton, FL, 1996.
- [11] J. J. Benedetto, *Wavelets: Mathematics and Applications*, CRC Press, Boca Raton, FL, 1993.
- [12] Y. Meyer, *Wavelets: Algorithms and Applications*, SIAM, Philadelphia, PA, 1993.
- [13] M. Akay (ed.), *Time Frequency and Wavelets in Biomedical Signal Processing*, Wiley and IEEE Press, New York, 1997.
- [14] I. Daubechies, *Different perspectives on wavelets*, American Mathematical Society Short Course, San Antonio, Texas, January 11–12, 1993.
- [15] Y. Nievergelt, *Wavelets Made Easy*, Birkhäuser, Boston, MA, 1999.
- [16] D. F. Walnut, *An Introduction to Wavelet Analysis*, Birkhäuser, Boston, MA, 2002.
- [17] www.wavelet.org.

Chapter 4

Analog Wavelet Filters: The Need for Approximation

4.1 Introduction

The purpose of this chapter is to construct a set of wavelet filters which will perform (a part of) the wavelet transform on an ECG input signal. Each wavelet filter computes one scale. Hence, to implement the required scales, all filters are scaled versions of one basis filter.

As mentioned before, approximation methods should be applied to obtain the required transfer function corresponding to a particular desired wavelet impulse response. In many respects, a time-domain approximation problem invokes the general theory of mathematical approximation.

Several mathematical techniques are frequently used to achieve the best approximation possible [1]. These will be presented in the sections that follow.

In addition, any approximation method should be associated with some measure of error. Therefore we employ an error criterion based on the Mean Square Error (MSE) which is defined as [9]

$$\text{MSE} = \frac{1}{b-a} \int_a^b |h(t) - h'(t)|^2 dt \quad (4.1)$$

where $h(t)$ and $h'(t)$ are the desired impulse response and the approximated impulse response, respectively.

To obtain an approximated transfer function, in this chapter, three main approaches will be presented. They are the CFOS-based, Padé and L_2 wavelet bases approximations. Also, to benchmark these approaches, a few other time-domain approximation methods will be described.

4.2 Complex first order filters

In this section, an analog wavelet filter design based on Complex First Order Systems (CFOS) [2], [3] will be presented. The CFOS-based approach will be

mainly used to approximate Gaussian window functions, such as Gaussian, Gabor and Morlet wavelet bases, and it will be shown that, in order to have an increasingly better approximation to the Gaussian function, we need to connect the CFOS stages in cascade. Thus, the starting point of the CFOS-based wavelet filter design is the definition of the number of stages which defines the appropriate Gaussian envelope to set the width of the wavelet. Before this, we will first present the properties of a Complex First Order System.

A complex filter has a transfer function with complex-valued coefficients, which is not limited to complex-conjugate pairs of poles or zeros. A single-pole complex filter with a real-axis coordinate σ and an imaginary-axis coordinate ω has the transfer function given by

$$H(s) = \frac{V_{out}(s)}{V_{in}(s)} = \frac{1}{s + (\sigma - j\omega)} = \frac{s + \sigma + j\omega}{(s + \sigma)^2 + \omega^2} \quad (4.2)$$

Applying complex feedback to an integrator stage, it is possible to design an efficient complex pole realization, as one can see in Fig. 4.1

$$H(s) = \frac{\frac{1}{s}}{1 - \frac{1}{s}(-\sigma + j\omega)} \quad (4.3)$$

In Fig. 4.2, one can see the effects of this complex feedback on the pole position of the integrator in the S-plane.

A complex lossy integrator can be realized by means of two cross-coupled real integrators. This representation, denominated Complex First Order System (CFOS), is given in Fig. 4.3.

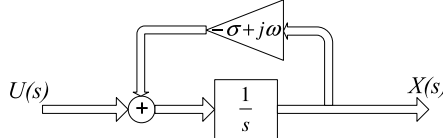


Fig. 4.1. Complex feedback diagram

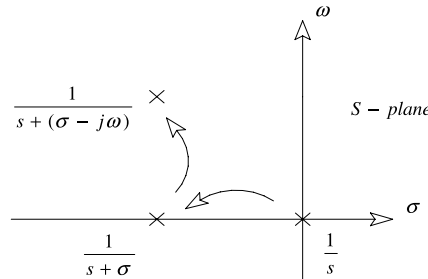


Fig. 4.2. Pole positions of an integrator with complex feedback

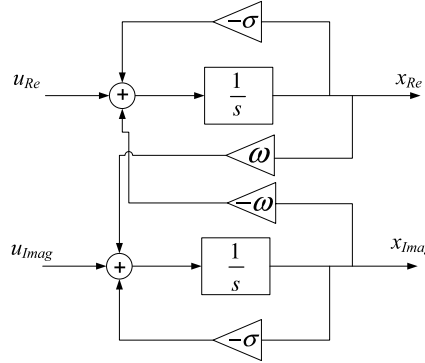


Fig. 4.3. Complex First Order System block diagram

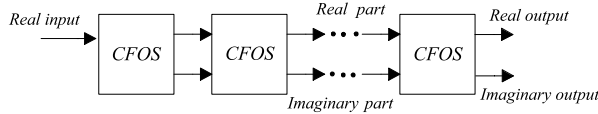


Fig. 4.4. Cascade connection of CFOS

A CFOS is defined by the following set of equations [3]:

$$\dot{x}(t) = (\sigma - j\omega)x(t) + (c_{re} + jc_{imag})u(t) \quad (4.4)$$

$$x(t) = x_{re}(t) + jx_{imag}(t) \quad (4.5)$$

where u is an input signal assumed to be real, x is a state variable assumed to be complex, σ , ω , c_{re} and c_{imag} are system parameters assumed also to be real. After substitution of Eq. 4.5 into Eq. 4.4, the real and imaginary part of x , x_{re} and x_{imag} , can be described by

$$\dot{x}_{re} = \sigma x_{re} - \omega x_{im} + c_{re}u \quad (4.6)$$

$$\dot{x}_{imag} = \sigma x_{imag} + \omega x_{re} + c_{imag}u \quad (4.7)$$

From Eq. 4.4, we can represent the envelope of the impulse response of the first order real input circuit by the following equation

$$h(t) = (c_{re} + jc_{imag})e^{\sigma t}U_{-1}(t) \quad (4.8)$$

where $U_{-1}(t)$ denotes the unit step function. Subsequently, we can connect CFOS's in cascade, as shown in Fig. 4.4, in order to make a sufficient approximation to a Gaussian function.

The envelope of the impulse response of these $n+1$ CFOS stages connected in cascade, with all poles at the same location, is given by

$$h(t) = (c_{re} + jc_{imag})^{n+1} \frac{t^n}{n!} e^{\sigma t} U_{-1}(t) \quad (4.9)$$

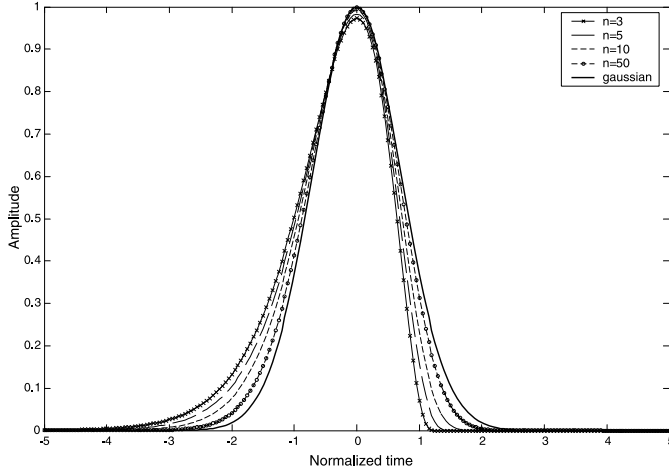


Fig. 4.5. Envelope of the impulse response when increasing the number of CFOS stages

Equation 4.9 can also be defined as a Poisson function. In the theory of statistics, it is well-known that when $n \rightarrow \infty$, the Poisson function approaches a Gaussian function. Therefore, by increasing the number of stages, we can achieve an increasingly better approximation to the Gaussian function.

As one can see in Fig. 4.5 (time domain) and in Fig. 4.6 (frequency domain), an improvement in the approximation to a Gaussian is obtained for a larger number of stages [4].

This improvement is also verified in Table 4.1, where the time resolution (Δt), the frequency resolution ($\Delta\omega$) and their product ($\Delta t \Delta\omega$) have been given for a cascade of n stages.

Subsequently, once the Gaussian envelope has been defined, the real and the imaginary impulse responses are obtained. Applying Eq. 4.4 and Eq. 4.5, the complex impulse response of $n + 1$ CFOS stages is given by

$$h(t) = (c_{re} + jc_{imag})^{n+1} \frac{t^n}{n!} e^{(\sigma+j\omega)t} U_{-1}(t) \quad (4.10)$$

From Eq. 4.10, one easily calculates the general transfer functions of the $n + 1$ CFOS system for the real and the imaginary outputs:

$$H_{re}(n) = \frac{(s + \sigma) \cdot H_{re}(n - 1) - \omega \cdot H_{imag}(n - 1)}{(s + \sigma)^2 + \omega^2} \quad (4.11)$$

$$H_{imag}(n) = \frac{(s + \sigma) \cdot H_{imag}(n - 1) + \omega \cdot H_{re}(n - 1)}{(s + \sigma)^2 + \omega^2} \quad (4.12)$$

with

$$H_{re}(1) = \frac{(s + \sigma)}{(s + \sigma)^2 + \omega^2} \quad (4.13)$$

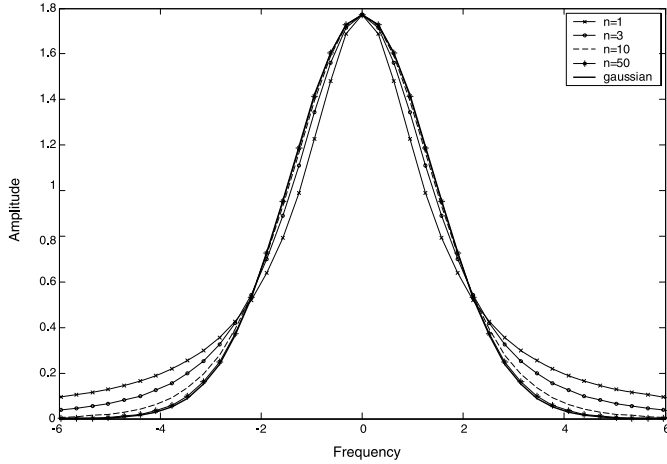


Fig. 4.6. Envelope frequency response when increasing the number of CFOS stages

Table 4.1. Number of CFOS stages versus time-frequency resolution

| n | Δt | $\Delta\omega$ | $\Delta t \Delta\omega$ |
|----------|------------|----------------|-------------------------|
| 1 | 0.7068 | 1.3732 | 0.9705 |
| 2 | 0.6124 | 1.1544 | 0.7069 |
| 3 | 0.5773 | 1.0954 | 0.6323 |
| 5 | 0.5477 | 1.0541 | 0.5773 |
| 11 | 0.5222 | 1.0235 | 0.5344 |
| 50 | 0.5050 | 1.005 | 0.5075 |
| Gaussian | 0.5 | 1 | 0.5 |

$$H_{imag}(1) = \frac{\omega}{(s + \sigma)^2 + \omega^2} \quad (4.14)$$

which correspond to the transfer function of the first order complex filter (Eq. 4.2).

Choosing the right values for σ and ω , we can obtain the first and the second derivatives of the Gaussian for the imaginary and the real part, respectively, as one can see in Fig. 4.7 for various numbers of stages.

Finally, as an example, we show that the complex Morlet wavelet can also be approximated in a similar manner. Again, we need to choose the right value for ω in order to have the appropriate frequency component for the Morlet wavelet. In Fig. 4.8, the impulse response of a tenth order Morlet wavelet filter is shown.

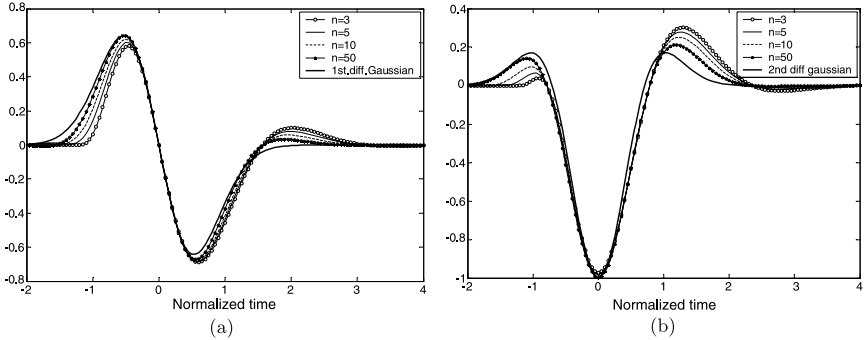


Fig. 4.7. Complex Gaussian wavelet approximation using CFOS's. **a** Imaginary output (First derivative of Gaussian). **b** Real output (Second derivative of Gaussian)

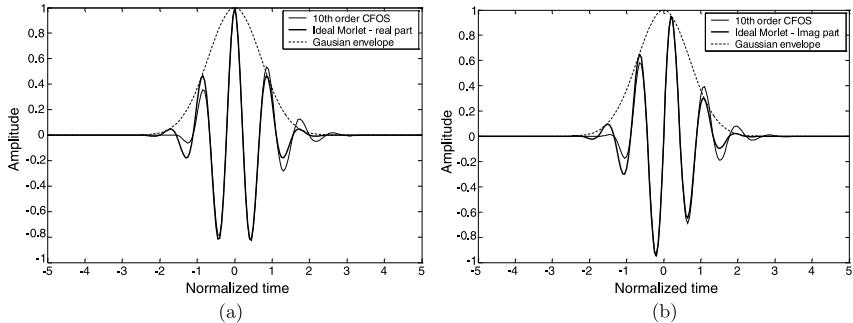


Fig. 4.8. Complex Morlet wavelet approximation using CFOS's. **a** Real output. **b** Imaginary output

4.3 Padé approximation in the Laplace domain

A method which proves to be more successful than the method presented in the previous section is provided by the Padé approximation of the Laplace transform of the impulse response $h(t)$ of the filter. The Padé approximation is an approximation that concentrates around one point of the function that needs to be approximated. In the Padé approximation, the coefficients of the approximating rational expression are computed from the Taylor coefficients of the original function [5], [6]. If the approximation rational function has a numerator of order m and a denominator of order n , the original function can be approximated up to order $m + n$.

The reason to apply the Padé approximation to the Laplace transform of $h(t)$ is that it immediately yields a rational expression that is suitable for implementation. Actually, a Padé approximation of $H(s)$ represents the transfer function of a possible filter. If we would apply the Padé approximation to $h(t)$

in the time domain, we would have to transform this function to the Laplace domain, which would possibly yield difficult non-polynomial expressions or even a non-causal or unstable filter.

Now we will derive the Padé approximation of a general function $F(s)$. Suppose we have the truncated the Taylor series expansion of $F(s)$ around some point, e.g., $s = 0$

$$F(s) = c_0 + c_1 s + \cdots + c_k s^k + O(s^{k+1}) \quad (4.15)$$

The constants c_0 to c_k are called the Taylor coefficients of $F(s)$. Unfortunately, $F(s)$ is not a suitable expression to build a filter, since it has only zeros. Henceforth, to resolve this, a Padé approximation of function $F(s)$ is applied, according to

$$\hat{F}(s) = \frac{P(s)}{Q(s)} = \frac{p_0 + p_1 s + \cdots + p_m s^m}{q_0 + q_1 s + \cdots + q_n s^n} \quad (4.16)$$

where $\hat{F}(s)$ is the truncated Taylor series given by Eq. 4.15, with $k = m + n$ [8]. The coefficients of $P(s)$ can be computed as follows. When a product of two polynomials is taken, the coefficients of the product polynomial can be computed by taking the convolution of the coefficients of both factors. Thus, the coefficients of $P(s)$ can be computed from the convolution of the Taylor coefficients of $\hat{F}(s)$ with the finite number of coefficients of $Q(s)$. We can write this convolution in a matrix–vector form [5], [7]

$$[\hat{F}] \cdot [Q] = [P] \rightarrow \begin{bmatrix} c_0 & 0 & \dots & 0 \\ c_1 & c_0 & & \vdots \\ \vdots & c_1 & \ddots & 0 \\ \vdots & \vdots & \ddots & c_0 \\ \vdots & \vdots & & c_1 \\ \vdots & \vdots & & \vdots \\ c_k & c_{k-1} & \dots & c_{k-n} \end{bmatrix} \cdot \begin{bmatrix} q_0 \\ q_1 \\ \vdots \\ q_n \end{bmatrix} = \begin{bmatrix} p_0 \\ p_1 \\ \vdots \\ p_k \end{bmatrix} \quad (4.17)$$

As the entries of $[\hat{F}]$ are given by the Taylor coefficients of $F(s)$, the entries of $[P]$ depend only on the choice of $[Q]$. In other words, the choice of $[Q]$ is determined by the restrictions on $[P]$. Note that the desirable value of $[P]$ is defined by two constraints: k should be as large as possible, since this gives the most accurate approximation; $P(s)$ should have the desired order m ($m \leq n$) for a causal filter.

From these constraints it can be concluded that the coefficients p_{m+1} to p_k should be zero. Let $[\hat{F}]_{m+1,k}$ denote the submatrix of $[\hat{F}]$, containing rows

$m + 1$ to k of $[\hat{F}]$. Then $[Q]$ can be expressed as

$$\begin{bmatrix} p_{m+1} \\ \vdots \\ p_k \end{bmatrix} = [\hat{F}]_{m+1,k} \cdot [Q] = 0 \quad (4.18)$$

which yields

$$\underline{q} \in \text{Nullspace} \begin{bmatrix} c_{m+1} & \dots & c_0 & 0 \\ c_{m+2} & & c_1 & c_0 \\ \vdots & & & \vdots \\ c_{m+n} & \dots & & c_m \end{bmatrix} \quad (4.19)$$

with $q_n = 1$ for normalization. Finally, the coefficients of $[P]$ are defined by

$$\begin{bmatrix} p_0 \\ p_1 \\ \vdots \\ p_m \end{bmatrix} = \begin{bmatrix} c_0 & 0 & \dots & 0 \\ c_1 & c_0 & & \vdots \\ \vdots & c_1 & \ddots & 0 \\ \vdots & \vdots & \ddots & c_0 \\ \vdots & \vdots & & c_1 \\ \vdots & \vdots & & \vdots \\ c_m & c_{m-1} & \dots & c_{m-n} \end{bmatrix} \cdot \begin{bmatrix} q_0 \\ q_1 \\ \vdots \\ q_n \end{bmatrix} \quad (4.20)$$

with $c_k = 0$ for $k < 0$. If the approximating rational function has a numerator of order m and a denominator of order n , the original function can be approximated up to order $m + n$. For instance, one can apply the Padé function to approximate the first or the second derivative of Gaussian as seen in Fig. 4.9. We apply a [6/10] Padé approximation, i.e. $m = 6$ and $n = 10$, which yields an approximation of order $k = 16$ of the Taylor series expansion, resulting in

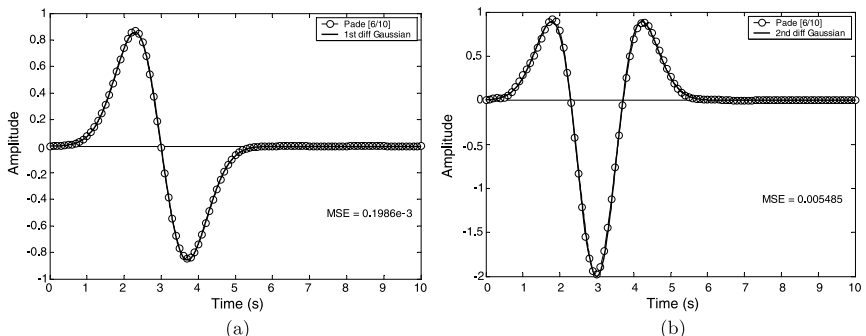


Fig. 4.9. Impulse response approximation using Padé [6/10]. **a** First derivative of Gaussian. **b** Second derivative of Gaussian

Table 4.2. Taylor and Padé coefficients of the first and the second derivative of Gaussian

| Expression (time) | 1st diff. Gaussian | | 2nd diff. Gaussian | |
|--|--|---|--|---|
| | $\psi(t) = -2(t-3)e^{-(t-3)^2}$ | $\psi(t) = (-2 + 4(t-3)^2)e^{-(t-3)^2}$ | $\bar{F}(s) = 0 + 1.77s - 5.31s^2$ | $\bar{F}(s) = 0s + 1.77s^2 - 5.31s^3$ |
| Taylor expansion (Laplace domain) $k = 16$ | $+ 8.41s^3 - 9.3s^4$ $+ 8.03s^5 - 5.74s^6$ $+ 3.54s^7 - 1.92s^8$ $+ 0.94s^9 - 0.42s^{10}$ $+ 0.17s^{11} - 0.066s^{12}$ $+ 0.023s^{13} - 0.008s^{14}$ $+ 0.002s^{15} - 0.007s^{16}$ | | $+ 8.41s^4 - 9.3s^5$ $- 9.3s^5 + 8.03s^6$ $- 5.74s^7 + 3.54s^8$ $- 1.92s^9 + 0.94s^{10}$ $- 0.42s^{11} + 0.17s^{12}$ $- 0.066s^{13} + 0.023s^{14}$ $- 0.008s^{15} + 0.002s^{16}$ | |
| [Q] coefficients $n = 10$ | $q_0 = 38.6 \cdot 10^3$ $q_1 = 103.6 \cdot 10^3$ $q_2 = 130.5 \cdot 10^3$ $q_3 = 102.2 \cdot 10^3$ $q_4 = 55.3 \cdot 10^3$ $q_5 = 21.7 \cdot 10^3$ | $q_6 = 6.3 \cdot 10^3$ $q_7 = 1.35 \cdot 10^3$ $q_8 = 205.6$ $q_9 = 20.27$ $q_{10} = 1$ | $q_0 = 37.8 \cdot 10^3$ $q_1 = 100.7 \cdot 10^3$ $q_2 = 126.4 \cdot 10^3$ $q_3 = 98.6 \cdot 10^3$ $q_4 = 53.3 \cdot 10^3$ $q_5 = 20.9 \cdot 10^3$ | $q_6 = 6.1 \cdot 10^3$ $q_7 = 1.30 \cdot 10^3$ $q_8 = 199.7$ $q_9 = 19.91$ $q_{10} = 1$ |
| [P] coefficients $n = 6$ | $p_0 = -4.77$ $p_1 = 68.5 \cdot 10^3$ $p_2 = -22 \cdot 10^3$ $p_3 = 6.1 \cdot 10^3$ | $p_4 = -576.95$ $p_5 = 44.67$ $p_6 = 5.81$ | $p_0 = -4.67$ $p_1 = -13.21$ $p_2 = 11.1 \cdot 10^3$ $p_3 = -3.7 \cdot 10^3$ | $p_4 = 1.08 \cdot 10^3$ $p_5 = -131.28$ $p_6 = 13.54$ |

an MSE of $0.19 \cdot 10^{-4}$ and $0.548 \cdot 10^{-3}$ for the first and the second derivative, respectively. In Table 4.2 one can see the Taylor and Padé coefficients of both functions.

In order to compare the Padé approximation with the approximation using CFOS one can verify the associated mean-square error for both approximation. The results obtained varying the order of the filter are illustrated in Table 4.3, where the first and the second derivatives of a Gaussian function (Gaussian wavelet bases) have been approximated, respectively.

As seen from the mean-square error comparison, the Padé method yields a much better approximation than the method using CFOS for a filter of the same order.

One of the main advantages of the Padé approximation is that the linear system of equations yield a unique solution, which is generically easy to compute. Moreover, a good match is guaranteed between the given function $\Psi(s)$ and its approximation $H(s)$ in a neighborhood of the selected point s_0 . However, the selection of the expansion point s_0 is a trade-off between stability and a good fit around zero in the time domain. Indeed, in order to obtain a good fit near $t = 0$ by choosing $s_0 = \infty$, it may easily happen that the resulting approximation becomes unstable [10]. In this respect, the Padé approximation described in this section was obtained with the choice $s_0 = 0$, which corresponds to a good fit in the time domain for large values of t [6].

Table 4.3. Order of the filter versus mean-square error for CFOS and Padé approximation

| Order, n | CFOS | | Padé | |
|------------|-------------|--------------|-------------|--------------|
| | First diff. | Second diff. | First diff. | Second diff. |
| 3 | – | – | 0.0899 | 0.0927 |
| 4 | 0.0570 | 0.0605 | 0.0454 | 0.0468 |
| 5 | – | – | 0.0178 | 0.0185 |
| 6 | 0.0444 | 0.0513 | 7.75e-3 | 6.05e-3 |
| 7 | – | – | 2.30e-3 | 1.01e-3 |
| 8 | 0.0382 | 0.0380 | 0.074e-3 | 0.040e-3 |
| 9 | – | – | 0.034e-3 | 0.033e-3 |
| 10 | 0.0339 | 0.0302 | 0.013e-3 | 0.020e-3 |

Furthermore, the selection of the orders m and n is not a straightforward task. An unlucky choice may yield an inconsistent system or an unstable approximation. Nevertheless, this is not an important issue, because one can easily solve this problem [10] by changing the value of m , for a certain n th order approximation.

In addition, the Padé approximation presents some problems of convergence when we try to approximate a function which has many oscillations, for instance, the Morlet wavelet. Due this reason we introduced the procedure described in the next section in order to obtain a stable transfer function for this kind of wavelet bases. By this, we obtain a more general procedure, which is suitable for implementation as an analog filter, to obtain various types of wavelet bases.

Oscillatory wavelet bases approximation

The proposed procedure that generates a transfer function of a wavelet base can be seen in the flow chart in Fig. 4.10 [7]. The procedure is based on the Padé approximation described in the previous section. The starting point is the definition of an expression in the time domain which represents the wavelet under investigation. If the wavelet base does not have an explicit expression (e.g., Daubechies wavelets), a splines interpolation method [9] can be used. Subsequently, one determines the appropriate envelope to set the width of the wavelet. Once again, if the envelope does not have an explicit expression, the splines interpolation is applied. The Gaussian pulse has been chosen as the envelope, which is perfectly local in both the time and frequency domain. Once the envelope has been defined, the Padé approximation is executed to find a stable and rational transfer function which is suitable for implementation as an analog filter. As the main advantage of the Padé method is its computational simplicity and its general applicability [5], it can easily be applied to other envelopes as well. The Padé approximation is preceded by a two-step proce-

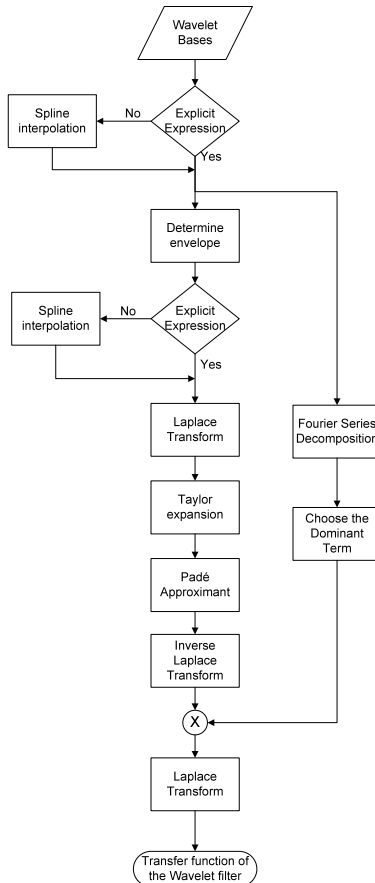


Fig. 4.10. Flowchart for the design of oscillatory wavelet filters

dure. First, a Laplace transform is executed, and then a Taylor expansion is performed on the expression of the envelope in the Laplace domain. Finally, the wavelet is decomposed into a Fourier series to find the dominant term (the term with the largest coefficient) such that when multiplied with the envelope in the time domain, it results in the approximated wavelet base. The results obtained from the use of this method are illustrated in Fig. 4.11, where the Morlet and the Daubechies (db6) wavelet bases have been approximated, respectively. Other wavelet bases can also be approximated in a similar manner.

As an example we consider a Morlet wavelet filter. The related expression of the Morlet wavelet base approach, the Padé expression of the envelope function and the transfer function of the Morlet wavelet filter are given in Table 4.4. \mathcal{L} and \mathcal{L}^{-1} represent the Laplace transform and the inverse Laplace transform, respectively.

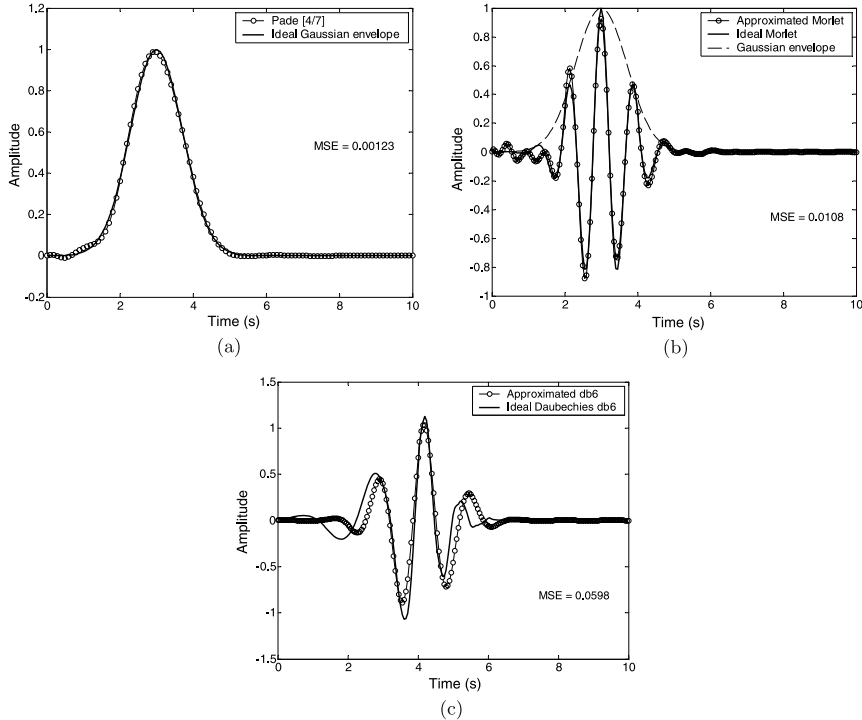


Fig. 4.11. Ideal impulse (*solid line*) and the approximated (*dashed line*) response of example Wavelets filters: Gaussian envelope (a), Morlet (b) and db6 wavelet base (c). The mean-square errors between the ideal and the approximated impulse responses equal 0.00123, 0.0108 and 0.0598 for the Gaussian, the Morlet and the Daubechies wavelets, respectively

Table 4.4. Morlet wavelet base approach parameters

| | Morlet wavelet base |
|-----------------------------------|--|
| Expression (time) | $\psi(t) = \cos[5\sqrt{2}(t - 3)]e^{-(t-3)^2}$ |
| Envelope | Gaussian $\Rightarrow e^{-(t-3)^2}$ |
| Fourier series (Dominant term) | $\cos[5\sqrt{2}(t - 3)]$ |
| Padé [3/5](Gaussian) | $H_{gaussian}(s) = \frac{-1.31s^3 + 8.82s^2 - 25.11s + 31.74}{s^5 + 6.66s^4 + 21.14s^3 + 38.59s^2 + 39.56s + 17.91}$ |
| Morlet transfer function | $H(s) = \mathcal{L}^{-1}\{H_{gaussian}(s)\} \times \cos[5\sqrt{2}(t - 3)]$ |
| | $H(s) = \frac{0.9s^8 - 13s^7 + 177s^6 - 618s^5 + 345s^4 + 7 \cdot 10^4 s^3 - 4 \cdot 10^5 s^2 + 2 \cdot 10^6 s - 3 \cdot 10^6}{s^{10} + 13s^9 + 336s^8 + 3 \cdot 10^3 s^7 + 4 \cdot 10^4 s^6 + 2 \cdot 10^5 s^5 + 2 \cdot 10^6 s^4 + 8 \cdot 10^6 s^3 + 4 \cdot 10^7 s^2 + 9 \cdot 10^7 s + 3 \cdot 10^8}$ |

4.4 L_2 approximation

Another approach to finding a suitable wavelet base approximation is provided by the theory of L_2 approximation. Approximation techniques are usually based on particular assumed criteria of measuring the error and subsequently the error is minimized. One of the most frequently used criteria is the least-mean-square-error approximation [14]. The L_2 approximation technique is based on minimizing the least-mean-square-error.

The advantage of the L_2 method compared to the Padé approximation is that the L_2 approximation offers a more global approximation, i.e., not concentrating on one particular point [10]; Padé is usually computed at the origin. Also, the fit is performed directly in the time domain yielding good control and easy interpretation of the optimization criteria. In addition, according to Parseval's identity [9]

$$\int_0^\infty [\psi(t) - h(t)]^2 dt = \frac{1}{2\pi} \int_{-\infty}^\infty |\Psi(j\omega) - H(j\omega)|^2 d\omega \quad (4.21)$$

the L_2 criterion can equivalently be used in the frequency domain, too. In this scheme the error integral, which is the difference between $\psi(t)$ and its approximation $h(t)$, is defined by

$$\varepsilon_{L_2} = \int_0^\infty [\psi(t) - h(t)]^2 dt \quad (4.22)$$

This means that the L_2 criterion value corresponds to the energy of the difference between the wavelet and its approximation and, by this, we have an interpretation of the optimization in the time domain as well as in the frequency domain.

In this L_2 approach [10], [11], [12], we first express the impulse response (in the time domain) of a general filter. After that, the error ε_{L_2} is minimized with respect to the poles and zeros of the filter. For the generic situation of stable systems with distinct poles [13], $h(t)$ may typically have the following form

$$\begin{aligned} h(t) &= \sum_{i=1}^n A_i e^{P_i t} \\ &= \sum_{i=1}^k c_i e^{p_i t} + c_{k+1} e^{p_{k+1} t} \sin(p_{k+2} t) + c_{k+2} e^{p_{k+1} t} \cos(p_{k+2} t) \\ &\quad + \cdots + c_{n-1} e^{p_{n-1} t} \sin(p_n t) + c_n e^{p_{n-1} t} \cos(p_n t) \end{aligned} \quad (4.23)$$

where A_i and P_i can be real or complex numbers; c_i and p_i are real numbers, representing the impulse response function $h(t)$ as a linear combination of damped exponentials and exponentially damped harmonics. k corresponds to the number of real poles and n is the order of the filter.

Given the explicit form of a wavelet base $\psi(t)$ and the approximated impulse response $h(t)$, the L_2 -norm of the difference $\psi(t) - h(t)$ can now be minimized in a straightforward way using standard numerical optimization techniques and software. The most direct way to find the minimum of Eq. 4.22 is by computation of all partial derivatives of ε_{L_2} with respect to A_i and P_i and setting them equal to zero, namely

$$\frac{\partial \varepsilon_{L_2}}{\partial A_i}, \frac{\partial \varepsilon_{L_2}}{\partial P_i} = 0 \quad \text{for } i = 1, \dots, n \quad (4.24)$$

Note that, due to the fact that A_i and P_i can be complex numbers, we have to perform the differentiation with respect to the real parts and the imaginary parts of A_i and P_i separately.

One important aspect of the L_2 approximation is that the zero-mean constraint of the wavelet bases is imposed in the computation of the error in Eq. 4.22. Thus, the resulting transfer function is such that the numerator of the transfer function does not have a constant term. In other words, the transfer function becomes zero for $s = 0$, which implies that the integral of the wavelet approximation is zero [10].

One example of wavelet base approximation using the L_2 approach is given in Fig. 4.12, where the Morlet wavelet base has been approximated using a 7th order transfer function.

Again, to compare the L_2 approximation with Padé and CFOS approaches, one can check the associated Mean-Square Error for approximations, shown in Fig. 4.13. The MSE has been calculated for two different wavelet bases, being the first derivative of the Gaussian and the Morlet, using several filter orders. As seen from the plots, the Padé and the L_2 approximations present a much better approximation than the CFOS, especially for high-order sys-

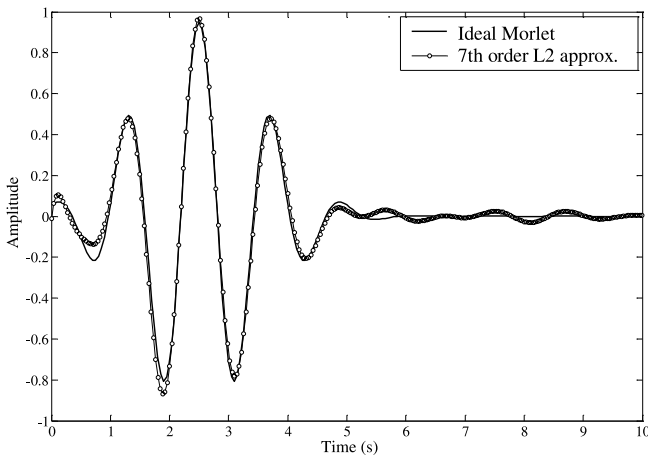


Fig. 4.12. Morlet wavelet base approximation using the L_2 approach

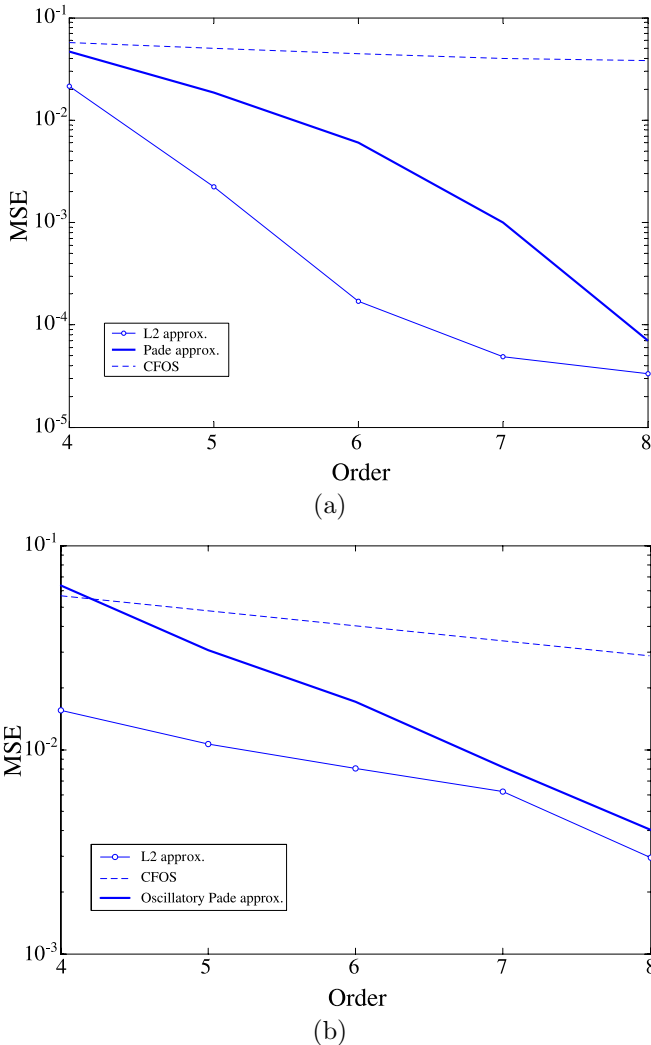


Fig. 4.13. Order of the filter versus mean-square error for L_2 , Padé and CFOS approximations. **a** First derivative of Gaussian and **b** Morlet wavelet bases

tems, whereas in particular for low-order systems L_2 presents a much better performance.

As mentioned before, the L_2 approach has the advantage that it allows for a description in the time domain as well as in the Laplace domain, so that both frameworks can be exploited to develop further insight. Specific points can be defined in the Laplace domain at which the approximation is required

to be good, whereas in the Padé approach, the approximation is done at one specific point (usually at the origin).

One of the disadvantages of an L_2 -approximation approach is that there is a risk that the numerical optimization ends in a local, non-global optimum. In general, L_2 provides no global optimality guarantee. Different starting points can give different local optima and thus can be used to find better solutions [11]. Another drawback is that it is computationally more demanding than the Padé approach.

4.5 Other approaches to wavelet base approximation

4.5.1 Bessel–Thomson filters – a quasi-Gaussian impulse response

The pure, theoretical, Gaussian filter is not physically realizable. However, there are some well-known monotonic quasi-Gaussian filters, such as Bessel–Thomson filters, which try to approximate the ideal Gaussian in both the time domain and the frequency domain [16].

The Bessel filter is sometimes called the maximally-flat delay filter. The Bessel transfer function (also known as the Thompson function) has been optimized to obtain a linear phase, which implies a maximally flat (group) delay in the passband.

The transfer function for an ideal time delay is given by

$$T(s) = e^{-s} = \frac{1}{e^s} = \frac{1}{\sinh(s) + \cosh(s)} \quad (4.25)$$

Using the hyperbolic function identity

$$\coth(s) = \frac{\cosh(s)}{\sinh(s)} \quad (4.26)$$

and the truncated fraction expansion of the $\coth(s)$ function

$$\coth(s) = \frac{1}{s} + \frac{1}{\frac{3}{s} + \frac{1}{\frac{5}{s} + \frac{1}{\frac{7}{s} + \dots}}} \quad (4.27)$$

the result is a quotient of polynomials where the numerator is identified with $\cosh(s)$ and the denominator with $\sinh(s)$. The sum of the numerator and denominator polynomials is thus the approximation to e^s . Note that adding the numerator and denominator truncated after n terms we obtain the Bessel polynomials [16]. The general Bessel polynomial becomes

$$B_n = (2n - 1)B_{n-1} + s^2 B_{n-2} \quad (4.28)$$

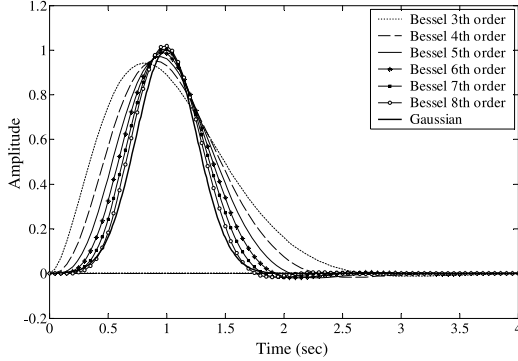


Fig. 4.14. Approximated Gaussian function using Bessel filter

where $B_0 = 1$ and $B_1 = s + 1$.

Thus, the n th Bessel filter transfer function is given by

$$H_n(s) = \frac{B_0}{B_n} = \frac{1}{(2n-1)B_{n-1} + s^2 B_{n-2}} \quad (4.29)$$

One can notice that the above transfer function represents an all-pole filter topology. The Bessel poles lie on a unit circle where the vertical spacing between the poles is equal.

As shown in Fig. 4.14, the impulse response, of Bessel–Thomson filters tends towards a Gaussian as the filter order is increased.

4.5.2 Filanovsky's filter approach [15]

Filanovsky's method describes synthesis of pulse-forming networks with quasi-Gaussian impulse responses using passive networks. It is well known that the $\sin^2(\pi t/\tau)$ function over one semi-period is a sufficiently good approximation to the Gaussian response. In this approach, the transfer function is obtained using the first semi-period of the $\frac{2}{\tau} \sin^2 \frac{\pi}{\tau}(t - \frac{\pi}{2} + \frac{\tau}{2})$ function, with $\tau \leq \pi$, as an initial approximation to the network impulse response. The corresponding Laplace-domain function is given by

$$F(s) = \frac{8(\pi/\tau)^2 \sinh(\tau s/2)}{\tau s[s^2 + (2\pi/\tau)^2]} e^{-\frac{\pi}{2}s} \approx e^{-\frac{\pi}{2}s} \quad (4.30)$$

where the function \sinh has been represented by the first two terms of the infinite product, $\sinh(x) = \prod_{i=1}^{\infty} (1 + \frac{x^2}{i^2 \pi^2})$. One can note that the above function is a non-realizable transfer function. In [15] a realizable transfer function $\tilde{F}(s)$ was presented that approximates the previous function $F(s)$

$$\tilde{F}(s) = \frac{A_1}{\prod_{i=0}^{n_1} [s^2 + (2i+1)^2] + A_2 s \prod_{i=1}^n [s^2 + 4i^2]} \quad (4.31)$$

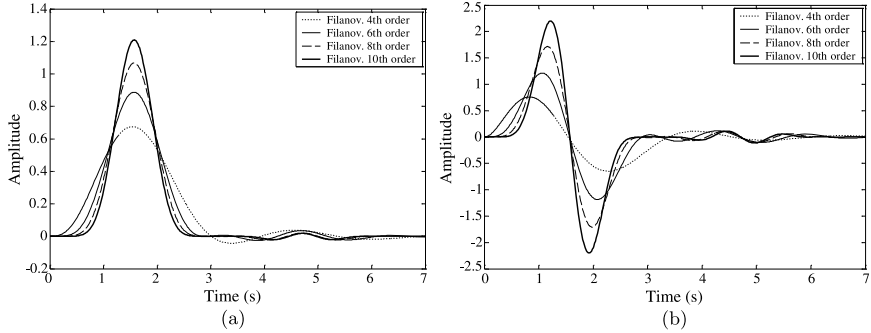


Fig. 4.15. Approximated Gaussian function (a) and first Gaussian wavelet base using Filanovsky's method (b)

where A_1 and A_2 are constants and should be positive and real. To find both constants A_1 and A_2 , one equates $F(s)$ and $\tilde{F}(s)$ at $s = 0$ and $s = j$, respectively, which yields

$$\begin{aligned} A_1 &= \prod_{i=1}^{n_1} (2i+1)^2 \\ A_2 &= \frac{\tau[(2\pi/\tau)-1]A_1}{8(\pi/\tau)^2 \sin(\tau/2) \prod_{i=1}^n [(2i)^2 - 1]} \end{aligned} \quad (4.32)$$

As an example, we consider the approximation of a Gaussian using the described method. The approximated impulse responses are shown in Fig. 4.15a.

In addition, the first derivative of Gaussian can be described by delayed positive and delayed negative semi-periods of sine-squared functions. Applying the same procedure, one can also obtain a transfer function which describes the first derivative of a Gaussian. The resulting impulse responses are shown in Fig. 4.15b.

4.5.3 Fourier-series method

The Fourier-series method is an orthogonal-function approximation in the time domain. The big advantage of this method is that the series is readily transformable into the frequency domain, as given by

$$f(t) = \sum_{k=-N}^N a_k e^{j k \omega t} \iff F(s) = \sum_{k=-N}^N \frac{a_k}{s - j \omega k} \quad (4.33)$$

where this Fourier series is truncated to include only terms inside the interval $-N < k < N$. However, the disadvantage of the Fourier-series method lies in the fact that $f(t)$ is a periodic function. Thus, the Fourier series cannot always be used to approximate an impulse response $h_T(t)$ limited in time (i.e.,

$h(t) = 0$ for $t < 0$ and $t > T$) directly. To overcome this limitation, the following scheme may be employed.

First, to eliminate the part of $f(t)$ for $t > T$, we may use the double-step weighting function [1], $w(t)$, given by

$$w(t) = u_o(t) - u_o(t - T) \quad (4.34)$$

to be convolved with the function $f(t)$, resulting in

$$h_T(t) = w(t) \otimes f(t) \iff H_T(s) = (1 - e^{-sT}) \cdot F(s) \quad (4.35)$$

Thus, the effect of convolving a function with $w(t)$ is to add to the function its own negative delayed by T . However this function is not rational and cannot be realized. To make use of this Fourier-series technique and its associated properties, some additional mathematical artifices are necessary.

Assuming that $h_T(t)$ may be considered zero for $t > T$, we may create two periodic functions, $h_{p1}(t)$ and $h_{p2}(t)$, such that

$$h_{p1}(t) = h_{p2}(t) = \frac{1}{2}h_T(t), \quad 0 < t < T, \quad (4.36)$$

and $h_{p1}(t)$ repeats every T with alternate sign while $h_{p2}(t)$ repeats every T with the same sign. Due to the symmetry of these functions, $h_{p1}(t)$ will have only odd harmonics and $h_{p2}(t)$ will have only even harmonics. Two other series h_{sum} and h_{sub} , which are related to $h_{p1}(t)$ and $h_{p2}(t)$ can also be defined by

$$\begin{aligned} h_{sum}(t) &= h_{p1}(t) + h_{p2}(t) \\ h_{sub}(t) &= h_{p2}(t) - h_{p1}(t) \end{aligned} \quad (4.37)$$

where h_{sum} and h_{sub} are the summation and subtraction series, respectively, of period $2T$. Note that the subtraction series h_{sub} represents $h_{sum}(t)$ delayed by T seconds. Hence, in the Laplace domain

$$H_{sub}(s) = H_{sum}(s)e^{-sT} \quad (4.38)$$

Substituting Eq. 4.37 into Eq. 4.38 and squaring both side gives

$$e^{-2sT} = \left[\frac{H_{p2}(s) - H_{p1}(s)}{H_{p2}(s) + H_{p1}(s)} \right]^2 \quad (4.39)$$

From Eq. 4.35 one can derive the approximated transfer function $H_T(s)$, yielding

$$H_T(s) = (1 - e^{-2sT})H_{sum}(s) = \frac{4H_{p2}(s)H_{p1}(s)}{H_{p2}(s) + H_{p1}(s)} \quad (4.40)$$

Thus a rational function has been generated that approximates the particular $h_T(t)$.

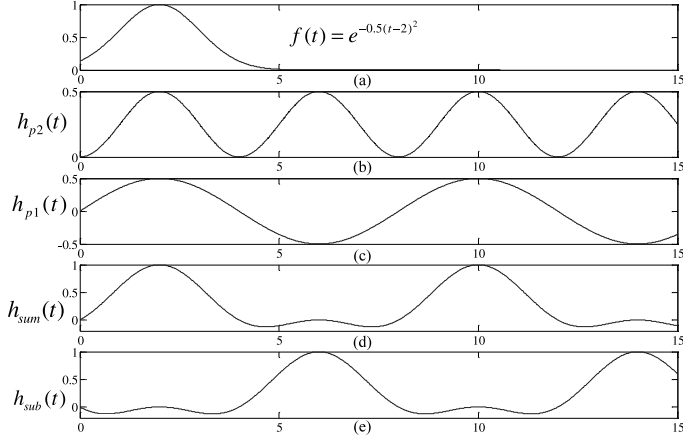


Fig. 4.16. Periodic Fourier series for the approximation method. **a** Ideal Gaussian; **b** $h_{p2}(t)$; **c** $h_{p1}(t)$; **d** $h_{sum}(t)$; **e** $h_{sub}(t)$

As an example, one can find the approximated transfer function of a Gaussian function, $e^{-0.5(t-2)^2}$, shown in Fig. 4.16a. As mentioned before, a Gaussian function can be approximated by $\sin^2(\pi t/\tau)$. Following the methodology presented before, the periodic Fourier series $h_{p2}(t)$ and $h_{p1}(t)$ become

$$\begin{aligned} h_{p2}(t) &= 0.5 \sin^2\left(\frac{\pi t}{4}\right) = 0.25 - 0.25 \cos\left(\frac{2\pi t}{4}\right) \\ h_{p1}(t) &= 0.5 \sin\left(\frac{\pi t}{4}\right) \end{aligned} \quad (4.41)$$

as shown in Fig. 4.16b and Fig. 4.16c, respectively. The corresponding transfer functions are given by

$$\begin{aligned} H_{p2}(s) &= \frac{0.25}{s} - \frac{0.25s}{s^2 + 2.467} \\ H_{p2}(s) &= \frac{0.3926}{s^2 + 0.6168} \end{aligned} \quad (4.42)$$

Finally, applying Eq. 4.40 in order to obtain the rational transfer function for the approximated Gaussian yields

$$H_T(s) = \frac{2.467}{s^3 + 1.57s^2 + 2.467s + 0.968} \quad (4.43)$$

The approximated function in time is plotted in Fig. 4.17, together with the ideal Gaussian function.

From this example it is shown that the Fourier-series method is very easy to implement, especially when the Fourier series of a given function is already available. Also, the approximated function has a good matching with the

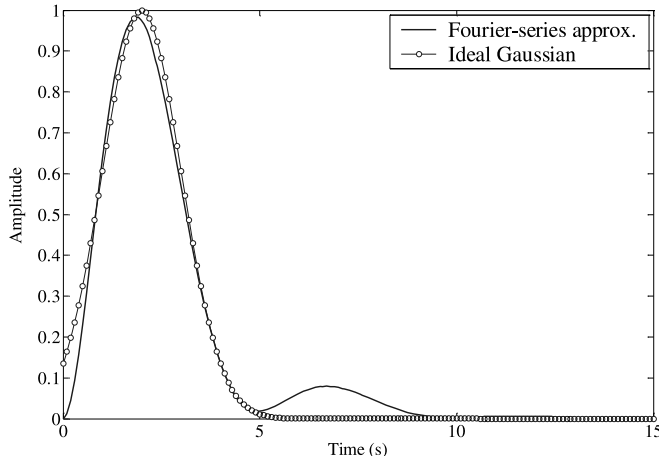


Fig. 4.17. Approximated Gaussian function using the Fourier-series method

desired impulse response with a very low-order system, in this case third order system for a Gaussian function approximation.

However, the drawback of this method is that the resulting transfer function is not always stable, i.e., it can have poles in the right half plane. Although the poles of both $H_{p1}(s)$ and $H_{p2}(s)$ are all on the j -axis, the poles of $H_T(s)$ (from Eq. 4.40) are the zeros of $H_{p1}(s) + H_{p2}(s)$, which could be anywhere on the s plane.

4.6 Discussion

In this chapter we have presented several methods to obtain good approximations in the time domain of the wavelet bases functions. One important objective of the introduced approaches is that the resulting approximated function should be rational and stable in the Laplace domain. This means that the approximating function must lead to a physically realizable network.

Nevertheless, one can notice that due to limitations in chip area, power consumption and coefficient matching, there is a trade-off between the approximation accuracy versus the order of the implemented filter. Thus, the design challenge is to obtain a low-order system while preserving a good approximation to the intended function.

We first proposed a wavelet function approximation based on Complex First Order Systems (CFOS). The Gaussian approximation using CFOS is related to a Poisson distribution, $\frac{t^n}{n!}$, where n represents the number of CFOS stages. Therefore, we can achieve an increasingly better approximation to the Gaussian function by increasing n . As a consequence, from the CFOS-based

approach, one can obtain wavelet bases related to the Gaussian function, such as Gaussian, Gabor and Morlet wavelet bases.

To obtain a more general procedure, the Padé approximation was introduced, which can theoretically implement any function that is represented by a Taylor series. The Padé approximation is used to approximate the Laplace transform of the desired wavelet transfer function by a suitable rational function around a selected point s_0 . In the example we used $s_0 = 0$.

Another approach that can approximate all kinds of wavelet functions was given by the L_2 method. The advantage of this method compared to the Padé is that the L_2 offers a more global approximation, i.e., not concentrating on one particular point. Also the L_2 method can be applied in the time domain as well as in the Laplace domain. However, the computation complexity of this method is much higher than that of the CFOS-based and the Padé approximation, and, depending on the starting point, there is a risk for non-global optimum numerical approximation for particular n th order systems.

From a Mean-Square Error (MSE) comparison, we have analyzed the performance of the given approximation methods. For low-order systems, the L_2 approximation yields better wavelet matching than the CFOS-based and Padé approaches. However, increasing the order of the filter the approximation accuracy becomes very similar for both L_2 and Padé.

In addition, three other approaches for time-domain approximation were presented. First, a Bessel–Thomson filter was presented. The transfer function of this filter, an all-pole transfer function, is based on the Bessel polynomial. The approximation of a Gaussian function using the Bessel–Thomson filter results in a high-order system, mainly because the transfer function is found indirectly from the requirements in the frequency domain. Another limitation of this method is that it is restricted to just Gaussian function approximation.

The approach defined here as the Filanovsky's method obtains the approximated transfer function using the first semi-period of the sine squared function as an initial approximation to the network impulse response. From the obtained Gaussian and first derivative of Gaussian approximations, one can conclude that the approximation accuracy of this method is not so good compared to the Padé and the L_2 approaches.

Finally, a very simply method based on Fourier-series has been presented. The Fourier-series method leads to the same order of accuracy as the Fourier-series approximation of $h(t)$ in the time interval $0 < t < T$.

Hence Bessel, Filanovsky and Fourier-series approximations are most suitable for those impulse responses that do not have any discontinuity or in situations where a large number of poles is acceptable.

4.7 Conclusions

Due to their general applicability, and the excellent accuracy results, in this book, the Padé and the L_2 approximations have been chosen, which generate reasonable low-order and good fit transfer functions.

Thus, the Padé and the L_2 transfer functions describing the wavelet filter will be implemented in a suitable filter topology in the next chapter. We will map these transfer functions onto suitable state space descriptions that allow for low-power implementation.

References

- [1] K. L. Su, *Time Domain Synthesis of Linear Networks*, Prentice-Hall, Englewood Cliffs, NJ, 1971.
- [2] H. Kamada and N. Aoshima, *Analog Gabor transform filter with complex first order system*, in: Proc. SICE, Tokushima, Japan, pp. 925-930, Jul 1997.
- [3] N. Aoshima, *Analog realization of complex first order system and its application to vowel recognition*, in: Proc. SICE, Hokkaido, Japan, pp. 1239-1244, 1995.
- [4] S. A. P. Haddad, R. P. M. Houben and W. A. Serdijn, *Analog wavelet transform employing dynamic translinear circuits for cardiac signal characterization*, in: Proc. ISCAS, Bangkok, Thailand, vol. 1, pp. I-121-124, May 25-28, 2003.
- [5] G. A. Baker Jr., *Essentials of Pade Approximants*, Academic Press, New York, 1975.
- [6] A. Bultheel and M. Van Barel, *Pade techniques for model reduction in linear system theory: a survey*, J. Comput. Appl. Math., vol. 14, pp. 401-438, 1986.
- [7] S. A. P. Haddad, S. Bagga and W. A. Serdijn, *Log-domain wavelet bases*, IEEE Transactions on Circuits and Systems – I: Regular Paper, vol. 52, no. 10, pp. 2023-2032, 2005.
- [8] S. A. P. Haddad, N. Verwaal, R. Houben and W. A. Serdijn, *Optimized dynamic translinear implementation of the Gaussian wavelet transform*, in: Proc. IEEE Int. Symp. Circuits and Systems, Vancouver, Canada, vol. 1, pp. 145-148, May 23-26, 2004.
- [9] D. Zwillinger, *Standard Mathematical Tables and Formulae*, 30th edn, CRC Press, Boca Raton, FL, 1996.

- [10] J. M. H. Karel, R. L. M. Peeters, R. L. Westra, S. A. P. Haddad and W. A. Serdijn, *Wavelet approximation for implementation in dynamic translinear circuits*, in: Proc. IFAC World Congress 2005, Prague, July 4-8, 2005.
- [11] J. M. H. Karel, R. L. M. Peeters, R. L. Westra, S. A. P. Haddad and W. A. Serdijn, *An L_2 -based approach for wavelet approximation*, in: Proc. CDC-ECC 2005, Seville, Spain, December 12-15, 2005.
- [12] J. M. H. Karel, R. L. M. Peeters, R. L. Westra, S. A. P. Haddad and W. A. Serdijn, *Optimal discrete wavelet design for cardiac signal processing*, in: Proc. EMBC 2005, Shanghai, China, September 1-4, 2005.
- [13] T. Kailath, *Linear Systems*, Prentice Hall, Englewood Cliffs, NJ, 1980.
- [14] J. Leblond and M. Olivi, *Weighted H_2 -approximation of transfer functions*, Math. Control Signals Syst., vol. 11, pp. 28-39, 1998.
- [15] I. M. Filanovsky and P. N. Matkhanov, *Synthesis of time delay networks approximating the pulse response described by an integer power of a sinusoid over its semi-period*, Analog Integrated Circuits and Signal Processing, vol. 28, no. 1, pp. 83-90, 2001.
- [16] R. Schaumann and M. V. Valkenburg, *Design of Analog Filters*, Oxford University Press, London, ISBN: 0-19-511877-4.

Chapter 5

Optimal State Space Descriptions

This chapter describes the next step towards the implementation of the wavelet filter. Departing from the transfer functions defined in Chapter 4, we derive a state space description of the filter. Since state space descriptions are not unique representations of a dynamical system, they allow the designer to find an implementation that fits the best to the requirements, e.g. coefficients that are readily implemented, a prescribed circuit topology, or maximum dynamic range. The description is transformed into the desired form by state space transforms or similarity transforms. In the context of low-power, low-voltage analogue integrated circuits, the most important requirements are dynamic range, sensitivity, and sparsity, all of which will be treated in the sections that follow.

5.1 State space description

In the state space method, the n th-order differential equation (DE) describing a dynamic system is organized as a set of first-order DEs. The common form of a state space description is given by

$$\begin{aligned}\frac{dx(t)}{dt} &= Ax(t) + Bu(t) \\ y(t) &= Cx(t) + Du(t)\end{aligned}\tag{5.1}$$

The input and output signals of the system are $u(t)$ and $y(t)$, respectively. The vector variable $x(t)$ represents the state of the system. The minimum number of state variables required to represent a given system is usually equal to the order n of the system's defining differential equation. A , B and C are the state, input, and output matrices of the state space description, respectively, as illustrated by the block diagram in Fig. 5.1. The entries of A , B , C and D are derived directly from the coefficients of the transfer function [1], [2], [3], [4].

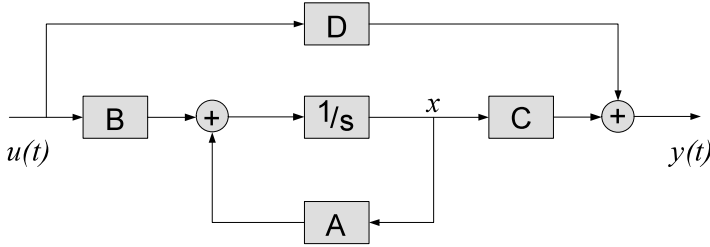


Fig. 5.1. Block diagram of the state space description

The state of a dynamic system directly describes the distribution of internal energy in the system [1]. State variables must be linearly independent. So, we can relate the state to the system inputs and outputs and thus connect the internal variables to the external inputs and outputs, whereas the transfer function relates only the input to the output and does not show the internal behavior [2].

The general expression of the transfer function corresponding to a state space description can be easily derived from Eq. 5.1 and is given by

$$H(s) = C \cdot (sI - A)^{-1} \cdot B + D \quad (5.2)$$

The entries of the matrices A , B , C and D are derived directly from the coefficients of the transfer function. The poles of the transfer function are the eigenvalues of A . In other words, the denominator of the transfer function is given by the determinant of $sI - A$, where I is the identity matrix. The zeros of the filter are constituted from the contents of all four system matrices, and are given by $C \cdot \text{adj}(sI - A) \cdot B + D$, where adj computes the adjoint of the respective matrix [2].

One can also derive from Eq. 5.1 two intermediate transfer functions, $F(s)$ and $G(s)$, which are the signal and noise transfer functions, respectively [5]. $F(s)$ represents the transfer function from the filter input $u(s)$ to the integrator outputs $x(s)$,

$$F(s) = \frac{x(s)}{u(s)} = (sI - A)^{-1} \cdot B \quad (5.3)$$

and $G(s)$ represents the transfer function from integrator inputs to the filter output $y(s)$,

$$G(s) = \frac{y(s)}{\epsilon(s)} = C \cdot (sI - A)^{-1} \quad (5.4)$$

where $\epsilon(s)$ models the noise generated at the input of the integrator.

The internal state variables are the smallest possible subset of system variables that can represent the entire state of the system at any given time. Hence, the output of a system at any instant is determined completely from the knowledge of the system state and the input at that instant. Nevertheless,

a given transfer function can be converted into a state equation in several ways. This is due to the fact that the initial conditions of a system can be specified in many different ways, and consequently, the system state can be specified in many forms. This means that state variables (and as a consequence, the state space equations) are not unique.

5.2 Dynamic range

A system's dynamic range is essentially determined by the maximum processable signal magnitude and the internally generated noise. It is well known that the system's controllability and observability gramians play a key role in the determination and optimization of the dynamic range [10], [5].

The controllability and observability gramians are derived from the state space description. The definition of the controllability gramian, related to the system matrices A and B equals:

$$K = \int_0^\infty e^{At} BB^T e^{A^T t} dt = \frac{1}{2\pi} \int_{-\infty}^{+\infty} F(j\omega) F^*(j\omega) d\omega \quad (5.5)$$

The observability gramian, related to the system matrices A and C equals:

$$W = \int_0^\infty e^{A^T t} C^T C e^{At} dt = \frac{1}{2\pi} \int_{-\infty}^{+\infty} G^*(j\omega) G(j\omega) d\omega \quad (5.6)$$

If A is stable, the controllability (K) and observability (W) gramians are the unique, symmetric solutions of the following two Lyapunov equations

$$AK + KA^T + 2\pi BB^T = 0 \quad (5.7)$$

$$A^T W + WA + 2\pi C^T C = 0 \quad (5.8)$$

where A , B and C are the state, input, and output matrices of the state-space description, respectively.

In [6] it is shown that, in order to maximize the dynamic range of the system, one should minimize the objective functional, which represents the relative improvement of the dynamic range and contains all parameters which are subject to manipulation by the designer. The objective functional is given by

$$F_{DR} = \frac{\max_i k_{ii}}{(2\pi)^2} \sum_i \frac{\alpha_i}{C_i} w_{ii} \quad (5.9)$$

where k_{ii} and w_{ii} are the main diagonal elements of K and W , respectively, $\alpha_i = \sum_j |A_{ij}|$ is the absolute sum of the elements on the i th row of A , and C_i is the capacitance in integrator i .

5.2.1 Dynamic range optimization

Departing from the transfer function derived in Chapter 4, one can generate a state space description of the filter, which is optimized with respect to its dynamic range [7], [6]. In [6] a method to optimize the state space description of a dynamical system is presented, based on the observability and controllability gramians. The resulting system has, under certain conditions, the maximum dynamic range achievable, given the total amount of capacitance.

The optimization is based on space transforms, also known as similarity transforms. A similarity (coordinate) transform, indicated by an invertible matrix T , defines a new state vector

$$x' = T^{-1}x \quad (5.10)$$

assuming $\det(T) \neq 0$.

And consequently, the transformation results in new system matrices, given by

$$\begin{aligned} A' &= T^{-1}AT \\ B' &= T^{-1}B \\ C' &= CT \\ D' &= D \end{aligned} \quad (5.11)$$

By the state space transformation the controllability and observability gramians become optimal

$$\begin{aligned} K' &= T^{-1}KT^{-T} \\ W' &= T^TWT \end{aligned} \quad (5.12)$$

where $T^{-T} = (T^{-1})^T$.

As the dynamic range of a circuit is defined as the ratio of the maximum and the minimum signal level that it can process, optimization of the dynamic range is equivalent to the simultaneous maximization of the (distortionless) output swing and the minimization of the overall noise contribution [7].

From the state space representation, geometry concepts can be useful in visualizing the solution of a system. In [6], Rocha gives a geometric interpretation of the optimization of the dynamic range. A visualization of the optimization procedure can be seen in Fig. 5.2, for a system with three state variables. The output swing is related via the controllability gramian to the space of ‘occurring’ state-space vectors. Under the assumption of a random input signal, the shape of this space is generally a multidimensional ellipsoid. The constraint that each integrator has a maximum representation capacity (M) defines a multidimensional cuboid, which, for a distortionless transfer, should contain the former mentioned ellipsoid completely. As the mean square radius of the ellipsoid is equivalent to the maximum output swing, the

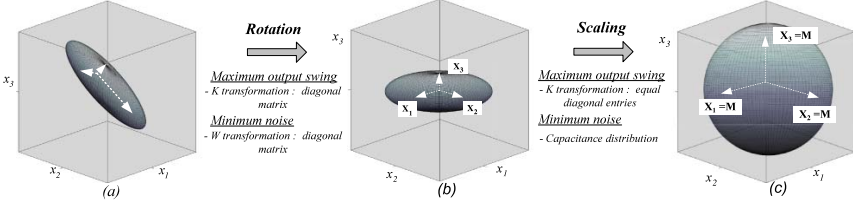


Fig. 5.2. Dynamic Range optimization based on the similarity transformation of K and W and capacitance distribution. The coordinate axes represent the state variables and the cuboid represents the maximum signal amplitude (M) that the integrators are able to handle. **a** The initial state space representation (ellipsoid) is usually not well adapted to the integrator’s representations capacity bounds (cuboid). **b** The (rotated) ellipsoid’s principal axes are now aligned to the coordinate axes, as a result of the diagonalization procedure to the matrices K and W . **c** Finally, the optimized state representation is obtained by scaling the states variables. Note that the sphere represents the maximum possible mean square radius which can be fitted into the integrator’s capacity cuboid

output swing is maximal when the mean square radius is. This can occur if and only if the ellipsoid becomes a spheroid. In that case the controllability gramian is a diagonal matrix with equal diagonal entries, which means that all axes of the ellipsoid have equal length. Thus, the first optimization step boils down to a similarity transform, such that the controllability gramian of the new system becomes a diagonal matrix with equal diagonal entries. This transform is given by

$$T_K = P_K D_K^{1/2} \quad (5.13)$$

where P_K is the eigenvector matrix of K and D_K is a diagonal matrix whose diagonal entries are the eigenvalues of K .

In the second step of the optimization procedure, the system is optimized with respect to its noise contribution. Rocha defines another ellipsoid, which describes the noise that is added to the state vector in each direction. While preserving the result of the first optimization step, it is possible to rotate the state space, such that the observability gramian becomes a diagonal matrix as well. In that case, the axes of the noise ellipsoid are aligned with the ‘system axes’. The transformation of W is defined as

$$T_W = P_W \quad (5.14)$$

where P_W is the eigenvector matrix of W .

Finally, profiting from the well-known fact that the relative noise contribution of an integrator decreases when the capacitance and bias current increase, we match the optimal normalized capacitance distribution to the noise contributions of each individual integrator (noise scaling), i.e., the diagonal entries

of W , combined with the coefficients in matrix A , which yields [6], [7]:

$$C_i = \frac{\sqrt{\alpha_i w_{ii} k_{ii}}}{\sum_j \sqrt{\alpha_j w_{jj} k_{jj}}} \quad (5.15)$$

5.3 Sparsity

The drawback of a dynamic-range optimal system is that its state-space matrices are generally fully dense, i.e., all the entries of the A , B , C matrices are filled with non-zero elements. These coefficients will have to be mapped onto circuit components, and will result in a complex circuit with a large number of interconnections. For high-order filters it is therefore necessary to investigate how a realization of the desired transfer function having sparser state-space matrices would compare to the one having maximal dynamic range.

By definition, a sparse matrix is a matrix populated primarily with zeros. For a less complex circuit, it is possible, for instance, to transform the state space matrix A in a similar decomposition and by this reducing the number of non-zero coefficients in A . One important characteristic of a similarity transformation matrix T is that, considering a system of order n , T has n^2 degrees of freedom. Thus, the system can be transformed in several ways, achieving the desired sparsity requirements.

However, these transformations lead to an increase in the system noise and consequently to an increase in the objective functional, Eq. 5.9. Considering the fact that for a given system the choice of state is not unique, in the next subsections we will review some well-known state forms and analyze the state space matrices with respect to dynamic range and sparsity.

5.3.1 Orthogonal transformations

The orthogonal (unitary) transformation-based forms are called condensed forms. Some examples of these condensed forms are the Hessenberg and the Schur decomposition, which will be described below.

Any orthogonal transformation, described by $T^T T = I$, has $n(n - 1)/2$ degrees of freedom and, consequently, it is possible to create $n(n - 1)/2$ zeros. In other words, these transformations are extremely useful in zeroing specified elements in a matrix.

Hessenberg decomposition

A Hessenberg decomposition is a matrix decomposition of a matrix A into a unitary matrix U and a Hessenberg matrix A_{Hess} such that

$$A = U A_{Hess} U^T \quad (5.16)$$

For real matrices, a unitary matrix is a matrix U for which $U^{-1} = U^T$. A_{Hess} is similar to A and has the same eigenvalues as A . The Hessenberg

decomposition transforms a matrix in an upper diagonal matrix where only the elements of the main sub-diagonal are different from zero

$$A_{Hess} = \begin{bmatrix} a_{11} & a_{12} & a_{13} & \dots & a_{1,n-1} & a_{1,n} \\ a_{21} & a_{22} & a_{23} & \dots & a_{2,n-1} & a_{2,n} \\ 0 & a_{32} & a_{33} & \dots & a_{3,n-1} & a_{3,n} \\ 0 & 0 & a_{43} & \dots & a_{4,n-1} & a_{4,n} \\ \vdots & \vdots & \vdots & \ddots & \vdots & \vdots \\ 0 & 0 & 0 & \dots & a_{n,n-1} & a_{n,n} \end{bmatrix} \quad (5.17)$$

where the matrices B and C have no specific structure, being defined by $B_{Hess} = U^{-1}B$ and $C_{Hess} = CU$. Then, as one can see in Eq. 5.17, an upper Hessenberg matrix has zero everywhere below the diagonal except for the first subdiagonal row. However, if matrix A is symmetric, the Hessenberg form becomes a tridiagonal representation.

Schur decomposition

The Schur decomposition of a square matrix A is a matrix decomposition of the form

$$A_{Schur} = Q^T A Q = D + N \quad (5.18)$$

where Q is a orthogonal (unitary) matrix and A_{Schur} is an upper triangular matrix which is the sum of a $D = \text{diag}(\lambda_1, \lambda_2, \dots, \lambda_n)$ (i.e., a diagonal matrix consisting of eigenvalues λ of A) and a strictly upper triangular matrix N . Thus, the eigenvalues of A appear on the main diagonal of A_{Schur} .

The Schur decomposition of a square matrix A involves finding a unitary matrix Q that can be used for a similarity transformation of A to form a block upper triangular matrix A_{Schur} , defined by

$$A_{Schur} = \begin{bmatrix} a_{11} & a_{12} & a_{13} & \dots & a_{1,n-1} & a_{1,n} \\ 0 & a_{22} & a_{23} & \dots & a_{2,n-1} & a_{2,n} \\ 0 & 0 & a_{33} & \dots & a_{3,n-1} & a_{3,n} \\ 0 & 0 & 0 & \dots & a_{4,n-1} & a_{4,n} \\ \vdots & \vdots & \vdots & \ddots & \vdots & \vdots \\ 0 & 0 & 0 & \dots & 0 & a_{n,n} \end{bmatrix} \quad (5.19)$$

The Schur decomposition always exists and so the similarity transformation of A to upper triangular always exists. This contrasts with the eigensystem similarity transformation, used to diagonalize a matrix, which does not always exist.

For complex values, the Schur decomposition produces a quasi-triangular matrix. Under real (orthogonal) transformations one cannot triangularize a matrix if it has complex conjugate eigenvalues. Instead one can always obtain a quasi-triangular form with 1×1 or 2×2 blocks on the diagonal corresponding to the real and complex conjugate eigenvalues, respectively.

With respect to sparsity, the preference is for the Schur decomposition rather than for the Hessenberg decomposition, because it returns a matrix with a larger number of zeros.

5.3.2 Canonical form representations

From control theory, it is known that a general transfer function, as described in Eq. 5.20, can be written directly into (controllable or observable) canonical form [1], [4].

$$H(s) = \frac{p_{n-1}s^{n-1} + p_{n-2}s^{n-2} + \cdots + p_1s + p_0}{s^n + q_{n-1}s^{n-1} + \cdots + q_1s + q_0} \quad (5.20)$$

The entries of A , B , C and D of a canonical form are derived from coefficients inspection of the transfer function, as given below.

A state-space system in controllable canonical form has the following structure

$$\begin{aligned} A_c &= \begin{bmatrix} 0 & 1 & 0 & \dots & 0 \\ 0 & 0 & 1 & \dots & 0 \\ \vdots & \vdots & \vdots & \vdots & \vdots \\ 0 & 0 & 0 & \dots & 1 \\ -q_0 & -q_1 & -q_2 & \dots & -q_{n-1} \end{bmatrix}, & B_c &= \begin{bmatrix} 0 \\ 0 \\ \vdots \\ 0 \\ 1 \end{bmatrix} \\ C_c &= \begin{bmatrix} p_0 & p_1 & \dots & p_{n-2} & p_{n-1} \end{bmatrix}, & D &= [0] \end{aligned} \quad (5.21)$$

This state-space realization is called controllable canonical form because the resulting model is guaranteed to be controllable. The coefficients of the numerator appear in the C_c matrix and the coefficients of the denominator appear (with opposite sign) as the last row of the A_c matrix. The central feature of the controllable form is that each state variable is connected by the feedback to the control input, as shown in Fig. 5.3.

The transfer function coefficients can also be used to construct another type of canonical form, the observable canonical form defined by

$$\begin{aligned} A_o &= \begin{bmatrix} 0 & 0 & \dots & 0 & -q_0 \\ 1 & 0 & \dots & 0 & -q_1 \\ \vdots & \vdots & \vdots & \vdots & \vdots \\ 0 & 0 & \dots & 0 & -q_{n-2} \\ 0 & 0 & \dots & 1 & -q_{n-1} \end{bmatrix}, & B_o &= \begin{bmatrix} p_0 \\ p_1 \\ \vdots \\ p_{n-2} \\ p_{n-1} \end{bmatrix} \\ C_o &= \begin{bmatrix} 0 & 0 & \dots & 0 & 1 \end{bmatrix}, & D &= [0] \end{aligned} \quad (5.22)$$

This state-space realization is called observable canonical form because the resulting model is guaranteed to be observable. The coefficients of the numerator appear in the B_o matrix and the coefficients of the denominator

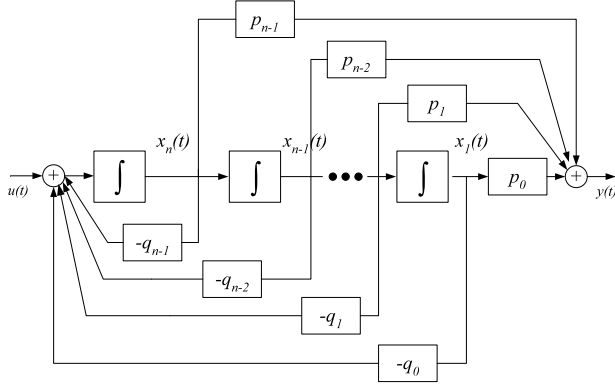


Fig. 5.3. Controllable canonical form realization

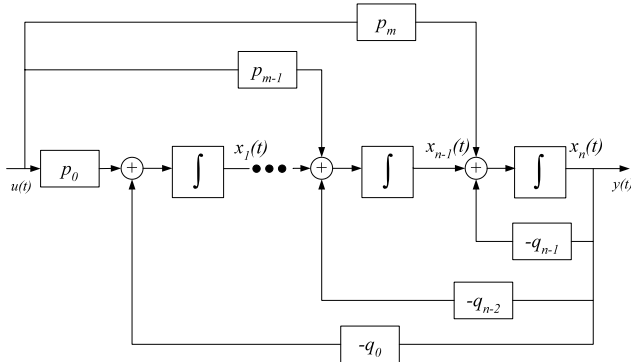


Fig. 5.4. Observable canonical form realization

appear (with opposite sign) as the last column of the A_o matrix. Figure 5.4 shows the implementation of these matrices in a block diagram.

One can note the relationship between the controllable and observable canonical forms. The A matrices in these two cases are the transpose of one another, and the B of one is the transpose of C in the other, and vice versa. This is defined as a duality relation.

Controllability and observability are qualitative properties of a system. These properties depend on the elements of the A , B and C matrices. Controllability refers to the ability of the input to control (or affect) each of the system modes, whereas the observability occurs when each of the modes can be detected at the output. A basic result in control theory is that a system in state-space form is controllable if and only if the matrix $[B, AB, A^2B, \dots, A^{n-1}B]$ has a full rank n (i.e., is invertible). The rank of an arbitrary rectangular matrix A is the dimension of the largest square submatrix that has a nonzero determinant, i.e., defines the number of linearly independent rows or

columns in a matrix. Similarly, a state-space system is observable if and only if $[C C A \dots C A^{n-1}]^T$ is non-singular with rank equals n .

The advantage, with respect to sparsity, of a canonical decomposition is that the canonical forms have n^2 elements assigned either to 0 or to 1, which corresponds to a extremely sparse matrix.

5.3.3 Biquad structure

A high-order transfer function $H(s)$ can be factored into the product of first- and second-order transfer functions. Hence, as shown in Fig. 5.5, a filter can be implemented as a cascade of second-order biquadratic blocks, also called biquad stages (and a first-order block, if necessary) [8].

The signal flow graph of a biquad stage is shown in Fig. 5.6.

The corresponding second-order transfer function of a biquad, $H_i(s)$, is expressed in terms of A , B , C and D .

$$H_i(s) = \frac{(c_1 b_1 + c_2 b_2)s + c_1 a_{12}b_2 + c_2 a_{21}b_1 - c_1 a_{22}b_1 - c_2 a_{11}b_2}{s^2 + (-a_{11} - a_{22})s + a_{11}a_{22} - a_{12}a_{21}} + d \quad (5.23)$$

Cascading of n stages means that we connect the output of $H_{n-1}(s)$ to the input of $H_n(s)$, such that the product of the individual transfer functions $H_i(s)$ implements the prescribed function $H(s)$. Note that the numerators and denominators of $H_i(s)$ can be combined in different ways in order to obtain the final transfer function $H(s)$. One way to decrease the coefficients sensitivity, is by grouping the zeros with the nearest pole pair. Finally, one can derive the combined state space description of the cascade connected system which

$$H(s) = H_1(s).H_2(s).H_3(s)\dots H_N(s)$$

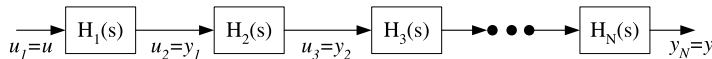


Fig. 5.5. Biquad cascade realization of an n th-order transfer function

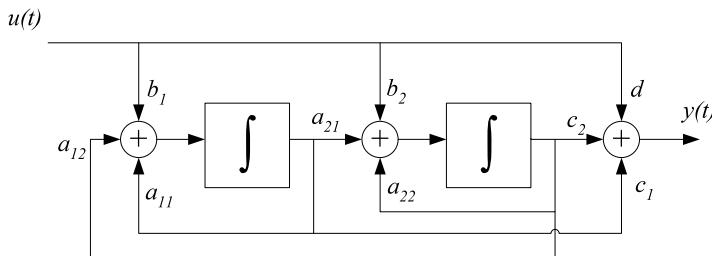


Fig. 5.6. Block diagram of the second-order biquad

is given by

$$A = \begin{bmatrix} A_1 & 0 & 0 & \dots & 0 \\ B_2 C_1 & A_2 & 0 & \dots & 0 \\ B_3 D_2 C_1 & B_3 C_2 & A_3 & \dots & 0 \\ B_4 D_3 D_2 C_1 & B_4 D_3 C_2 & B_4 C_3 & \dots & 0 \\ \vdots & \vdots & \vdots & \vdots & \vdots \\ B_N D_{N-1} \dots D_2 C_1 & B_N D_{N-1} \dots D_3 C_2 & B_N D_{N-1} \dots D_4 C_3 & \dots & A_N \end{bmatrix} \quad (5.24)$$

$$B = \begin{bmatrix} B_1 \\ B_2 D_1 \\ B_3 D_2 D_1 \\ B_4 D_3 D_2 D_1 \\ \vdots \\ B_N D_{N-1} \dots D_1 \end{bmatrix}, \quad C^T = \begin{bmatrix} D_N \dots D_2 C_1 \\ D_N \dots D_3 C_2 \\ D_N \dots D_4 C_3 \\ \vdots \\ D_N C_{N-1} \\ C_N \end{bmatrix}$$

The main advantage of cascade filters is their generality, i.e., any arbitrary stable transfer function can be realized as a cascade circuit, and very easy tuning because each biquad is responsible for the realization of only one pole-zero pair. By this, the realizations of the individual critical frequencies of the filter are decoupled from each other. The disadvantage of this decoupling is that for high-order filters, cascade designs are often found to be too sensitive to component variations.

5.3.4 Diagonal controllability gramian – an orthonormal ladder structure

When designing high-order filters, it is very desirable to concentrate on circuits that are less sensitive to component variations. It is known that an optimal dynamic range system will also have optimal sensitivity [7]. Nevertheless, in order to improve the state-space matrices' sparsity, an orthonormal ladder structure can be implemented, which still presents a good behavior with respect to sensitivity. Figure 5.7 shows a block diagram of a general orthonormal ladder filter [9]. As shown in the block diagram, the filter output is obtained from a linear combination of the outputs of all integrators.

Another useful property of orthonormal ladder filters is the ability to realize any stable transfer function. Arbitrary poles are realized using the ladder feedback structure while transmission zeros are realized using an output summing stage. Additionally, since for a given transfer function the orthonormal ladder realization is unique, the design procedure is more easily automated than the process of finding an optimal biquad cascade design where pole-zero pairing and cascade ordering are important.

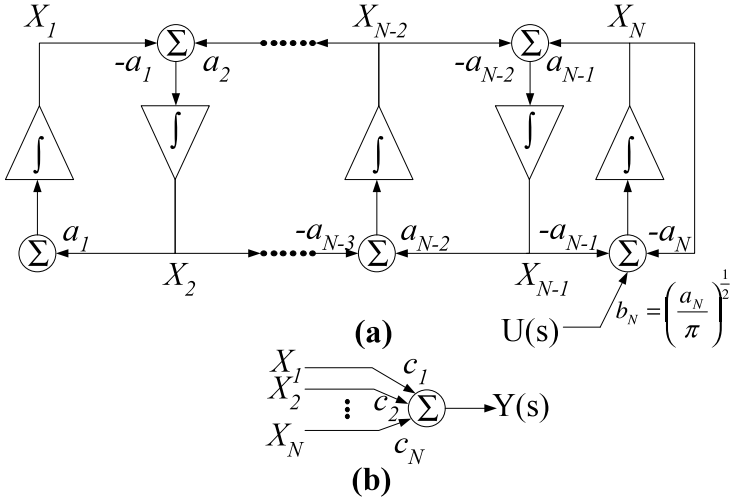


Fig. 5.7. Block diagram of an orthonormal ladder filter. **a** Leapfrog structure. **b** Output summing stage

The A , B and C matrices of this structure are given by

$$A = \begin{bmatrix} 0 & \alpha_1 & & \dots & & 0 \\ -\alpha_1 & 0 & \alpha_2 & \dots & & 0 \\ & -\alpha_2 & 0 & \alpha_3 & \dots & \\ \vdots & \ddots & \ddots & \ddots & & \vdots \\ 0 & & \dots & -\alpha_{n-2} & 0 & \alpha_{n-1} \\ 0 & & \dots & & -\alpha_{n-1} & \alpha_n \end{bmatrix} \quad (5.25)$$

$$B = \begin{bmatrix} 0 \\ 0 \\ 0 \\ \vdots \\ 0 \\ \sqrt{\frac{\alpha_n}{\pi}} \end{bmatrix}, \quad C^T = \begin{bmatrix} c_1 \\ c_2 \\ c_3 \\ \vdots \\ c_{n-1} \\ c_n \end{bmatrix}$$

The A matrix is tridiagonal and is very nearly skew-symmetric except for a single non-zero diagonal element. One important property of orthonormal ladder filters is the fact that the resulting circuits are inherently state scaled, i.e., the controllability gramian is already a identity matrix [9]. From the Lyapunov equation in Eq. 5.7 and assuming $K = I$, B results in an all zeros matrix except for the n th element with b_n given by $\sqrt{\frac{\alpha_n}{\pi}}$. The drawback of this structure is that the system is not optimized with respect to its noise contribution, i.e. the observability gramian W is not transformed.

The coefficients α of the A matrix are defined as

$$\begin{aligned}\alpha_i &= \sqrt{\frac{1}{x_i x_{i+1}}}, \quad 1 \leq i < n \\ \alpha_n &= \frac{1}{x_n}, \quad i = n\end{aligned}\tag{5.26}$$

where x_i are the reactive components of a singly terminated LC ladder structure. In order to calculate the values of the reactive elements x_i one needs to apply a continued fraction expansion on the denominator of the transfer function $H(s) = \frac{N(s)}{D(s)}$. The denominator can be converted into a simple continued fraction by the following procedure. First, the polynomial $D(s)$ of degree n is represented by

$$D(s) = D_{even}(s) + D_{odd}(s)\tag{5.27}$$

where $D_{even}(s)$ and $D_{odd}(s)$ are the even and the odd parts of $D(s)$, respectively. Then, applying the ratio between both parts such as

$$\begin{aligned}D_{cf}(s) &= \frac{D_{even}(s)}{D_{odd}(s)} \quad \text{if } n \text{ is even} \\ D_{cf}(s) &= \frac{D_{odd}(s)}{D_{even}(s)} \quad \text{if } n \text{ is odd}\end{aligned}\tag{5.28}$$

we end up with the continued fraction expansion of $D(s)$ in the following manner

$$D_{cf}(s) = \frac{P}{Q} = x_0 + \frac{r_0}{Q} = x_0 + \frac{1}{x_1 + \frac{r_1}{r_0}} = \cdots = x_0 + \frac{1}{x_1 + \frac{1}{x_2 + \frac{1}{\ddots + \frac{1}{x_n}}}}\tag{5.29}$$

where the r_i are the remainders and the x_i the integral parts of the intermediate fractions which define the reactive components values.

Finally, in order to implement the numerator $N(s)$ of the transfer function $H(s)$, the proper C vector must be obtained. Using the intermediate functions F_i , the coefficients c_i can be written as

$$N(s) = c_1 \cdot F_1 + c_2 \cdot F_2 + \cdots + c_n \cdot F_n\tag{5.30}$$

where

$$\begin{aligned}F_1 &= \sqrt{\frac{x_1}{\pi}} \cdot N(0) \\ F_2 &= \frac{s}{\alpha_1} F_1 \\ F_i &= \frac{1}{\alpha_{i-1}} (s F_{i-1} + \alpha_{i-2} F_{i-2}), \quad 3 \leq i \leq n\end{aligned}\tag{5.31}$$

The result is the state-space structure given in Eq. 7.36 with the coefficients calculated from Eq. 5.26 and Eq. 5.30.

5.3.5 Sparsity versus dynamic range comparison

A comparative analysis of the Dynamic Range and the Sparsity properties of several state space representations will be performed in this section. First, Fig. 5.8 shows the obtained objective functionals (FDRs) for a specific transfer function, in this case the Padé [8/10] Morlet wavelet filter transfer function given in Table 4.4. As one can see, the FDR of the orthonormal ladder structure ($FDR_{orth} = 21.6$ dB) is very close to the optimal representation ($FDR_{opt} = 19.8$ dB), only 1.8 dB larger than the optimum one, whereas the canonical forms present the largest FDRs ($FDR_{cont,can} = 149$ dB and $FDR_{obs,can} = 167$ dB).

Furthermore, in order to compare the Dynamic Range versus the order of the system, Fig. 5.9 illustrates the FDR of different state space descriptions applied to a Gaussian wavelet filter transfer function. The transfer function of the filter was obtained by a Padé approximation with order varying from 2 to 10. Note that for lower order, all the state space representations present a similar performance, with FDR values close to each other, whereas for higher order, the FDRs of some representations deviate too much from the optimal case. In this case, the Dynamic Range optimization becomes a very important requirement in high-order analog filters design. Again, one can see that the orthonormal state space is very close to the optimal representation even for high-order systems.

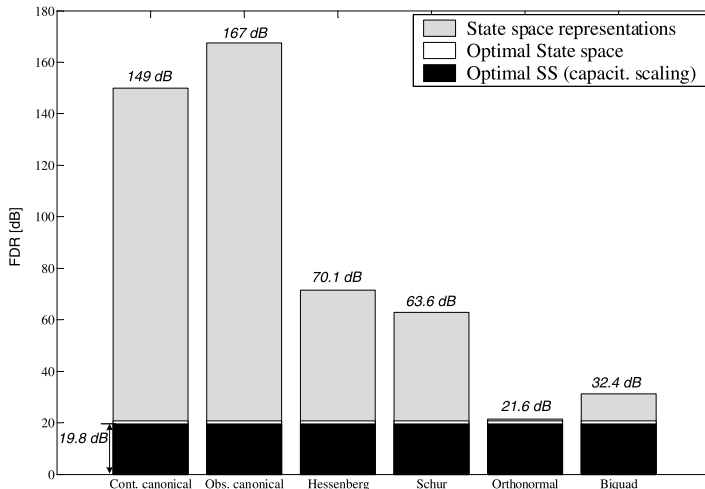


Fig. 5.8. FDR comparison of different state space descriptions for the Padé [8/10] Morlet wavelet filter transfer function in Table 4.4

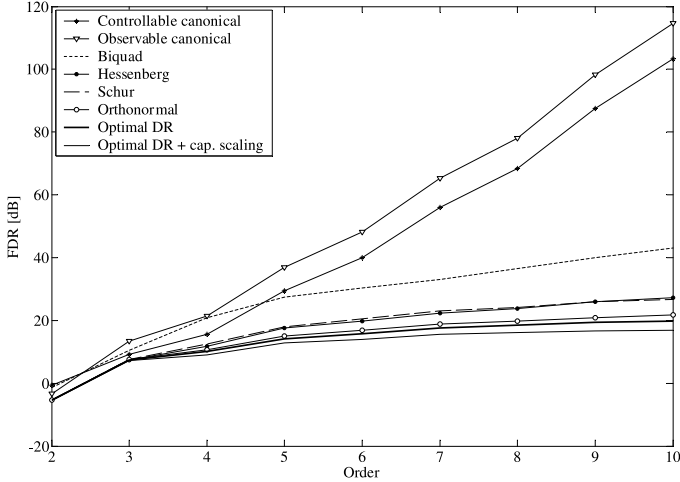


Fig. 5.9. FDR versus order of the filter for different state space representations

5.3.6 New Sparsity Figure-of-Merit (SFOM)

In order to define the sparsity property versus dynamic range for a specific state space description, we derive a new figure-of-merit. The static power consumption of an analog active filter is basically determined by the bias currents inside the filter. From a state space representation one can define the total bias current by $N_c I_o$ where N_c represents the number of non-zero coefficients presented in the state matrix A , B and C and I_o is the current necessary to implement each coefficient. As a result, the static power consumption of a filter can be written as

$$P_{\text{static}} = N_c I_o V_{cc} \quad (5.32)$$

On the other hand, in [6], the dynamic power dissipation of a n th order filter has been expressed in terms of the dynamic range, and yields

$$P_{\text{dynamic}} = 8n f k T \xi f \text{DR} = 4n f \left(\frac{M}{\delta(p)} \right)^2 \text{Tr}(KQ) \frac{1}{\text{FDR}} \quad (5.33)$$

where n is the order of the filter, f is the operating frequency, M is the maximum output amplitude, $\delta(p)$ is a non-linear monotonically increasing function of the fraction of time p that the integrators are allowed to clip, and is represented by $\delta(p) = -2 \ln(1 - p)$. Tr represents the trace of a matrix and $Q = C^T C$ is the state weighting matrix.

$$\text{Tr}(KQ)$$

is invariant under a similarity transformation and is thus beyond the designer's control.

Table 5.1. Number of non-zero coefficients N_c in A , B and C

| | |
|-------------|-----------------------------|
| Optimal | $n^2 + 2n$ |
| Hessenberg | $\frac{n(n+1)}{2} + 3n - 1$ |
| Schur | $\frac{n(n+1)}{2} + 2n$ |
| Canonical | $3n$ |
| Biquad | $5n$ |
| Orthonormal | $3n$ |

Dividing P_{static} by $P_{dynamic}$ we end up with

$$\frac{P_{static}}{P_{dynamic}} = \frac{N_c I_o V_{cc}}{4n \left(\frac{M}{\delta(p)}\right)^2 \text{Tr}(KQ) \frac{1}{\text{FDR}}} = \frac{I_o V_{cc}}{4 \left(\frac{M}{\delta(p)}\right)^2 \text{Tr}(KQ)} \frac{N_c \text{FDR}}{n} \quad (5.34)$$

where $\frac{I_o V_{cc}}{4 \left(\frac{M}{\delta(p)}\right)^2 \text{Tr}(KQ)}$ is defined by the circuit implementation, while $\frac{N_c \text{FDR}}{n}$ can be controlled at system level. So, in order to design an optimal state space description with respect to Dynamic Range and Sparsity, we present a new figure-of-merit, given by

$$\text{SFOM} = \frac{N_c \times \text{FDR}}{n} \quad (5.35)$$

From Eq. 5.35 one can see that the optimal case is the one with SFOM minimum, i.e., the system which presents a good sparsity (large number of zeros) while preserving a low FDR (i.e., a large dynamic range).

The number of non-zero coefficients N_c for different state space representations is given in Table 5.1.

Finally, several SFOMs versus the order of the system are plotted in Fig. 5.10. As expected, the orthonormal presents the best performance (lowest SFOM) mainly due to its excellent sparsity behavior and its near-optimum FDR property.

5.4 Sensitivity

To accurately realize a transfer function using analog integrated filters, the circuit components of the filter must match closely, and the sensitivity of the transfer function to the values of the filter's components must be low. This sensitivity depends on the filter network, and thus depends on the state-space representation. Hence, the sensitivity of the transfer function of a particular state-space representation is an important criterion for the comparison of different network realizations.

The sensitivity of the transfer function $H(s)$ to the component values of a state-space realization depends on the sensitivity to the entries of the state matrices A , B and $C - D$ is usually zero. Here we will consider an absolute

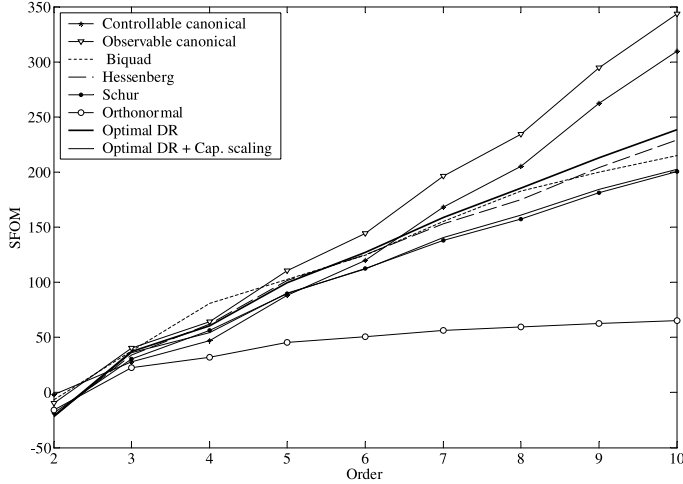


Fig. 5.10. SFOM versus order of the filter for different state space description

sensitivity measurement, which can be used to establish the relationship between the absolute changes Δa_{ij} , Δb_i and Δc_j [8].

The absolute sensitivities of $H(s)$ with respect to variations of the coefficients can be given by [10].

$$\begin{aligned} S_{a_{ij}}(s) &= \frac{\partial H(s)}{\partial a_{ij}} = c(sI - A)^{-1}e_i e_j (sI - A)^{-1}b = G_i(s)F_j(s) \\ S_{b_i}(s) &= \frac{\partial H(s)}{\partial b_i} = c(sI - A)^{-1}e_i = G_i(s) \\ S_{c_i}(s) &= \frac{\partial H(s)}{\partial c_i} = e_i(sI - A)^{-1}b = F_i(s) \end{aligned} \quad (5.36)$$

where e_i is the unit vector with i th element unity. In the case of a statistical derivation analysis, the frequency dependent variances of the transfer function are defined as

$$\begin{aligned} \Sigma_{\Delta H, A}^2(s) &= E \left\{ \left| \sum_{i=1}^n \sum_{j=1}^n S_{a_{ij}} \Delta a_{ij} \right|^2 \right\} \\ &= \sum_{i=1}^n \sum_{j=1}^n |S_{a_{ij}}|^2 = G(s)G^*(s)F(s)F^*(s) \end{aligned} \quad (5.37)$$

$$\Sigma_{\Delta H, B}^2(s) = E \left\{ \left| \sum_{i=1}^n S_{b_i} \Delta b_i \right|^2 \right\} = \sum_{i=1}^n |S_{b_i}|^2 = G(s)G^*(s)$$

$$\Sigma_{\Delta H, C}^2(s) = E \left\{ \left| \sum_{j=1}^n S_{c_j} \Delta c_j \right|^2 \right\} = \sum_{j=1}^n |S_{c_j}|^2 = F^*(s)F(s)$$

where the variations of the coefficients have been considered statistically independent. Integrating the transfer function variances over the whole frequency range, new sensitivity measures related to the observability and controllability gramians have been defined in [10], and are given by

$$\begin{aligned} m_A &\leq \text{Tr}(K) \text{Tr}(W) \\ m_B &= \text{Tr}(W) \\ m_C &= \text{Tr}(K) \end{aligned} \quad (5.38)$$

where m_A , m_B and m_C , represent, respectively, the sensitivity of the matrices A , B and C to their coefficients. Finally, the total sensitivity measure, m_T , of a transfer function with respect to the state space representation matrices can be obtained as

$$m_T = m_A + m_B + m_C \leq \text{Tr}(K) \text{Tr}(W) + \text{Tr}(K) + \text{Tr}(W) \quad (5.39)$$

The maximum sensitivity measure (worst-case sensitivity), considering $m_T = \text{Tr}(K) \text{Tr}(W) + \text{Tr}(K) + \text{Tr}(W)$, can be seen in Fig. 5.11 as function of the order n of a specific transfer function, for different state space representations. One can note that the optimal DR state space representation will also be optimal with respect to sensitivity. The Schur and Hessenberg decomposed from an optimal system also present an optimal sensitivity because the orthogonal transformation does not affect the sensitivity. The orthonormal structure has a reasonable low sensitivity to coefficient mismatch, close to the optimal case. Both controllable and observable canonical forms have the worst sensitivity measures for high-order filters, as expected.

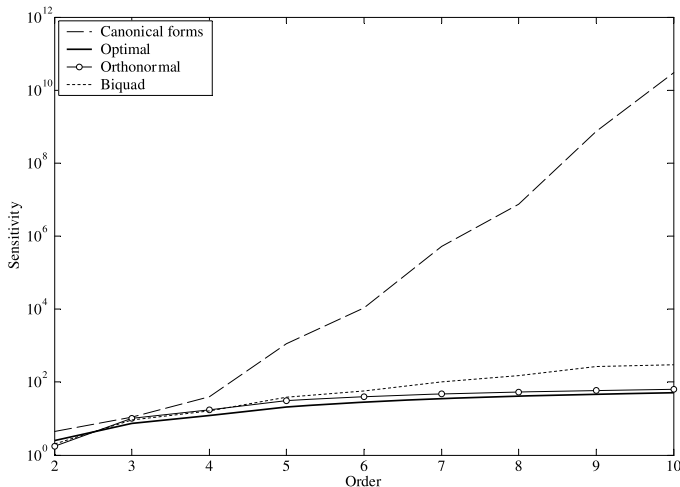


Fig. 5.11. Sensitivity versus order of the filter for different state space descriptions

5.4.1 New Dynamic Range-Sparsity-Sensitivity (DRSS) figure-of-merit

To conclude the analysis of the state space descriptions we will present a new figure-of-merit that expresses the correlation of Dynamic Range, Sparsity and Sensitivity parameters. In order to relate these three aspects, we introduce the Dynamic Range-Sparsity-Sensitivity figure-of-merit (DRSS), given by

$$\text{DRSS} = \frac{N_c \times \text{FDR} \times m_T}{n} \quad (5.40)$$

As one can see from Eq. 5.40, the objective functional, FDR, gives the relative improvement of the dynamic range, $\frac{N_c}{n}$ is related to the sparsity of the system and m_T defines the sensitivity of the matrices A , B and C with respect to their coefficients. Figure 5.12 shows the DRSS figure-of-merit versus the order of the system. Again, the orthonormal ladder structure presents the best performance (minimum DRSS) compared to the other state space descriptions presented in this chapter. Thus, we can state that the orthonormal structure is the optimal state space description for a system design where the most important requirements are dynamic range, sparsity and sensitivity. Although the state space description obtained from the optimization procedure in Section 5.2.1 gives us the optimal representation with respect to dynamic range and sensitivity, its matrices are fully dense, and consequently, its SFOM and DRSS performances are relatively poor.

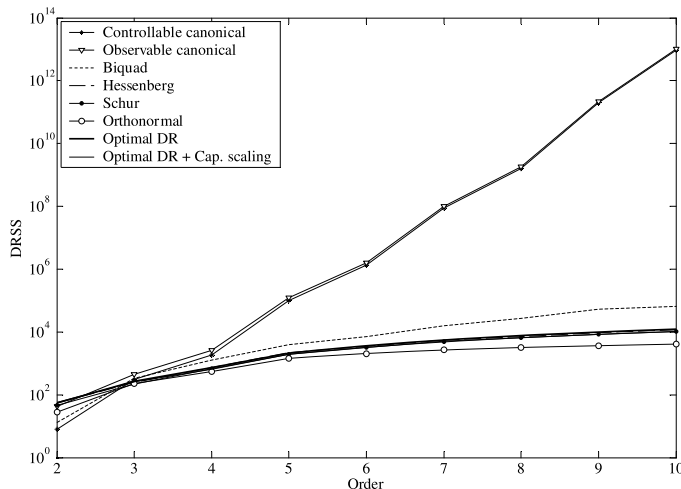


Fig. 5.12. DRSS figure-of-merit versus order of the system

5.5 Conclusion

In this chapter we presented the description and a comparison of several state space representations. The analysis was based on dynamic range, sparsity and sensitivity properties, which are the most relevant aspects for an ultra low-power analog dynamic system. From the two new figure-of-merits described above, viz., the SFOM and DRSS, we concluded that the orthonormal ladder structure is the optimal state space representation, and therefore, it will be used for the design of wavelet filters and biomedical systems in Chapter 7.

References

- [1] T. Kailath, *Linear Systems*, Prentice Hall, Englewood Cliffs, NJ, 1980.
- [2] B. P. Lathi, *Linear Systems and Signals*, Oxford University Press, New York, 2002.
- [3] P. M. DeRusso, R. J. Roy, C. M. Close and A. A. Desrochers, *State Variables for Engineers*, 2nd edn, Wiley, New York, 1998.
- [4] J. D. Aplevich, *The Essentials of Linear State-Space Systems*, Wiley, New York, 2000.
- [5] W. M. Snelgrove and A. S. Sedra, *Synthesis and analysis of state-space active filters using intermediate transfer function*, IEEE Transactions on Circuits and Systems, vol. 33, no. 3, pp. 287-301, March 1986.
- [6] D. P. W. M. Rocha, *Optimal design of analogue low-power systems, A strongly directional hearing-aid adapter*, PhD thesis, Delft University of Technology, April 2003.
- [7] G. Groenewold, *Optimal dynamic range integrators*, IEEE Transactions on Circuits and Systems I, vol. 39, no. 8, pp. 614-627, August 1992.
- [8] W. K. Chen (Editor-in-Chief), *The Circuits and Filters Handbook*, CRC Press and IEEE Press, Boca Raton, FL, 1995.
- [9] D. A. Johns, W. M. Snelgrove and A. S. Sedra, *Orthonormal ladder filters*, IEEE Transactions on Circuits and Systems, vol. 36, no. 3, pp. 337-343, March 1989.
- [10] L. Thiele, *On the sensitivity of linear state-space systems*, IEEE Transactions on Circuits and Systems, vol. 33, no. 5, pp. 502-510, May 1986.

Chapter 6

Ultra Low-Power Integrator Designs

The trends towards lower power consumption, lower supply voltage and higher frequency operation have increased the interest in new design techniques for analogue integrated filters. In this chapter, we will focus only on ultra low-power integrated continuous-time filter designs. The current state-of-the-art design approaches for such filters are transconductor–capacitor (G_m –C) and translinear (log-domain) methods, which will be described in the following sections.

As mentioned in previous chapters, one can implement an n th-order linear differential equation, which describes a filter of the same order, by means of n intercoupling integrators. An on-chip integrator is an electronic circuit that realizes the transfer function $\frac{G}{sC}$, where G is implemented by a (trans)conductor stage (which converts voltage into current), and the integrating component $\frac{1}{sC}$ is usually realized by a (trans-)capacitor (integrating a current into a voltage). Therefore, integrators can be seen as the main building blocks of a filter topology and, consequently, in this chapter we will concentrate on the design of ultra low-power integrators.

6.1 G_m –C filters

One of the most popular technique for realizing analog integrated filters is the transconductor–capacitor, or simply G_m –C technique [1]. The main circuit building block of a G_m –C integrator, as shown in Fig. 6.1, is a linear transconductance cell, which converts the input voltage into an output current. The output current of the G_m block and, consequently, the capacitance current, are linearly related to the differential input voltage signal by

$$I_{cap} = G_m V_{in} \quad (6.1)$$

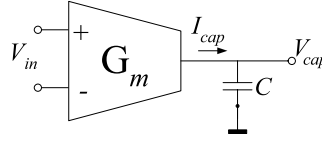


Fig. 6.1. A single-ended G_m -C integrator

This output current is applied to the integrating capacitor, C , resulting in a voltage across C , given by

$$V_{cap} = \frac{I_{cap}}{sC} = \frac{G_m V_{in}}{sC} \quad (6.2)$$

which defines the integrator time constant to be $\tau = C/G_m$. Besides the linearity, an additional requirement for this transconductance amplifier, in order to be applied in a filter, is that it should have a well-known transconductance value, which is not the case, for instance, for an operational amplifier (op amp).

As one will see in the next chapter, in the field of medical electronics, active filters with large time constants are often required to design low cut-off-frequency filters (in the Hz and sub-Hz range), necessitating the use of large capacitors or very low transconductances. To limit capacitors to practical values, a transconductor with an extremely small transconductance G_m (typically a few nA/V) is needed. Two very low-frequency transconductor designs, that rely on CMOS transistors operating in the triode region, will be presented here.

6.1.1 nA/V CMOS triode transconductor

The transconductor proposed in [2] is based on the use of CMOS transistors operating in the strong-inversion triode region (SI-TR). As shown in [2], transistors kept in the triode region benefit from a lower G_m/I_D ratio than the ones operating in saturation (active) or weak-inversion regions. This means that, for a particular bias current I_D , the triode transconductor presents the lowest G_m value. In addition, triode-based transconductors have better linearity performance than transconductors with transistors operating in saturation.

The triode-transconductor is shown in Fig. 6.2. It should be stated here that in this circuit not all transistors are in the triode region. Only M_{1A} and M_{1B} are biased in the strong-inversion triode region, whereas the other transistors are operating in the weak inversion saturation region.

Input transistors M_{1A} - M_{1B} have their drain voltages regulated by an auxiliary amplifier that comprises the current conveyor M_{2A} - M_{2B} , M_{3A} - M_{3B} and M_{4A} - M_{4B} , and bias current sources M_{7A} - M_{7B} and M_{8A} - M_{8B} . Internal voltages V_B , V_C and V_{DC} are derived from the bias circuit shown in Fig. 6.3 [2]. The bias generator is structurally alike the transconductor so that the external

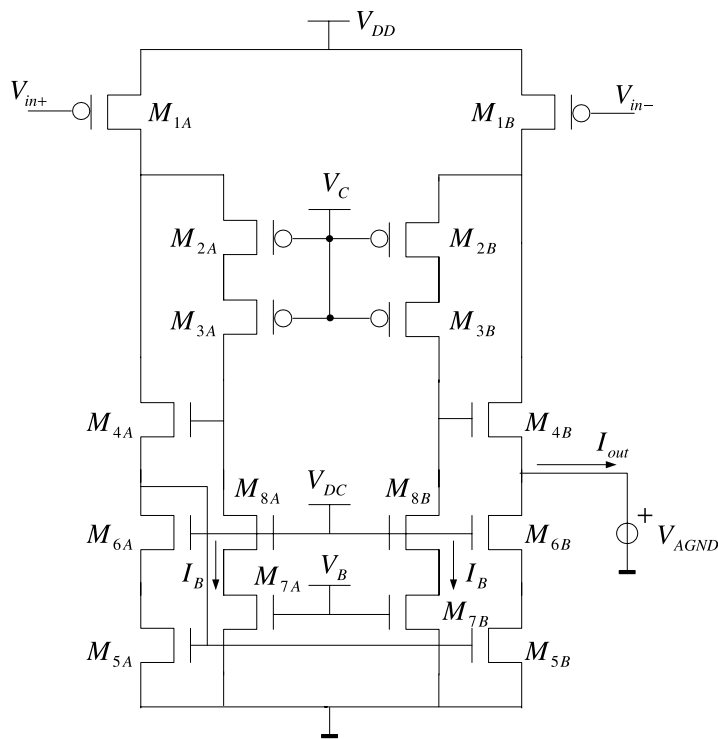


Fig. 6.2. Schematic of the nA/V CMOS triode-transconductor [2]

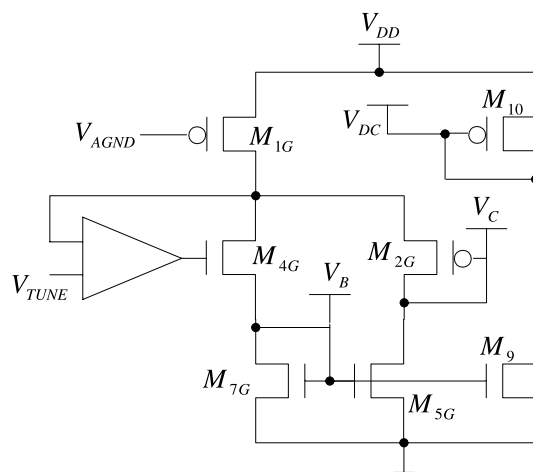


Fig. 6.3. Circuit diagram of the bias generator [2]

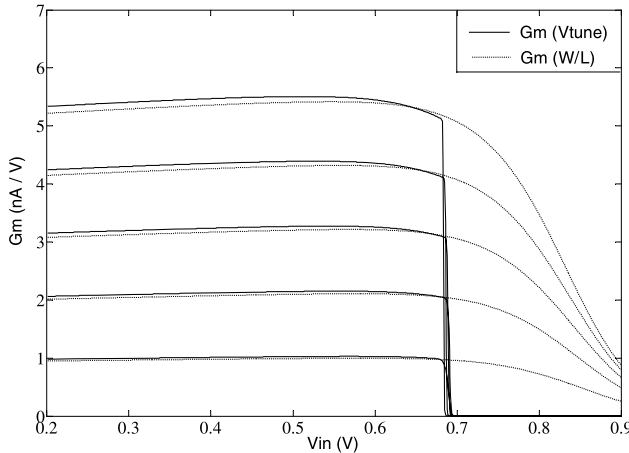


Fig. 6.4. Different G_m values obtained by varying V_{TUNE} (solid line) or $W_{M1A,M1B}$ (dashed line)

voltage V_{TUNE} is reflected to the drain of $M_{1A}-M_{1B}$. A low-voltage cascade current mirror comprising $M_{5A}-M_{5B}$ and $M_{6A}-M_{6B}$ provides a single-ended output. Referring V_{TUNE} to V_{DD} , one can define the G_m of the transconductor as

$$G_m = \beta \cdot V_{TUNE} \quad (6.3)$$

with $\beta = \frac{W}{L} \mu C_{ox}$. In order to obtain a G_m -C filter realization using the proposed integrator, we must be able to map the corresponding filter coefficients on the respective G_m values. From the transconductance definition in Eq. 6.3, one can notice that we may vary the value of G_m by changing the drain-source voltage (V_{TUNE}) or, alternatively, β (by the aspect ratio W/L) of transistor M_1 . In Fig. 6.4 one can see the acquired G_m values varying from 1 nA/V to 5 nA/V with V_{TUNE} changing from 10 mV to 50 mV, respectively, for a fixed aspect ratio $\frac{W}{L} = \frac{0.6 \text{ } \mu\text{m}}{240 \text{ } \mu\text{m}}$ (solid line).

However, due to the additional bias stages required to obtain different filter coefficients, realization of the various V_{TUNE} bias generators would increase the power consumption by a factor of $(n - 1) \cdot P_{Bias}$, where n is the number of implemented coefficients and P_{Bias} represents the power consumption of the biasing stage. Hence, from a power consumption perspective, the best choice to obtain the G_m values is by tuning β . Various values of G_m , ranging from 1 nA/V to 5 nA/V are also shown in Fig. 6.4 for $W_{M1A,M1B}$ linearly varying from 0.6 μm to 3 μm , respectively, with V_{TUNE} equal to 10 mV (dashed line).

6.1.2 A pA/V Delta-Gm ($\Delta-G_m$) transconductor

In order to decrease the values of G_m even further, a new CMOS triode-transconductor design is presented here. The schematic of the pA/V Delta- G_m transconductor is given in Fig. 6.5.

The description of the proposed integrator is given as follows. The G_{mT} of the transconductor is given by

$$G_{mT} = \frac{I_{out}}{V_{in}} \quad (6.4)$$

Current I_{out} can be defined in terms of the currents flowing through transistors M_{1A}-M_{1B}-M_{1C}-M_{1D}, resulting in

$$I_{out} = -I_{M1A} - I_{M1C} + I_{M1D} + I_{M1B} \quad (6.5)$$

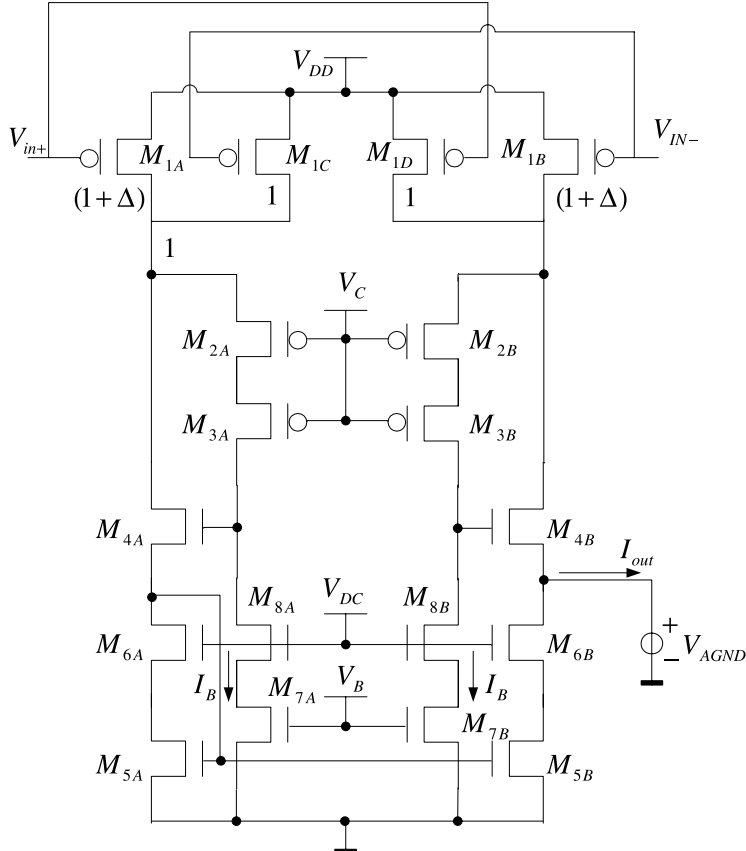


Fig. 6.5. Schematic of the pA/V Delta- G_m transconductor

which can be expressed as

$$I_{out} = G_{m_{M1A}} V_{in+} + G_{m_{M1C}} V_{in-} - G_{m_{M1D}} V_{in+} - G_{m_{M1B}} V_{in-} \quad (6.6)$$

Employing Eq. 6.3 for a transistor operating in strong-inversion triode region and assuming that the aspect ratios of M_{1A} and M_{1B} are (1 + Δ) times larger than the ones of M_{1C} and M_{1D}, we end up with

$$\begin{aligned} I_{out} &= \frac{W(1 + \Delta)}{L} \mu C_{ox} V_{TUNE} V_{in+} + \frac{W}{L} \mu C_{ox} V_{TUNE} V_{in-} \\ &\quad - \frac{W}{L} \mu C_{ox} V_{TUNE} V_{in+} - \frac{W(1 + \Delta)}{L} \mu C_{ox} V_{TUNE} V_{in-} \quad (6.7) \\ &= \Delta \frac{W}{L} \mu C_{ox} V_{TUNE} (V_{in+} - V_{in-}) \quad (6.8) \end{aligned}$$

Assuming $V_{in} = V_{in+} - V_{in-}$ and $\beta = \frac{W}{L} \mu C_{ox}$, the transconductance of the circuit in Fig. 6.5 is thus given by

$$G_{m_T} = \Delta \beta V_{TUNE} = \Delta G_m \quad (6.9)$$

where G_m is the transconductance of the triode-transconductor shown in Fig. 6.2.

In order to verify the circuit principle, we have simulated the new pA/V Delta- G_m transconductor using transistor models of a standard 0.35 μm CMOS IC technology. The G_{m_T} values can be seen in Fig. 6.6 with Δ varying from 1 to 0.1. As one can see, extremely small values of G_{m_T} can now be obtained, ranging from 1 nA/V down to 100 pA/V for a triode-tranconductance G_m equal to 1 nA/V.

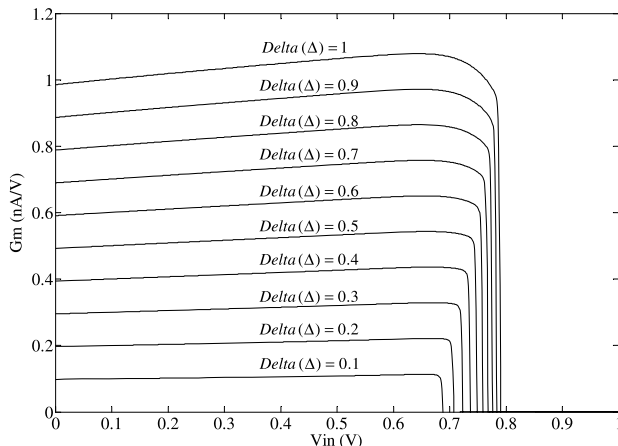


Fig. 6.6. G_m values obtained by varying Δ from 0.1 to 1

6.2 Translinear (log-domain) filters

The supply voltage severely restricts the maximum Dynamic Range (DR) achievable using conventional filter implementation techniques, such as opamp-MOSFET-C, G_m -C and switched-capacitor. In addition, since transistors are inherently non-linear transconductors, these techniques require the development of linearization or compensation schemes, usually at the expense of power consumption or bandwidth. The class of translinear (TL) filters has emerged in recent years [3], [4] as a promising approach to face the analog filters' challenges, i.e., lower power consumption, lower supply voltage and higher frequency operation.

The translinear approach is a current-mode technique [5], which is inherently non-linear and performs a compression and an expansion on the processed signal. This property is called the companding (compressing and expanding) principle [4]. The benefit of a companding system is that a signal with a particular DR can be processed in a system block with a smaller DR than the signal, and by this, offer low-voltage and low-power operation.

Translinear circuits [6], [7], also known as log-domain [8], Externally Linear Internally Nonlinear systems (ELIN) [9] or Exponential-State Space (ESS) [10] circuits, exploit the exponential large-signal transfer function of the semiconductor devices to implement a desired linear or nonlinear differential equation, which will be explained below.

6.2.1 Static and dynamic translinear principle

Translinear circuits are based on the exponential relation between voltage and current, a characteristic for any device whose operation is dominated by minority carriers, such as diodes, bipolar transistors and MOS transistors operating in the weak inversion region. They can be divided into Static and Dynamic Translinear circuits.

Static Translinear (STL) circuits are implemented to realize any static transfer function. Their principle applies to loops of semiconductor junctions [5]. A TL loop is characterized by an even number of junctions. The number of devices with a clockwise orientation equals the number of counterclockwise oriented devices. An example of a four-PN junction TL loop is shown in Fig. 6.7. The STL principle states that this circuit can be best described in

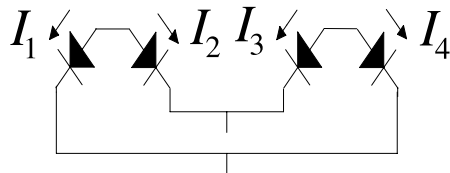


Fig. 6.7. A four-PN junction translinear loop

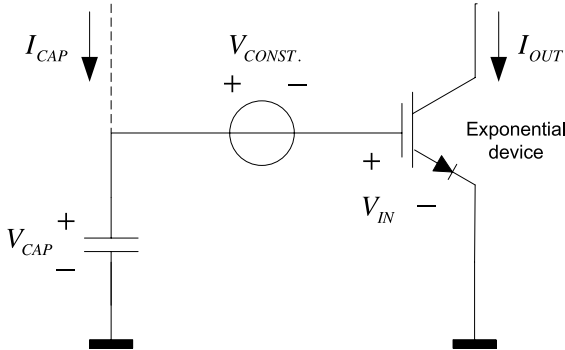


Fig. 6.8. Principle of dynamic translinear circuits

terms of the collector currents I_1 – I_4 . The translinear loop is thus described by a simple equation in terms of products of currents, being

$$I_1 I_3 = I_2 I_4 \quad (6.10)$$

Linear or nonlinear dynamic, i.e., frequency-dependent, functions (differential equations) can be implemented by Dynamic Translinear (DTL) circuits. The DTL principle is shown in the sub-circuit in Fig. 6.8 [11].

The circuit is described in terms of the output current I_{out} of the exponential device and the capacitance I_{cap} flowing through the capacitance C . Note that the DC voltage source V_{const} does not affect I_{cap} . I_{out} is based on the exponential law and can thus be described by:

$$I_c = I_s e^{\frac{V_{cap}}{V_T}} \quad (6.11)$$

V_{cap} , I_s , V_T being the capacitance voltage, a specific current and a specific voltage respectively. An expression for I_{cap} can be derived from the time derivative of the output current:

$$CV_T \dot{I}_{out} = I_{cap} I_{out} \quad (6.12)$$

where the dot represents differentiation with respect to time. This expression defines the principle of dynamic translinear circuits: “A time derivative of a current can be mapped onto a product of currents.” For the realization of this product of currents the conventional static translinear principle can be used. Using dynamic translinear circuits, several classes of filters have been proposed [5, 6]. The characteristics of these classes can be derived from their output structures. Strictly speaking, the class of log-domain filters is based on a single-transistor output structure in line with Fig. 6.8. Nevertheless, other output stages can be used to implement non-linear differential equations, e.g., the ones that belong to oscillators [12] and RMS–DC converters [13].

6.2.2 Log-domain integrator

Electronics circuits map mathematical operations on silicon. In order to accomplish this, the mathematical equations (in case of filters, differential equations) should be transformed into a set of electrical equations, which represent voltage or current relations. In log-domain circuits, the mathematical input and output variables are related linearly to currents (current mode operation), whereas the relation between the state variables and the capacitance voltages has a logarithmic character. However, by proper use of the correspondence relation, the linearity of the overall transfer function of the system can be maintained.

A typical log-domain integrator can be characterized by the diode-capacitance circuit in Fig. 6.9a and the corresponding block diagram is given by Fig. 6.9b [14].

The capacitance current I_{cap} can be expressed in terms of the voltages V_{in} and V_C and obeys the exponential law of the device (in this case, the diode)

$$I_{cap} = I_d = CV_C = I_s e^{\frac{V_{in}-V_C}{V_T}} \quad (6.13)$$

where I_s is the reverse saturation current and, assuming that the capacitor is not loaded, $I_{cap} = I_d$. From the basic log-domain equation presented above, one can notice that such an integrator is inherently non-linear. In order to maintain overall linearity of the log domain system, an input current signal is converted into a voltage by a logarithmic converter (typically, a bipolar transistor), and is then processed internally by the nonlinear integrator before it

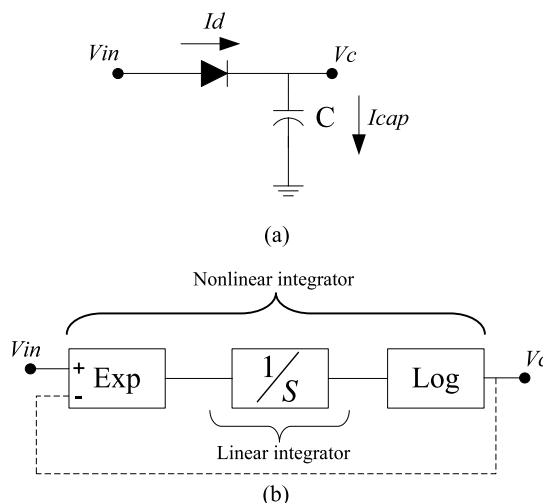


Fig. 6.9. a Typical representation of the log-domain integrator. b Corresponding block diagram [14]

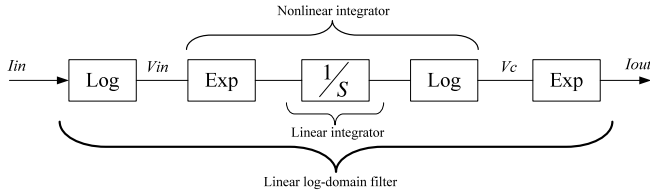


Fig. 6.10. Linear log-domain filter block diagram

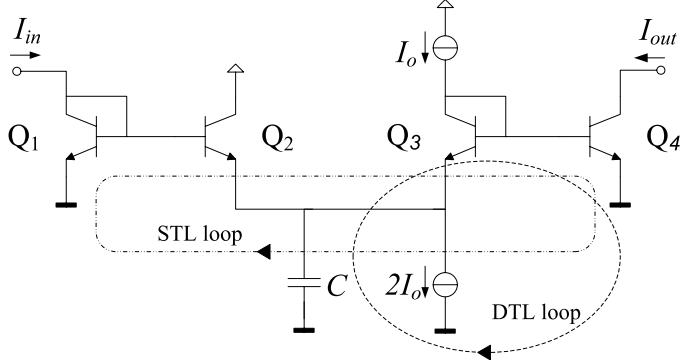


Fig. 6.11. First-order low-pass log-domain filter

is converted into an output current signal by an exponential converter (another bipolar transistor). The block diagram of a linear log-domain filter is illustrated in Fig. 6.10.

One can see the linearity of the expression of the log-domain filter applying $V_{in} = V_T \ln(\frac{I_{in}}{I_s})$ and $V_C = V_T \ln(\frac{I_{out}}{I_s})$ into Eq. 6.13

$$CV_T \frac{d}{dt} \left[\ln \left(\frac{I_{out}}{I_s} \right) \right] = I_s \frac{e^{\ln(\frac{I_{in}}{I_s})}}{e^{\ln(\frac{I_{out}}{I_s})}} \implies CV_T \dot{I}_{out} = I_{in} \quad (6.14)$$

which represents a first-order linear differential equation in the current domain.

From a circuit design perspective, the most simple implementation of a first-order log-domain filter is given by the combination of the static and the dynamic translinear loops, shown in Fig. 6.7 and Fig. 6.8, respectively. A bipolar filter implementation is given in Fig. 6.11. According to the STL principle, the products of the currents of forward biased junctions in the clockwise and counter-clockwise oriented devices are equal. Hence

$$I_1 I_3 = I_2 I_4 \Rightarrow I_{in} I_o = (I_o + I_{cap}) I_{out} \quad (6.15)$$

The DTL loop equation, defined by the capacitor and transistor Q4, is given by

$$I_{cap} I_{out} = CV_T \dot{I}_{out} \quad (6.16)$$

Using Eq. 6.15 and Eq. 6.16, this yields

$$CV_T \dot{I}_{out} + I_o I_{out} = I_o I_{in} \quad (6.17)$$

which is a linear differential equation, describing a low-pass filter with cutoff frequency ω_c according to

$$\omega_c = \frac{I_o}{CV_T} \quad (6.18)$$

In the next sections, we will present some log-domain integrator designs, which are suitable for high-frequency and/or low-power low-voltage applications.

6.3 Class-A log-domain filter design examples

Under class-A operation, the collector currents of the transistors in the log-domain filter have to be strictly positive for the transistor to work in the active exponential region. Consequently, the ac signal has to be superimposed on a DC bias current I_o . That is, for a correct operation of the input and output filter stages without clipping distortion, the relation $I_{in}, I_{out} > -I_o$ has to be satisfied at all times.

A few class-A log-domain integrator design examples will be presented here.

6.3.1 Bipolar multiple-input log-domain integrator

One example of an low-power log-domain integrator is given in Fig. 6.12 [15], which represents a bipolar multiple-input log-domain integrator.

A pair of log-domain cells with opposite polarities and an integrating capacitor form the core of the integrator. V_{ip} and V_{in} are the non-inverting and inverting input voltages, respectively, and the input currents are I_{ip} and I_{in} , which are superimposed on the dc bias currents. The output voltage V_o is given by the voltage across the capacitor. The circuit is composed of two identical log-domains cells, a voltage buffer, and a current mirror. The log-domain cells Q₁–Q₂ and Q₃–Q₄ generate the log-domain currents I_{c2} and I_{c4} , respectively. A voltage buffer realized by Q₅–Q₆ is inserted between them. Therefore, the output log-domain voltage V_o at the emitter of Q₂ also appears at the emitter of Q₄. Finally, to obtain a log-domain integrator equation, a current mirror Q₇–Q₈ is used to realize the difference between the two log-domain currents on the capacitor node. The connection from the bases of transistors Q₇ and Q₈ to the collector of Q₆ closes the feedback loop around Q₆ and Q₇. This connection is convenient because it ensures that the overall voltage headroom is minimized. The equation that relates the input and output voltages to the current flowing in the integrating capacitor becomes

$$C_i \frac{dV_o}{dt} = (I_o + I_{ip}) e^{\frac{V_{ip}-V_o}{V_T}} - (I_o + I_{in}) e^{\frac{V_{in}-V_o}{V_T}} \quad (6.19)$$

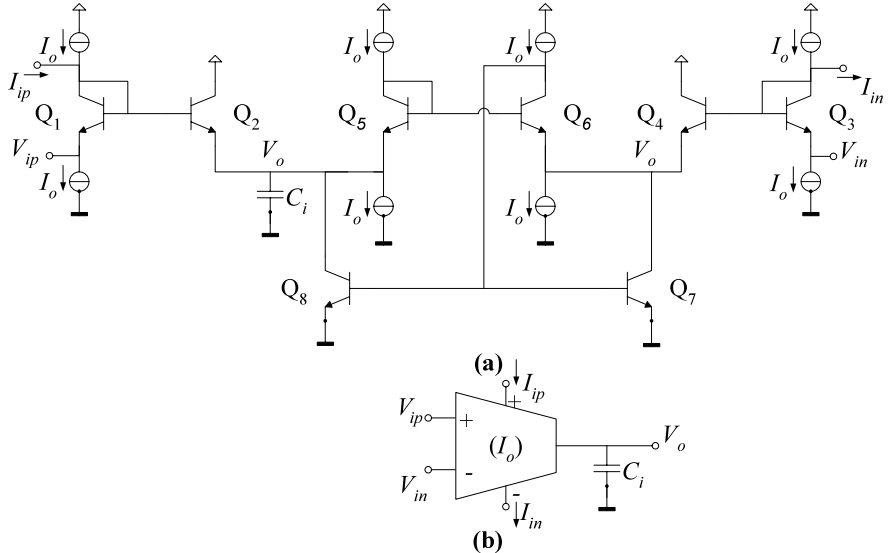


Fig. 6.12. The multiple-input low-power log-domain integrator (a) and its symbol (b) [15]

Notice that the input and output voltages of the integrator are at the same dc level. Therefore log-domain filter synthesis can easily be achieved by direct coupling of these integrators.

6.3.2 CMOS multiple-input log-domain integrator

Log-domain filters can also be implemented using MOS transistors biased in weak inversion (WI) in order to preserve the exponential $I-V$ characteristic required by the log-domain companding principle. MOS transistors do not suffer from the base current drawback of bipolar transistors. On the other hand, maintaining the transistors biased in weak inversion usually requires large devices and results in frequency limitations. The CMOS integrator proposed in [16] is given in Fig. 6.13.

Note that the relation between the input and output voltages and the capacitance current is also given by Eq. 6.19. In the previous implementation, shown in Fig. 6.12, the integration capacitor is connected to the emitter (or source for MOS in WI) of a transistor. In this way, the capacitor is charged/discharged by a current which is exponentially dependent on the capacitor voltage, representing an inherent feedback. In the implementation in Fig. 6.13, the same feedback is accomplished by connecting the capacitor to the drain of the exponential transconductors, M₂ and M₃, while the capacitance voltage is sensed at their source through the adjustable level shifter made of current source I_o and transistors M₅ and M₆. The capacitor is now

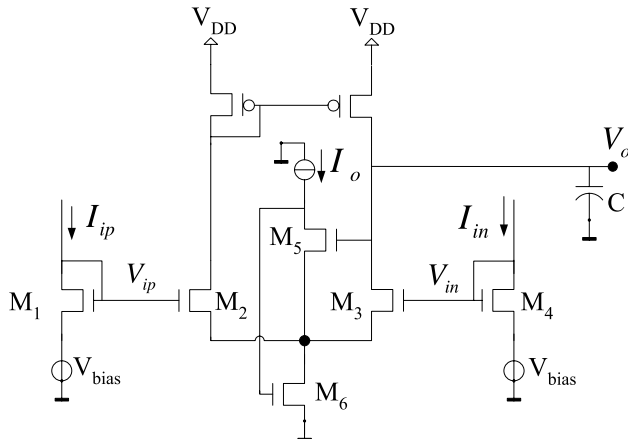


Fig. 6.13. Inverting and non-inverting class-A CMOS log-domain integrator [16]

discharged by the drain current of transistor M₃ and charged by the drain current of M₂ through the current mirror.

6.3.3 High-frequency log-domain integrator in CMOS technology

Usually, only active devices are used to implement translinear circuits, being bipolar transistors [17], MOS transistors in the weak inversion region [18] or lateral bipolar transistors in standard CMOS technology [19].

Due to its low-cost fabrication process, efforts have been taken to extend the log-domain approach from bipolar to CMOS technology. In addition to the economic reason, MOS transistors do not suffer from the base current drawback of bipolar transistors. The exponential dependence of the drain current upon the gate-source voltage in subthreshold operation may suggest the use of MOS devices in DTL circuits. However, since such conditions are met by only a large device width, thus at low current densities, the speed of subthreshold circuits is severely limited. The same high frequency limitation holds for lateral bipolar transistors in standard CMOS technology [19]. An alternative topology to implement DTL and log-domain circuits, which improves the high-frequency performance, is proposed here [20]. It is based on the exponential relation between voltage and current of passive PN-diodes and uses the CMOS transistor only to provide gain, in accordance with the original idea proposed by Adams [3].

The earliest log-domain filter as proposed by Adams, 1979, lends itself to be implemented in any CMOS IC technology and does not require exponential

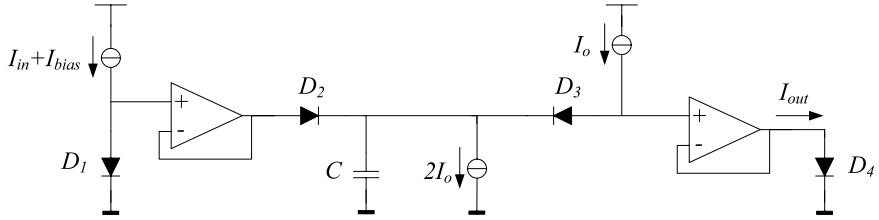


Fig. 6.14. Adams' low-pass log-domain filter [3]

behavior of the CMOS transistors. See Fig. 6.14. The circuit is a first-order low-pass filter. The analysis of this circuit is given below.

The four (exponential) diodes, D_1 - D_4 , constitute a TL loop. The combination of the capacitor C , the right voltage follower (an opamp in unity-gain configuration) and diode D_4 is similar to the output sub-circuit shown in Fig. 1. Diode D_3 is biased by a dc current I_o and therefore complies with a constant voltage source. The output current flows through diode D_4 . The current through D_2 equals $(I_o + I_{cap})$ and the input current, together with biasing current I_{bias} , flows through diode D_1 . According to the TL principle, the products of the currents of forward biased junctions in the clockwise and counter-clockwise oriented devices are equal. Hence:

$$(I_{bias} + I_{in})I_o = (I_o + I_{cap})(I_{dc} + I_{out}) \quad (6.20)$$

Using Eqs. 6.16 and 6.20, this yields:

$$CV_T \dot{I}_{out} + I_o I_{out} = I_o I_{in} \quad (6.21)$$

which represents the linear differential equation of a low-pass filter.

Voltage follower

The main requirements of the voltage followers that are employed in the circuit of Fig. 6.14 are high-frequency response, low gain error, high linearity and a sufficiently low output resistance. The proposed voltage follower, to be implemented in CMOS technology, is based on a symmetrical structure of a two-stage topology [21]. Compared to single-stage topologies, two-stage topologies increase the loop gain and therefore decrease the output impedance of the circuit. The characteristics of this particular circuit are a nominally zero systematic offset and highly reduced harmonic distortion and transfer gain error.

The two-stage topology adopts the Miller compensation technique to achieve stability in closed-loop conditions. However, such compensation also results in a right half-plane zero in the open-loop gain, due to the forward path through the compensation capacitor to the output. The right half-plane zero reduces the maximum achievable gain-bandwidth product, since it makes

a negative phase contribution to the open-loop gain at a relatively high frequency. An optimized compensation strategy is based on the use of a voltage follower [22]. It efficiently uses the finite output conductance of a voltage buffer to provide pole-zero compensation, thus allowing a great increase in the loopgain-poles [23] product to be achieved. The voltage buffer is implemented with the common-drain configuration shown in Fig. 6.15.

The circuit diagram of the voltage follower is depicted in Fig. 6.16. M1 and M2 form the source-coupled pair of the differential stage. M3 and M4 are both diode-connected to improve the symmetry of the topology. Transistors M5 and M6 enhance the overall loop gain while maintaining identical source-drain voltage drops across transistors M7 and M8. Transistors M7–M14 implement the bias circuit. M13 is employed to obtain a good matching between p-channel and n-channel current sources. Finally, transistor M15 is used for the frequency compensation described above. M1–M4 and M5–M9 have the same aspect ratios respectively.

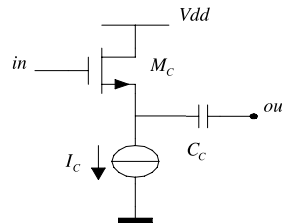


Fig. 6.15. Voltage buffer for frequency compensation

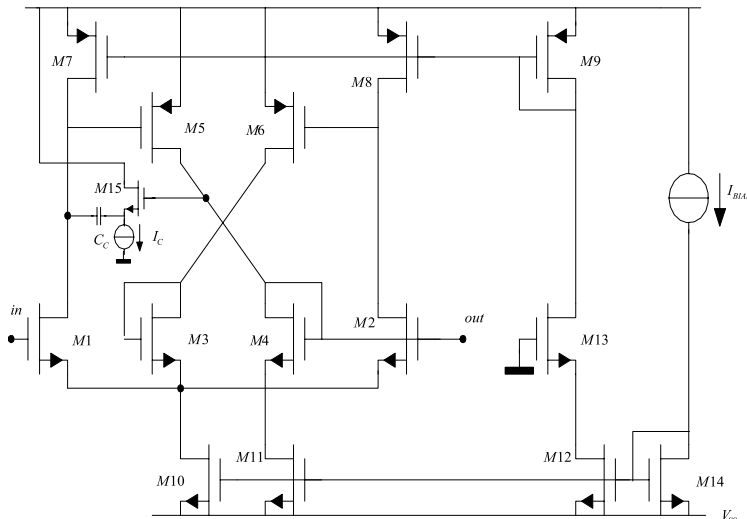


Fig. 6.16. Circuit diagram of the voltage follower

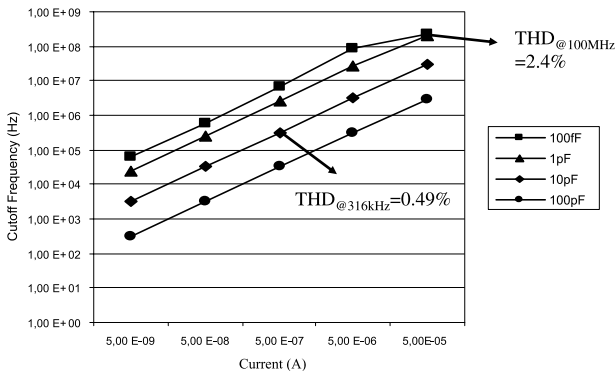


Fig. 6.17. Simulated cut-off frequency as a function of current I_o for five different capacitor values

Simulation results

The circuit was simulated using PSPICE transistor and diode models of the 0.35 μm CMOS Si-gate AMS IC process. The filter has been designed to operate from a 3.3-V supply. Bias current I_o ranges from 50 nA to 0.5 mA.

Figure 6.17 depicts the cut-off frequency as a function of current I_o for four different capacitance (C) values: 100 fF, 1 pF, 10 pF and 100 pF.

From this plot, it can be deduced that this filter can be controlled over a wide frequency range. Also indicated is that the filter exhibits less than 1% THD for a capacitance equal to 10 pF for a 316 kHz input signal and 2.4% THD for a capacitance equal to 100 fF at 100 MHz. The cut-off frequency for $I_o = 50 \mu\text{A}$ and $C = 100 \text{ fF}$ equals 222 MHz. Note that this circuit exhibits a better high-frequency performance than the circuit presented in [19] which yields a cut-off frequency below 30 MHz.

The AC response of the low-pass filter with I_o equal to 5 nA, 50 nA, 0.5 μA , 5 μA and 50 μA , respectively, and C equal to 10 pF is shown in Fig. 6.18. The cut-off frequencies of these filter responses are 3.13 kHz, 31.6 kHz, 316.2 kHz, 3.10 MHz and 31.62 MHz, respectively.

Note that either lossless or inverting lossy integrators can be realized by adding appropriate unity-gain positive feedback or applying current mirrors respectively.

As was mentioned before, using the companding principle, one can design analog integrated circuits with higher dynamic range compared to conventional circuit design techniques. Moreover, the dynamic range of low-voltage companding analog circuits can further be extended using class-AB current-mode circuit topologies, which will be discussed in the next section.

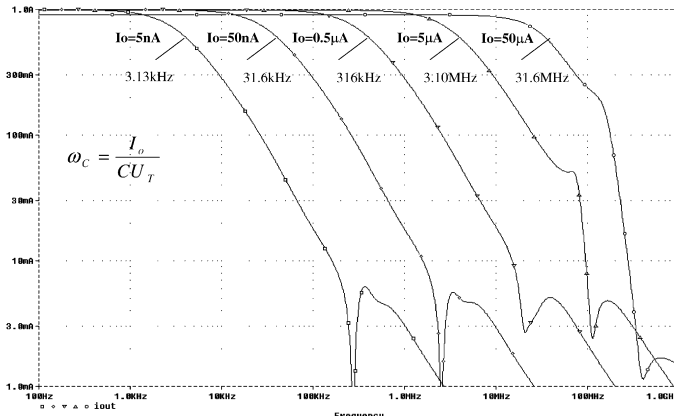


Fig. 6.18. Simulated log-domain filter response with $C = 10\text{ pF}$

6.4 Low-power class-AB *sinh* integrators

Class-AB circuit design is an efficient approach to matching the requirements of good linearity, low noise contribution and low power consumption. In a class-AB topology the quiescent bias levels in the active devices are set at relatively low levels, usually much lower than the expected signal swings. Consequently, for small signals the circuit operates in class-A and for large signal swings operates with the efficiency of a class-B design. This results in a higher Dynamic Range (DR) compared to conventional class-A operation together with an improvement in power efficiency.

In log-domain filters operating in class A, the currents are limited by $I_{in}, I_{out} > -I_o$. This means that the restriction in current-mode circuits is only single-sided. Hence, the combination of the companding circuit technique and class-AB operation enables us to obtain more power-efficient analog signal processing where the DR can be extended without increasing the maximum SNR or the quiescent power consumption.

The hyperbolic-sine (*sinh*) function is at the base of most of the class-AB translinear filters. Instead of a single transistor in common-emitter configuration as for class A integrators, the class-AB *sinh* filter is characterized by hyperbolic-sine transconductors, as described in the following sections.

6.4.1 A state-space formulation for class-AB log-domain integrators

In [24], a general state-space description for a *sinh* filter has been proposed. The formulation consists of the hyperbolic sine mapping on the state variable.

As an example, consider a first-order lowpass state-space description

$$\begin{aligned}\dot{x} &= -\omega_0 x + \omega_0 u \\ y &= x\end{aligned}\quad (6.22)$$

Applying the state variable mapping, the state-space variables can now be expressed as

$$\begin{aligned}x &= 2CV_T \sinh(V_{cap}/2V_T) \\ u &= 2CV_T \sinh(V_{in}/2V_T)\end{aligned}\quad (6.23)$$

resulting in the externally linear internally non-linear system defined by

$$\begin{aligned}C\dot{V}_{cap} &= 2CV_T\omega_0\{\cosh[(V_{in} - V_{cap})/2V_T] - 1\} \tanh(V_{cap}/2V_T) \\ &\quad + 2CV_T\omega_0 \sinh[(V_{in} - V_{cap})/2V_T] \\ I_{out} &= 2CV_T \sinh(V_{cap}/2V_T)\end{aligned}\quad (6.24)$$

The circuit that realizes this state-space representation is shown in Fig. 6.19. The corresponding mapping contains compound transistors in order to implement the *tanh* function.

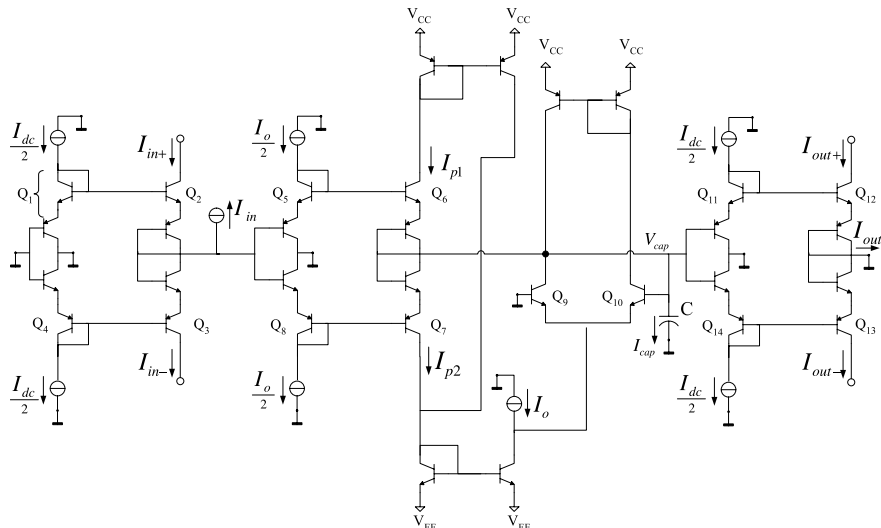


Fig. 6.19. Class-AB *sinh* low-pass filter [24]

The analysis of this first-order low-pass filter involves 5 static and 1 dynamic translinear loops, given by STL:

$$I_{Q2}I_{Q3} = I_{Q1}I_{Q4} \implies I_{in+}I_{in-} = I_{dc}^2/4 \quad (6.25)$$

$$I_{Q6}I_{Q7} = I_{Q5}I_{Q8} \implies I_{p1}I_{p2} = I_o^2/4 \quad (6.26)$$

$$I_{Q12}I_{Q13} = I_{Q11}I_{Q14} \implies I_{out+}I_{out-} = I_{dc}^2/4 \quad (6.27)$$

$$I_{Q2}I_{Q6}I_{Q12} = I_{Q1}I_{Q5}I_{Q11} \implies 8I_{in+}I_{p1}I_{out+} = I_oI_{dc}^2/4 \quad (6.28)$$

$$I_{Q9}I_{Q12}I_{Q12} = I_{Q10}I_{Q11}I_{Q11} \implies 4I_9I_{out+}^2 = I_{10}I_{dc}^2 \quad (6.29)$$

and DTL:

$$I_{cap} = 2CV_T \frac{\dot{I}_{out+}}{I_{out+}} \quad (6.30)$$

where the dot represents differentiation with respect to time. It is interesting to notice that the corresponding loops in Eqs. 6.25, 6.26 and 6.27 implement geometric mean TL loop equations and the loop defined by Eq. 6.29 contains both compound transistors, Q₁₁ and Q₁₂, and single bipolar transistors, Q₉ and Q₁₀.

Thus, for the differential pair, currents I_{Q9} and I_{Q10} can be defined and are given by

$$I_9 = \frac{1}{2}(2I_{p1} - I_o - I_{cap}) \quad (6.31)$$

$$I_{10} = \frac{1}{2}(2I_{p2} - I_o + I_{cap}) \quad (6.32)$$

From Eqs. 6.25–6.28 we can define I_{p1} and I_{p2} in terms of I_{in+} , I_{in-} , I_{out+} and I_{out-} , which yields

$$I_{p1} = \frac{I_oI_{dc}^2}{8I_{in+}I_{out+}} \quad (6.33)$$

$$I_{p2} = \frac{I_oI_{dc}^2}{8I_{in-}I_{out-}} \quad (6.34)$$

Applying these equations to Eqs. 6.31–6.32 we can also represent I_9 and I_{10} in terms of the input and output currents, and substituting these values into Eq. 6.29, we finally end up with the linear differential equation representing the low-pass filter

$$I_{in} = I_{out} + \frac{2CV_T}{I_o} \dot{I}_{out} \quad (6.35)$$

6.4.2 Class-AB \sinh integrator based on state-space formulation using single transistors

The circuit shown in Fig. 6.19 contains compound and single transistors. In order to implement the TL loops with only single transistors, a new structure

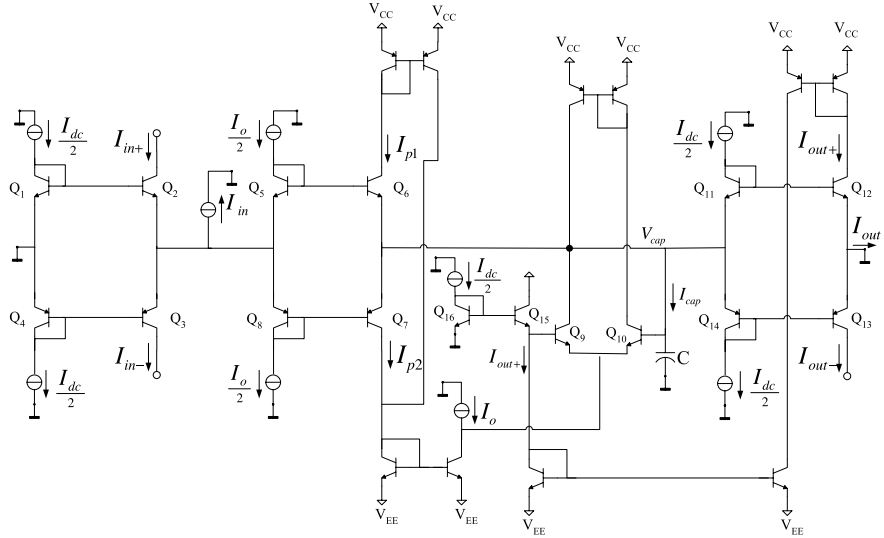


Fig. 6.20. New class-AB *sinh* low-pass filter

for the class-AB *sinh* lossy integrator is presented here. Its schematic is shown in Fig. 6.20.

The proposed integrator consists of three hyperbolic-sine transconductors, Q₁–Q₄, Q₅–Q₈ and Q₁₁–Q₁₄, two static TL loops comprising transistors Q₁₆–Q₁₅–Q₉–Q₁₀–Q₁₁–Q₁₂ and Q₁–Q₂–Q₅–Q₆–Q₁₁–Q₁₂ and one dynamic TL loop C–Q₁₁–Q₁₂. The translinear analysis of the new integrator is the same as the one presented in Section 6.4.1. As one can see, in order to implement Eq. 6.29, transistors Q₁₅ and Q₁₆ have been introduced.

To validate the correct mapping of the equations, we have implemented the lossy integrator using quasi-ideal exponential devices, i.e. bipolar transistors with very large current gain ($\beta = 10^6$). The transient responses of the input currents (I_{in+} and I_{in-}) and the output current (I_{out}), the capacitance current I_{cap} and the intermediate currents $I_{p1} - I_9$ and $I_{p2} - I_{10}$ are given in Fig. 6.21a and Fig. 6.21b, respectively, showing the correct mapping of the equations presented in the previous section. Note that from Eq. 6.31 and Eq. 6.32, we have

$$I_{p1} - I_9 = \frac{1}{2}(I_o + I_{cap}) \quad (6.36)$$

$$I_{p2} - I_{10} = \frac{1}{2}(I_o - I_{cap}) \quad (6.37)$$

which corresponds to the waveforms shown in Fig. 6.21b.

As one can see, the generic state-space formulation for *sinh* integrators is quite abstract and does not provide much insight into the operation of these filters. Due to this fact, we will present in the next sections other approaches

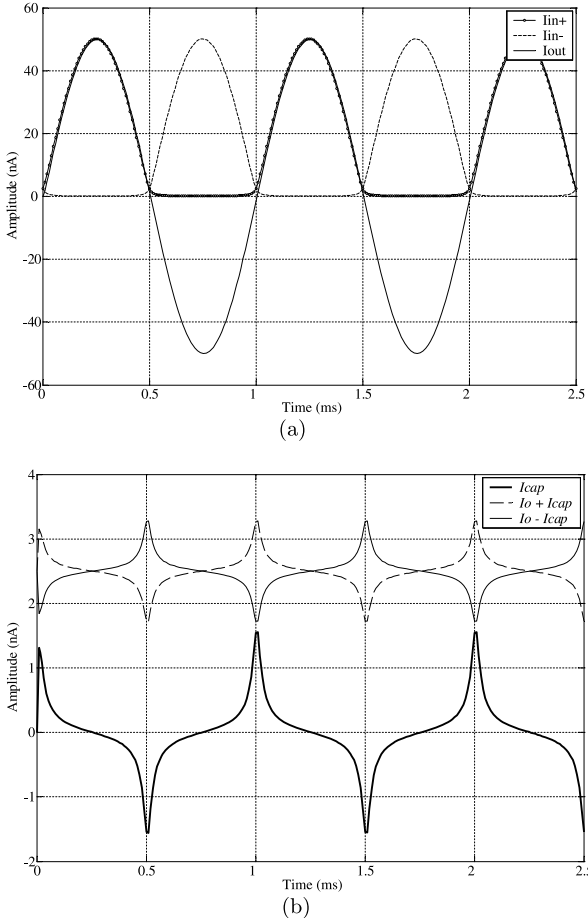


Fig. 6.21. Transient response of the class-AB *sinh* integrator based on state-space formulation: I_{in+} , I_{in-} and I_{out} (a), I_{cap} , $I_o + I_{cap}$ and $I_o - I_{cap}$ (b)

for *sinh* filter design which are much easier to apply to both the synthesis and analysis of class-AB filters.

6.4.3 Companding *sinh* integrator

The design proposed in [25] is based on the general block diagram of a companding integrator, defined by Seevinck [4].

The block diagram of a companding *sinh* integrator is given in Fig. 6.22. It consists of a divider, a linear time integrator, a hyperbolic-sine expander block that generates the output current I_{out} from the internal capacitance voltage V_{cap} , $I_{out} = \sinh(V_{cap})$, and a hyperbolic-cosine block that generates the

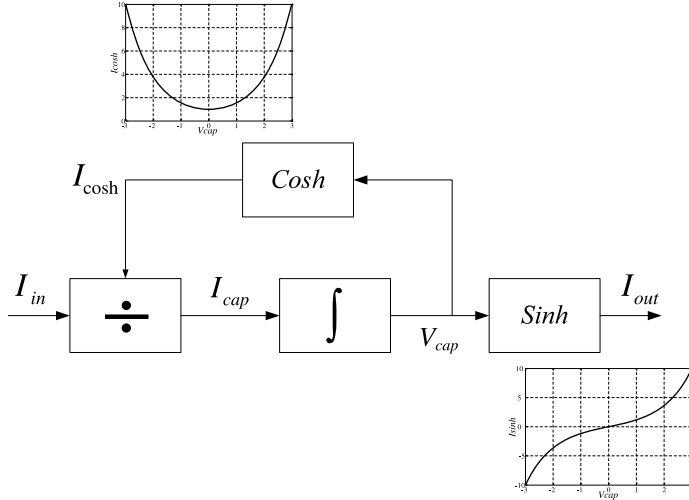


Fig. 6.22. Block diagram of the companding *sinh* integrator

derivative of the output signal I_{out} with respect to V_{cap} , $I_{cosh} = \frac{d \sinh(V_{cap})}{dV_{cap}} = \cosh(V_{cap})$.

From the block diagram given in Fig. 6.22, one can see that the capacitance current can be defined as

$$I_{cap} = \frac{I_{in}}{I_{cosh}} \quad (6.38)$$

The V - I transfer function of the *sinh* output structure is described by

$$I_{out} = 2I_o \sinh\left(\frac{V_{cap}}{V_T}\right) = I_o e^{\frac{V_{cap}}{V_T}} - I_o e^{-\frac{V_{cap}}{V_T}} \quad (6.39)$$

Despite the non-linear relations of the output current to the capacitance voltage and the capacitance current to the input current, the integrator can be considered to be an implementation of a first-order linear differential equation $I_{in} = dI_{out}/dt$ by applying the chain rule

$$I_{in} = I_{cap} \cdot I_{cosh} = C \cdot \frac{dV_{cap}}{dt} \cdot \frac{d \sinh(V_{cap})}{dV_{cap}} \implies I_{in} = C \cdot \frac{dI_{out}}{dt} \quad (6.40)$$

Circuit design

To implement the companding integrator presented in Fig. 6.22, a class-AB *sinh* integrator has been proposed in [25]. The basic schematic is shown in Fig. 6.23.

The translinear analysis of this circuit is as follows. First, a current splitter is required to split the input current I_{in} into two parts, I_{in+} and I_{in-} , both

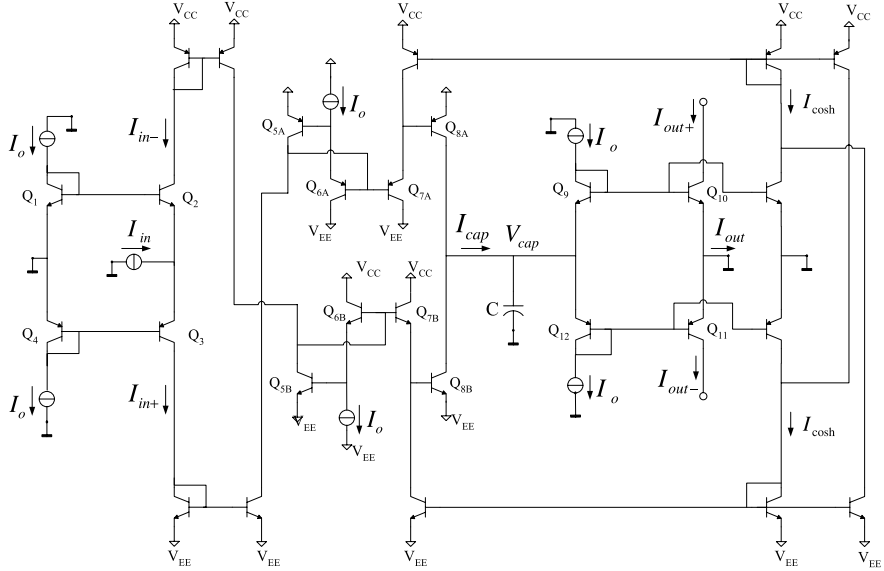


Fig. 6.23. Schematic of the lossless \sinh integrator [25]

strictly positive, such that

$$I_{in} = I_{in+} - I_{in-} \quad (6.41)$$

The current splitter comprising transistors Q_1 through Q_4 is a geometric-mean current splitter, and implements the function

$$I_{Q2}I_{Q3} = I_{Q1}I_{Q4} \implies I_{in+}I_{in-} = I_{dc}^2 \quad (6.42)$$

The dividers for both positive and negative inputs are given by the translinear loops $Q_{5A}-Q_{6A}-Q_{7A}-Q_{8A}$ and $Q_{5B}-Q_{6B}-Q_{7B}-Q_{8B}$, respectively, which yields

$$I_{5A}I_{6A} = I_{7A}I_{8A} \implies (I_{in+})I_o = (I_{out+} + I_{out-})I_{8A} \quad (6.43)$$

$$I_{5B}I_{6B} = I_{7B}I_{8B} \implies (I_{in-})I_o = (I_{out+} + I_{out-})I_{8B} \quad (6.44)$$

The current flowing through the capacitor is given by

$$I_{cap} = I_{8A} - I_{8B} \quad (6.45)$$

In addition, from the DTL loops, the capacitance current can be related to the output currents by

$$I_{cap} = CV_T \frac{\dot{I}_{out+}}{I_{out+}} = -CV_T \frac{\dot{I}_{out-}}{I_{out-}} \quad (6.46)$$

Finally, applying Eqs. 6.41, 6.43, 6.44 and 6.46 to 6.45 and considering a *sinh* output stage which implements $I_{out} = I_{out+} - I_{out-}$, we end up with

$$I_o I_{in} = C V_T \dot{I}_{out} \quad (6.47)$$

which represents a linear lossless integrator. Note that applying a unity-feedback path from the output to the input, one can obtain a lossy integrator configuration.

6.4.4 Ultra low-power class-AB *sinh* integrator

To implement the companding integrator presented in Fig. 6.22, we propose a new ultra low-power class-AB *sinh* integrator. The schematic of the complete integrator is given in Fig. 6.24.

Instead of a single transistor in common-emitter configuration, as in class-A integrators, the class-AB *sinh* filter is characterized by hyperbolic-sine transconductors. Instead of a single transistor in common-emitter configuration, as in class-A integrators, the class-AB *sinh* filter is characterized by hyperbolic-sine transconductors.

As seen from Fig. 6.24, the integrator consists mainly of 3 *sinh* transconductors, defined from the translinear loops $Q_{1A}-Q_{2A}-Q_{2B}-Q_{1B}$, $Q_{3A}-Q_{4A}-Q_{4B}-Q_{3B}$ and $Q_{5A}-Q_{6A}-Q_{6B}-Q_{5B}$, which implement the current splitter, the divider-cosh block and the *sinh* output stage, respectively.

At the output, the relation between I_{out} , I_{out+} and I_{out-} , defined from the *sinh* output stage $Q_{5A}-Q_{6A}-Q_{6B}-Q_{5B}$, is described by

$$I_{out} = I_{out+} - I_{out-} \quad (6.48)$$

$$I_{out+} \cdot I_{out-} = I_{dc}^2 \quad (6.49)$$

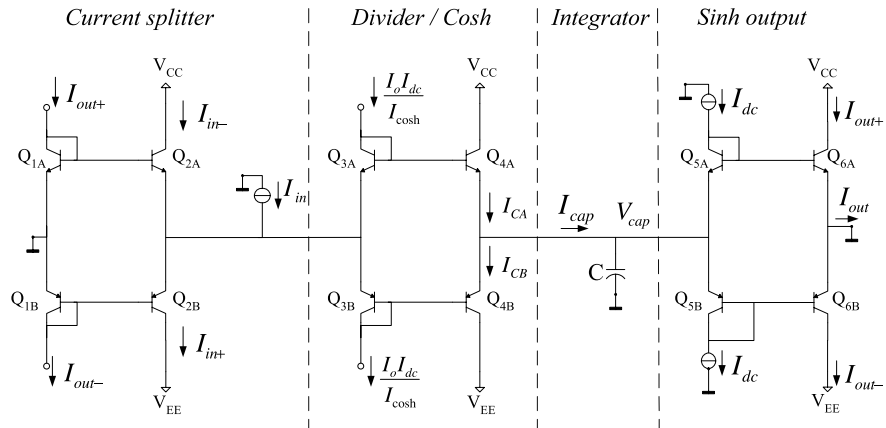


Fig. 6.24. Circuit diagram of the proposed class-AB *sinh* integrator

The current splitter comprising transistors Q_{1A} through Q_{1B}, which is a geometric-mean current splitter, implements

$$I_{in} = I_{in+} - I_{in-} \quad (6.50)$$

$$I_{in+} \cdot I_{in-} = I_{out+} \cdot I_{out-} = I_{dc}^2 \quad (6.51)$$

In addition, the third \sinh transconductor Q_{3A}–Q_{4A}–Q_{4B}–Q_{3B} realizes the divider- \cosh block, thus defining the correct non-linear current through the capacitor to obtain a global linearization, i.e., an externally linear transfer function. Currents I_{CA} , I_{CB} and I_{cap} are given by

$$I_{cap} = I_{CA} - I_{CB} \quad (6.52)$$

$$I_{CA} \cdot I_{CB} = \frac{I_{dc} I_o}{I_{cosh}} \cdot \frac{I_{dc} I_o}{I_{cosh}} \quad (6.53)$$

assuming $I_{cosh} = I_{out+} + I_{out-}$. Hence, considering also the static translinear loop Q_{1A}–Q_{2A}–Q_{3A}–Q_{4A}–Q_{5A}–Q_{6A}, we have

$$I_{Q_{1A}} I_{Q_{3A}} I_{Q_{5A}} = I_{Q_{2A}} I_{Q_{4A}} I_{Q_{6A}} \implies I_{out+} \cdot \frac{I_{dc} I_o}{I_{cosh}} \cdot I_{dc} = I_{in-} \cdot I_{CA} \cdot I_{out+} \quad (6.54)$$

Thus, substituting Eq. 6.51 into Eq. 6.54, we end up with

$$I_{CA} = \frac{I_{in+} I_o}{I_{cosh}} \quad (6.55)$$

and having Eq. 6.55, Eq. 6.53 and Eq. 6.51, current I_{CB} can be written as

$$I_{CB} = \frac{I_{in-} I_o}{I_{cosh}} \quad (6.56)$$

Subtracting Eq. 6.56 from Eq. 6.55 results in

$$I_{CA} - I_{CB} = \frac{I_{in+} I_o}{I_{cosh}} - \frac{I_{in-} I_o}{I_{cosh}} \implies I_{cap} = \frac{I_{in} I_o}{I_{cosh}} \quad (6.57)$$

From Eq. 6.57, we can verify that the proposed integrator indeed implements a companding \sinh integrator as shown in Fig. 6.22. Next, from the dynamic translinear loops, consisting of C–Q_{5A}–Q_{6A} and C–Q_{5B}–Q_{6B}, we obtain

$$I_{cap} I_{out+} = CV_T \dot{I}_{out+} \quad (6.58)$$

and

$$I_{cap} I_{out-} = -CV_T \dot{I}_{out-} \quad (6.59)$$

where the dot represents differentiation with respect to time. Finally, substituting Eq. 6.58 and Eq. 6.59 into Eq. 6.57, we obtain the input–output relation

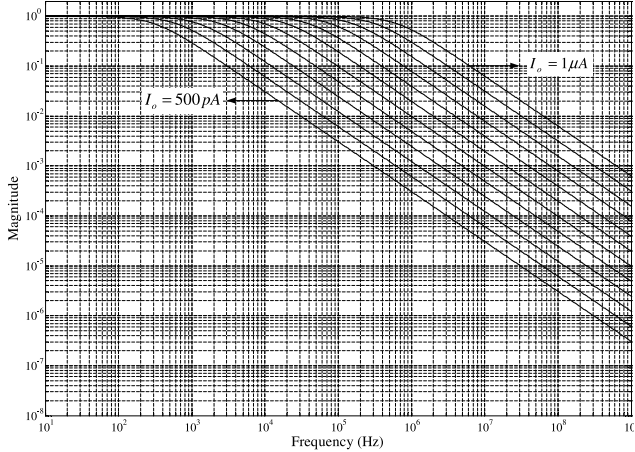


Fig. 6.25. Frequency response changing I_o from 500 pA to 1 μ A using quasi-ideal exponential devices

$$I_{in} = \frac{CV_T}{I_o} \dot{I}_{out} \quad (6.60)$$

which is a linear differential equation, describing an inherently lossless companding integrator with time constant $\tau = \frac{CV_T}{I_o}$. In order to obtain a lossy integrator we can easily introduce a negative feedback path from the output to the input of the integrator, resulting in

$$I_{in} = I_{out} + \frac{CV_T}{I_o} \dot{I}_{out} \quad (6.61)$$

describing a first-order low-pass filter with cutoff frequency ω_C , according to

$$\omega_C = \frac{I_o}{CV_T} \quad (6.62)$$

Simulating first the proposed integrator using quasi-ideal exponential devices, i.e. bipolar transistors with a very large current gain ($\beta = 10^6$), one can see in Fig. 6.25 the magnitude of the frequency response of the *sinh* lossy integrator, its cutoff frequency varying from 318 Hz to 636 kHz, showing the large frequency tuning range typical of translinear filters.

The externally linear internally nonlinear (ELIN) behavior of the integrator can be seen from the output current and the capacitance current, respectively, in Fig. 6.26 for an input signal swing much larger than bias current I_o .

CMOS integrator implementation

To validate the circuit principle, we have implemented and simulated the proposed integrator using models of AMSs 0.35 μ m CMOS IC technology. The

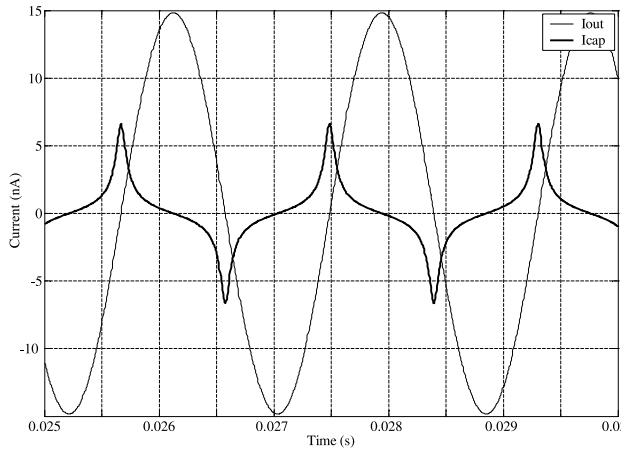


Fig. 6.26. Output current and capacitance current for large input signal swing using quasi-ideal exponential devices

circuit has been designed to operate from a 1.5-V (± 0.75 V) supply voltage. The schematic of the completed integrator is given in Fig. 6.27. The bipolar transistors have been replaced by equivalent CMOS transistors operating in weak inversion. The transistors have an aspect ratio of 100 $\mu\text{m}/1 \mu\text{m}$, in order to extend the weak inversion operation up to 2 μA . In addition, to realize the expression $\frac{I_o I_{dc}}{I_{cosh}}$, we added transistors M₇ and M₈ to the loops. Current I_{cosh} can be obtained easily by adding the positive and the negative output currents.

In class-AB operation, a static non-linear current splitter is used at the input to divide the bipolar input current I_{in} into two currents I_{in+} and I_{in-} , which are both strictly positive. The current splitter presented here is a geometric-mean splitter, comprising transistors M_{1A}–M_{2A}–M_{2B}–M_{1B}, where the corresponding equations are given by

$$I_{in+}, I_{in-} = \frac{\pm I_{in} + \sqrt{I_{in}^2 + 4I_o^2}}{2} \quad (6.63)$$

The output splitter currents are shown in Fig. 6.28, for a sinusoidal input signal with an amplitude of 10 nA and a bias current I_o of 1 nA.

As shown in Fig. 6.22, and in Eq. 6.48 and Eq. 6.57, the companding integrator can be characterized by a hyperbolic-sine transconductor at the output and a combined $cosh$ -divider block at the input, which relates the currents I_{out} and $I_{cosh} = \frac{I_{in} I_o}{I_{cap}}$ to the capacitance voltage V_{cap} , respectively. The simulated transfer functions of those blocks are shown in Fig. 6.29. The simulated output current with respect to the capacitance voltage is shown

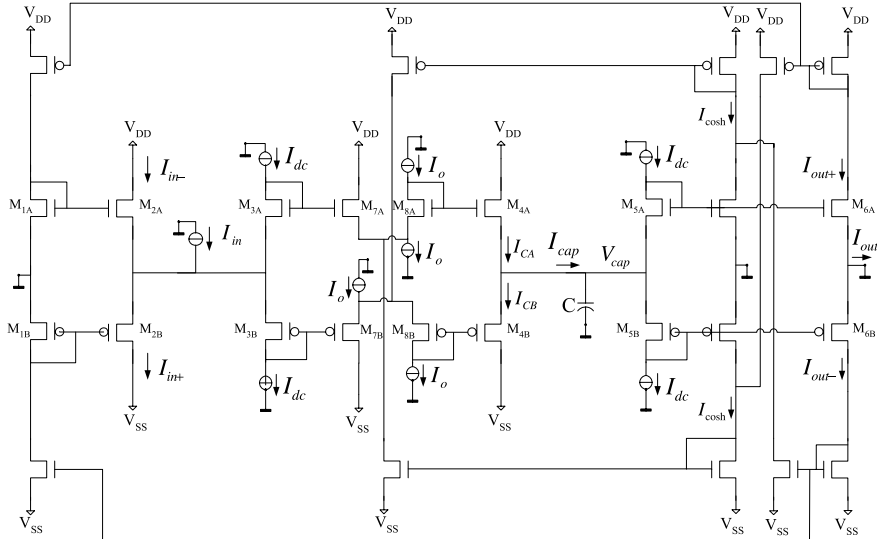


Fig. 6.27. Schematic of the CMOS class-AB \sinh integrator

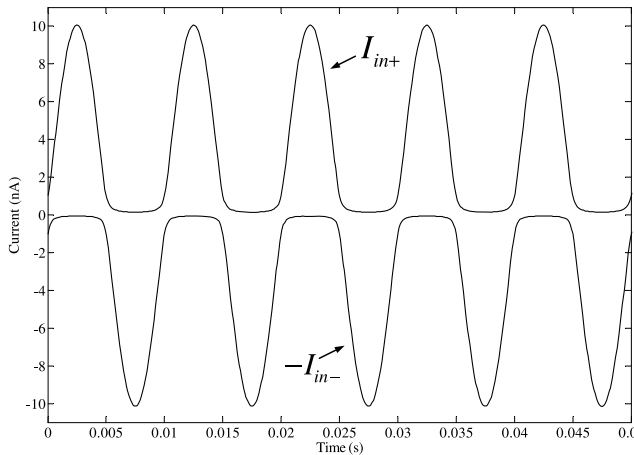


Fig. 6.28. Simulated current splitter output currents

in Fig. 6.29a whereas the ratio between the input and capacitance currents versus V_{cap} is illustrated in Fig. 6.29b.

The hyperbolic-sinusoidal transconductance of the output stage results in an inherently nonlinear dynamic relation between I_{cap} and I_{out} , which can be described by [7]

$$I_{cap} = CV_T \frac{I_{out}}{\sqrt{I_{out}^2 + 4I_o^2}} \quad (6.64)$$

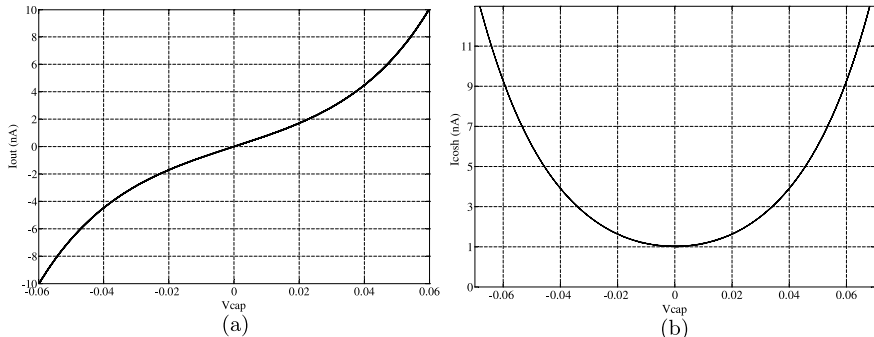


Fig. 6.29. Simulated currents with respect to the capacitance voltage V_{cap} : output current I_{out} (a) and I_{cosh} (b)

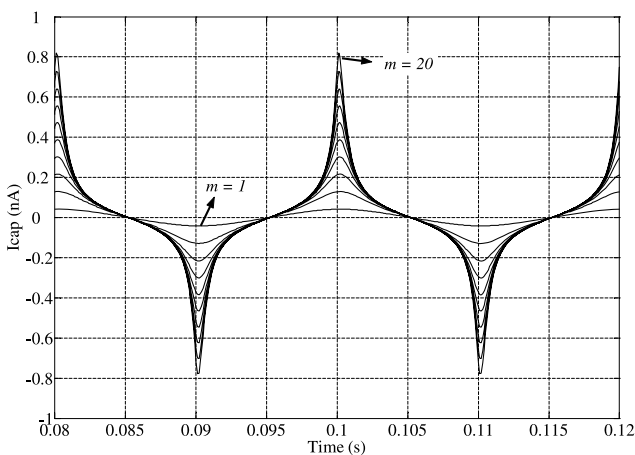


Fig. 6.30. Simulated capacitance current I_{cap} with I_o equal to 1 nA and the input amplitude changing from 1 nA to 20 nA

As shown in Fig. 6.30, I_{cap} is nearly sinusoidal for low values of m , where m represents the modulation index ($m = \hat{I}_{in}/I_o$). This linear behavior can be explained through the denominator of Eq. 6.64, which does not vary that much for low output currents. Thus, I_{cap} is more or less proportional to the derivative of I_{out} . The capacitance current becomes more non-linear when m increases, i.e. for large output swings, as seen in Fig. 6.30.

However, despite the nonlinear nature of the capacitance currents in \sinh integrators, an exactly linear transfer function can be realized, as one can see in Fig. 6.31, where the output is still defined by a sine function for m varying from 1 to 20.

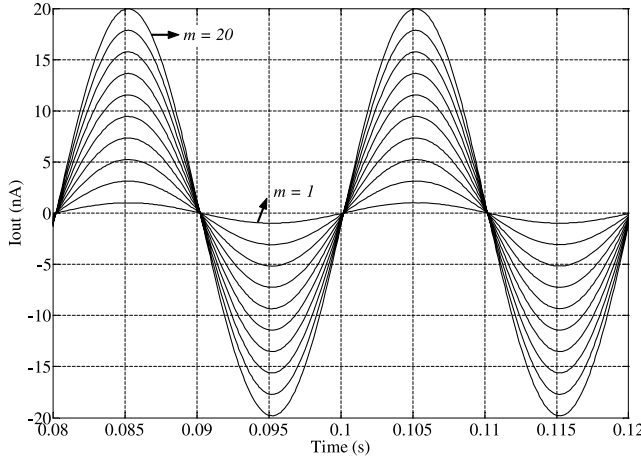


Fig. 6.31. Simulated output current I_{out} with I_o equal to 1 nA and the input amplitude changing from 1 nA to 20 nA

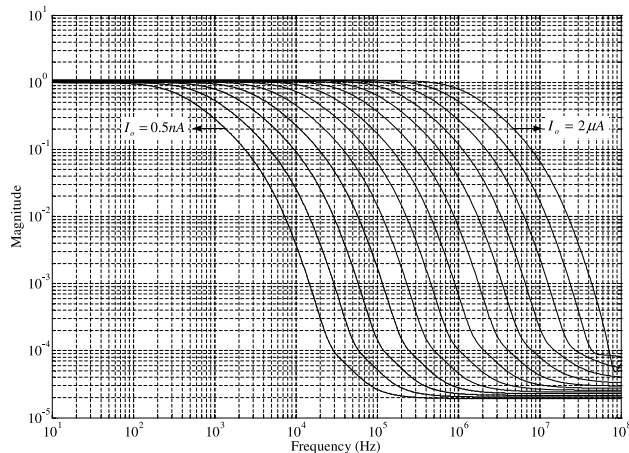


Fig. 6.32. Frequency response changing I_o from 500 pA to 2 μ A

In addition, one can see the linear tunability of the filter, described in Eq. 6.61, from the simulated frequency response, given in Fig. 6.32. With reference to Eq. 6.62, the cutoff frequency is directly proportional to bias current I_o , changing from 318 Hz to 1.2 MHz with I_o equal to 500 pA and 2 μ A, respectively, and C equal to 10 pF. Thus, it can be deduced that the cutoff frequency of the filter can be linearly controlled over a wide frequency range.

The Dynamic Range (DR), defined as the ratio between the maximum signal amplitude for a given distortion (in this case, 1-dB compression point)

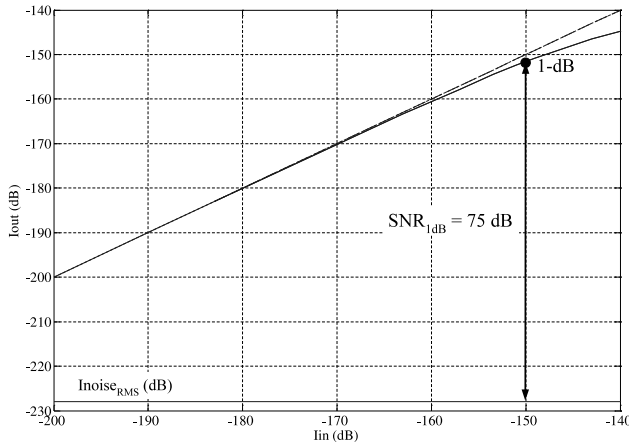


Fig. 6.33. Signal-to-noise ratio at 1-dB compression point for $I_o = 1$ nA

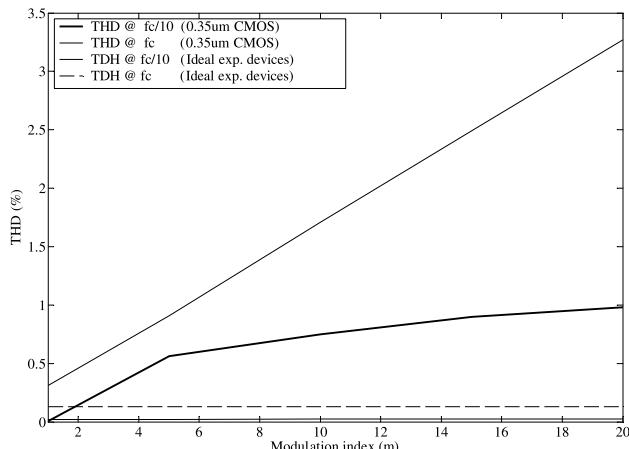


Fig. 6.34. Total harmonic distortion versus m at frequencies f_c and $f_c/10$

and the noise floor, is shown in Fig. 6.33. The output RMS current noise is 4.2 pA, resulting in a DR at the 1-dB compression point of approximately 75 dB.

Fig. 6.34 shows the total harmonic distortion (THD) at the output as a function of the modulation index m and input signal frequency. At a frequency much lower than the cut-off frequency (f_c), i.e. $f_c/10$, the THD is kept below 1%, with a modulation index as high as 20. As expected, the THD increases for an input signal frequency close to f_c . In this case, f_c equals 636 Hz and results in a THD at the cutoff frequency of 0.3% for $m = 1$ and 3.2% for $m = 20$. The performance of the filter is summarized in Table 6.1.

Table 6.1. Performance of the proposed integrator for two different cutoff frequencies

| Technology | 0.35 μm CMOS | |
|--|-------------------------|-----------------------|
| Bias current | $I_o = 1 \text{ nA}$ | $I_o = 2 \mu\text{A}$ |
| Capacitance | 10 pF | 10 pF |
| Supply voltage | 1.5 V | 1.5 V |
| Center frequency (f_c) | 636 Hz | 1.27 MHz |
| Total bias I_o (lossless integrator) | 11 nA | 22 μA |
| Total bias I_o (lossy integrator) | 14 nA | 28 μA |
| Power dissipation | 22.5 nW | 45 μW |
| Dynamic range (1-dB) | 75 dB | 75 dB |
| Noise current (rms) | 4.2 pA | 6.9 nA |
| Supply voltage range | 1–3 V | 1.5–3 V |
| Power diss. per pole and f_c | 35.37 pJ | 35.37 pJ |

Table 6.2. Performance comparison of the proposed class-AB integrator with other implementation

| | Serdijn et al. [25] | Punzenberger et al. [26] | El-Gamal et al. [27] | Python et al. [16] | Redondo et al. [28] | This work |
|--|---------------------|--------------------------|----------------------|--------------------|---------------------|--------------------|
| Technology | Bipolar | BiCMOS | Bipolar | CMOS | CMOS | CMOS |
| Capacitance | $1 \cdot C$ | $2 \cdot C$ | $2 \cdot C$ | $2 \cdot C$ | $2 \cdot C$ | $1 \cdot C$ |
| Bias current (without splitter) | $13 \cdot I_o$ | $11 \cdot I_o$ | $12 \cdot I_o$ | $12 \cdot I_o$ | $13 \cdot I_o$ | $9 \cdot I_o$ |
| Supply voltage | 3.3 V | 1.2 V | 1.2 V | 1.5 V | 1 V | 1.5 V |
| Cut-off frequency (ω_c) | $\frac{I_o}{CV_T}$ | $\frac{I_o}{CV_T}$ | $\frac{I_o}{CV_T}$ | $\frac{I_o}{CV_T}$ | $\frac{I_o}{CV_T}$ | $\frac{I_o}{CV_T}$ |
| P_{diss} per pole and ω_c (quiescent) | $42 \cdot CV_T$ | $13 \cdot CV_T$ | $14 \cdot CV_T$ | $18 \cdot CV_T$ | $13 \cdot CV_T$ | $13 \cdot CV_T$ |

Table 6.2 makes a comparison with other log-domain class-AB designs. The first advantage of this design is that it uses only one capacitor to implement a class-AB integrator, which saves considerable chip area. This is particularly important for low-frequency designs where we inevitably need to use large capacitance values. Furthermore, the proposed circuit presents an excellent performance with respect to power efficiency. The power efficiency of a continuous-time filter is a figure of merit used in comparing various filter topologies and can be estimated by means of the power dissipation per pole P_{diss} and cut-off frequency f_c , defined as $\frac{P_{diss}}{f_c}$ [29].

Conclusions

A new ultra low-power class-AB *sinh* integrator based on hyperbolic-sine transconductors is presented. The proposed integrator uses only one grounded capacitor and shows excellent power efficiency, compared to existing log-domain class-AB implementations. The lossy integrator is simulated using CMOS transistors in weak inversion, operating from a 1.5-V (± 0.75 V) supply voltage. The total current consumption of the first-order low-pass filter is 14 nA and the DR at the 1-dB compression point is 75 dB. The filter can handle signals much larger than the bias current, while keeping THD below 1%.

6.5 Discussion

In the linear transconductors presented here, the input transistors are kept in the triode-region to benefit from the lowest G_m/I_D ratio. The main advantage of this technique is the ability to obtain extremely small transconductances, which enable us to design very low-frequency filters. Translinear circuits become difficult to integrate when it's necessary to design low cut-off-frequency filters for use in the Hz and sub-Hz range. For example, for $G_m = 1$ nA/V, the proposed transconductor need to be biased with a quiescent current $I_o = 315$ pA. To achieve the same time constant and considering the same bias current, the translinear circuits needs an increase of 12.6 times in capacitor value. Or, to maintain the same capacitor, it is necessary to decrease the current to 25 pA, which is difficult to obtain precisely.

Contrary to the translinear approach, the time constant of the filter (and, of course, the corresponding cut-off frequency) is controlled by a voltage rather than by a current, which is limited by the supply voltage; whereas the frequency tunability of the translinear circuits can be controlled over a wide range, usually several decades. Moreover, in linear G_m -C filters, due to the inherently non-linear behavior of the transistors, the transconductors have to be linearized, in order to implement the desire transfer function. This unavoidably degrades the available transconductance, resulting in a poor current efficiency.

The main advantages of translinear circuits with respect to other low-power techniques are, first of all, the capability of handling a large dynamic range in a low-voltage environment. In contrast to G_m -C filters, the capacitor current is no longer a linear function of the input voltage, but an exponential one. This means, that the voltages in translinear filters are logarithmically related to the currents, and, as a result, the voltage excursions are small, typically only a few tens of millivolts. Thus, the maximum signal swing in a current-mode circuit is not limited by the supply voltage anymore.

Second of all, the static and dynamic translinear principles can be applied to the implementation of a wide variety of non-linear functions, static

nonlinear polynomial transfer functions and non-linear differential equations, respectively. Also, only transistors and capacitors are required to realize a filter function. Since in conventional ultra low-power designs resistors would become too large for on-chip integration, their superfluity is a very important advantage. Other advantages are that they present a high functional density and are theoretically process and temperature independent.

6.6 Conclusions

Several ultra low-power integrator designs were presented in this chapter. The integrators were based on two different techniques, being the G_m -C approach and the translinear (log-domain) method. The advantages and the limitations of these techniques were also highlighted. To summarize, both techniques can be directly used in low-power analog filters and ultra low-power biomedical systems designs, as can be seen in the next chapter.

References

- [1] R. Schaumann and M. E. van Valkenburg, *Design of Analog Filters*, 2nd edn, Oxford University Press, Oxford, USA, 2001.
- [2] J. A. de Lima and W. A. Serdijn, *A compact nA/V CMOS triode transconductor and its application to very-low frequency filters*, in: Proc. ISCAS, Kobe, Japan, May 23–26, 2005.
- [3] R. W. Adams, *Filtering in the log domain*, Preprint 1470, presented at the 63rd AES Conference, New York, May 1979.
- [4] E. Seevinck, *Companding current-mode integrator: a new circuit principle for continuous-time monolithic filters*, Electronics Letters, vol. 26, no. 24, pp. 2046-2047, 1990.
- [5] B. Gilbert, *Translinear circuits: a proposed classification*, Electronics Letters, vol. 11, no. 1, pp. 14-16, 1975.
- [6] J. Mulder, W. A. Serdijn, A. C. van der Woerd, and A. H. M. van Roermund, *Dynamic Translinear and Log-Domain Circuits: Analysis and Synthesis*, Kluwer, Boston, MA, 1999.
- [7] J. Mulder, *Static and dynamic translinear circuits*, PhD thesis, Delft University of Technology, Oct. 1998
- [8] D. R. Frey, *Log Domain filtering: An approach to current mode filtering*, Proc. Elect. Eng. G, vol. 140, pp. 406-416, 1993.

- [9] Y. Tsividis, *Externally linear, time-invariant systems and their application to companding signal processors*, IEEE Transactions on Circuits and Systems – II, vol. 44, pp. 65-85, 1997.
- [10] D. R. Frey, *Exponential state space filters: A generic current mode design strategy*, IEEE Transactions on Circuits and Systems – I, vol. 43, pp. 34-42, 1996.
- [11] J. Mulder, W. A. Serdijn, A. C. van der Woerd, and A. H. M. van Roermund, *Dynamic translinear circuits – An overview*, Analog Integrated Circuits and Signal Processing, vol. 22, nos 2-3, pp. 111-126, 2000.
- [12] W. A. Serdijn, J. Mulder, A. C. van der Woerd, and A. H. M. van Roermund, *The design of wide-tunable translinear second-order oscillators*, in: Proc. IEEE ISCAS, Hong Kong, vol. 2, pp. 829–832, May 1997.
- [13] J. Mulder, A. C. van der Woerd, W. A. Serdijn, and A. H. M. van Roermund, *An RMS-DC converter based on the dynamic translinear principle*, IEEE Journal of Solid-State Circuits, vol. 32, no. 7, pp. 1146-1150, 1997.
- [14] G. W. Roberts and V. W. Leung, *Design and Analysis of Integrator-Based Log-Domain Filter Circuits*, Kluwer, Dordrecht, The Netherlands, 2000.
- [15] M. N. El-Gamal and G. W. Roberts, *A 1.2 V NPN-only integrator for log-domain filtering*, IEEE Transactions on Circuits and Systems – II, vol. 49, no. 4, pp. 257-265, 2002.
- [16] D. Python and C. Enz, *A micropower class-AB CMOS log-domain filter for DECT applications*, IEEE Journal of Solid-State Circuits, vol. 36, no. 7, pp. 1067-1075, 2001.
- [17] W. A. Serdijn, M. Broest, J. Mulder, A. C. van der Woerd, and A. H. M. van Roermund, *A low-voltage ultra low-power translinear integrator for audio filter applications*, IEEE Journal of Solid-State Circuits, vol. 32, no. 4, pp. 577-582, 1997.
- [18] C. Toumazou, J. Ngarmnil and T. S. Lande, *Micropower log-domain filter for electronic cochlea*, IEE Electronics Letters, vol. 30, no. 22, pp. 1839-1841, 1994.
- [19] G. D. Duerden, G. W. Roberts and M. J. Deen, *The development of bipolar log domain filters in a standard CMOS process*, in: Proc. IEEE Int. Symp. Circuits and Systems, vol. 1, pp. 1470-1476, May 2001.
- [20] S. A. P. Haddad and W. A. Serdijn, *High-frequency dynamic translinear and log-domain circuits in CMOS technology*, in: Proc. IEEE Int. Symp. Circuits and Systems, vol. 3, pp. 313-316, May 2002.

- [21] G. Palumbo and S. Pennisi, *A high-performance CMOS voltage follower*, in: Proc. IEEE Int. Conf. Electronics, Circuits and Systems, vol. 2, pp. 21-24, 1998.
- [22] G. Palmisano and G. Palumbo, *An optimized compensation strategy for two-stage CMOS OPAMPS*, IEEE Transactions on Circuits and Systems – I, vol. 42, no. 3, pp. 178-182, March 1995.
- [23] C. J. M. Verhoeven, A. van Staveren, G. L. E. Monna, M. H. L. Kouwenhoven, and E. Yildiz, *Structured Electronic Design – Negative-Feedback Amplifiers*, Kluwer, Boston, MA, 2003.
- [24] D. R. Frey and A. T. Tola, *A state-space formulation for externally linear class AB dynamical circuits*, IEEE Transactions on Circuits and Systems – II, vol. 46, no. 3, pp. 306-314, 1999.
- [25] W. A. Serdijn, M. H. L. Kouwenhoven, J. Mulder, and A. H. M. van Roermund, *Design of high dynamic range fully integrable translinear filters*, in: Analog Integrated Circuits and Signal Processing, vol. 19, Kluwer, pp. 223-239, 1999.
- [26] M. Punzenberger and C. Enz, *A 1.2-V low-power BiCMOS class AB log-domain filter*, IEEE Journal of Solid-State Circuits, vol. 32, no. 12, pp. 1968-1978, 1997.
- [27] M. N. El-Gamal, R. A. Baki and A. Bar-Dor, *30–100-MHz NPN-only variable-gain class-AB instantaneous companding filters for 1.2-V applications*, IEEE Journal of Solid-State Circuits, vol. 35, no. 12, pp. 1853-1864, 2000.
- [28] X. Redondo and F. Serra-Graells, *1V Compact class-AB CMOS log filters*, in: Proceedings IEEE International Symposium Circuits and Systems, pp. 2000-2003, May 2005.
- [29] C. Toumazou, G. Moschytz, and B. Gilbert, *Trade-Offs in Analog Circuit Design*, Kluwer, Dordrecht, The Netherlands, 2002.

Chapter 7

Ultra Low-Power Biomedical System Designs

The methodology presented in previous chapters will now be employed in the design of several ultra low-power biomedical systems and analog wavelet filters.

In the first part of this chapter, a benchmark cardiac sense amplifier, i.e. the front end of a pacemaker, based on the Dynamic Translinear (DTL) circuit technique is presented. The system consists of a voltage-to-current converter, a bandpass filter, absolute value and RMS–DC converter circuits and an event detection circuit. From simulations, it is demonstrated that the DTL technique is a good alternative to conventional sense amplifiers for intra-cardiac applications since they handle the required dynamic range and perform non-linear operations at low supply voltages.

Another approach for ultra low-power analog QRS complex detection circuit, for pacemaker applications, is presented in this chapter. The system is based on the Wavelet Transform (WT) and detects the wavelet modulus maxima of the QRS complex. It consists of a wavelet filter based on the CFOS approach, an absolute value circuit, a peak detector and a comparator. Simulations indicate a good performance of the wavelet transform and the QRS complex detection.

To validate both systems principles and to check the circuits performances, the sub-circuits as well as the whole systems have been implemented in our in-house bipolar semi-custom DIMES IC process, SIC3A. Typical transistor parameters are $f_{T,npn,max} = 15$ GHz and $\beta_{F,npn} = 150$ (smallest emitter size) [1].

Moreover, a few wavelet filter designs will also be presented. Two convenient methods to provide the transfer function of the wavelet filter are given by the Padé and L_2 approximations and, thus, two designs based on these approaches, for a Gaussian wavelet base, will be designed using the G_m -C and the DTL circuit techniques, respectively. In addition, a complex wavelet filter design, based on the combination of the real and the imaginary state-space descriptions, is described.

Finally, the implementation of a Morlet wavelet filter using the procedure in Chapter 4 is presented. First, the approximation based on the Padé method is used to calculate the transfer function of the filter, whose impulse response is the Morlet wavelet base. Next, to meet low-power low-voltage requirements, we optimize the state-space description of the filter with respect to dynamic range, sensitivity and sparsity, as presented in Chapter 5. The filter design that follows is based on an orthonormal ladder structure and employs log-domain integrators as main building blocks. We have implemented the log-domain state-space wavelet filter in IBMs 0.18 μm BiCMOS IC process.

7.1 Dynamic translinear cardiac sense amplifier for pacemakers

Conventional pacemaker topologies usually are divided into an analog part (comprising a sense amplifier and a heart stimulator) and a digital part (comprising a micro controller). The sense amplifier plays a fundamental role in providing information about the current state of the heart. It is designed to detect and monitor intra-cardiac signal events (e.g., R-waves in the ventricle). After signal sensing, the signal is fed to the digital microprocessor that decides upon the appropriate pacing therapy to be delivered by the stimulator. However, the algorithm in the microprocessor requires from the sense amplifier the accurate measurement of the heart activity even in the presence of noise and interference. The diverse features of the intra-cardiac signals, therefore, require a large dynamic range, i.e., a large signal-to-noise-plus-interference level, for the sense amplifier.

This design presents the applicability of DTL circuits to the design of cardiac sense amplifiers to be implemented in pacemakers. In Fig. 7.1 a suitable block diagram of a sense amplifier for cardiac signal detection is given [2]. The system consists of a $V-I$ (voltage-to-current) converter, a bandpass filter, absolute value [3] and RMS-DC converter circuits [4], and a comparator circuit [3]. The chip microphotograph of the sense amplifier implemented in SIC3A semi-custom IC process is given in Fig. 7.2. Additionally, an EMI filter is implemented off-chip for electromagnetic interference cancellation (not shown). It is a 2nd-order bandpass filter to suppress DC and signals beyond 1 kHz. The $V-I$ converter is required as the input and output quantities of the EMI filter are voltages and translinear circuits are inherently current-mode as will be treated in Section 7.3. The bandpass filter is used to specifically select intra-cardiac signals, in our case being the QRS complex or R-wave, and to minimize the effect of the overlapping myocardial interference signals and low-frequency breathing artifacts. The center frequency of the bandpass filter is located at 25 Hz. The reason to use an absolute value circuit is to be independent from the electrode position in the heart. Accommodation to changes in the average input signal level is realized using the RMS-DC con-

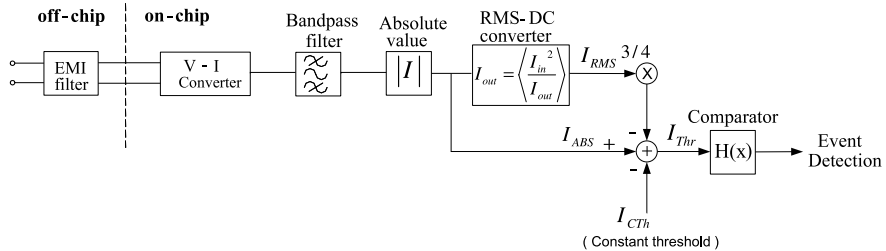


Fig. 7.1. Block diagram of the sense amplifier

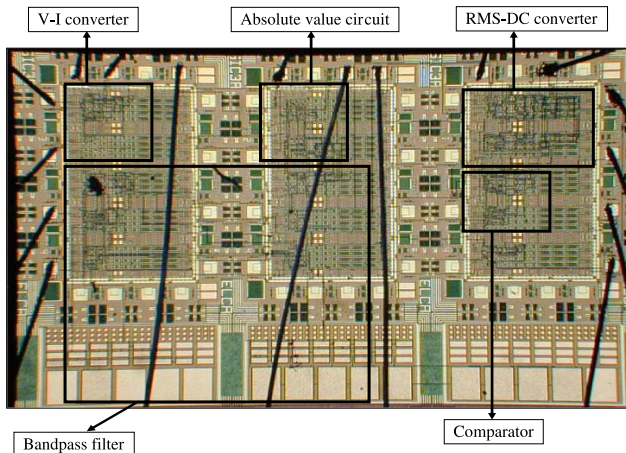


Fig. 7.2. Sense amplifier chip microphotograph

verter. This circuit implements two functions, a squarer-divider and a low-pass filter. At the end of the block schematic, the detection signal (a binary value) is generated depending upon an adaptive threshold level, which is given by:

$$I_{Thr} = I_{ABS} - \left(\frac{3}{4} I_{RMS} + I_{CTh} \right) \quad (7.1)$$

where I_{ABS} is the output signal of the absolute value circuit. I_{RMS} is the output of the RMS-DC converter. I_{CTh} is a constant value that can be derived from typical values of the input signal.

7.1.1 Differential voltage to single-ended current converter

The output signal of the EMI filter is a differential voltage, in the order of a few millivolts, and the input signal of the bandpass filter is a single-ended current. The required transformation of the differential input voltage into a single-ended current can be simply performed by a differential pair loaded

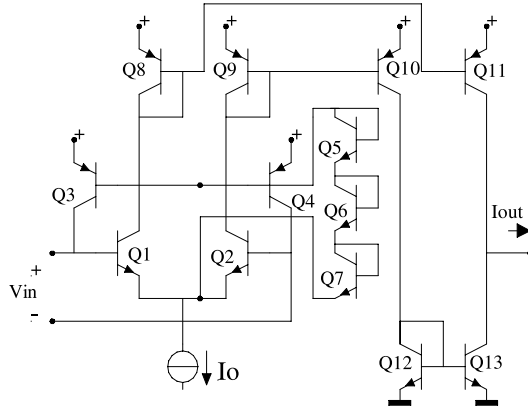


Fig. 7.3. Differential input voltage to single-ended current converter

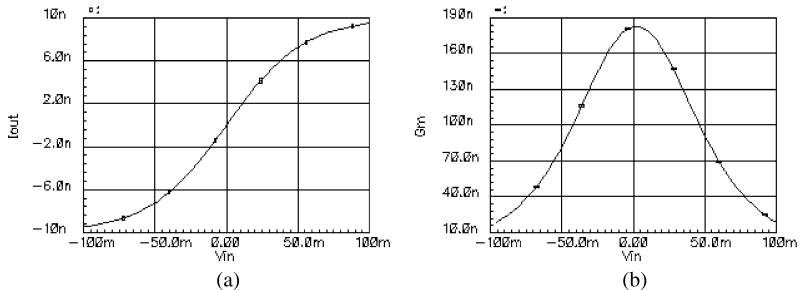


Fig. 7.4. DC transfer of the V - I converter. **a** V - I characteristic. **b** Transconductance factor

by two current mirrors as shown in Fig. 7.3. Note that the transconductance factor is determined by the value of the current I_o and equals $I_o/4V_T$. Since the output nodes of the EMI filter are floating, the differential input nodes of the V - I converter need to be biased at a voltage in between the power supplies. This CM (common-mode) input voltage is set by the CM loop comprising Q3–Q7 and approximates $V_{cc} - 3V_{be}$.

The DC transfer of the V - I converter circuit is given in Fig. 7.4. The value of current I_o is 10.4 nA, resulting in a transconductance factor of 0.18 $\mu\text{A}/\text{V}$ to accommodate the desired input signal range.

7.1.2 Bandpass filter

To achieve sufficient selectivity around 25 Hz the filter is implemented by a cascade of two biquadratic bandpass filter sections. These biquads, in turn, are realized by two lossy integrators according to the block diagram given in Fig. 7.5a. The integrators comprise four transistors and one capacitor in a

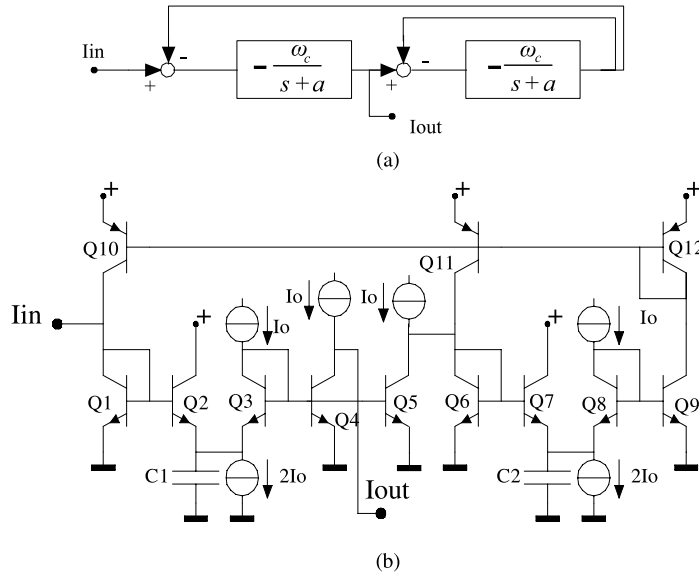


Fig. 7.5. a Block diagram of the bandpass biquad filter. b Circuit schematic

loop and implement

$$CV_T \dot{I}_{out} + I_o I_{out} = I_o I_{in} \quad (7.2)$$

where I_o is a DC bias current and I_{out} is the low-pass filtered version of I_{in} . The expression above is a linear differential equation, describing a low-pass filter with cut-off frequency ω_C according to

$$\omega_C = \frac{I_o}{CV_T} \quad (7.3)$$

In Fig. 7.5b, the circuit diagram of one biquad for realizing a part of the bandpass filter is given. The integrator loops are defined by transistors Q1–Q4 and capacitor C1 and Q5–Q8 and C2, respectively. A positive feedback network using current mirror Q11–Q12 turns the lossy integrator into a lossless integrator.

For a system having its poles in Butterworth position, the values of the capacitances are given by

Lossy integrator:

$$C_1 = \frac{I_o}{V_T(p_1 + p_2)} \quad (7.4)$$

Lossless integrator:

$$C_2 = \frac{I_o}{V_T \sqrt{p_1 p_2}} \quad (7.5)$$

where p_1 and p_2 are the poles of the Butterworth polynomial implemented by the biquad. The magnitude and phase response of the bandpass filter is shown

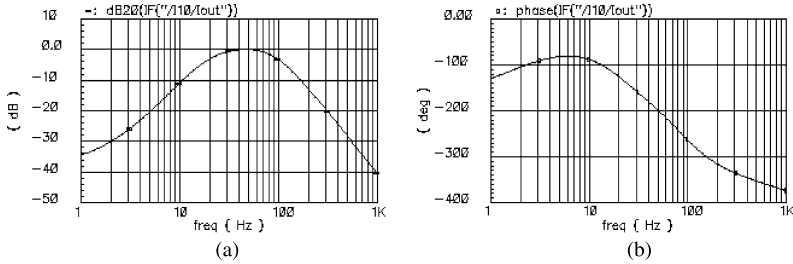


Fig. 7.6. Frequency response of the biquad. **a** Magnitude. **b** Phase

in Fig. 7.6a and Fig. 7.6b, respectively. Note that the center frequency of the bandpass is indeed located around 25 Hz. The first biquad has I_o and C_1 and C_2 equal to 2 nA, 80 pF and 170 pF respectively. For the second biquad these values are 0.4 nA, 94 pF and 131 pF, respectively.

7.1.3 Absolute value and RMS–DC converter circuits

Since the polarity of the input signal is not known, its absolute value is generated. The required function $I_{out} = |I_{in}|$ is realized with the circuit in Fig. 7.7 [3]. The translinear loop in the circuit consists of transistors Q2, Q1, Q5 and Q7, implementing

$$(I_o + I_{out})(I_o - I_{out}) = (I_o + I_{in})(I_o - I_{in}) \quad (7.6)$$

The DC transfer of the absolute value circuit is given in Fig. 7.8. The circuit provides correct operation up to I_o .

The RMS transfer is implemented by a squarer/divider circuit [4] and a low-pass filter and produces

$$I_{out} = \int \frac{I_{in}^2}{I_{out}} dt \quad (7.7)$$

Its translinear differential equation describing a first-order RMS–DC conversion then follows as

$$CV_T \dot{I}_{out} I_{out} + I_o I_{out}^2 = I_o I_{in}^2 \quad (7.8)$$

Note that this is a nonlinear differential equation. A possible implementation is shown in Fig. 7.9 [4]. Q1 through Q6 form the static translinear loop implementing $(I_{cap} + I_o)I_{out}^2 = I_o I_{in}^2$ and C, Q4–Q6 the dynamic translinear loop, implementing $2CV_T I_{out} = I_{cap} I_{out}$. The quadratic factors I_{in2} and I_{out2} are implemented by Q1–Q2 and Q5–Q6 respectively. Q7 and Q8 are buffers to avoid base current errors in Q2 and Q4.

The output current of the RMS–DC converter is a time average of the input signal as seen from Eq. 7.8. The cut-off frequency is given by Eq. 7.3. To achieve a cut-off frequency of 1.5 Hz, the values of I_o and C in Fig. 7.9 are

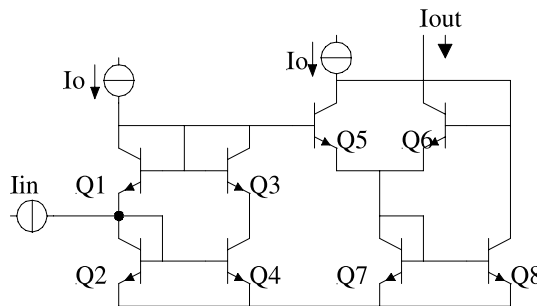


Fig. 7.7. Absolute value circuit

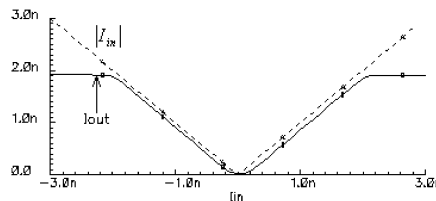


Fig. 7.8. DC transfer of the absolute value circuit

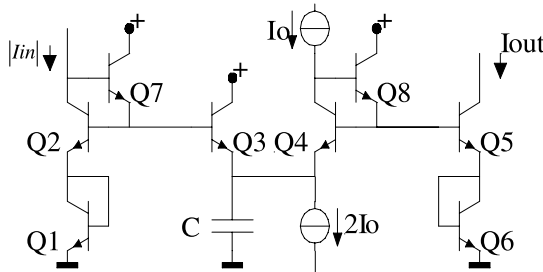


Fig. 7.9. RMS-DC converter circuit

0.125 nA and 1 nF respectively. The resulting signals from a transient analysis of the RMS-DC converter connected to the absolute value circuit is given in Fig. 7.10. With a sinusoid applied at the input to validate the operation of the circuit, having a frequency of 10 Hz and amplitude of 1.5 nA, the RMS-DC circuit produces an output (drawn line) amplitude around 1 nA, which is close to the ideal response (dotted line).

7.1.4 Detection (Sign function) circuit

Since TL circuits can implement polynomial functions only, we first need to approximate the Sign function by a polynomial function. A static translinear loop equation to achieve a good approximation to the Sign function is described

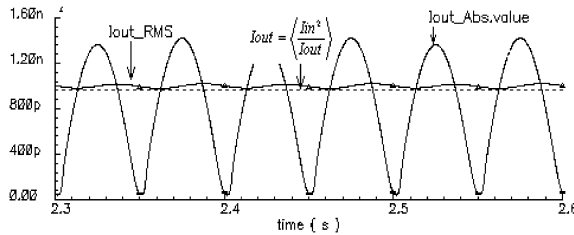


Fig. 7.10. RMS-DC converter signals (transient analysis)

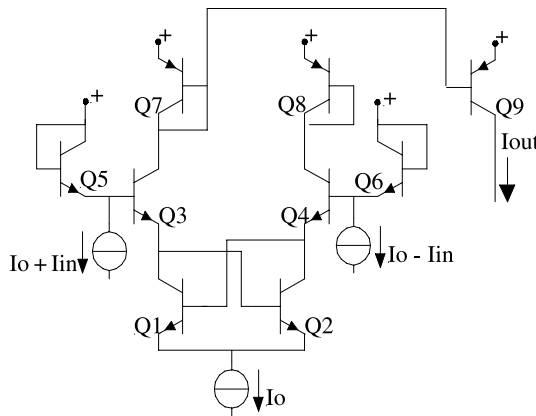


Fig. 7.11. Comparator circuit

by [3]

$$(I_o + I_{in})(I_o - I_{out})(I_o + I_{out}) = (I_o - I_{in})(I_o + I_{in})(I_o + I_{out}) \quad (7.9)$$

yielding

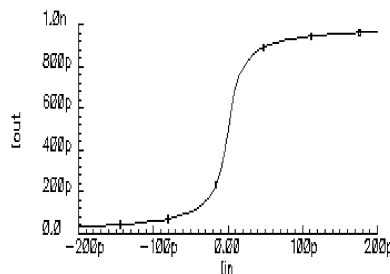
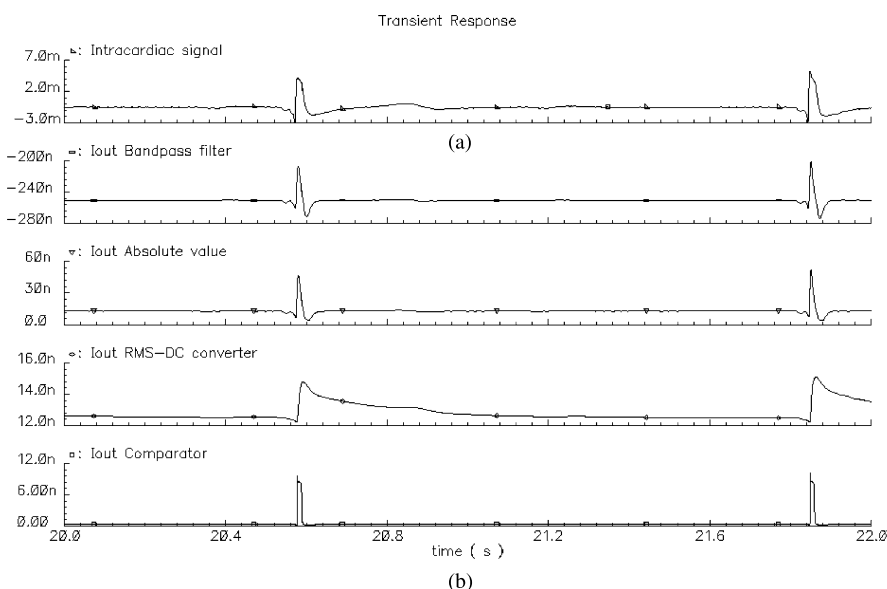
$$\begin{cases} I_{out} = 0 & \text{if } I_{in} < 0 \\ I_{out} = I_o & \text{if } I_{in} > 0 \end{cases} \quad (7.10)$$

Its corresponding TL circuit is given in Fig. 7.11 [3].

In Fig. 7.12, the DC transfer of the comparator circuit, with I_o equal to 1 nA, is shown.

Finally, a test signal is applied to the system to verify the performance and efficiency of the complete sense amplifier according to Fig. 7.1. A typical intra-cardiac signal measured in the ventricle, shown in Fig. 7.13a, is applied to the input of the system. The transient responses of the blocks are shown in Fig. 7.13b. The system is clearly able to detect the R-wave, which represents the cardiac event that the circuit was supposed to detect.

The characteristics of the sense amplifier are summarized in Table 7.1.

**Fig. 7.12.** DC response of the comparator circuit**Fig. 7.13.** **a** Intra-cardiac signal. **b** Transient response of the complete sense amplifier**Table 7.1.** Simulated sense amplifier characteristics

| | |
|--|--------|
| Power supply | 2.0 V |
| Total bias current | 120 nA |
| Power consumption | 240 nW |
| Eq. rms noise voltage @ $V-I$ converter input | 0.1 mV |
| Eq. rms noise current @ Abs. value circuit output | 3.6 pA |
| SNR @ Abs. value circuit output (10 Hz–1 kHz) | 39 dB |
| Eq. rms noise current @ comparator input while switching | 6.5 pA |

7.2 QRS-complex wavelet detection using CFOS

QRS complex detection is important for cardiac signal characterization. Many systems have been designed in order to perform this task. In [5] it was shown that, in spite of the existence of different types, a basic structure is common for many algorithms. This common structure is given in Fig. 7.14a. It is divided into a filtering stage (comprising linear and/or non-linear filtering) and a decision stage (comprising peak detection and decision logic).

The algorithm detection of the QRS complex presented here is based on detection of the modulus maxima of the wavelet transform. The two maxima with opposite signs of the WT correspond to the QRS complex and are illustrated in Fig. 7.14b.

The block diagram is given in Fig. 7.15 and contains the required circuits to design the QRS detection system [6].

At the input, a wavelet filter is situated which implements an approximation to the first-derivative Gaussian WT. The complete filter comprises multiple scales in parallel in order to compute the WT in real time. Subsequently, the signal is fed through an absolute value circuit, followed by a peak detector, to generate an adjustable threshold level according to

$$T_{thj} = Abs - \frac{3}{4} Peak \quad (7.11)$$

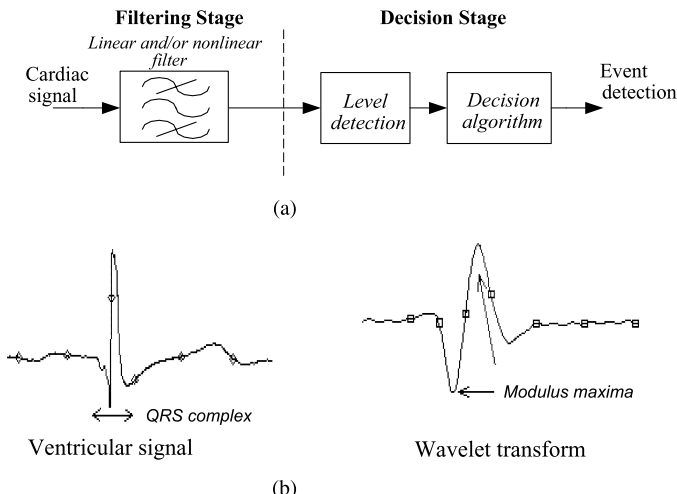


Fig. 7.14. a Block diagram of the basic structure of the QRS detectors [5]. b Cardiac signal and the modulus maxima of the WT

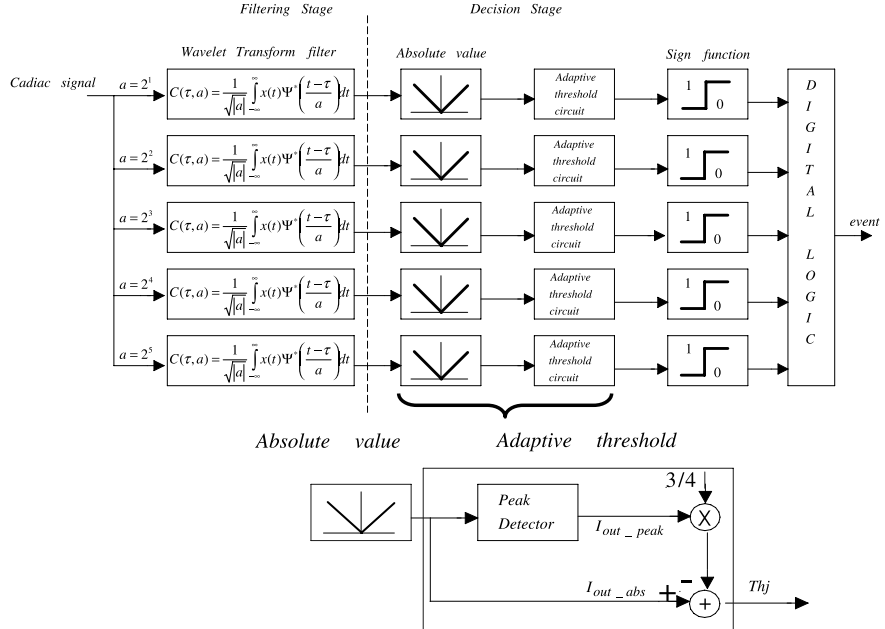


Fig. 7.15. Block diagram of the wavelet system

with

$$\begin{cases} Peak = Abs & \text{for } Abs \geq Peak \\ \frac{dPeak}{dt} = -\tau Peak & \text{for } Abs \leq Peak \end{cases} \quad (7.12)$$

where T_{hj} is the threshold value for scale $a = 2^j$, Abs is the absolute value and $Peak$ is the output value of the peak detector circuit. τ is the time constant of the peak detector and the $\frac{d}{dt}$ represents differentiation with respect to time.

The final signal processing block is a comparator in order to detect the modulus maxima position of the QRS complex. The time localization of the modulus maxima and the classification of characteristic points of the cardiac signal is processed by the digital logic circuit, and will not be described here.

7.2.1 Filtering stage – CFOS wavelet filter

We first propose an analog bandpass filter, of which the impulse response is an approximated first-derivative Gaussian window function. In order to achieve this, we adopted the wavelet filter introduced in [7]. This filter has been implemented with a cascade of Complex First Order Systems (CFOS) [8].

We apply the DTL circuit technique to the design of the analog implementation of the WT. In Fig. 7.16, the equivalent dynamic translinear circuit for

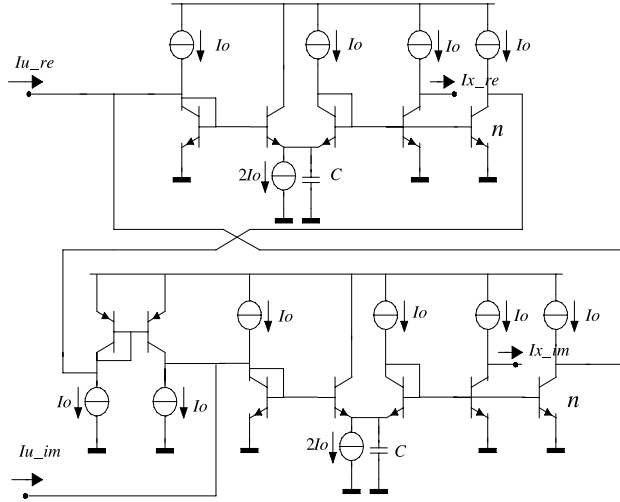


Fig. 7.16. Equivalent DTL circuit for complex input for the analog CFOS stages

realization of a CFOS is depicted. The related expressions are given by

$$\dot{I}_{x(re)} = \frac{I_o}{CV_T} I_{x(re)} - n \frac{I_o}{CV_T} I_{x(im)} + \frac{I_o}{CV_T} I_{u(re)} \quad (7.13)$$

$$\dot{I}_{x(im)} = \frac{I_o}{CV_T} I_{x(im)} + n \frac{I_o}{CV_T} I_{x(re)} + \frac{I_o}{CV_T} I_{u(im)} \quad (7.14)$$

where $I_{u(re)}$ is the real input signal, $I_{u(im)}$ is the imaginary input signal; $I_{x(re)}$ and $I_{x(im)}$ represent the real and imaginary part of the output signal, respectively. n is defined by $n = \frac{\omega}{\sigma}$, where ω and σ are the corresponding parameters of the complex first-order system equation presented in Chapter 4.

In order to implement a Wavelet Transform, we need to be able to scale and shift the Gaussian function in time. By changing the values of capacitance C accordingly we implement short windows at high frequencies and long windows at low frequencies.

Figure 7.17a shows the ideal impulse response of the wavelet filter with 3 CFOS stages, whereas in Fig. 7.17b the simulated impulse response is presented. The number of stages has been chosen by trading time-frequency resolution (Chapter 4) for power consumption and noise contribution. For cardiac signal characterization, we are interested in the approximation to a first-derivative Gaussian function, which is present in the imaginary output.

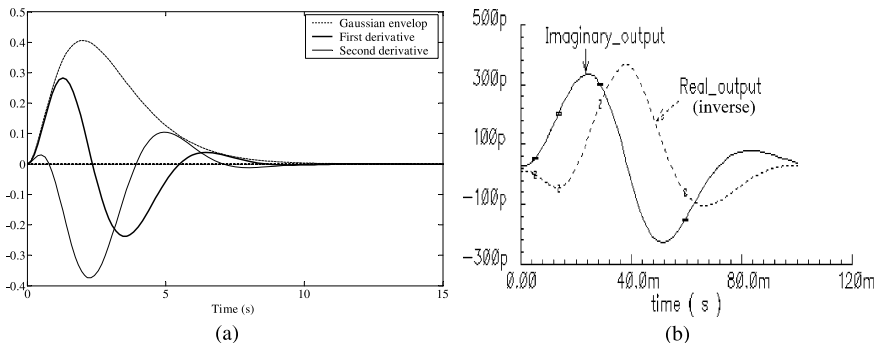


Fig. 7.17. Impulse response of the wavelet filter with 3 CFOS stages. **a** Ideal. **b** Simulated response

7.2.2 Decision stage – absolute value and peak detector circuits

Figure 7.18a shows a simple circuit [9] to implement an absolute value function. Its operation is given as follows: when I_{in} is positive, it is handled by current mirror Q1–Q2; when negative, it is conveyed to the summation node S by cascade transistor Q3. The bias voltage at the base of Q3 is obtained by the two diode-connected transistors Q4 and Q5.

The basic design of the employed peak detector is shown in Fig. 7.18b. Its operation is as follows: When $I_{in} > I_c$, Q1 (collector current of Q1), capacitor C is rapidly charged by Q4 until $I_{in} = I_c$, Q1. For $I_{in} < I_c$, Q1, C is discharged by the rather small base current of Q3. The comparator circuit described in Section 7.1 will also be used here.

The DC response of the absolute value circuit is given in Fig. 7.19a. $|I_{in}|$ is also shown, for reference purposes. The transient responses of the absolute value and the peak detector circuits are provided in Fig. 7.19b, respectively, for a ventricular signal at the absolute circuit input.

In order to verify the performance and efficiency of the whole system, a set of cardiac signals was applied to the input of the system. Figure 7.20a shows the ideal wavelet transform for 5 scales with a ventricular signal at the input. Figure 7.20b gives the simulation result of 3 CFOS stages; one can see the similarity between the ideal WT and the WT from the CFOS filter.

Finally, to show the denoising property of the wavelet, we apply a noisy signal to the QRS detection system. Figure 7.21b shows a typical ventricular signal with 50 Hz interference (input signal) and Fig. 7.21c gives the wavelet transform at various scales. We can see from Fig. 7.21d that the modulus maxima of the QRS complex for a specific scale ($a = 2^4$) of the WT indeed have been detected. The total power consumption is 55 nW per scale.

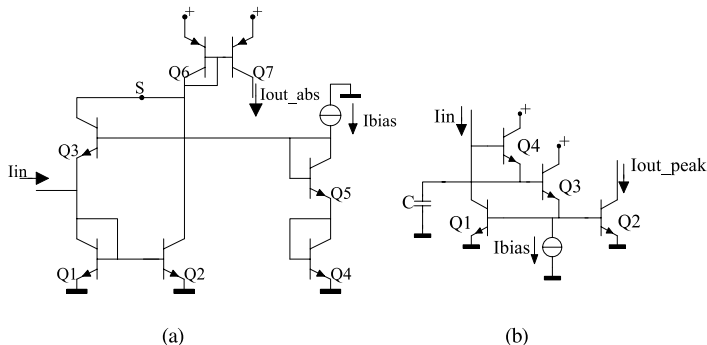


Fig. 7.18. **a** Absolute value circuit. **b** Peak detector circuit

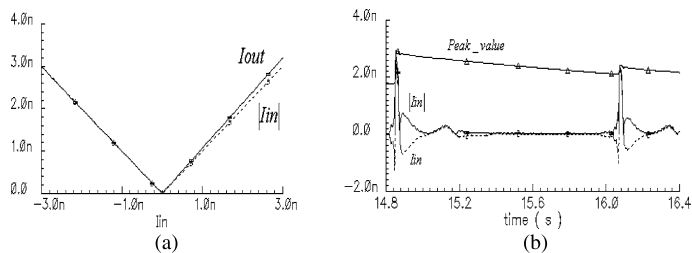


Fig. 7.19. **a** DC response of the absolute value circuit. **b** Transient response of the absolute value and peak detector circuits with a ventricular signal at the input

7.2.3 Measurement results

A microphotograph of the circuit implemented in the DIMES SIC3A IC process of Delft University of Technology is shown in Fig. 7.22. In this design, we have chosen to have off-chip capacitors. Hence, different wavelet scales can be obtained by simply using different capacitor values. From the characteristics of cardiac signals we have chosen to use the scales as defined in Table 7.2.

To check the performance of the wavelet filter, we first measure its impulse response. Ideally, an impulse is defined as a pulse with infinite amplitude and zero width. Nevertheless, since the input signal is limited by the bias current of the filter, we can not apply an impulse of infinite amplitude. Also, in order to deliver some energy to the circuit, we should give the pulse a finite length. Strictly speaking, the response to a finite length pulse is not the same as the mathematical impulse response. However, if the pulse length is short compared to the length of the dynamics in the impulse response, the difference is negligible. To measure properly the impulse response of the filter, we applied at the input a pulse signal of length 0.5 ms. The imaginary and

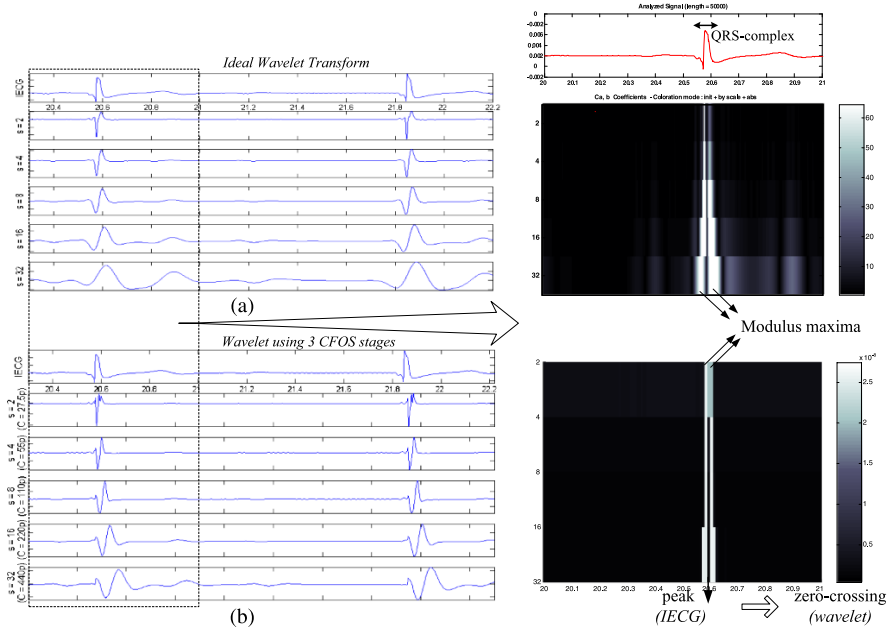


Fig. 7.20. **a** Ideal wavelet transform. **b** Wavelet using 3 CFOS stages

the real output responses of the filter with a 330 pF (6 times 55 pF) total capacitance and a bias current I_o equal to 1 nA are given in Fig. 7.23.

Figure 7.24 compares the measured impulse response from the imaginary output of the wavelet filter with the simulated and the ideal responses using 3 CFOS stages. As one can see, the responses are very similar which confirms the good performance of the filter.

As described above, the wavelet transform can be obtained by just scaling the impulse response of the filter in time. This is done by simply controlling the capacitor value C . Figure 7.25a shows a 3-scales wavelet system by scaling the off-chip capacitor values from 27.5 pF to 110 pF with a factor of 2 (dyadic scales). The resulting center frequencies, as shown in Fig. 7.25b, range from 174 Hz down to 43 Hz. The value of current I_o equals 1 nA.

The output transient response of the whole system, i.e., the filter, the absolute value and the comparator circuits, for a pulse input signal is given in Fig. 7.26. The circuit operates from a 2-V supply voltage and dissipates in total 110 nW per scale.

As stated before, wavelets allow analysis of the ECG signal focusing on the signal at various levels of detail. Analyzing the structure of the electrogram over multiple scales allows discrimination of electrogram features pertaining over all scales from those only seen at fine or coarse scales. As one can see in Fig. 7.27, at very fine scales (smaller values of scale a), details of the elec-

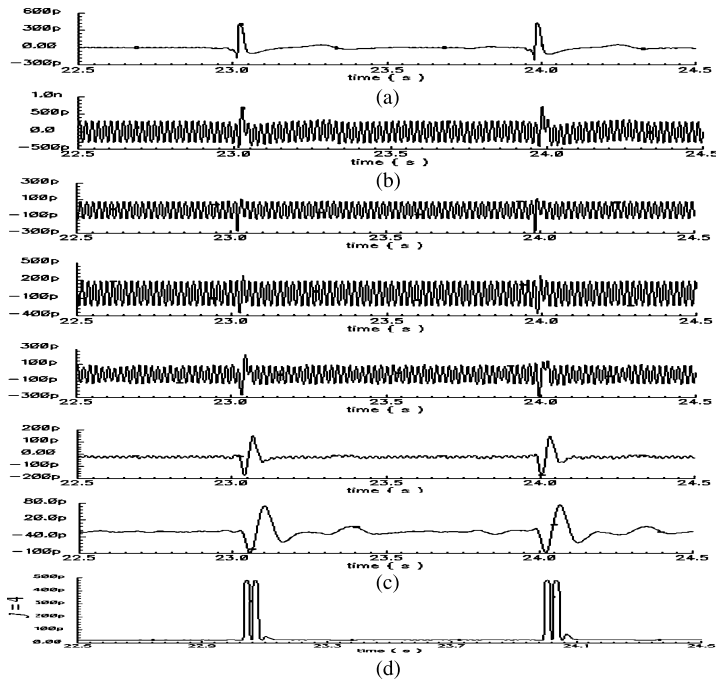


Fig. 7.21. **a** Ventricular signal. **b** Ventricular signal with 50 Hz interference. **c** Output of the wavelet transform at five subsequent scales. **d** QRS complex modulus maxima detection for $j = 4$

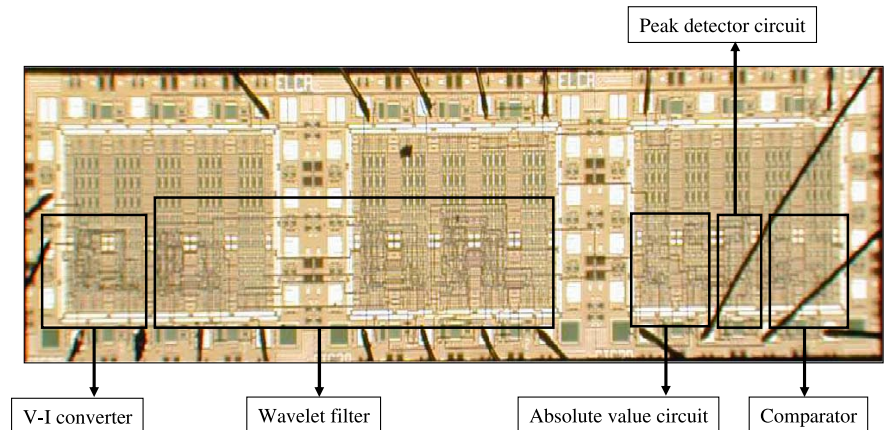


Fig. 7.22. Chip microphotograph of the QRS-complex wavelet detection

rogram, i.e. the QRS-complex, are revealed. At coarse scales (larger values of the scale factor a), the overall structure of the electrogram can be studied

Table 7.2. Frequency response and capacitance value of the wavelet system at dyadic scales

| Scale a | Capac. C (pF) | Center freq. (Hz) |
|-----------|-----------------|-------------------|
| 2^1 | 27.5 | 174 |
| 2^2 | 55 | 87 |
| 2^3 | 110 | 43.5 |
| 2^4 | 220 | 21.7 |
| 2^5 | 440 | 11 |



Fig. 7.23. Measured imaginary and real impulse responses

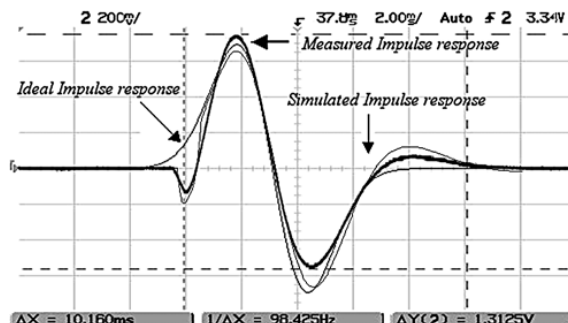


Fig. 7.24. Comparison of the measured imaginary impulse response with the simulated and the ideal impulse responses using 3 CFOS stages

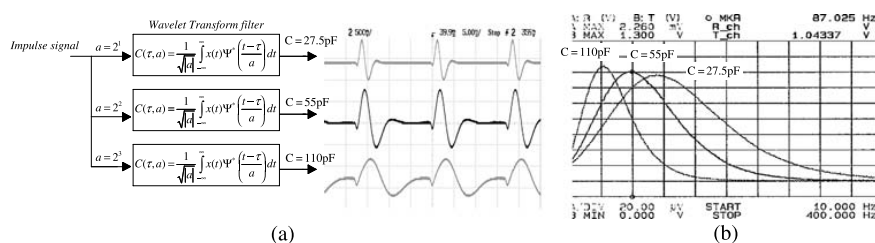


Fig. 7.25. Measured impulse (a) and frequency (b) response for 3 scales

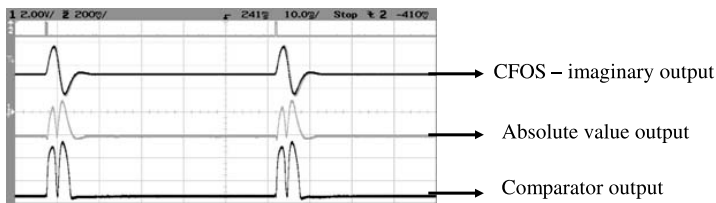


Fig. 7.26. Measured output transient of the filter, the absolute value and the comparator circuits, respectively

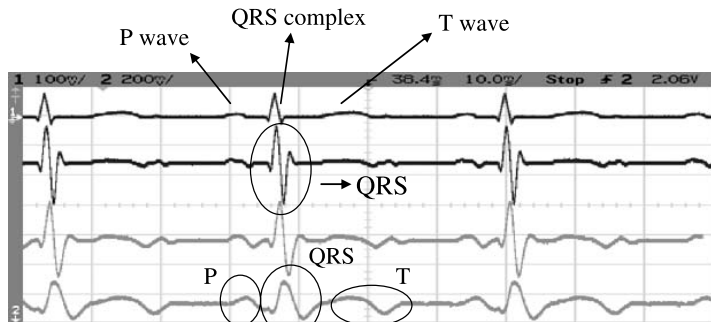


Fig. 7.27. Measured output transient of the filter with an ECG input signal

while overlooking the details. Note that by this global view, the P-wave, the QRS-complex and the T-wave can be detected.

One important application of wavelet transforms is for in-band noise removal or denoising. The out of band noise can be removed by applying a linear time-invariant filtering approach (Fourier analysis). However, it cannot be removed when it overlaps the signal spectrum. Being a multiscale analysis technique, the wavelet transform offers the possibility of selective noise filtering and reliable parameter estimation. Denoising is based on correlation factor (amplitude) discrimination. This feature can be used to distinguish cardiac signal points from noise and interference, regardless of the frequency content of the noise. Figure 7.28 shows a typical ventricular signal with additive white Gaussian noise (a random signal with a flat power spectral density). One can see in Fig. 7.28 that the wavelet can effectively remove the in-band and out-of-band noise present in the signal and the modulus maxima of the QRS-complex are identified.

The measured performance of the QRS complex detection wavelet system are summarized in Table 7.3.

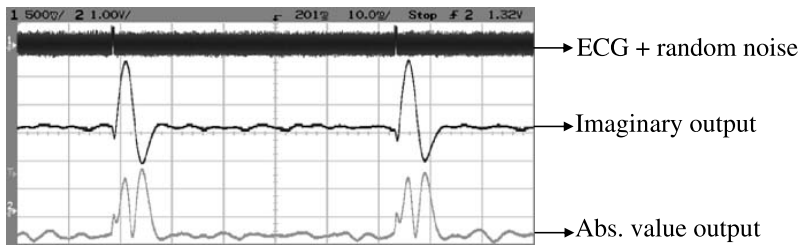


Fig. 7.28. Measured output transient of the filter for an ECG input signal with additive random noise

Table 7.3. Measured performance of the QRS complex detection complex wavelet system

| Technology | Bipolar DIMES SIC3A |
|---|---------------------|
| Supply voltage | 2.0 V |
| Total bias current (per scale) | 55 nA |
| CFOS bias current (per scale) | 35 nA |
| Power consumption | 110 nW |
| Eq. rms noise voltage @ input | 130 μ V |
| Dynamic range (1-dB compression point) | 41 dB |

7.3 Wavelet filter designs

7.3.1 Gaussian filters

In many biomedical research applications, the first-order derivative of the Gaussian function, is a favorite mother wavelet [10], which is given by

$$\Psi(t) = -2 \cdot t \cdot e^{-t^2} \quad (7.15)$$

There are two reasons for the use of the Gaussian wavelet. The main reason is that the product of its time resolution and its frequency resolution takes the theoretical minimum value of 1/2. Consequently, a wavelet transform with the Gaussian wavelet gives the most accurate estimation of frequency components localized in time. The second reason can be seen from detection theory. A particular waveform in a signal with additive Gaussian white noise will be detected optimally if the impulse response of the filter is the time-reverse of that waveform. Applying this to the case of ECG analysis, we denote some similarity between the contents of the ECG, particularly the QRS complex, and the Gaussian wavelet. Therefore the first-order derivative of the Gaussian function is a good approximation to the ‘matched’ filter.

Optimized Padé implementation using DTL circuits [11]

The first step of the implementation of a gaus1 wavelet filter is the approximation of the ideal Gaussian wavelet by using the Padé approach. On the basis of the mean-square error shown in Fig. 4.13a, one can see that the [3/5] Padé approximation is a suitable candidate for implementation. It is almost symmetrical, it has almost no overshoot and its time–frequency resolution product is only 5% above the Heisenberg limit of 1/2, while its order, 5, is reasonable. The corresponding transfer function is given by

$$H_{[3/5]}(s) = \frac{5.75s^3 - 18.3s^2 + 92.4s}{s^5 + 8.33s^4 + 33s^3 + 74.8s^2 + 94.5s + 52.3} \quad (7.16)$$

Second, the filter's state-space description is optimized with respect to dynamic range, using the method presented in Section 5.2.1. The fully optimized state-space description for the filter described by Eq. 7.16 is defined as

$$A = \begin{bmatrix} -0.176 & 1.36 & 0.309 & 0.192 & 0.0792 \\ -1.80 & -0.283 & -0.194 & -0.547 & -0.122 \\ -0.734 & -0.346 & -0.257 & -1.34 & -0.201 \\ 0.912 & 1.95 & 2.67 & -1.73 & -1.38 \\ -2.11 & -2.46 & -2.26 & 7.77 & -5.88 \end{bmatrix}, \quad C^T = \begin{bmatrix} 0.121 \\ -0.115 \\ -0.0615 \\ -0.08 \\ -0.026 \end{bmatrix}$$

$$B = \begin{bmatrix} 0.593 \\ 0.753 \\ 0.717 \\ -1.86 \\ 3.43 \end{bmatrix}, \quad (7.17)$$

The normalized capacitance distribution becomes

$$(C_1, \dots, C_5) = (0.342 \ 0.304 \ 0.168 \ 0.146 \ 0.039) \quad (7.18)$$

Compared to a straightforward implementation, viz., a controllable canonical form, the dynamic range of the optimized state-space description has increased by approximately 20 dB.

Next, we will design the circuit implementing of our wavelet filter, based on a multiple-input log-domain integrator. The multiple-input log-domain integrator is shown in Fig. 7.29. The operation of the circuit is as follows. A positive voltage across the base–emitter junction of Q1 causes a collector current, which discharges the capacitance through the collector–base connection. A positive voltage across the base–emitter junction of Q2 causes a collector current, which charges the capacitance via the current mirror on top. The net current flowing into the capacitance is the difference of collector currents from the positive and negative input side. V_{ip} and V_{in} are the positive and negative input voltages, respectively. In addition, we implement the state space coefficients (a_{ij} or b_i), by placing constant voltage sources, V_{mp} and V_{mn} ,

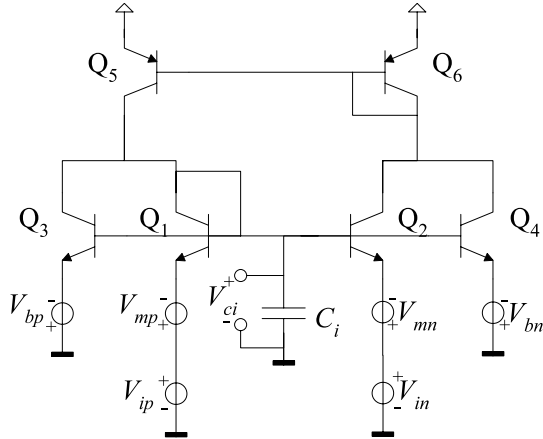


Fig. 7.29. Log-domain integrator

in series with each base-emitter junction. Finally, we propose to subtract a constant number α of each $\exp(\cdot)$ term in order to perform the integration operation for both positive and negative input variables. This is implemented by transistors Q3 and Q4 and the constant voltage sources V_{bp} and V_{bn} , respectively. An alternative view on subtracting a constant number is defining the operating point. This is basically the same as biasing. However, in contrast to the regular design of linear circuits, we cannot separate the design of the signal processing function and the design of the bias function. Since the circuit is nonlinear and intended to be used in the large signal range, the superposition principle is not valid. Therefore, the biasing function is an integral part of the signal processing design. Thus, the current flowing into the capacitance is defined as

$$\begin{aligned} I_{cap} = C \dot{V}_{cap} &= I_s e^{\frac{V_{cap} + V_{mp} - V_{ip}}{V_T}} - I_s e^{\frac{V_{cap} + V_{mn} - V_{in}}{V_T}} \\ &\quad + I_s e^{\frac{V_{cap} + V_{bp}}{V_T}} - I_s e^{\frac{V_{cap} + V_{bn}}{V_T}} \end{aligned} \quad (7.19)$$

with

$$V_{mp,mn} = V_T \ln \left(\frac{(a_{ij}, b_i) \cdot C_i V_T}{I_s} \right) \quad (7.20)$$

$$V_{bp,bn} = \alpha V_{mp,mn} \quad (7.21)$$

where a_{ij} , b_i are the multiplication coefficients of the matrix A or matrix B in the state-space description. V_{mp} and V_{mn} are the positive and negative multiplication voltages respectively. V_{bp} and V_{bn} are the positive and negative voltages that implement the biasing function. I_s is the saturation current.

In order to maintain overall linearity of a log-domain system, a LOG stage must be added to the input, while an EXP stage is required at the output. The

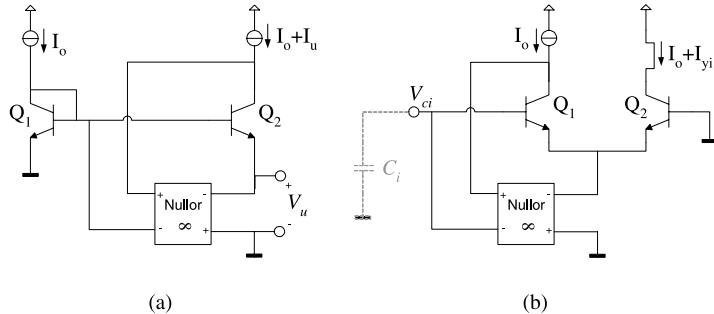


Fig. 7.30. **a** LOG stage. **b** EXP stage

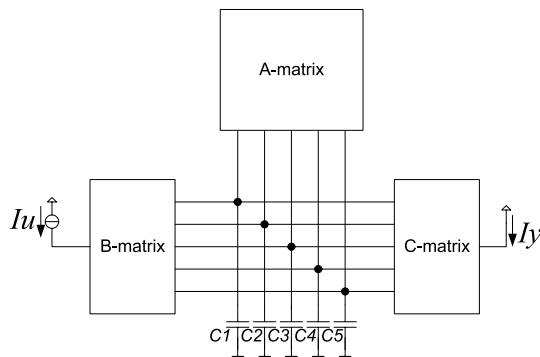


Fig. 7.31. Block diagram of the complete system

LOG and EXP stages are shown in Fig. 7.30. By adding a summation stage at the output, we can obtain the expression for output current. The nullors can be implemented by a cascade of a common-collector and a common-emitter stage, or, in case of a BiCMOS process, a single common-source stage.

The block schematic of the total filter is drawn in Fig. 7.31. The *A*-matrix, *B*-matrix and *C*-matrix each have five connections to the capacitances.

The state space representation for a fifth-order system can be written as

$$\begin{aligned} \dot{x}_i &= \sum_{j=1}^5 \tau^{-1} a_{ij} x_j + b_i u \\ y &= \sum_{i=1}^5 c_i x_i \end{aligned} \quad (7.22)$$

where $\tau = \frac{CV_T}{I_o}$ represents the time constant of the filter. We define the five states x_1-x_5 with an exponential relation to the capacitance voltages $V_{c1}-V_{c5}$. The input signal u and output signal y are linearly related to the currents I_u

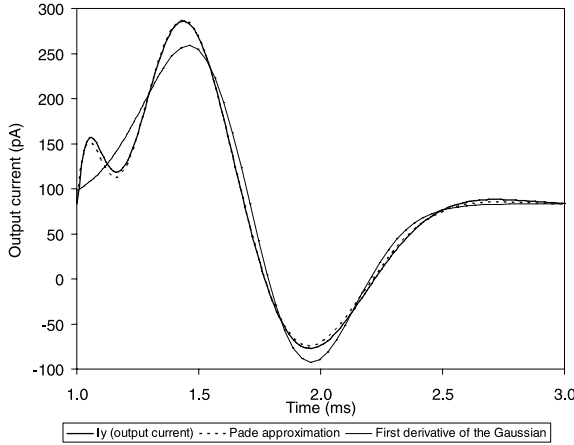


Fig. 7.32. Simulated impulse response of the filter

and I_y . So the correspondence relation is defined as

$$\begin{aligned}
 I_{Ci} &= - \sum_{j:a_{ij}>0} |a_{ij}| \tau^{-1} C_i V_T e^{\frac{V_{Ci}-V_{Cj}}{V_T}} + \sum_{j:a_{ij}<0} |a_{ij}| \tau^{-1} C_i V_T e^{\frac{V_{Ci}-V_{Cj}}{V_T}} \\
 &\quad + \sum_j a_{ij} \tau^{-1} C_i V_T e^{\frac{V_{Ci}}{V_T}} - b_i I_o I_u e^{\frac{V_{Ci}}{V_T}} \\
 &= - \sum_{j:a_{ij}>0} |a_{ij}| I_o e^{\frac{V_{Ci}-V_{Cj}}{V_T}} + \sum_{j:a_{ij}<0} |a_{ij}| I_o e^{\frac{V_{Ci}-V_{Cj}}{V_T}} \\
 &\quad + \sum_j a_{ij} I_o e^{\frac{V_{Ci}}{V_T}} - b_i I_o I_u e^{\frac{V_{Ci}}{V_T}}
 \end{aligned} \tag{7.23}$$

and

$$I_y = \sum_{i=1}^5 c_i (I_o e^{\frac{V_{Ci}}{V_T}} - I_o) \tag{7.24}$$

We see that the terms of the capacitance current have the same form as in Eq. 7.19 and thus the state space matrices can be implemented by interconnecting multiple-input log-domain integrator stages.

To check the circuit performance, the system has been simulated using models of our in-house bipolar semi-custom IC process, SIC3A. The circuit has been designed to operate from a 2-V supply voltage. First, we have set $\tau = 1$ ms, which gives $I_o = 1$ nA and $C = 40$ pF. The impulse response of the circuit was simulated by applying an input pulse waveform of length 0.1 μ s and of height 1 nA. The acquired output signal is plotted in Fig. 7.32. The output current presents an offset of approximately 80 pA. For comparison, we have added the plots of the mathematical impulse response of the original state space filter and the delayed first derivative of the Gaussian.

As we can see in Fig. 7.32, the simulated impulse response differs only slightly from the approximated response, which was acquired directly from the Padé approximation. We conclude that the coefficients have been implemented successfully.

***L₂* approximation employing CMOS triode transconductors**

The filter design that follows is based on an orthonormal ladder structure and employs the nA/V and the pA/V $\Delta-G_m$ transconductors described in Sections 6.1.1 and 6.1.2, respectively.

The wavelet base approximation using the proposed L_2 approach is given in Fig. 7.33, where the first derivative of a Gaussian wavelet base (gaus1) has been approximated using the corresponding 6th-order transfer function

$$H_{[4/6]}(s) = \frac{-0.16s^4 + 8.32s^3 - 6.64s^2 + 139s}{s^6 + 5.9s^5 + 30.5s^4 + 83.1s^3 + 163s^2 + 176s + 93.3} \quad (7.25)$$

The block diagram of the wavelet filter is given in Fig. 7.34, where two different transconductors have been employed as basic building blocks, being the nA/V and the pA/V $\Delta-G_m$ (with $\Delta = 0.4$) transconductors. The values of G_m and the total capacitance, required to implement the transfer function in Eq. 7.25, are also shown in Fig. 7.34. Note that, maintaining the same time constant for both transconductors and using the $\Delta-G_m$ block with $\Delta = 0.4$, we are able to reduce the corresponding G_m values, and, consequently reduce the total capacitance by a factor of 0.6.

The wavelet G_m -C filters have been simulated using AMS's 0.35 μm CMOS transistors model. In order to implement the different coefficients of the state-space representation, we can vary the width of transistors M_{1A} and M_{1B} , as mentioned previously. Figure 7.35 shows the simulated impulse response of the wavelet filter for $V_{TUNE} = 20$ mV. An excellent approximation of the obtained

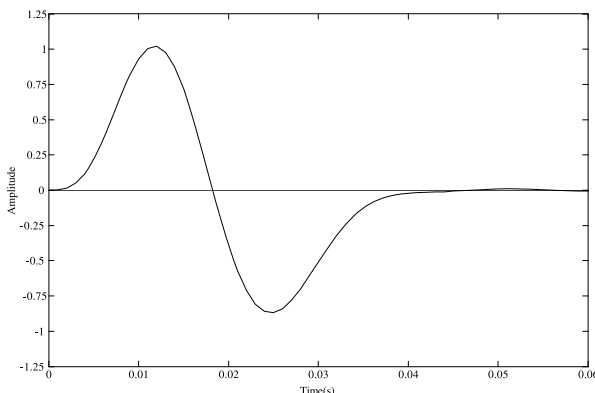


Fig. 7.33. 6th-order L_2 approximation of the gaus1

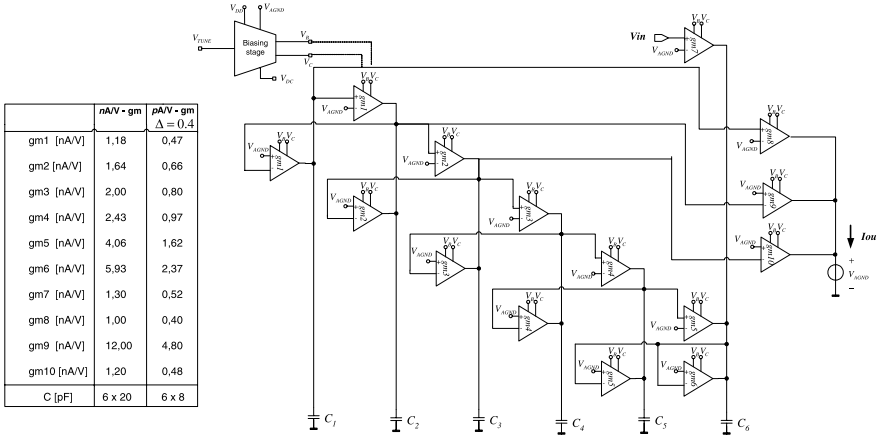


Fig. 7.34. Block diagram of the wavelet filter

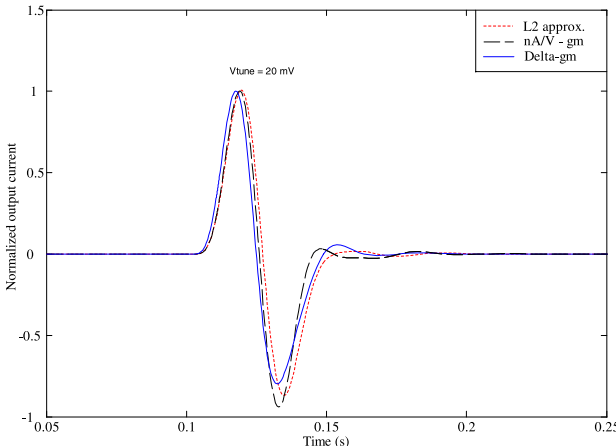


Fig. 7.35. Simulated and L_2 -approximated impulse response

first Gaussian wavelet (gaus1) to the L_2 -approximated function confirms the performance of the G_m -C filter. The total filter's current consumptions, using the nA/V and the pA/V Δ - G_m transconductors, is 56 nA and 114 nA, respectively, operating from a 1.5-V supply voltage. The performance of both filters is summarized in Table 7.4.

Finally, to implement a wavelet transform, we need to be able to scale and shift in time (and, consequently in frequency) the gaus1 function. By changing the values of the V_{TUNE} accordingly we implement different scales, while preserving the impulse response waveform, as one can see in Fig. 7.36a. Figure 7.36b illustrates 4 dyadic scales with center frequencies ranging from 14 Hz to 120 Hz for V_{TUNE} varying from 10 mV to 80 mV, respectively.

Table 7.4. Performance of the nA/V and pA/V G_m -C wavelet filters

| | nA/V- G_m | pA/V- G_m ($\Delta = 0.4$) |
|--------------------------------------|-------------|--------------------------------|
| Technology | | 0.35 μm CMOS |
| Minimum G_m (nA/V) | 1 | 0.4 |
| G_m variation (%) (Monte Carlo) | 2.7 | 2.9 |
| Total capacitance (pF) | 120 | 48 |
| V_{TUNE} (mV) | 20 | 20 |
| Filter power (nW) | 51 | 114 |
| Supply voltage (V) | 1.5 | 1.5 |
| Input RMS noise (μV) | 119 | 460 |
| THD (dB) | -53 | -51 |

7.3.2 Complex wavelet filter implementation

Next, we present an analog implementation of the complex Gabor wavelet transform using the Padé approximation. The complex wavelet filter design is based on the combination of the real and the imaginary state-space descriptions that implement the respective transfer functions. In other words, a complex filter is implemented by an ordinary state-space structure for the real part and just an extra C matrix for the imaginary part [12].

The Gabor wavelet is obtained from a complex Gaussian function (complex exponential, windowed by a Gaussian function) as basic function, as described by

$$\psi(t) = C \cdot e^{-j\omega t} e^{-t^2} = C \cos(\omega t) e^{-t^2} - jC \sin(\omega t) e^{-t^2} \quad (7.26)$$

where $e^{-j\omega t} e^{-t^2}$ is the complex Gaussian function and C is a normalizing constant. From the Gabor wavelet, one can derive some complex wavelet families, e.g., the complex Gaussian and the complex Morlet. The complex Morlet wavelet is obtained by simply applying $\omega = \pi \sqrt{\frac{2}{\ln 2}} \simeq 5.3364$ [13] in Eq. 7.26.

The complex Gaussian wavelet family is defined from the derivatives of the Gabor wavelet [14] and is given by

$$\psi_n(t) = C_n \cdot \frac{d^n}{dt^n} (e^{-j\omega t} e^{-t^2}) \quad (7.27)$$

where n denotes the order, $\frac{d}{dt}$ is the symbolic derivative and C is a normalizing constant, which depends of n .

In order to implement the complex Gabor wavelet filter, we first apply a [2/5] Padé approximation (i.e. $m = 2$ and $n = 5$, which yields an approximation of order $k = 7$ of the Taylor series expansion) to obtain the Gaussian envelope. The transfer function resulting from this approximation is given by

$$H_{gaus}(s) = \frac{5.7s^2 - 18.2s + 92.416}{s^5 + 8.3s^4 + 33s^3 + 74.8s^2 + 94.5s + 52.3} \quad (7.28)$$

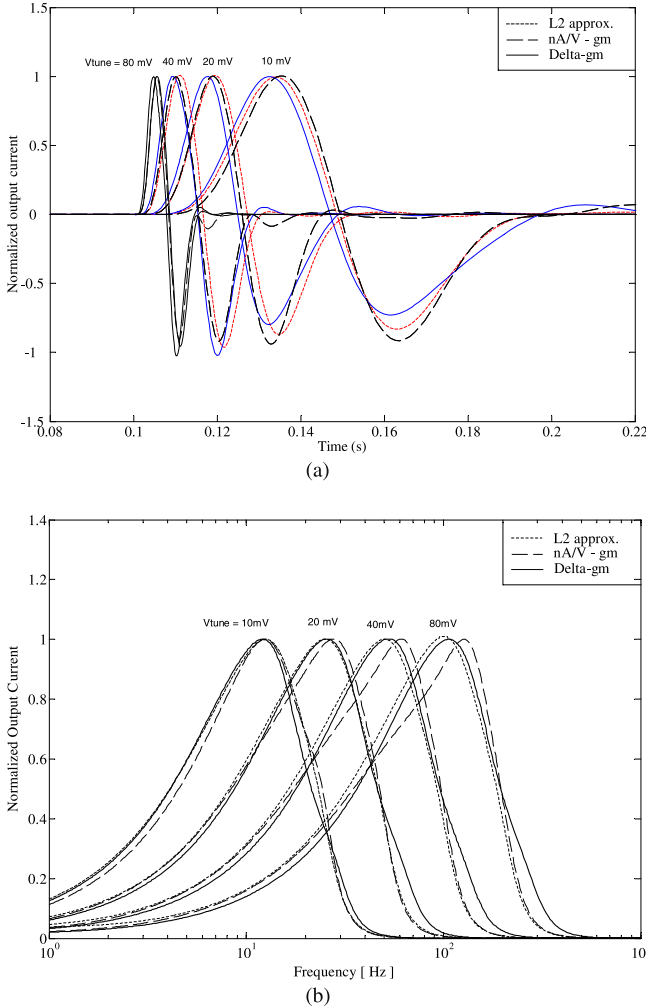


Fig. 7.36. Wavelet filter scaling by changing V_{TUNE} . **a** Impulse response.
b Frequency response

To obtain the transfer function of the real and the imaginary parts of the Gabor function of Eq. 7.26, one can easily apply

$$H_{Gabor}(s) = \frac{s}{s^2 + \omega^2} * H_{gaus}(s) - j \frac{\omega}{s^2 + \omega^2} * H_{gaus}(s) \quad (7.29)$$

where the asterisk $*$ is the symbol for convolution and $\frac{s}{s^2 + \omega^2}$ and $\frac{\omega}{s^2 + \omega^2}$ are the Laplace transforms of $\cos(\omega t)$ and $\sin(\omega t)$, respectively. Notice that both transfer functions are related by

$$H_{\text{Real}}(s) = -\frac{s}{\omega} * H_{\text{Imag}}(s) \quad (7.30)$$

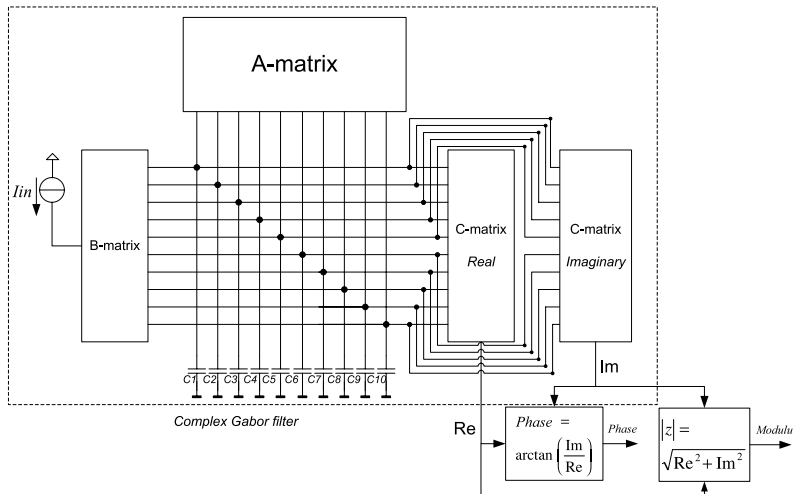


Fig. 7.37. Block diagram of the complex wavelet system

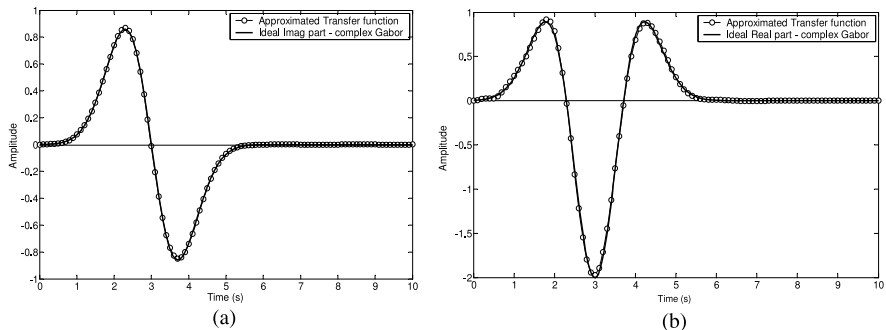


Fig. 7.38. Complex Gabor impulse response approximation. **a** Imaginary output. **b** Real output

From Eq. 7.30, one can verify that the poles of the real and the imaginary transfer function are the same, only differing in the zeros. Therefore, we can implement both transfer functions by changing only the C -matrix of the state-space representation, as shown in Fig. 7.37.

Using the procedure described in Eq. 7.29, yields a tenth-order transfer functions with 7 zeros. Its corresponding impulse responses are given in Fig. 7.38.

Circuit design

The filter design that follows is also based on an orthonormal ladder structure. The bipolar multiple-input low-power log-domain integrator presented in Sec-

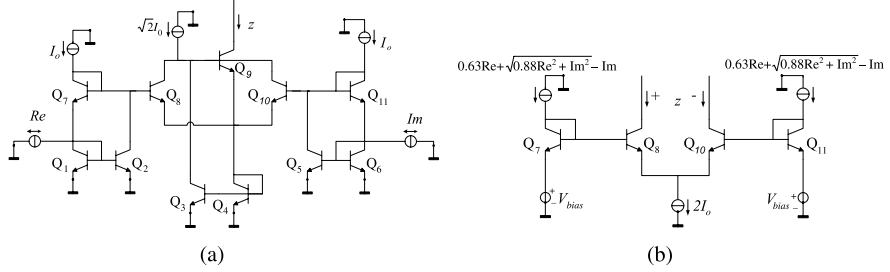


Fig. 7.39. **a** Modulus (vector magnitude) circuit [3]. **b** Divider circuit for the arctangent stage [15]

tion 6.3.1 will be used as the basic building block for the implementation of the tenth order state space equations of the Gabor wavelet filter.

The static translinear principle can be applied to the implementation of the required non-linear transfer functions of the modulus and arctangent stages. First, the required modulus function $|z| = \sqrt{Re^2 + Im^2}$ is realized with the circuit in Fig. 7.39a [3]. The translinear loops in the circuit consist of transistors Q₁, Q₇, Q₈ and Q₄ and Q₆, Q₁₁, Q₁₀ and Q₄, implementing

$$\begin{aligned} 2(I_o - Re)(I_o + Re) &= (\sqrt{2}I_o - z)(\sqrt{2}I_o + z + p) \\ 2(I_o - Im)(I_o + Im) &= (\sqrt{2}I_o - z)(\sqrt{2}I_o + z - p) \end{aligned} \quad (7.31)$$

where I_o is the bias current and p is an intermediate parameter equal to $\frac{2Re^2 - z^2}{z - \sqrt{2}I_o}$. Notice that both variables, Re and Im, are bipolar quantities.

From the complex waveforms shown in Fig. 7.38, we can now obtain the phase information by simply applying the arctangent to the ratio between the imaginary and the real outputs. This operation can be approximated using the translinear principle as [4]

$$\text{Phase} = \frac{\text{Im}}{0.63 \text{Re} + \sqrt{0.88 \text{Re}^2 + \text{Im}^2}} \simeq \frac{2}{\pi} \arctan\left(\frac{\text{Im}}{\text{Re}}\right) \quad (7.32)$$

where the square root term is provided by the modulus circuit of the previous section. The division operation can easily be implemented using the factorization $z = \frac{x}{y} \Rightarrow \frac{I_o + z}{I_o - z} = \frac{y + x}{y - x}$ [3] and its schematic is given in Fig. 7.39b [15].

We have simulated the filter, the modulus stage and the phase stage using models of IBM's 0.18 μm BiCMOS IC technology. The filter has been designed to operate from a 1.2 V supply and a 100 pF total capacitance. Figure 7.40 shows the impulse response of the real and imaginary outputs of the wavelet filter. An excellent approximation of the obtained complex Gabor wavelet to the ideal Gabor function confirms the performance of the filter.

Finally, Fig. 7.41 shows the modulus stage and phase stage outputs, which are close to the ideal cases for the complex Gabor wavelet in Fig. 3.8.

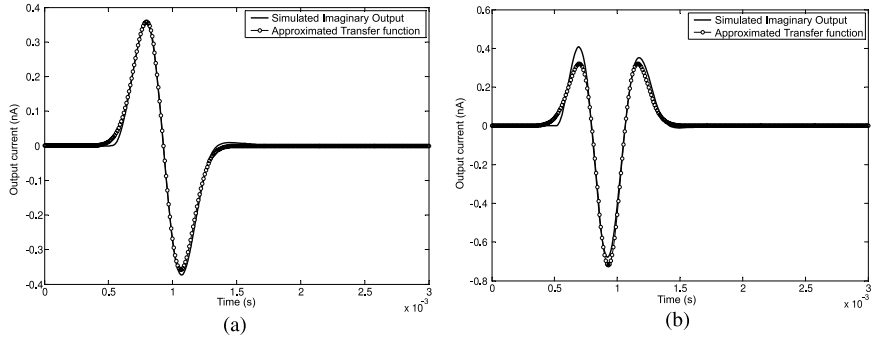


Fig. 7.40. Simulated impulse responses of the complex Gabor wavelet filter. **a** Imaginary output. **b** Real output

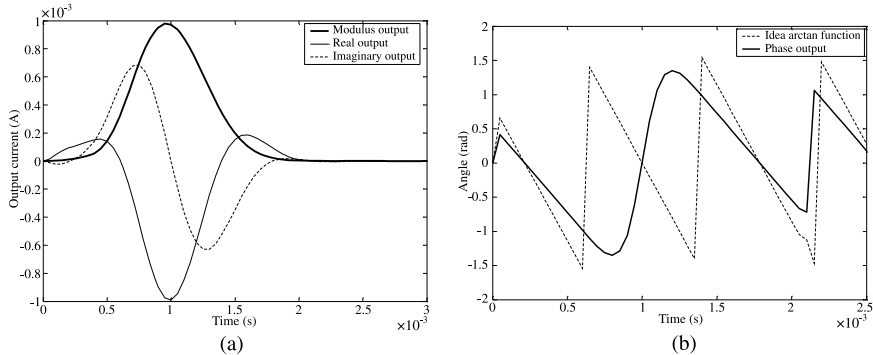


Fig. 7.41. Simulated complex Gabor wavelet filter. Modulus (a) and phase (b) responses

7.4 Morlet wavelet filter

The discussion in this section will deal with the design and implementation of a Morlet wavelet filter [16].

The Morlet wavelet base is obtained from a Gaussian envelope multiplied by a cosine function (cosine windowed by a Gaussian function) [14]. Its time-shifted version (by $t_0 = 3$) is described by

$$\psi(t) = \cos[5\sqrt{2}(t - 3)]e^{-(t-3)^2} \quad (7.33)$$

In order to control the frequency range of the wavelet system and the respective scales, one can add a time constant term τ into Eq. 7.33, resulting in

$$f(t) = \cos\left[\frac{5\sqrt{2}}{\tau}(t - 3 \cdot \tau)\right]e^{-(\frac{t-3 \cdot \tau}{\tau})^2} \quad (7.34)$$

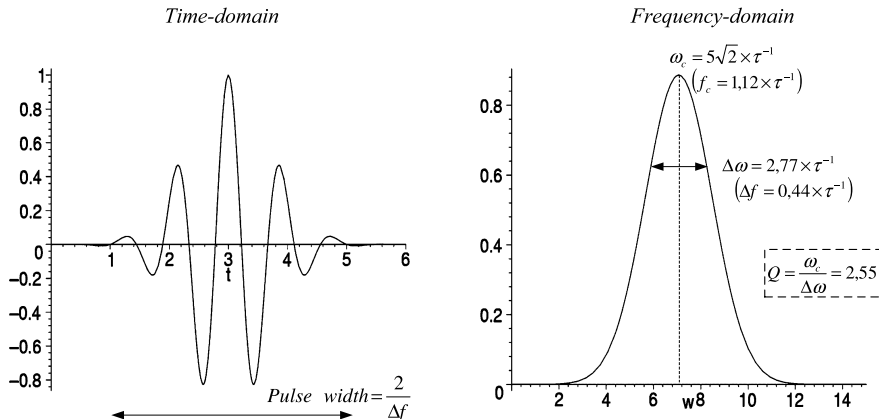


Fig. 7.42. Ideal Morlet function. Time and frequency response

and the corresponding Fourier transform is giving by

$$F(\omega) = \frac{\sqrt{\pi}}{2} [e^{-\frac{1}{4}(\frac{\omega - 5\sqrt{2}\tau^{-1}}{\tau^{-1}})^2} + e^{-\frac{1}{4}(\frac{\omega + 5\sqrt{2}\tau^{-1}}{\tau^{-1}})^2}] \quad (7.35)$$

The time and frequency responses of the Morlet wavelet base are given in Fig. 7.42. Note that by changing τ , the Q -factor of the filter remains constant and in this case equals 2.55.

As described before, the Padé approximation has some convergence problems when one tries to approximate a function with many oscillations, such as the Morlet wavelet. Thus, in Section 4.3 we presented a generalized procedure for implementing analog filters of various types of wavelet bases. The results obtained from the use of this method have been illustrated in Fig. 4.11 and in Table 4.4.

The flow chart in Fig. 7.43 summarizes the implementation of this procedure to obtain the tenth-order Morlet wavelet filter transfer function.

From the discussion in Chapter 5, we opt again for an orthonormal state space representation. The A , B and C matrices of this structure for the defined transfer function are given by

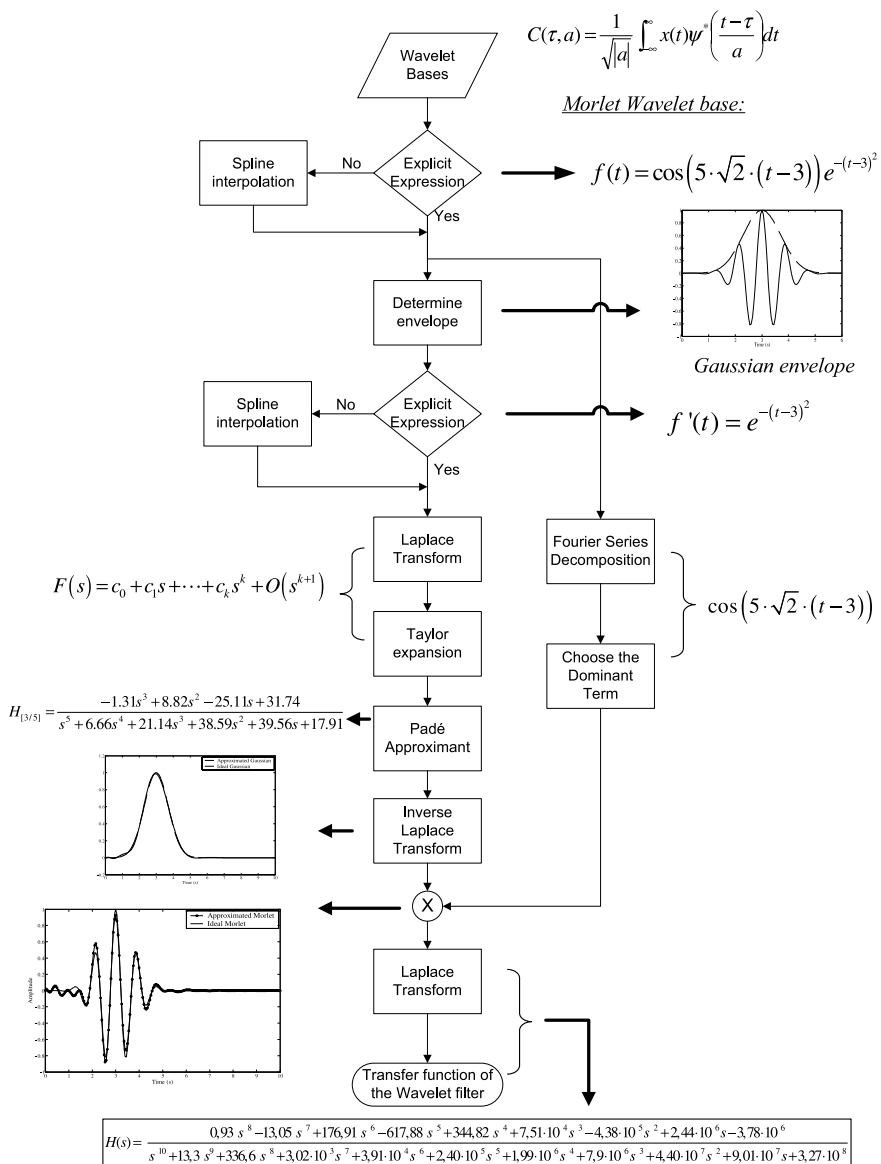


Fig. 7.43. Flowchart of the wavelet base approximation

$$B = \begin{bmatrix} 0 \\ 0 \\ 0 \\ 0 \\ 0 \\ 0 \\ 0 \\ 0 \\ 0 \\ 0 \\ 2.05 \end{bmatrix}, \quad (7.36)$$

$$C = [0.75 \ -1.34 \ 0.75 \ 0.68 \ -0.57 \ 0.44 \ -0.002 \ -0.10 \ 0.04 \ 0]$$

In this case, the objective functional becomes $F_{DR} = 147.90$, which is not so far from the optimum case ($F_{DR} = 96.98$), which is the absolute minimum value of the objective functional associated with this transfer function. The Dynamic Range has decreased by only 1.83 dB. Finally, the normalized capacitance distribution is given by $(C_1, \dots, C_{10}) = (0.142, 0.162, 0.110, 0.117, 0.086, 0.091, 0.073, 0.080, 0.073, 0.061)$.

7.4.1 Circuit design

By applying a simple mapping to the linear state-space Eq. 7.36, we can obtain the corresponding log-domain circuit realization which employs the log-domain integrator cell. Note that the implemented filter is a tenth-order filter.

The block diagram of the log-domain filter implementation of Eq. 7.36 is illustrated in Fig. 7.44, using the log-domain integrator cell described in Section 6.3.1 [17]. Note that each column of the filter structure corresponds to a row in the state-space formulation. The parameter A_{ij} is implemented by the corresponding log-domain integrator with bias current $I_{A_{ij}}$, defined by

$$I_{A_{ij}} = A_{ij} \cdot \frac{2\pi\tau^{-1}}{2Q} C_i V_T \quad (7.37)$$

where τ^{-1} and Q are the inverse of the time constant and the quality factor mentioned in Section 3.6, respectively, and C_i represents the i th capacitance of the filter. The input section, as governed by the state-space vector B , can be defined as the input LOG operator and is realized by the first row from the top of Fig. 7.44. Current I_{B_i} is related to parameter B_i by

$$I_{B_i} = B_i \cdot \frac{2\pi\tau^{-1}}{2Q} C_i V_T \quad (7.38)$$

In the orthonormal case, only one non-zero parameter of the B vector is present (B_{10}). Consequently, $I_{B_i} = I_B$. Finally, in order to restore the overall system linearity, one should realize the weighted summation state with the

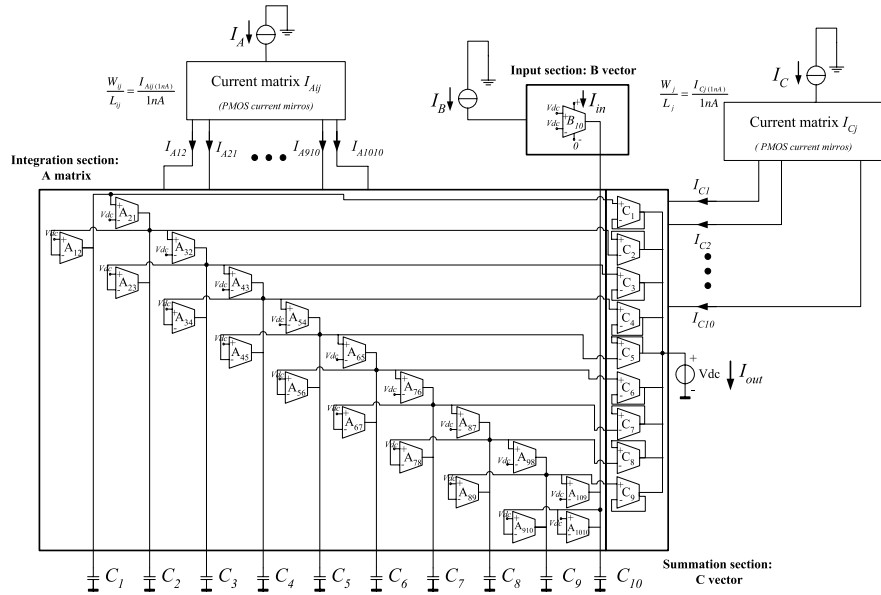


Fig. 7.44. Complete state-space filter structure

corresponding EXP operators. Bias current vector I_{C_j} , which is controlled by vector C , is defined as

$$I_{C_j} = C_j \cdot I_B \quad (7.39)$$

Normalizing current I_A in Fig. 7.44, which will control the overall time constant of the filter, is implemented by

$$I_A = \frac{I_{A_{ij}}}{\frac{W_{A_{ij}}}{L_{A_{ij}}}} \quad (7.40)$$

with

$$\frac{W_{A_{ij}}}{L_{A_{ij}}} = \frac{I_{A_{ij}(1\text{nA})}}{1\text{nA}} \quad (7.41)$$

where $\frac{W_{A_{ij}}}{L_{A_{ij}}}$ are the aspect ratios of the PMOS current mirrors and were defined for I_A equal to 1 nA. The current I_C is obtained in a similar way, given by

$$I_C = \frac{I_{C_j}}{\frac{W_{C_j}}{L_{C_j}}} \quad (7.42)$$

for $\frac{W_{C_j}}{L_{C_j}}$ being the aspect ratios of the transistors in current matrix I_{C_j} and defined by

$$\frac{W_{C_j}}{L_{C_j}} = \frac{I_{C_j(1\text{nA})}}{1\text{nA}} \quad (7.43)$$

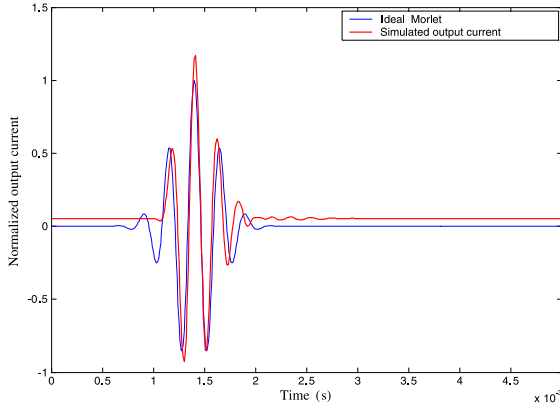


Fig. 7.45. Simulated impulse response

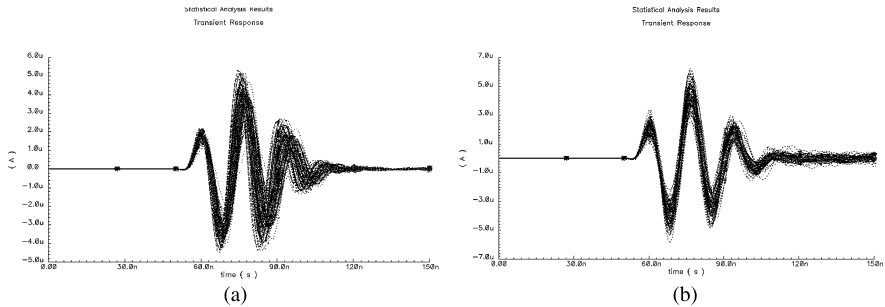


Fig. 7.46. Monte Carlo analysis of the impulse response for process variations (a), mismatch variations (b)

Figure 7.45 shows the impulse response of the wavelet filter for $I_A = I_C = 1$ nA and $I_B = 2$ nA, which corresponds to $\tau^{-1} = 5,178 \cdot 10^3$. The excellent approximation of the Morlet wavelet can be compared with the ideal Morlet function to confirm the performance of the log-domain filter. Figure 7.46 shows the Monte Carlo analysis for process and mismatch variation of the technology in use. As evident from the Monte Carlo simulation (i.e., after 100 runs), the system characteristics show insensitivity to both absolute and relative variations in process parameters. Even though the impulse response may be slightly affected, the wavelet analysis is not completely distorted.

In order to verify the performance of the whole wavelet system, one needs to scale and shift the wavelet base function. By changing the values of the bias currents accordingly, one can obtain a dyadic scale system, as illustrated in Fig. 7.47. Alternatively, one may also change the capacitance values, C_i . To implement a wavelet system, which usually consists of 5 dyadic scales, one needs to implement a filter bank (a parallel structure) with a total capacitance

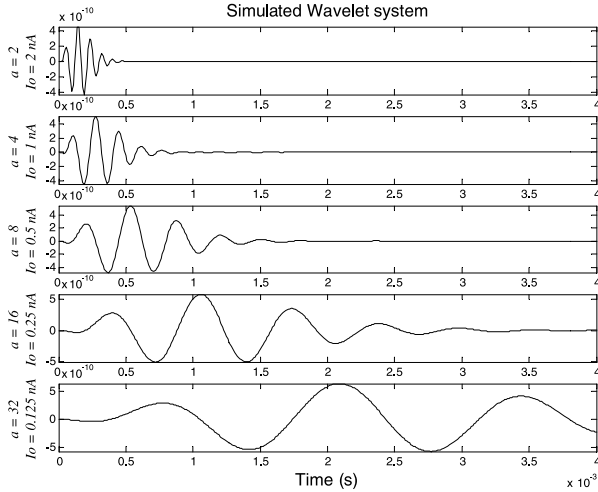


Fig. 7.47. Simulated impulse responses of a wavelet system with 5 scales. The scales are obtained by varying the current (from 0.125 nA to 2 nA) or the capacitance (from 100 pF to 6.25 pF)

of 193.75 pF (capacitance value scaled by a factor of two, i.e., 100 pF for the first scale, 50 pF for the second, 25 pF for the third, 12.5 pF for the fourth and 6.25 pF for the last scale), preserving the same bias current. This result indicates that the system shown in Fig. 7.15 is feasible.

7.4.2 Measurement results of the Morlet wavelet filter

To validate the circuit principle, we have implemented the log-domain state-space wavelet filter in IBM's 0.18 μ m BiCMOS IC process. A microphotograph of the circuit is shown in Fig. 7.48 [18].

The measurement setup is presented in Fig. 7.49. Log-domain filters process signals in the current domain. Accurate current measurements require linear transconductance and transimpedance stages at the input and at the output, respectively. These are implemented by a large resistor at the input and by a Keithley 428 nA transimpedance amplifier at the output. However, the transimpedance amplifier has a cut-off frequency up to 175 kHz, depending on the gain factor. To be able to measure beyond 100 kHz, a transimpedance stage implemented by a low noise op amp (LF 356) and a 1 k Ω shunt feedback resistor is used. The cut-off frequency of this stage is 10 MHz.

The circuit has been designed to operate from a 1.5 V supply. Figure 7.50 shows the measured impulse response of the wavelet filter and the frequency response (magnitude) for $I_A = I_C = 4.3$ nA and $I_B = 8.5$ nA, which corresponds to $\tau^{-1} = 22 \cdot 10^3$. The transient response of the Morlet wavelet filter

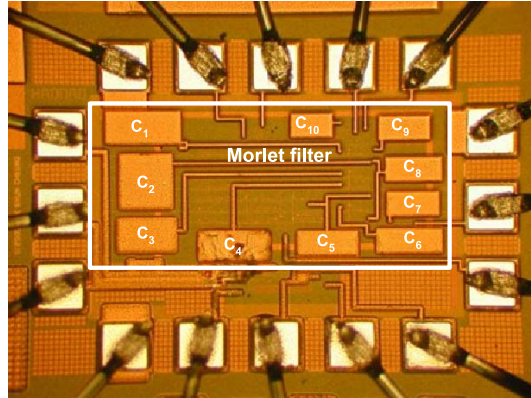


Fig. 7.48. Chip microphotograph. The die area is 0.89 mm² (0.78 mm by 1.14 mm) and the filter active area is 0.28 mm² (0.35 mm by 0.79 mm)

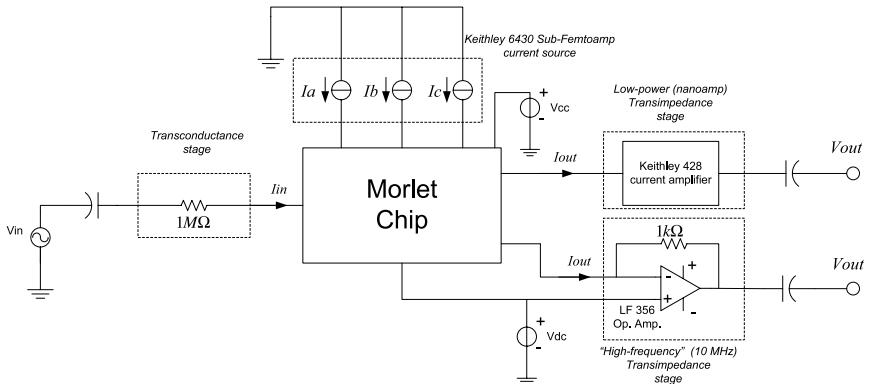


Fig. 7.49. Measurement setup

can be compared with the simulated filter response to confirm the performance of the log-domain filter.

The total filter's current consumption is 4.5 μ A with a 100 pF total capacitance. The rms output current noise is 66.97 pA, resulting in a DR at the 1-dB compression point of approximately 30 dB. The power efficiency of any bandpass continuous-time filter is a figure of merit to be able to compare various filter topologies and can be estimated by means of the power dissipation per pole, center frequency (f_c), and quality factor (Q) defined as [29]

$$\text{Power per pole and bandwidth} = \frac{P_{diss}}{n \cdot f_c \cdot Q} \quad (7.44)$$

where P_{diss} is the total power dissipation and n is the order of the filter. The power efficiency of this filter equals to 10.58 pJ.

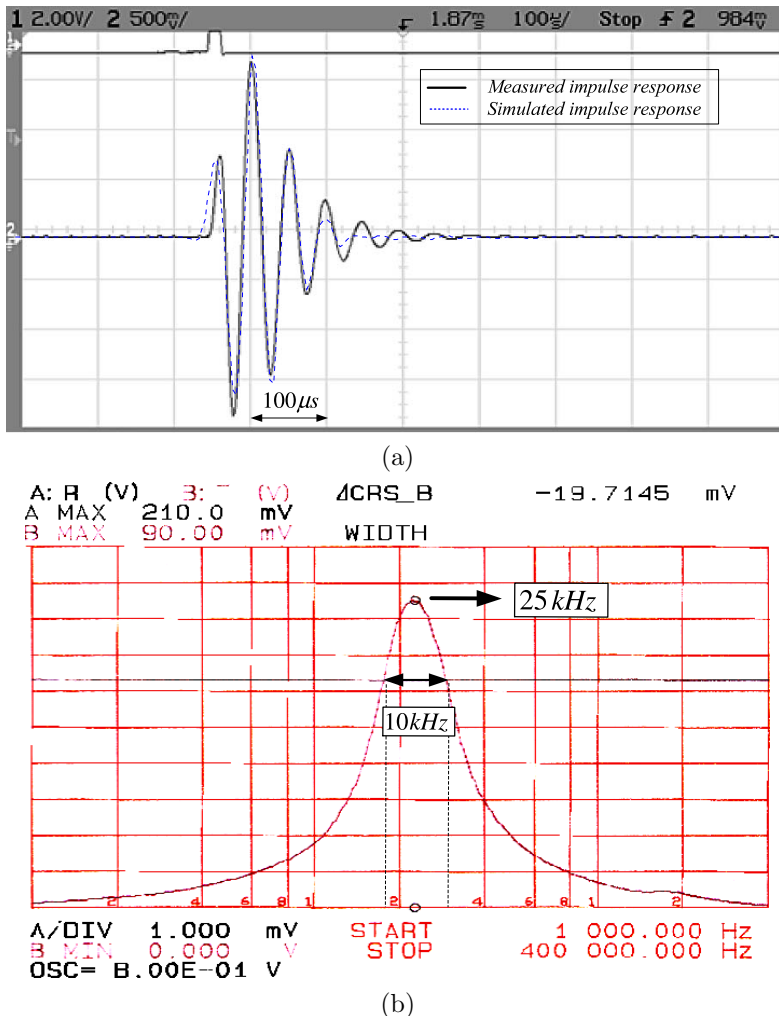


Fig. 7.50. Measurement results. **a** Measured and simulated impulse response. **b** Measured frequency response

By changing the values of the bias currents accordingly, one can obtain a dyadic scale system, as illustrated in Fig. 7.51. The current I_A has been scaled from 2 nA to 8 nA, resulting in a 3-scales wavelet system.

Finally, in order to show that the same procedure can be applied for medium frequency applications, we tuned the frequency response of the filter by varying the bias current over about three decades with center frequencies ranging from 14 kHz to 8.1 MHz, while preserving the impulse response wave-

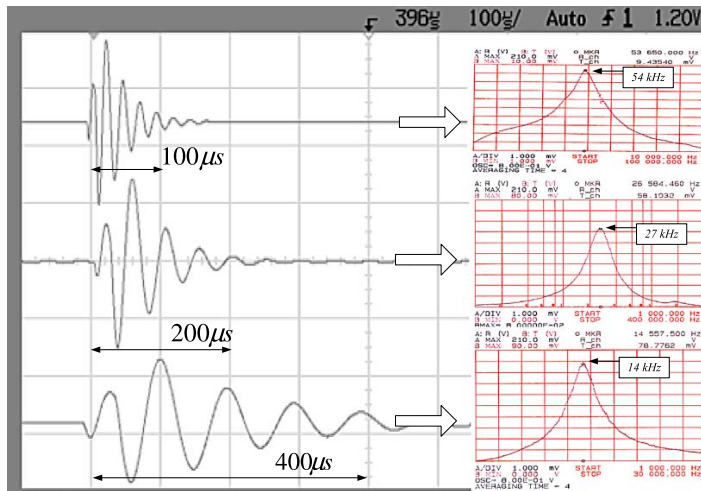


Fig. 7.51. Measured impulse and frequency responses for 3 scales

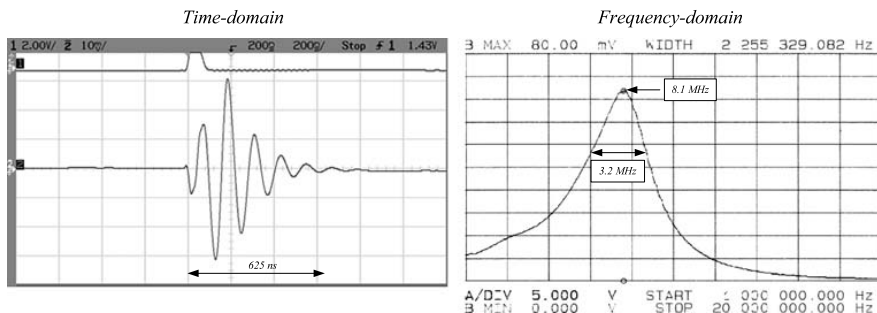


Fig. 7.52. Time and frequency responses of the Morlet filter varying the bias current I_a to $1.4 \mu\text{A}$ for high-frequency operation

form. Again, one can obtain the wavelet scales around this frequency (i.e. 8.1 MHz) by scaling the current, accordingly.

The performance of the filter is summarized in Table 7.5.

7.5 Conclusions

Several ultra low-power biomedical system and wavelet filter designs were presented in this chapter. First, a cardiac sense amplifier based on the dynamic translinear circuit technique has been proposed. It comprises a $V-I$ converter, a bandpass filter and absolute value, RMS-DC converter and comparator circuits. The obtained results in the sense amplifier demonstrate the desired

Table 7.5. Performance per scale for two different operating frequencies

| | | |
|----------------------------|---------------------------|----------------------------------|
| Technology | 0.18 μm BiCMOS | |
| Die area | 0.89 mm^2 | |
| Active area | 0.28 mm^2 | |
| Bias current | $I_o = 4.3 \text{ nA}$ | $I_o = 1.4 \text{ } \mu\text{A}$ |
| Total capacitance | 100 pF | 100 pF |
| Supply voltage | 1.5 V | 1.6 V |
| Center frequency, f_c | 25 kHz | 8.1 MHz |
| Power dissipation | 6.75 μW | 2.3 mW |
| Dynamic range (1-dB) | 30 dB | 30 dB |
| Noise current (rms) | 66.97 pA | 481.3 nA |
| Supply voltage range | 1.2 V–1.8 V | 1.5 V–2.1 V |
| Power dissipation per pole | | |
| f_c and Q | 10.58 pJ | 11.13 pJ |

performance of the sub-circuits and efficient detection of the R-wave for a typical intra-cardiac signal in an ultra low-power environment.

Secondly, a new QRS-complex detection circuit for pacemaker applications has been proposed. The circuit is based on the wavelet transform. Applying the DTL principle, an analog system consisting of a wavelet filer, an absolute value circuit, a peak detector and a comparator has been designed. The simulated and measured results for a typical cardiac signal demonstrate a good performance in generating the desired wavelet transform and achieving correct QRS-complex detection.

Next, two analog implementations of the Gaussian wavelet transform in an ultra low-power environment, using the G_m -C and the DTL circuit techniques have been presented. Simulations from different continuous-time integrator designs demonstrated excellent approximations to the ideal wavelets using both Padé and L_2 approaches.

Furthermore, an analog implementation of the complex wavelet transform was presented. The complex wavelet filter design was derived from the combination of the real and the imaginary state-space descriptions. By this, we were able to implement a complex filter, i.e., having both real and imaginary transfer functions, with just an extra C matrix in an ordinary state-space structure.

Finally, a Morlet wavelet filter using the wavelet filter design procedure in Chapter 4 has been presented. Measurements demonstrated an excellent approximation of the Morlet wavelet base. The filter was optimized with respect to dynamic range. Moreover, sensitivity and sparsity were also taken into account in the design of the filter, in order to meet the requirements imposed by a low-power environment. From the results obtained, we deduced that this procedure could very well be used to approximate other wavelet

bases, arbitrary impulse responses and transfer functions, and to implement these on chip in an analog fashion using little power.

References

- [1] W. Straver, *Design Manual – SIC3A*, Internal Report, Delft University of Technology, Jan. 1999.
- [2] S. A. P. Haddad, S. Gieljes, R. P. M. Houben and W. A. Serdijn, *An ultra low-power dynamic translinear sense amplifier for pacemakers*, in: Proc. ISCAS, Bangkok, Thailand, vol. 5, pp. 37-40, May 25-28, 2003.
- [3] E. Seevinck, *Analysis and Synthesis of Translinear Integrated Circuits*, Elsevier, Amsterdam, 1988.
- [4] J. Mulder, A. C. van der Woerd, W. A. Serdijn and A. H. M. van Roermund, *An RMS-DC converter based on the dynamic translinear principle*, IEEE Journal of Solid-State Circuits, vol. 32, no. 7, pp. 1146-1150, 1997.
- [5] B. U. Kohler, C. Hennig and R. Orglmeister, *The principles of software QRS detection*, IEEE Engineering in Medicine and Biology, vol. 1, pp. 42-57, February 2002.
- [6] S. A. P. Haddad, R. P. M. Houben and W. A. Serdijn, *Analog wavelet transform employing dynamic translinear circuits for cardiac signal characterization*, in: Proc. ISCAS, Bangkok, Thailand, vol. 1, pp. 121-124, May 25-28, 2003.
- [7] S. A. P. Haddad and W. A. Serdijn, *Mapping the wavelet transform onto silicon: the dynamic translinear approach*, in: Proc. ISCAS, Phoenix, USA, vol. 5, pp. 621-624, May 26-29, 2003.
- [8] H. Kamada and N. Aoshima, *Analog Gabor transform filter with complex first order system*, in: Proc. SICE, pp. 925-930, 1997.
- [9] B. Gilbert, *Current-mode circuits from a translinear viewpoint: a tutorial*, in: *Analogue IC Design: The Current-Mode Approach*, C. Toumazou, F. J. Lidgey, D. G. Haigh (eds.) IEE Circuits and Systems, Series 2, Peter Peregrinus, London, 1990 (Chapter 2).
- [10] J. S. Sahambi, S. N. Tandon and R. K. P. Bhatt, *Using wavelet transform for ECG characterization*, IEEE Engineering in Medicine and Biology, vol. 16, pp. 77-83, February 1997.
- [11] S. A. P. Haddad, N. Verwaal, R. Houben and W. A. Serdijn, *Optimized dynamic translinear implementation of the Gaussian wavelet transform*, in: Proc. ISCAS, vol. 1, pp. 145-148, Vancouver, Canada, May 23-26, 2004.

- [12] S. A. P. Haddad, J. M. H. Karel, R. L. M. Peeters, R. L. Westra and W. A. Serdijn, *Analog complex wavelet filters*, in: Proc. ISCAS, pp. 3287-3290, Kobe, Japan, May 23-26, 2005.
- [13] I. Daubechies, *Ten Lectures on Wavelets*, Society for Industrial and Applied Mathematics, Philadelphia, PA, 1992.
- [14] S. Mallat, *A Wavelet Tour of Signal Processing*, Academic Press, San Diego, CA, 2001.
- [15] C. Toumazou, F. J. Lidgey and D. G. Haigh, *Analogue IC Design: The Current-Mode Approach*, IEE Circuits and Systems, Series 2, Peter Peregrinus, London, 1990.
- [16] S. A. P. Haddad, S. Bagga and W. A. Serdijn, *Log-domain wavelet bases*, IEEE Transactions on Circuits and Systems – I: Regular Papers, vol. 52, no. 10, pp. 2023-2032, October 2005.
- [17] G. W. Roberts and V. W. Leung, *Design and Analysis of Integrator-Based Log-Domain Filter Circuits*, Kluwer, Dordrecht, The Netherlands, 2000.
- [18] S. A. P. Haddad, J. M. H. Karel, R. L. M. Peeters, R. L. Westra and W. A. Serdijn, *Ultra low-power analog Morlet wavelet filter in 0.18 μ m BiCMOS Technology*, in: Proc. ESSDERC-ESSCIRC, pp. 323-326, Grenoble, France, September 12-16, 2005.

Chapter 8

Conclusions and Future Research

Since the first artificial pacemaker was introduced, much has changed and will continue to change in the future. The complexity and reliability in modern pacemakers has increased significantly, mainly due to developments in integrated circuit design, providing, for instance, diagnostic analysis, adaptive rate response and programmability. Nevertheless, the future trends for pacemakers indicate that much more advanced signal processing methods will be required than nowadays. Signal analysis methods improving discrimination of signals from noise and interference are of great importance. Also, due to various pathological states of the heart recently reported, morphological aspects of the cardiac signal need to be taken into account.

The Wavelet Transform (WT) has been shown to be a very efficient tool for analysis of non-stationary signals, like cardiac signals. Being a multiscale analysis technique, it offers the possibility of selective noise filtering and reliable parameter estimation and can therefore contribute efficiently to their morphological analysis. WT has been extensively used in biomedical signal processing, mainly due to the versatility of the wavelet tools. Signal analysis methods derived from wavelet analysis carry large potential to support a wide range of biomedical signal processing applications including noise reduction, feature recognition and signal compression.

In implantable medical devices, such as pacemakers, the power consumption is a critical issue, due to the limited power density and the longevity of currently available portable batteries. This implies that the design of such devices has to be optimized for very low power dissipation. Due to the relatively huge amount of power required for the analog-to-digital conversion and its improvement in power efficiency over the years, we now predict that the implementation of a fully digital wavelet signal processor in implantable pacemakers will not be feasible for many years to come.

For this reason, we proposed a method for implementing the novel biomedical signal processing based on wavelet transform using continuous-time analog circuitry. The methodology is based on the development of ultra low-power analog integrated circuits that implement the required signal processing, taking into account the limitations imposed by an implantable device.

First, a brief overview of the history and development of circuit designs applied in pacemakers was presented in Chapter 2. Also, based on future trends for pacemakers, some features and improvements for modern cardiac sensing systems were described and we pointed out the need for a morphological wavelet analysis of the cardiac signal.

Next, in Chapter 3, a comparison between frequency analysis, by means of the Fourier transform, and time-frequency representation, by means of the wavelet transform, was depicted. From a example of a non-stationary signal, the good extraction of the time and frequency characteristics of the wavelet was revealed. In addition, the properties of wavelet bases functions and WT signal processing applications were described.

From the wavelet definition, we stated that the implementation of the wavelet transform is based on a bandpass filter design that presents an impulse response equal to a wavelet base. In order to obtain the transfer function of a particular wavelet filter, mathematical approximation techniques are required. In Chapter 4, we indicated several methods to obtain good approximations in the time domain of the wavelet bases functions. One important objective of the introduced approaches is that the resulting approximated function should be rational and stable in the Laplace domain. This means that the approximating function must lead to a physically realizable network. Nevertheless, we can notice that due to limitations in chip area, power consumption and coefficient matching, there is a trade-off between the approximation accuracy versus the order of the implemented filter. Thus, the design challenge is to obtain a low-order system while preserving a good approximation to the intended function. Due to their general applicability, and the excellent accuracy, the Padé and L_2 approximations were chosen, which generate reasonable low-order and good-fit transfer functions.

Subsequently, in Chapter 5, we presented the description and a comparison of several state space representations. There are many possible state space descriptions for a circuit that implements a particular transfer function. The same holds for practical realizations. This allows the designer to find a circuit that fits his specific requirements. From the two figure-of merits defined in this chapter, we concluded that the orthonormal ladder structure is the optimal state space representation with respect to dynamic range, sparsity and sensitivity, which represent the most important design aspects in low-power low-voltage analog filters.

The trend towards lower power consumption, lower supply voltage and higher frequency operation has increased the interest in new design techniques for analogue integrated filters. A few ultra low-power integrator designs were

presented in Chapter 6, being, a pA/V $\Delta-G_m$ CMOS triode-transconductor, two Class-A log-domain integrators and an ultra low-power Class-AB \sinh integrator. The integrators were based on two different techniques, being the G_m -C approach and the translinear (log-domain) method, which can be directly used in low-power analog filters and ultra low-power biomedical system designs. The advantages and the limitations of these techniques were also highlighted.

Finally, the methodology presented in the previous chapters was employed in the design of several ultra low-power biomedical systems and analog wavelet filters. Two ultra low-power biomedical systems and four wavelet filter designs were presented in Chapter 7. First, a cardiac sense amplifier based on the dynamic translinear circuit technique was proposed. The obtained results in the sense amplifier demonstrate the desired performance of the sub-circuits and efficient detection of the R-wave for a typical intracardiac signal in an ultra low-power environment. Moreover, a new QRS-complex detection circuit, based on the wavelet transform, for pacemaker applications was proposed. The simulated and measured results for a typical cardiac signal demonstrate a good performance in generating the desired wavelet transform and achieving correct QRS-complex detection. A few wavelet filter designs were also presented. Two convenient methods to provide the transfer function of the wavelet filter are given by the Padé and L_2 approximations and, thus, some wavelet filters based on these approaches, for Gaussian, complex Gabor and Morlet wavelet bases, were designed using the G_m -C and the DTL circuit techniques. Simulations and measurements demonstrated an excellent approximation of the desired wavelet base.

From the results obtained, we deduced that this procedure can very well be used to approximate various wavelet bases and other time-domain waveforms or arbitrary transfer functions as well as to implement them on chip in an analog fashion using little power.

8.1 Future research

In this book, the transient detection capability of the WT has been exploited for detection of the QRS complex. However, other important aspects in the cardiac signal, such as the T wave or the QT interval can also be detected using wavelets.

Further analysis techniques of cardiac signals using wavelets are being developed by the Electronics Research Laboratory of Delft University of Technology and the Mathematics Department of Maastricht University, both in The Netherlands. Research on concepts such as the mathematical modelling of cardiac signals and pathologies, and the design of WT-based algorithms for intelligent sensing and feature extraction are under progress. In addition, a fully integrated implementation of the analog WT circuit to be used in pacemakers is currently being investigated.

It remains to be demonstrated in clinical practice that these novel signal analysis methods will contribute to the further development and application of dynamical electrocardiography in implantable devices.

Biomedical applications of wavelets

In this book we presented the application of the WT in cardiac signal (ECG) analysis. Nevertheless, the WT has become a powerful method in many other medical ultra low-power applications due to their suitability for analyzing non-stationary signals.

The WT is extremely versatile for the analysis of various electrophysiological signals (ExG), i.e., Electroencephalogram (EEG), Electromyogram (EMG), and Electrocardiogram (ECG). As an example, neurological EEG signals represent rhythmic potential fluctuations on the head surface created by the synchronous discharge of nerve cells and has been used to diagnose epilepsy. One of the early signs of a seizure is the presence of characteristics transient waveforms in the EEG (spikes and sharp waves). The shape and size of these waveforms can vary from one patient to another substantially. The WT can be used as a detection tool due to the very mixed nature of these phenomena and wavelet analysis has been shown to be useful in identifying the features localized within the EEG signal. Hence, one could apply the proposed low-power wavelet filter design methodology for EEG characterization in closed-loop implantable neurostimulator devices.

Finally, one can consider the applications of 2-D wavelets to biomedical imaging in an ultra low-power environment, for instance artificial retinae. Human beings have the capacity to recognize objects in natural visual scenes with high efficiency despite the complexity of such scenes, which usually contain multiple objects. Each object in our environment can cause considerably different patterns of excitation in our retinae depending on the observed viewpoint of the object. One possible mechanism for dealing with this situation is selective attention. The scene is first analyzed at a coarse resolution level, and the focus of attention enhances iteratively the resolution at the location of an object until the object is identified, similar to the principle of multiresolution wavelet analysis. Thus, the 2-D wavelet transform can be very well used for image processing tasks like detection, extraction, or classification of the various features in the images. In addition, the amount of information is usually very large and compression methods are highly needed in order to reduce the required processing time and/or archiving space. High level of compression should be achieved without loss of information. Because wavelet transform coefficients are localized in both frequency and space, they are theoretically better suited to image compression than other common transform methods. Wavelets have recently been applied to medical image compression and were found to be very effective. However, power consumption is an important issue in a battery-operated artificial retinae design. Image computation usually

requires large arrays of pixels. Thus, due to the massive parallel processing necessary for artificial implantable vision systems, digital processing, where a huge amount of A/D converters would be required (one A/D converter per pixel), turns out to be impracticable. This makes an analog implementation much more efficient than a digital one with respect to power consumption and chip area, and again the approach described in this book can be used for a complex biomedical image processor design in an ultra low-power environment.

Ultra Wideband Applications

Impulse radio, one flavor of Ultra Wideband (UWB) radio, is a promising new technology for wireless communications. Rather than modulating the information on a carrier, the data is transmitted using a coded series of very narrow pulses, carrying information in the time and the frequency domain. From the properties of the WT described before, one can say that wavelet bases are good candidates for these pulses. In the AIRLINK research project, a collaboration of TNO and various groups within Delft University of Technology in The Netherlands, impulse radio is being investigated. The real-time synthesis of UWB pulses by means of low-power analog integrated circuits is one of the core research issues in this project and as shown in Appendix D, the same methodology procedure described in this book can be very well used to the design of UWB pulse generators and time-domain delays.

Appendix A

High-Performance Analog Delays

A delay is a fundamental block in signal-processing systems. Pure delays should ideally not change the magnitude or shape of the input signal. Considering a fixed delay of τ , its frequency-domain transfer function is defined by the exponential $H(s) = e^{-\tau s}$, which cannot be realized with a finite number of lumped elements. The best solution is an approximation with a rational quotient of polynomials: $G(s) = N(s)/D(s)$. One common approach to approximate a delay transfer function is through the use of Bessel polynomials leading to an all-pole filter approximation called Bessel–Thomson realization. Another approximation, yielding a rational expression suitable for implementation through the use of a Taylor expansion of the frequency-domain non-rational transfer function around one point is called the Padé approximation. By narrowing of a Gaussian impulse-response function with the use of smaller pulse width σ , the delta time-domain impulse response of a delay is approximated as a third method in this work. The new delay-approximation method is completed through the application of a Padé approximation on the Laplace transform of the Gaussian function. The performance of these different approximations of a delay filter has been systematically compared, in regard to achievable cut-off frequency and time-domain characteristics. It was revealed that our Gaussian approximation of the time domain transfer function decreased overshoot in the step response, while keeping the other characteristics fixed.

A.1 Bessel–Thomson approximation

Bessel–Thomson is the most widely used approximation method of delay filters. This method leads to a family of low-pass all-pole transfer functions $T(s)$, which would give approximately constant time delay over as large frequency range as possible. The resultant transfer functions are of the form:

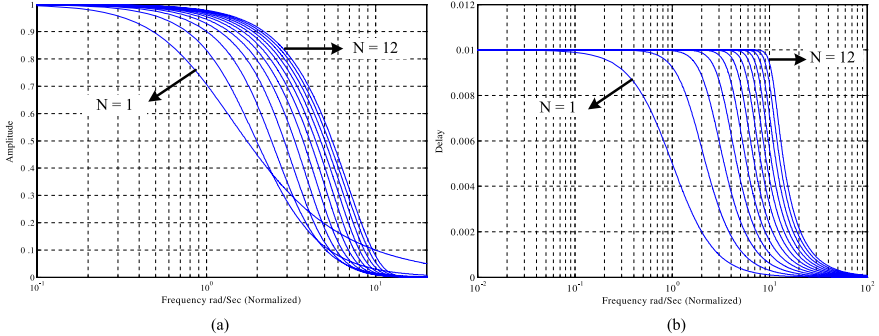


Fig. A.1. **a** Bessel–Thomson filter amplitude responses for orders 1–12. **b** Delay responses of the same filters

$$T_n(s) = \frac{B_0(s)}{B_n(s)} = \frac{1}{(2n - 1) \cdot B_{n-1}(s) + s^2 \cdot B_{n-2}(s)} \quad (\text{A.1})$$

where $B_n(s)$ is the general Bessel polynomial of order n with $B_0(s) = 1$ and $B_1(s) = s + 1$. In this approximation, the only degree of freedom available is the filter order, determined by the number of poles. A frequency-domain analysis of these filters illustrates a low-frequency behavior in which the roll-off frequencies are increased by filter-order increase. Figure A.1 illustrates the correspondent amplitude and delay responses of Bessel–Thomson filters of order 1–12.

Figure A.2 illustrates the step responses of different orders of Bessel–Thomson delay filters. The most important characteristic of the Bessel–Thomson filter, which is an overshoot-free step response, in addition to the resultant decrease of rise time due to filter-order increase can also be viewed here.

A.2 Padé approximation

Figure A.3 illustrates that in a Padé-approximated delay filter, for an increase of denominator order, the 3-dB cut off frequency of amplitude response increases, while peaking occurs for increase of order difference between numerator and denominator.

A delay-response simulation of Padé-approximated delay filters for different order differences between numerator and denominator order ($n - m$), while increasing the denominator order (n) from 5 to 12 is illustrated in Fig. A.4. This figure illustrates that for higher denominator order, higher delay roll-off frequency is achieved, while the peaking effect near the roll-off frequency increases for higher numerator and denominator order differences. More ac-

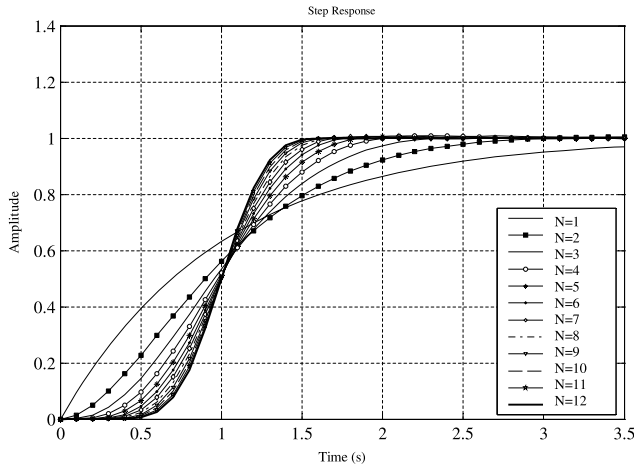


Fig. A.2. Step response of different order Bessel–Thomson filters

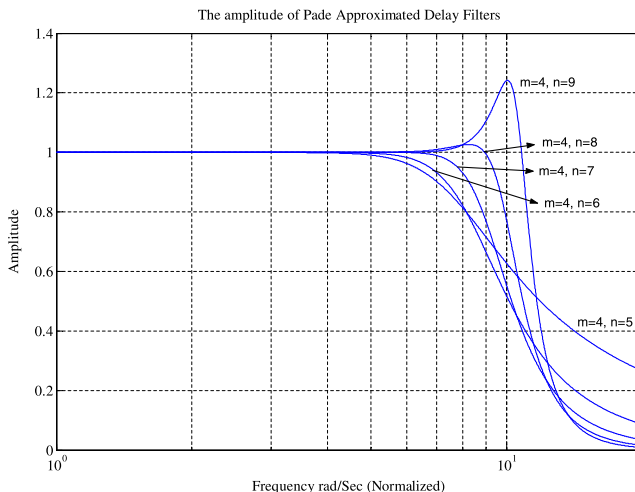


Fig. A.3. Amplitude response of Padé-approximated delay filters with $m = 4$ and $n = 5, \dots, 9$

curate delay response is achieved for smaller order difference and higher denominator order.

A series of time-domain simulations of the step response of Padé-approximated delay filters illustrates that the rise time decreases with an increase of the denominator order (Fig. A.5), while zero-time oscillations are generated when the order difference between the denominator and numerator decreases.

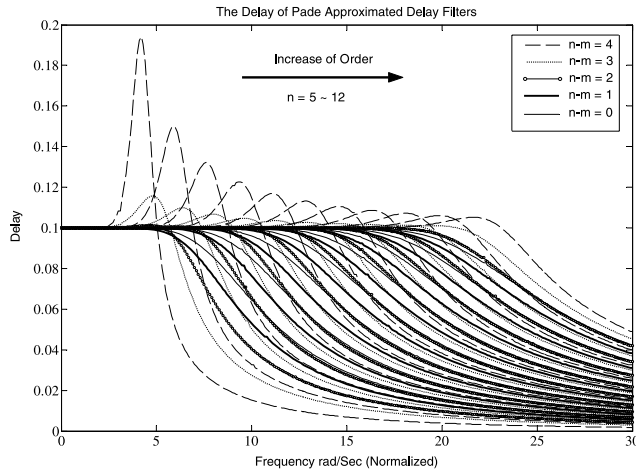


Fig. A.4. Delay response of Padé-approximated delays for different order difference and different denominator order

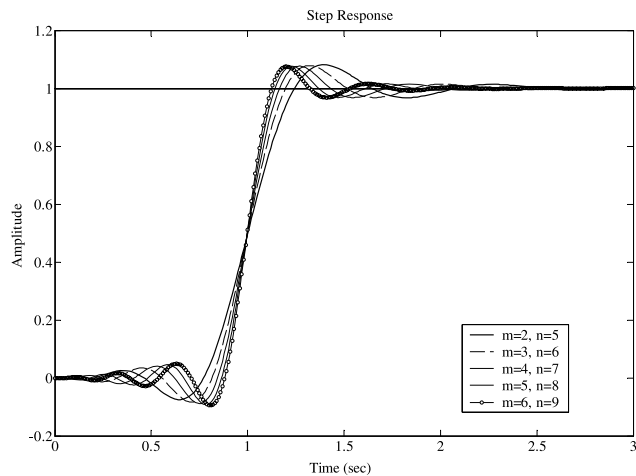


Fig. A.5. Rise-time decrease with filter order increase

These zero-time oscillations are not favorable and might cause instability in some applications.

Figure A.6 illustrates that the filter order increase results in a faster step response while filters with larger numerator and denominator order difference provide smaller rise times.

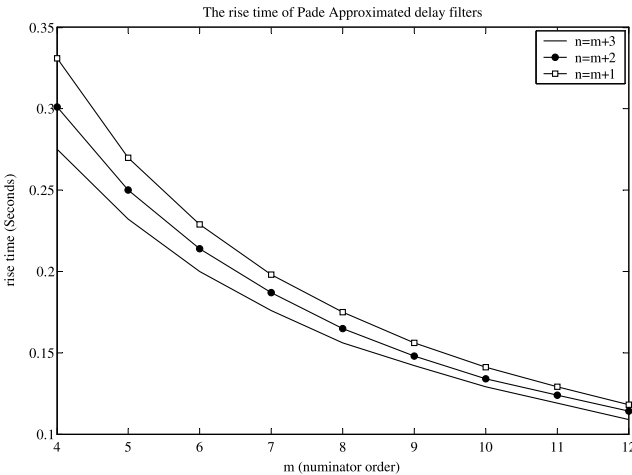


Fig. A.6. Rise-time comparison for different combination of numerator and denominator orders

A.3 Comparison of Bessel–Thomson and Padé approximation delay filters

In this section, a comparison of the frequency-domain and time-domain performance metrics of Bessel–Thomson and Padé-approximated delay filters is made. According to the amplitude and delay responses sketched for different order combinations of Bessel–Thomson and Padé delay filters, in Fig. A.7 and Fig. A.8 respectively, the lower orders of Padé approximation can always achieve higher frequencies than the highest reasonable Bessel–Thomson approximations.

A comparison of the step responses of both approximations (Fig. A.9a) illustrates that Padé-approximated delay filters always introduce more overshoot and oscillations than their Bessel–Thomson counterparts, while the former has smaller rise times (Fig. A.9b).

In order to benefit from the higher frequency and faster time-domain response of the Padé approximation, together with the reduced overshoot provided by the Bessel–Thomson approximation, a new approximation method is introduced in the following section.

A.4 Gaussian time-domain impulse-response method

The time-domain impulse response of a delay function is a delta function. A delta function can be approximated by narrowing a Gaussian impulse re-

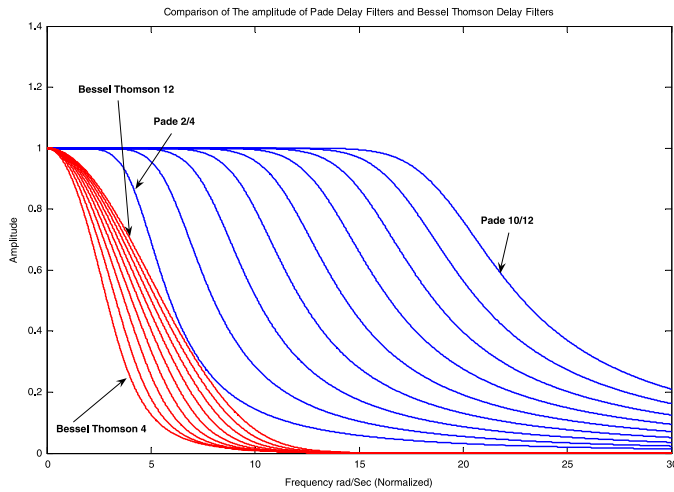


Fig. A.7. Amplitude comparison of Bessel–Thomson delay filters of orders 4–12 vs. Padé-approximated delay filters of order 2/4 to 10/12

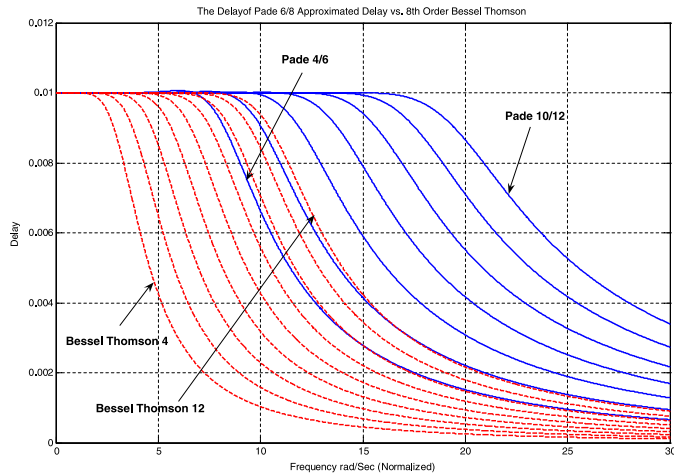


Fig. A.8. Delay comparison of Bessel–Thomson delay filters of orders 4–12 vs. Padé-approximated delay filters of order 2/4 to 10/12

sponse with the use of a smaller pulse width σ , as illustrated by Eq. A.2 and Fig. A.10.

$$h(t) = \frac{1}{\sigma\sqrt{2\pi}} e^{\frac{-(t-\mu)^2}{2\sigma^2}} \quad (\text{A.2})$$

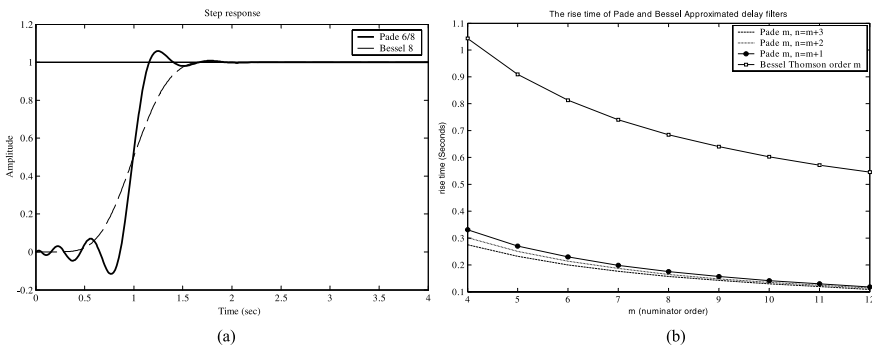


Fig. A.9. Comparison of step response (a) and rise-time in both approximations (b)

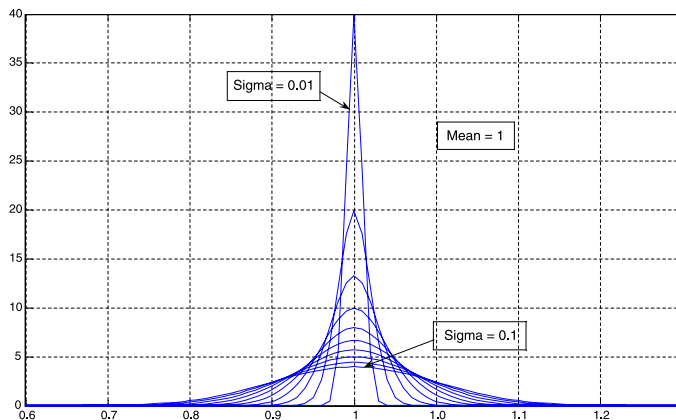


Fig. A.10. A Gaussian function's response vs. the change of σ

In this method, a Padé approximation is applied to the Laplace transform of a Gaussian impulse response. Figure A.11 illustrates that the amplitude response of the Gaussian impulse-response delay filter becomes closer to the response of a Bessel–Thomson approximation for larger values of σ , decreasing the roll-off frequency, while Fig. A.12 illustrates that the effect on the delay response is minimum.

An investigation of the Gaussian impulse-response delay filter's step response proves that the increase of σ , making the impulse response wider, leads to a decrease of the zero-time oscillations and overshoots, while it hardly increases the rise time. It is revealed that using a time-domain Gaussian impulse response gives the possibility of decreasing the overshoots and zero-time ringings in a Padé approximation of the delay by increasing σ , while the price paid is an increase of insertion loss in the amplitude response and a slightly slower

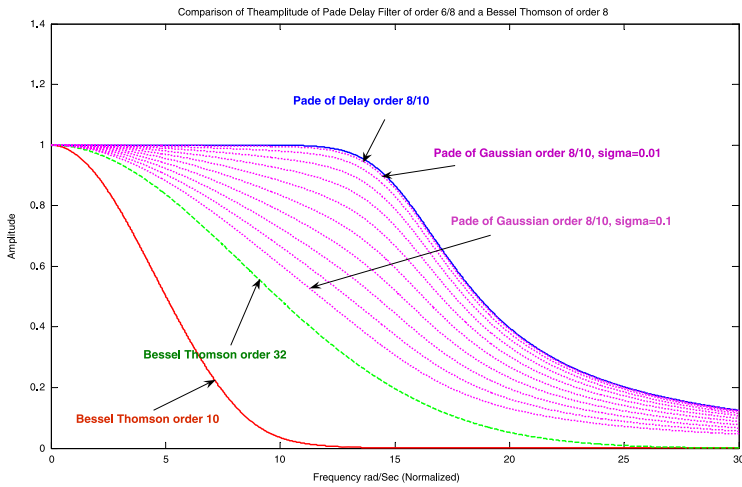


Fig. A.11. The amplitude response of the Gaussian impulse-response delay vs. σ in comparison to normal Padé-approximated delay and Bessel–Thomson responses

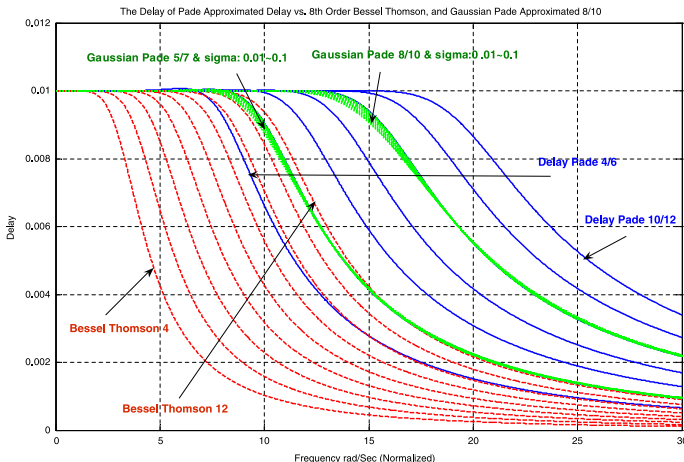


Fig. A.12. The delay response of the Gaussian impulse-response delay for various values of σ in comparison to normal Padé-approximated delay and Bessel–Thomson responses

rise time in the system step response. Figure A.13 compares the step response of a 6/8 Padé-approximated delay filter with the same order Gaussian impulse response delay filter with σ equal to 0.05. As illustrated by this graph, for the same nominator and denominator order, the Gaussian impulse response delay has less overshoot.

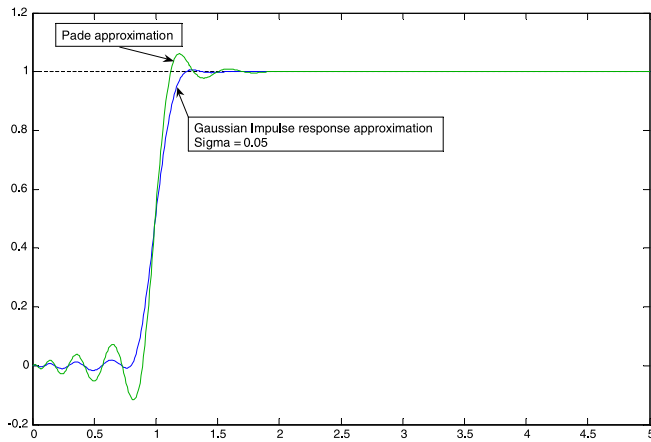


Fig. A.13. The step response of a Gaussian impulse-response delay for a value of $\sigma = 0.05$ vs. a Padé-approximated delay filter of the same (6/8) filter order

We can conclude that while Bessel–Thomson is the most widely used method of delay-filter approximation, higher frequency and faster delay responses can be achieved through the use of Padé approximation at the expense of more overshoot. The here introduced method of Gaussian time-domain impulse responses produces a rational transfer function that is ready for implementation in an analog fashion and realizes a delay with both a large bandwidth and little overshoot.

Appendix B

Model Reduction – The Balanced Truncation Method

A wavelet filter design trade-off involves the approximation accuracy versus the complexity (model order) of the implemented filter. On the other hand, for analog active filters, the power consumption is directly proportional to the order of the filter. Thus, the design challenge is to obtain a low-order system while preserving a good approximation matching.

To overcome these difficulties, one can employ model order reduction that consists of an approximation of the dynamical system by a reduced order system. It is required that the approximate system preserves the properties of the original system. Clearly, it is also desirable that the approximation error is small.

There exist various model reduction approaches for standard state space systems such as balanced truncation and moment matching approximations. The balanced truncation method, which will be described here, usually presents better approximation results compared to moment matching method. Also, this method is strongly related to the controllability and observability Gramians, already involved in the dynamic range optimization procedure presented in Section 5.2.1. The balanced truncation method (BT) consists in transforming the state space system into a balanced form whose controllability and observability Gramians become diagonal and equal.

Hence, the model reduction problem is one of finding a state-space system of order $k < n$, such that the error E with respect to the L_∞ norm is minimized over all state-space systems of order k , or

$$E = \|H(s) - H_k(s)\|_{L_\infty} \quad (\text{B.1})$$

where $H(s)$ is the original transfer function and $H_k(s)$ is the transfer function of the reduced-order model. The balanced truncation method produces a guaranteed stable reduced model with globally accurate frequency response approximation (L_∞ -error bound). In the continuous-time case, a reduced-order model computed by the BT method approximates the original one well

at high frequencies, with a perfect match at $\omega = \infty$, which is suitable for time-domain approximation around $t = 0$.

The starting point of the k th order (square-root) balanced truncation reduction is the calculation of the Cholesky factors Z^B and Z^C of the Gramians K and W , respectively. Any square matrix can be written as the product of a lower triangular matrix Z and an upper triangular matrix Z^T ; this is called the Cholesky decomposition and is given with respect to the Gramians by

$$\begin{aligned} K &= Z^B(Z^B)^T \\ W &= Z^C(Z^C)^T \end{aligned} \quad (\text{B.2})$$

A merit of the BT method is that it relies on the Cholesky factors Z^B and Z^C of the Gramians K and W rather than the Gramians themselves, which has advantages in terms of numerical stability.

The next step of the reduction method is the calculation of the Singular Value Decomposition (SVD) of the product $(Z^C)^T Z^B$

$$(Z^C)^T Z^B = U^L \Sigma (U^R)^T \quad (\text{B.3})$$

with

$$U^R = [u_1^R \dots u_n^R], \quad U^L = [u_1^L \dots u_n^L], \quad \Sigma = \begin{bmatrix} \sigma_1 & \dots & 0 \\ \vdots & \ddots & \vdots \\ 0 & \dots & \sigma_n \end{bmatrix} \quad (\text{B.4})$$

where U^L and U^R are orthogonal matrices, and Σ is a diagonal matrix containing the singular values of $(Z^C)^T Z^B$. The singular values $\sigma_1, \dots, \sigma_n$ are known as the Hankel singular values of the system.

If the system is normalized properly, i.e. internally balanced, the diagonal $\text{diag}(\sigma_1, \sigma_2, \dots, \sigma_n)$ of the joint Gramian can be used to reduce the model order. Because this diagonal reflects the combined controllability and observability of individual states of the balanced model, one can delete those states with a small σ_i while retaining the most important input–output characteristics of the original system.

Finally, most model reduction methods for dynamic systems are proceeded by projection, which is usually implemented using orthogonal projection matrices. BT is a projection method with left projection matrix S^C and right projection matrix S^B , such that $(S^C)^T S^B = I_{k \times k}$, given by

$$S^B = Z^B [u_1^R \dots u_k^R] \begin{bmatrix} 1/\sqrt{\sigma_1} & \dots & 0 \\ \vdots & \ddots & \vdots \\ 0 & \dots & 1/\sqrt{\sigma_k} \end{bmatrix} \quad (\text{B.5})$$

and

$$S^C = Z^C [u_1^L \dots u_k^L] \begin{bmatrix} 1/\sqrt{\sigma_1} & \dots & 0 \\ \vdots & \ddots & \vdots \\ 0 & \dots & 1/\sqrt{\sigma_k} \end{bmatrix} \quad (\text{B.6})$$

Then, the new k th order BT realization is given by

$$A'_k = (S^C)^T A S^B, \quad B'_k = (S^C)^T B, \quad C'_k = C S^B \quad (\text{B.7})$$

To conclude, from Eq. B.5 and Eq. B.6, one can see that every state space system can be transformed to balanced form by means of a state change $x' = T x$, where the balancing transformation is given by $T = \Sigma^{\frac{1}{2}} U^L (Z^B)^{-1} = \Sigma^{-\frac{1}{2}} U^R (Z^C)^T$. The controllability and observability Gramians of the balanced k th-order reduced system are diagonal and equal, defined by

$$K'_k = W'_k = \Sigma = \text{diag}(\sigma_1, \sigma_2, \dots, \sigma_k) \quad (\text{B.8})$$

To illustrate the model reduction method for the design of wavelet filters, we applied the BT approach to state space systems obtained from the Padé and L_2 approximations, as shown in Fig. B.1a and Fig. B.1b, respectively.

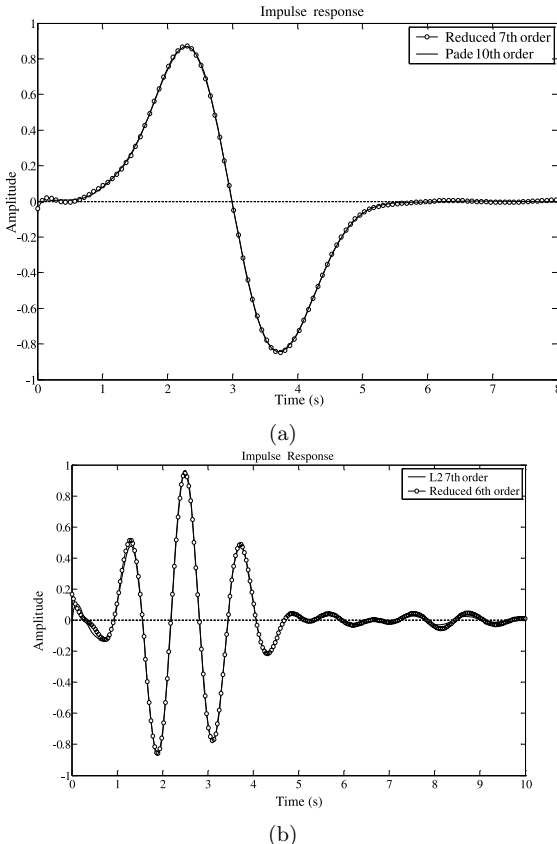


Fig. B.1. Model reduction for first derivative of Gaussian Padé approximation (a) and Morlet wavelet L_2 approximations (b)

One can note that it is possible to reduce the 10th-order (first derivative of Gaussian) state space obtained by the Padé method to a 7th order system and the 7th-order L_2 Morlet approximation into a 6th order, without noticeable reduction in accuracy.

Reduced model and optimal dynamic transformations comparison

In order to obtain the optimal dynamic range for the reduced model, we compare the similarity transformations for the balanced realization with the one presented in Section 5.2.1.

One can see that the first step for both transformations is similar, which makes the controllability Gramian equal to the identity matrix. Since K is symmetric, its singular value decomposition has the form $K = P_K D_K P_K^T$, defining the first transformation as $T_{K1} = P_K D_K^{1/2}$. In these first transformed coordinates, $K_1 = I$ and $W_1 = T_{K1}^T W T_{K1}$.

In the second step of the balanced realization, we perform an SVD on W_1 to get $W_1 = P_{W1} D_{W1} P_{W1}^T$. The second transformation is defined as $T_{W2,bal} = P_{W1} D_{W1}^{-1/4}$. In the new coordinates, both Gramians are equal and diagonal: $K_{2,bal} = W_{2,bal} = D_{W1}^{1/2}$. Whereas, for dynamic range optimization, we do not apply the scaling $D_{W1}^{-1/4}$, and the transformation is just the rotation $T_{W2,opt} = P_{W1}$.

Thus, considering the fact that the composite transformation $(T_1 T_2)$ for the balanced and optimized realization are given by $T_{bal} = D_K^{1/2} P_K P_{W1} D_{W1}^{-1/4}$ and $T_{opt} = D_K^{1/2} P_K P_{W1}$, respectively, to optimize the reduced model with respect to the dynamic range, we need to apply just a scaling transformation $T_{scal} = W_2^{1/2}$.

Appendix C

Switched-Capacitor Wavelet Filters

In this appendix, we will present two discrete-time wavelet base implementations, being the first derivative of a Gaussian, *gaus1*, and the Morlet, by means of the switched-capacitor filter technique.

As a filtering technique, Switched-Capacitor (SC) filters have become extremely popular due to their accurate frequency response as well as good linearity and dynamic range. Accurate discrete-time frequencies are obtained since filters coefficients are determined by capacitance ratios which can be set quite precisely in an integrated circuit. Once the coefficients of a SC discrete time filter are accurately determined, its overall frequency response remains a function of the clock (or sampling) frequency and the capacitors ratio.

To design wavelet switched-capacitor filters, we will first obtain their equivalent transfer functions. However, in order to obtain the approximation of the desired wavelet base, we will apply first the Padé and the L_2 approximations in the continuous-time domain to have the Laplace-domain transfer function and after that use an impulse-invariant z -transformation to obtain a proper transfer function in the z -domain.

The Padé and L_2 approximated transfer functions for the Gaussian and the Morlet wavelet bases, respectively, and the corresponding approximated waveforms (Fig. C.1) are given below.

Padé [3/7] approximation of the *gaus1* wavelet base:

$$H_{gaus1}(s) = \frac{8.06s^3 - 50.67s^2 + 151.65s}{s^7 + 8.35s^6 + 37.07s^5 + 107.56s^4 + 213.23s^3 + 282.58s^2 + 228.17s + 85.58} \quad (\text{C.1})$$

L_2 [6/8] approximation of the Morlet wavelet base:

$$H_{mor}(s) = \frac{0.88s^6 + 1.61s^5 + 45.48s^4 + 128.4s^3 - 451.3s^2 + 1576s}{s^8 + 5.34s^7 + 117.9s^6 + 440.9s^5 + 4610s^4 + 11020s^3 + 69880s^2 + 82960s + 337900} \quad (\text{C.2})$$

In order to implement the filter in discrete time in the z -domain, the impulse invariance technique has been chosen to preserve the impulse response

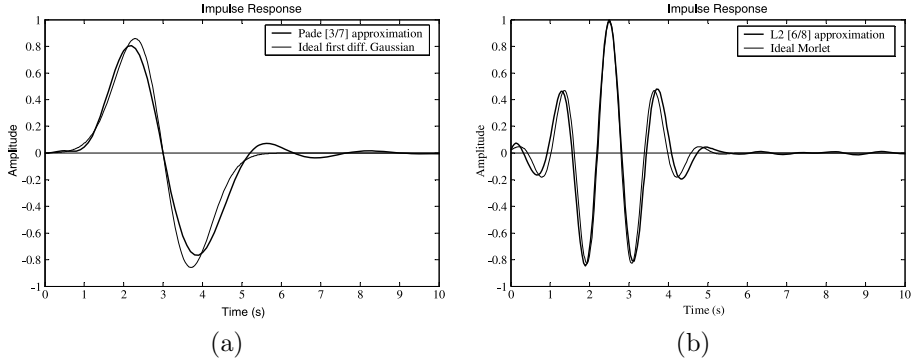


Fig. C.1. Continuous-time approximated impulse response for Padé [3/7] approximation of the *gaus1* (a) and L_2 [6/8] approximation of the Morlet wavelet base (b)

of the continuous-time wavelet filter by defining the relationship

$$h_d[k] = T_s h_c(kT_s) \quad (\text{C.3})$$

where T_s is the sample frequency, $h_d[k]$ and $h_c(kT_s)$ are the discrete and continuous time impulse response, respectively. This means that, the discrete and continuous time impulse responses match, up to a scale factor T_s , at the sample instance. The corresponding discrete-time z -domain transfer functions, applying an impulse invariant z -transformation yields

$$H_{\text{gaus1}}(z) = \frac{0.0039z^7 - 0.011z^6 + 0.026z^5 + 0.014z^4 - 0.03z^3 - 0.003z^2}{z^8 - 4.2z^7 + 7.7z^6 - 8.3z^5 + 5.7z^4 - 2.4z^3 + 0.58z^2 - 0.06z} \quad (\text{C.4})$$

and

$$H_{\text{mor}}(z) = \frac{0.0021z^8 - 0.0067z^7 + 0.0015z^6 + 0.024z^5 - 0.05z^4 + 0.047z^3 - 0.022z^2 + 0.004z}{z^8 - 6.5z^7 + 19.4z^6 - 34.3z^5 + 39.4z^4 - 30z^3 + 14.8z^2 - 4.3z + 0.58} \quad (\text{C.5})$$

Figure C.2 shows both discrete-time impulse responses for the Gaussian and the Morlet wavelets.

Next, to design the SC wavelet filter, we will obtain the spate space representation in z -domain, applying the same procedure described in Chapter 5. In this case, we have chosen to obtain first the optimal DR state space and then apply the Schur transformation. Nevertheless, we must take into account that switched-capacitor integrators implement $H(z) = \frac{1}{z-1}$ instead of $H(s) = \frac{1}{s}$. So, the state space description of a SC filter is given by

$$\begin{aligned} zx &= (A - I)x + Bu \\ y &= Cx + Du \end{aligned} \quad (\text{C.6})$$

which is different from the usual state space description. I is the identity matrix. As described before, the different coefficients in the state space matrices represent the interconnections and multiplicative factors between the

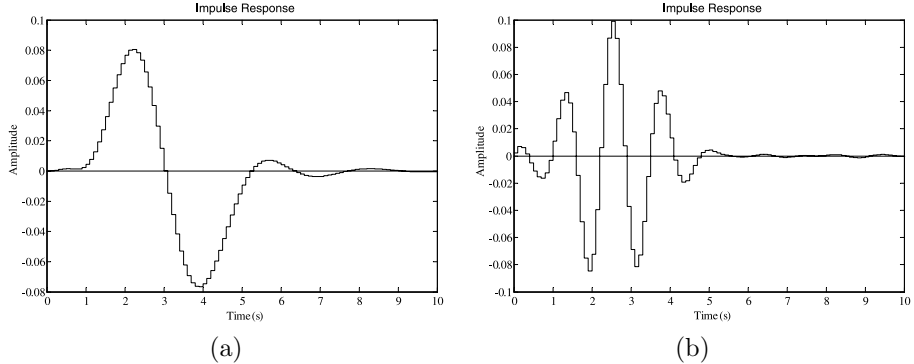


Fig. C.2. Discrete-time approximated impulse response for Gaussian (a) and Morlet wavelet bases (b)

various integrators and the input and output signals. Every coefficient in the A and B matrices will be realized by means of switched capacitors. The C matrix scales the output signals from the integrators so it will be realized by using capacitors and adders.

A switched-capacitor filter is realized with the use of basic building blocks such as op-amps, capacitors and switches driven by non-overlapping clock signals. The operation of a switched-capacitor integrator is as follows. Capacitors are charged and discharged by periodically opening and closing the switches located on either side of the capacitor. This generates a charge transfer that results in a pulsing current flow. The average current can be calculated and, if the frequency is high enough, this current will be equivalent to a current through a resistor. This means than the resistive elements in the circuit can be replaced by capacitors. The amount of current, and thus the equivalent resistance, depends on two variables: the size of the capacitor and the switching frequency, and this means that also the frequency behavior of the filter will depend on this two parameters.

Non-inverting and inverting SC integrators

As previously mentioned, we implement each of the coefficients of the state-space matrices by means of capacitance ratios in the integrators. As we have positive and negative coefficients it's necessary to choose a different topology for each kind, leading to non-inverting and inverting integrators. The circuit diagram of the non-inverting integrator is given in Fig. C.3. It implements the first-order transfer function given by

$$H(z) = \left(\frac{C_1}{C_2} \right) \frac{1}{z - 1} \quad (\text{C.7})$$

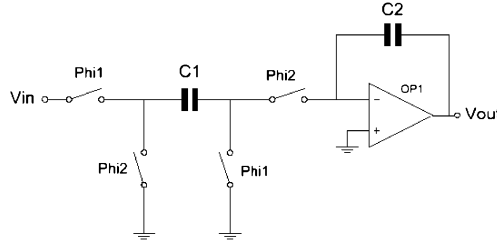


Fig. C.3. Non-inverting SC integrator

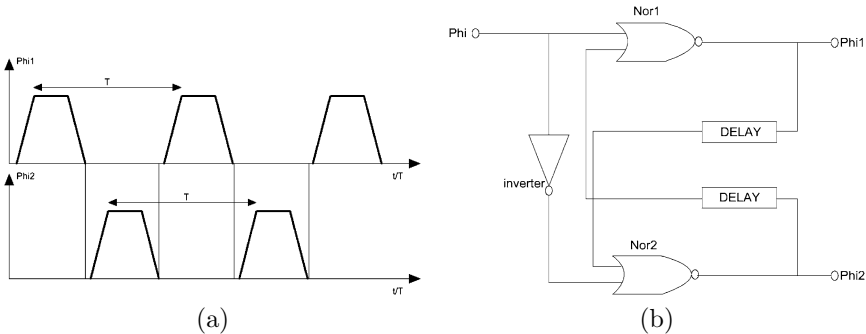


Fig. C.4. Non-overlapping clock signals and their generation

Phi₁ and Phi₂ represent the clock phases. A correct behavior of the clocks is essential for proper functioning of the switches. The clocks set the time when C₁ and C₂ will be charged and they must be non-overlapping in order to guarantee that charge is not inadvertently lost. The term non-overlapping refers to two logic signals running at the same frequency and arranged in such way that at no time both signals are high, as illustrated in Fig. C.4a. The rise and fall times of the signals also play an important role in the circuit behavior since an ideal clock signal will cause the switches to induce more charge into the circuit and thus to have clock feed through in the output signal. A simple circuit to provide these non-overlapping clock signals is shown in Fig. C.4b.

Finally, to implement the negative coefficients of the state space description, Fig. C.5 shows one possible topology for the inverting SC integrator. It implements

$$H(z) = -\left(\frac{C_1}{C_2}\right) \frac{1}{z-1} \quad (\text{C.8})$$

The switches of both integrators can be implemented with just simple NMOS transistors. The most important characteristics they must fulfill are a very high off resistance (so little charge leakage occurs), a relatively low on resistance (so the circuit can settle in less than half the clock period) and introducing no offset voltage when they are turned on.

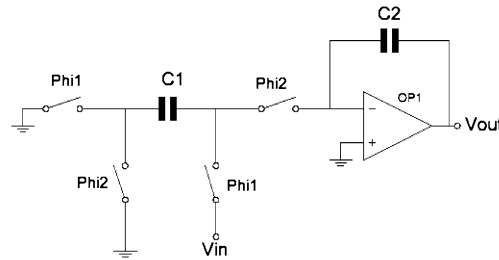


Fig. C.5. Inverting SC integrator

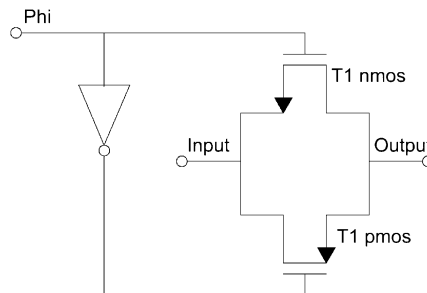


Fig. C.6. Transmission gate

As one can see, the non-idealities of the switches lead to glitches in the output signal. The MOS switch couples the clock transitions to the sampling capacitor through its gate-drain or gate-source capacitance and this effect introduces an error in the output sampled voltage. In order to reduce this clock feed-through effect, we can use Transmission Gates (TG). A TG is a combination of PMOS and NMOS transistors, as shown in Fig. C.6. For this circuit, ideally, the clock feed-through signals at the transistor drain and source nodes cancel each other.

In order to cancel the effects of charge injection, we can use dummy switches. We can assume that the charge deposited by the transistors in the capacitor can be removed by means of another transistor that will absorb it to create a channel.

Finally, in order to design the proper operational amplifier (op amp) for the SC filter, we must take in account some important aspects as dc gain, unity-gain frequency, phase margin, slew-rate and dc offset. The op amps can, e.g., be realized by a two-stage CMOS amplifier, as depicted in Fig. C.7.

Simulation results using models from AMSs 0.35 μm CMOS IC technology are given in Fig. C.8. As one can see, the obtained results are pretty close to the ideal impulse response shown in Fig. C.2, which confirms the good performance of the switched-capacitor wavelet filter.

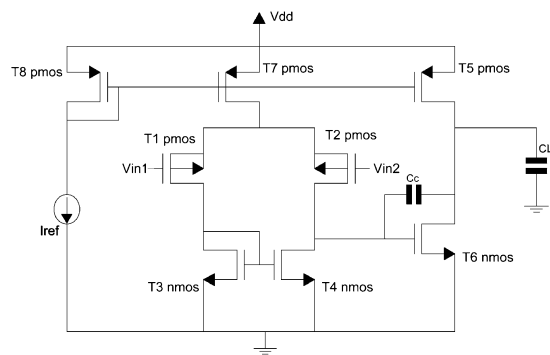


Fig. C.7. Two stages CMOS operational amplifier

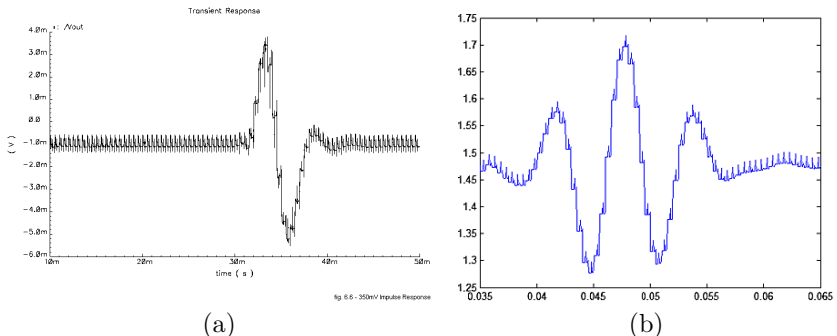


Fig. C.8. Impulse response of the SC wavelet filters. (a) First derivative of a Gaussian. (b) Morlet

Appendix D

Ultra-Wideband Circuit Designs

In today's marketplace for emerging communication technologies, the focal point of attention is ultra-wideband (UWB) radio as it not only promises enhanced data throughput with low-power consumption, but also provides high immunity against electromagnetic interference (EMI) and robustness to fading. It is expected that future short-range indoor ultra-wideband (UWB) telecommunication systems will operate in the frequency band from 3.1–10.6 GHz according to the Federal Communications Commission (FCC) mask. Ultra-wideband communication offers significant contributions and advantages but simultaneously a number of challenges also need to be addressed.

When implemented as impulse radio (IR-UWB) (i.e., where the information is transmitted by very short EM pulses) this new communication technology may revolutionize the way we think in wireless technology by modulating data in time rather than in frequency with low-power consumption. From the perspective of traditional narrow-band systems, the wideband nature of the front-end architecture employed in UWB systems requires a totally different design methodology of both the UWB front-end architecture and its constituting UWB circuit building blocks. In the following sections we describe some UWB circuit designs using the methodology presented in this book.

D.1 Impulse generator for pulse position modulation

Pulse Position Modulation (PPM)) is used to encode the binary transmitted data. The waveform to be transmitted is the Gaussian monocycle due to its intrinsic time-frequency resolution product, which is important for applications such as positioning and imaging. The impulse generator consists of a cascade of a fast triangular pulse generator and a pulse-shaping network or Gaussian filter (i.e., a filter having the first derivative of a Gaussian as its impulse re-

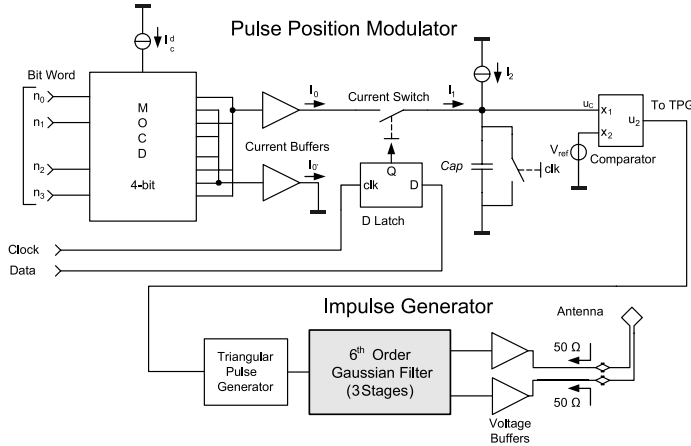


Fig. D.1. Impulse radio UWB transmitter block diagram

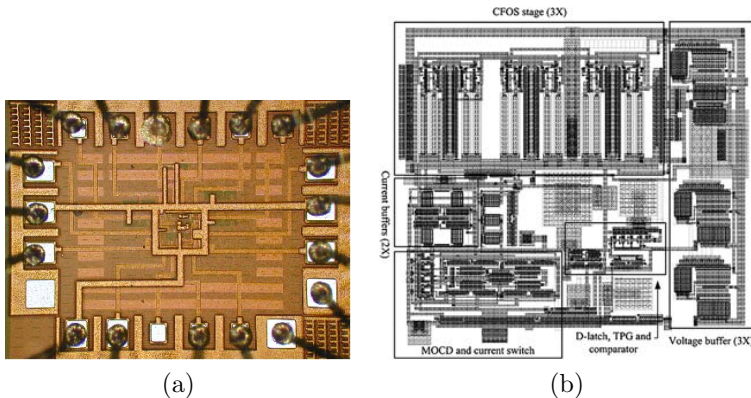


Fig. D.2. **a** Microphotograph. **b** Layout of the impulse radio UWB transmitter

sponse). As mentioned in Chapter 4, a Gaussian filter can be implemented by a cascade of complex first-order systems (CFOS). Here we employ a cascade of three complex first-order systems (CFOS), which, in turn, consist of G_m -C sections that employ differential pairs with partial positive feedback. The entire impulse radio UWB transmitter is a combination of a PPM modulator and a pulse generator. Its block diagram is shown in Fig. D.1.

The chip microphotograph and the layout of the Pulse Position Modulator core are given in Fig. D.2. The circuit has been designed using IBM 0.18 μ m BiCMOS IC technology.

Figure D.3 shows the measured Gaussian monocycle waveform. There is a 75 ps discrepancy in the pulse width as compared to the simulated results.

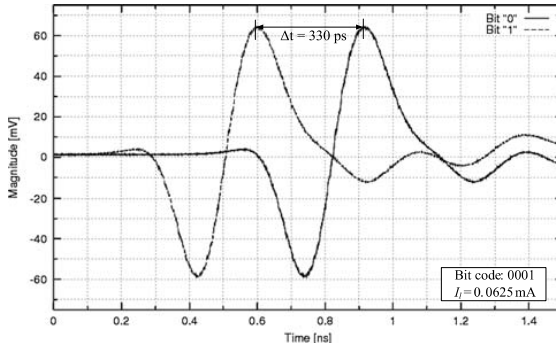


Fig. D.3. Measured impulse response of a monocyte Gaussian and pulse position modulation for bit code 0001

Table D.1. Measured performance of the impulse generator

| | |
|--|--------------------------|
| Technology | 0.18 μ m BiCMOS |
| Die area | 1.25 mm ² |
| Active area | 0.306 mm ² |
| Pulse width Gaussian Monocycle | 375 ps – measured on PCB |
| Time delay | |
| Bit code: 0001 | 315 ps |
| Current consumption of Gaussian filter | 14.4 mA @ 1.8 V |

Furthermore, to verify pulse position modulation, a clock signal (15 MHz), which acts as the binary input signal, is streamed into the D-latch. A bit code (0001) is chosen to verify that the least significant bit would vary the position of the pulse by approximately 315 ps. Finally, Table D.1 highlights the measured parameters of the impulse generator.

D.2 A delay filter for an UWB front-end

A continuous-time analog delay is designed as a requirement for the autocorrelation function in the Quadrature Downconversion Autocorrelation Receiver (QDAR). Figure D.4 shows a QDAR, which is designed to operate in the presence of strong narrow-band interference, while still being able to detect the incoming UWB signal. Hence, to further reduce the influence of the narrow-band interferers, frequency selectivity is introduced in the delay element.

Assuming that the incoming waveform at the receiver, $x(t)$, is a Morlet given by

$$x(t) = \cos[\omega_0(t - \tau)]e^{-(t-\tau)^2} \quad (\text{D.1})$$

where ω_0 is the center frequency and τ is the time instant at which the Morlet waveform is centered, the impulse response, $h(t)$, of the delay filter is chosen

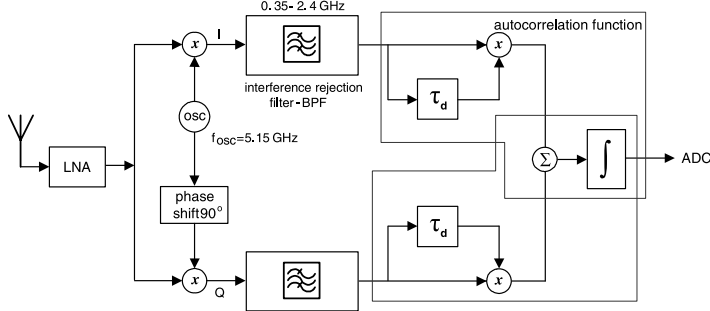


Fig. D.4. Quadrature Downconversion Autocorrelation Receiver (QDAR)

to match the incoming signal (i.e., $h(t) = x(t)$) and therefore the output of the time delay, $y(t)$, is the convolution of the incoming signal and the impulse response of the filter, given by,

$$x(t) = \cos[\omega_0(t - 2\tau)]e^{-(t-2\tau)^2} \quad (\text{D.2})$$

where β is the gain factor of the convolved waveform. On comparing Eq. D.1 with Eq. D.2, one can see the distinct resemblance between the convolved waveform and the incoming Morlet signal. As a result, the Morlet signal is delayed by a time period equal to τ .

In regards to the transmit reference scheme and from an implementation point of view, one is drawn to the conclusion that the bottleneck to this concept is the physical realization of an accurate continuous-time delay required to execute the autocorrelation function at high frequencies. An eight-order Padé approximation of a Morlet function is selected to implement this delay. Subsequently, the orthonormal state space is adopted for the same reason as described in Chapter 5. Each coefficient in the state-space description of the orthonormal ladder filter is implemented at circuit level using a novel 2-stage G_m cell employing negative feedback.

Simulation results in IBM's BiCMOS 0.13 μm technology show that through convolution, the Morlet signal is delayed by a time period equal to τ , as shown in Fig. D.5.

This delay filter requires a total current of 70 mA at a 1.6 V power supply. The 1-dB compression point of the delay is at 565 mV and the SNR is 47.5 dB. On performing a Monte Carlo simulation it becomes evident that the response of the frequency selective analog delay does not suffer drastically from neither process variations nor component mismatch.

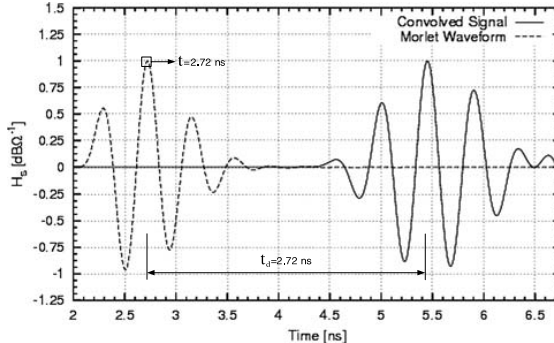


Fig. D.5. Time delay between the incoming Morlet waveform and convolved signal

D.3 A FCC compliant pulse generator for UWB communications

In this book, we have shown that it is feasible to design filters with arbitrary waveform responses. Therefore we propose an ultra-wideband pulse generator incorporating a filter with a Daubechies' impulse response (i.e., maximally flat over the desired frequency range).

As seen in Fig. D.6, by generating a window-like response in the baseband (i.e. with the Daubechies' filter) and then through up-conversion, the energy spectrum of the pulse generator can be matched to that of the FCC frequency mask. For detection in the receiver, the absolute shape of the transmitted waveform is not relevant. Biphase modulation of the transmitted waveform can be achieved by alternating the polarities of the “impulses” that are used to drive the Daubechies' scaling function filter.

An eight-order Padé approximation of its transfer function is selected to implement the FCC stipulated frequency spectrum. Again, the orthonormal ladder structure has been chosen and the coefficients in the state-space description are implemented at circuit level using a novel 2-stage G_m cell employing negative feedback.

From simulation results in IBM's CMOS 0.13 μm technology, Fig. D.7 demonstrates that the pulse generator response is close to the ideal impulse response. The Daubechies filter requires a total current of 25 mA from a 1.2 V power supply.

Finally, Fig. D.8 shows the frequency spectrum of the Daubechies' scaling function upconverted with a 7 GHz carrier. As seen in the figure, the pulse generator's performance can now be optimized for maximum energy efficiency. The frequency coverage of the simulated waveform is about 85% of the FCC mask.

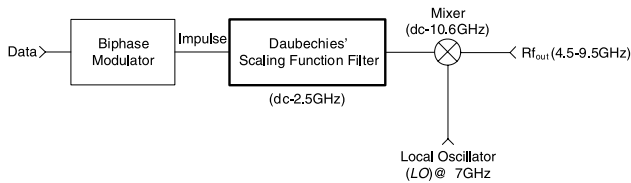


Fig. D.6. Proposed pulse generator block diagram

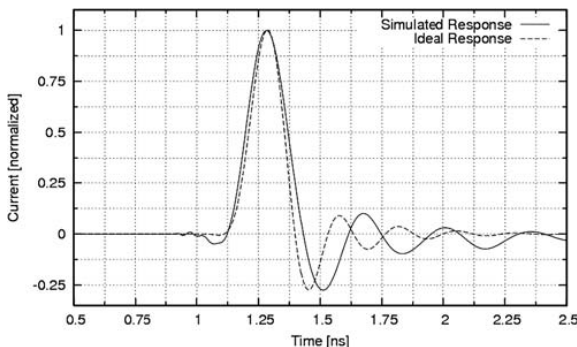


Fig. D.7. Impulse response of an 8th order Daubechies' scaling function filter

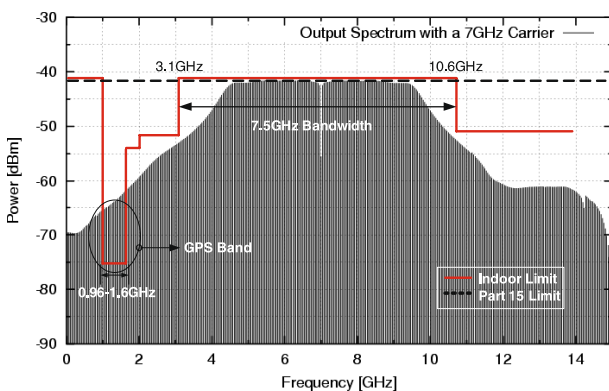


Fig. D.8. Frequency spectrum of the up-converted Daubechies' scaling function

Summary

The purpose of this book is to describe novel signal processing methodologies and analog integrated circuit techniques for low-power biomedical systems.

Physiological signals, such as the electrocardiogram (ECG), the electroencephalogram (EEG) and the electromyogram (EMG) are mostly non-stationary. The main difficulty in dealing with biomedical signal processing is that the information of interest is often a combination of features that are well localized temporally (e.g., spikes) and others that are more diffuse (e.g., small oscillations). This requires the use of analysis methods sufficiently versatile to handle events that can be at opposite extremes in terms of their time-frequency localization.

The Wavelet Transform (WT) has been extensively used in biomedical signal processing, mainly due to the versatility of the wavelet tools. The WT has been shown to be a very efficient tool for local analysis of non-stationary and fast transient signals due to its good estimation of time and frequency (scale) localizations. Being a multiscale analysis technique, it offers the possibility of selective noise filtering and reliable parameter estimation. Signal analysis methods derived from wavelet analysis carry large potential to support a wide range of biomedical signal processing applications including noise reduction, feature recognition and signal compression. The discussion here deals with wavelet techniques for cardiac signals analysis.

Often WT systems employ the discrete wavelet transform, implemented on a digital signal processor. However, in ultra low-power applications such as biomedical implantable devices, it is not suitable to implement the WT by means of digital circuitry due to the relatively high power consumption associated with the required A/D converter. Low-power analog realization of the wavelet transform enables its application *in vivo*, e.g. in pacemakers, where the wavelet transform provides a means to extremely reliable cardiac signal detection.

In this book we present a novel method for implementing signal processing based on the WT in an analog way. The methodology presented focuses on the development of ultra low-power analog integrated circuits that implement the required signal processing, taking into account the limitations imposed by an implantable device.

From the wavelet definition, we state that the implementation of a wavelet filter is based on the design of a bandpass filter that presents an impulse response equal to a wavelet base. To obtain the transfer function of a particular wavelet filter, mathematical approximation techniques are required. We indicate several methods to obtain good approximations in the time domain of the wavelet bases functions. One important objective of the introduced approaches is that the resulting approximated function should be rational and stable in the Laplace domain. This means that the approximating function must lead to a physically realizable network. Nevertheless, we can notice that due to limitations in chip area, power consumption and coefficient matching, there is a trade-off between the approximation accuracy versus the order of the implemented filter. Thus, the design challenge is to obtain a low-order system while preserving a good approximation to the intended function. Due to their general applicability and excellent accuracy, the Padé and the L_2 approximations were chosen, which generate reasonably low-order and good-fit transfer functions.

Subsequently, there are many possible state space descriptions for a circuit that implements a particular transfer function. The same holds for practical realizations. This allows the designer to find a circuit that fits specific requirements. From two newly defined figure-of merits, we concluded that the orthonormal ladder structure is the optimal state space representation with respect to dynamic range, sparsity and sensitivity, which represent the most important design aspects in low-power low-voltage analog filters.

A promising technique for the design of ultra low-power analog integrated circuits is the one of Dynamic Translinear (DTL) circuits. The translinear circuit approach is a current-mode technique, which is inherently non-linear and performs a compression and an expansion on the processed signal. The benefit of a companding (compressing-expanding) system is that a signal with a specific DR can be processed in a system block with a smaller DR than the signal, and by this, offer low-voltage and low-power operation. In addition, only transistors and capacitors are required to realize a filter function. Since in conventional ultra low-power designs resistors would become too large for on-chip integration, their superfluity is a very important advantage. Moreover, the DTL principle can be applied to the implementation of functions described by linear and non-linear polynomial differential equations.

Another suitable technique for low-power low-frequency filter design is based on CMOS triode strong-inversion nA/V transconductors for linear G_m -C filters. In the field of medical electronics, active filters with large time constants are often required to design low cutoff-frequency filters (in the Hz and sub-Hz range), necessitating the use of large capacitors or very low transconductances. To limit capacitors to practical values, a transconductor with an extremely small transconductance G_m (typically a few nA/V) is needed and transistors kept in the triode region benefit from a lower transconductance than the ones operating in saturation or weak-inversion regions.

Finally, the methodology presented is employed in the design of several ultra low-power biomedical systems and analog wavelet filters. The simulated and measured results demonstrate an excellent performance in generating the desired wavelet transform and achieving correct cardiac signal detection in an ultra low-power environment.

Acknowledgements

Certainly, this book would not have been possible without the support and understanding of many people.

This book evolved from Sandro Haddad's PhD thesis. Henceforth, we are obliged to the thesis' promotor John Long for his careful review and the members of the PhD defense committee, Arthur van Roermund, Igor Filanovsky, Paddy French, Michel Verhaegen and Ralf Peeters for their valuable feedback, which really improved the quality of this book.

We are indebted to our MSc students, Nanko Verwaal, Bas Gieltjes, Pietro Salvo, Alejandra Guillén and Mahdi Kashmiri for their relevant contributions to this work. Also, we would like to thank to Sumit Bagga, Jader de Lima and Peterson Agostinho for collaborating on some topics of our research.

Special thanks to the members of the BioSens project, Ronald Westra, Ralf Peeters and Joël Karel, for their inspiring discussions and support; and to Richard Houben, for the valuable and pleasant cooperation with Medtronic Bakken Research Center.

The financial support of the Dutch Technology Foundation (STW), under grant no. DTC 6418, is kindly acknowledged.

Thanks to the Delft Institute of Microsystems and Nanotechnology (DIMES) and IBM Microelectronics for fabrication access.

To all the members of the Electronic Research Laboratory of Delft University of Technology, for providing an excellent working environment.

Last, but certainly not least, we are very thankful to our family and friends. Their dedication and enthusiasm always encouraged us to pursue our objectives. Especially, we would like to express our deepest gratitude to our wives and children. For sure, this book would not have been completed successfully without their unconditional support and love.

About the Authors

Sandro A. P. Haddad was born in Anápolis, Brazil, on February 8, 1977. He received his B.Eng. degree from the University of Brasília (UnB), Brazil, in 2000, with honors. He was awarded the best-graduated student of the year, from the Faculty of Electrical Engineering, UnB. In February 2001, he joined the Electronics Research Laboratory, Delft University of Technology (TUDelft), The Netherlands, where he started research towards his PhD degree. His project was part of BioSens (Biomedical Signal Processing Platform for Low-Power Real-Time Sensing of Cardiac Signals). His research interests include low-voltage, ultra low-power analog electronics and biomedical systems, and high-frequency analog integrated circuits for UWB communications. He received his PhD degree in December 2006, with the thesis entitled “Ultra Low-Power Biomedical Signal Processing – An Analog Wavelet Filter Approach for Pacemakers”. In January 2007 he joined Freescale Semiconductor as Analog IC Designer. He authored and co-authored more than 40 publications.

Wouter A. Serdijn was born in Zoetermeer ('Sweet Lake City'), The Netherlands, in 1966. He started his course at the Faculty of Electrical Engineering at the Delft University of Technology in 1984, and received his ‘ingenieurs’ (M.Sc.) degree in 1989. Subsequently, he joined the Electronics Research Laboratory of the same university where he received his PhD in 1994. His research interests include low-voltage, ultra-low-power, high-frequency and dynamic-translinear analog integrated circuits along with circuits for RF and UWB wireless communications, cochlear implants, portable, wearable, implantable and injectable ExG recorders and pacemakers.

Dr. Serdijn is co-editor and co-author of the books Power Aware Architecting for data dominated applications (Springer, 2007), Adaptive Low-Power Circuits for Wireless Communications (Springer, 2006), Research Perspectives on Dynamic Translinear and Log-Domain Circuits (Kluwer Academic Publishers, Boston, 2000), Dynamic Translinear and Log-Domain Circuits (Kluwer Academic Publishers, Boston, 1998) and Low-Voltage Low-Power Analog Integrated Circuits (Kluwer Academic Publishers, Boston, 1995). He authored and co-authored more than 200 publications and presentations. He teaches Analog Electronics, Analog Signal Processing, Micropower Analog IC Design

and Electronic Design Techniques. In 2001 and 2004, he received the EE Best Teacher Award.

He has served as an Associate Editor for the IEEE Transactions on Circuits and Systems-I: Regular Paper (2004–2005) and the IEEE Transactions on Circuits and Systems-II: Express Briefs (2002–2003 and 2006–2007), as tutorial session Co-Chair for ISCAS 2003, as Analog Signal Processing Track Co-Chair for ISCAS 2004 and ISCAS 2005, as Chair of the Analog Signal Processing Technical Committee of the IEEE CAS society, as Analog Signal Processing Track Co-Chair for ICECS 2004, as Technical Program Committee member for the 2004 International Workshop on Biomedical Circuits and Systems, as International Program Committee member for IASTED CSS 2005 and CSS 2006, as Technical Program Committee member for APCCAS 2006, as Technical Program Committee member for the 2006 IEEE Biomedical Circuits and Systems Conference (BioCAS 2006), as Special-Session Co-Chair for ISCAS'2007 and currently serves as a member of the Board of Governors (BoG) of the Circuits and Systems Society, a member of the Conference Division of the CAS BoG, as a member of the CAS Long Term Strategy Committee. Recently, Dr. Serdijn was elected Deputy Editor in Chief for IEEE Transactions on Circuits and Systems-I: Regular Papers for 2008 and 2009, International Program Committee member of the 2009 International Conference on Biomedical Electronics and Devices, as Special Session Co-Chair for ISCAS 2009 and Technical Program Co-Chair for ISCAS 2010.

Index

- Analog delays, 179
Bessel–Thomson, 179
comparison of Bessel–Thomson and Padé, 183
Gaussian impulse-response method, 183
Padé approximation, 180
- Analog filters
 G_m –C, 95
log-domain, 101
switched-capacitor, 193
- Analog wavelet filter
approximations, 51
design, 48
- Analysis
cardiac signal, 3
morphological, 28
- Bessel–Thomson filters, 66
- Biomedical
low-power system designs, 131
signal processing, 1
- Biomedical systems
cardiac sense amplifier, 132
QRS-complex detection, 140
- Cardiac
diseases, 17
signal analysis, 3
signals, 16
- Chip microphotograph
impulse generator for ultra-wideband, 200
- Morlet wavelet log-domain filter, 166
- QRS-complex wavelet detection, 144
- translinear cardiac sense amplifier, 133
- Class-AB sinh integrator, 111
block diagram, 116
companding, 115
current splitter, 121
dynamic translinear loop, 119
linear differential equation, 120
low-power CMOS design, 120
low-power design, 118
state-space formulation, 111
static translinear loop, 118
V–I sinh transfer function, 116
- CMOS triode transconductor, 96
bias generator, 96
nA/V, 96
pA/V Delta- G_m , 99
wavelet filter design, 154
- Complex first-order filters, 51
complex Gaussian wavelet, 55
complex Morlet wavelet, 55
equation, 53
frequency response, 54
impulse response, 54
Poisson function, 54
transfer function, 54
- Dynamic range, 77
matrices transformation, 78
objective functional, 77
optimization, 78
optimum capacitance distribution, 80
- Dynamic range versus sparsity, 88
- Dynamic range-sparsity-sensitivity FOM, 93

- Filanovsky's filter approach, 67
 Fourier transform, 33
 Fourier-series method, 68
- Gramians
 controllability, 77
 observability, 77
- Heart, 14
 excitation and conduction system, 15
 Hyperbolic-sine integrator, 111
 low-power design, 118
- L_2 approximation, 63
 function, 64
 impulse response, 64
 mean-square error, 65
 Morlet wavelet bases, 64
- Lipschitz exponent, 43
- Log-domain class-AB filters
 performance comparison, 126
- Log-domain filter
 Adams' low-pass, 108
 bandpass biquad, 134
 block diagram, 104
 class-A, 105
 class-AB, 111
 complex first-order system, 141
 complex Gabor wavelet filter, 156
 differential equation, 105
 first-order low-pass, 104
 Gaussian wavelet filter, 149
 Morlet wavelet filter, 160
- Log-domain integrator, 103
 bipolar multiple-input, 105
 CMOS multiple-input, 106
 examples, 105
 high-frequency CMOS, 107
- Low-power integrators, 95
 Lyapunov equations, 77
- Mean square error, 51
- Measurements results
 impulse response and pulse position modulation, 201
 Morlet wavelet log-domain filter, 166
 QRS-complex wavelet detection, 144
- Model reduction
 balanced truncation method, 189
- Modulus maxima, 43
- Pacemaker, 18
 cardiac sense amplifier, 132
 demand, 22
 dual-chamber, 25
 history, 18
 Hyman's, 19
 implantable, 19
 new features, 26
 rate-responsive, 26
- Padé approximation, 56
 coefficients, 58
 function, 57
 Gaussian wavelet bases, 59
 mean-square error, 59
 Morlet wavelet bases, 63
 oscillated wavelet bases, 59
 Taylor series, 57
- Parseval's identity, 63
- Power consumption
 A/D converters, 6
 analog filters, 6
 analog sense amplifiers, 5
 analog versus digital circuitry, 4
 digital filters, 8
 digital sense amplifiers, 6
- Sensitivity, 90
- Sparsity, 80
 orthogonal transformations, 80
- Sparsity figure-of-merit, 89
- State space
 biquad structure, 84
 canonical form, 82
 description, 75

- Hessenberg decomposition, 80
orthonormal ladder structure, 85
Schur decomposition, 81
Switched-capacitor filter, 193
- Time-frequency resolution, 38
Translinear
 dynamic principle, 102
 filters, 101
 static principle, 101
Translinear circuits
 absolute value, 136, 143
 arctangent (phase detector), 159
 bandpass biquad filter, 134
 cardiac sense amplifier for pacemaker, 132
 CFOS wavelet filter, 141
 comparator (sign function), 137
 modulus (vector magnitude), 159
 peak detector, 143
 QRS-complex wavelet detection, 140
 RMS-DC converter, 136
 V-I converter, 133
- Ultra-wideband circuits, 199
autocorrelation receiver, 201
delay filter, 201
FCC compliant pulse generator, 203
- impulse generator, 199
pulse position modulator, 200
- Wavelet bases
 complex continuous-time, 41
 complex Gabor, 41
 continuous-time, 39
 Daubechies, 41
 Gaussian, 40
 Morlet, 40
- Wavelet bases approximation
 flowchart, 161
- Wavelet filter designs
 complex first-order system, 141
 complex Gabor, 156
 Gaussian, 149
 L_2 approximation, 154
 Morlet, 160
 optimized Padé implementation, 150
 switched-capacitor, 193
- Wavelet transform, 35
 biomedical applications, 2
 compression, 47
 denoising, 47
 regularity measurements, 45
 signal processing, 42
 singularity detection, 42
 vanishing moments, 45
- Windowing function, 34